Karlsruher Institut für Technologie

Damage mechanisms in superconductors due to the impact of high energy proton beams and radiation tolerance of cryogenic diodes used in particle accelerator magnet systems

Zur Erlangung des akademischen Grades eines
Doktors der Naturwissenschaften (Dr. rer. nat.)
von der KIT-Fakultät für Physik des
Karlsruher Instituts für Technologie (KIT)

genehmigte
Dissertation
von

M.Sc. Andreas Will

Tag der mündlichen Prüfung: 23.04.2021
Referentin: Prof. Dr. Anke-Susanne Müller
Korreferent: Prof. Dr. Rüdiger Schmidt

Contents

Symbols and Abbreviations

Abbreviations and Acronyms

CERN	*Conseil Européen pour la Recherche Nucléaire*
CHARM	*CERN High energy Accelerator Mixed field facility*, see [Tho+16; Tho16; Inf17; CHA]
HiRadMat	*High Radiation to Materials* irradiation facility at CERN, see [Eft+11; HiR; Evr+11]
HL-LHC	*High Luminosity Large Hadron Collider*
HTS	high temperature superconductor
LHC	*Large Hadron Collider*
LTS	low temperature superconductor
MQE	minimum quench energy
NIEL	non-ionizing energy loss
Quench	transition from superconducting to normal conducting state
RRP®	*Restack Rod Process ®*
RRR	residual resistivity ratio

Symbols

Φ_{neq}	1 MeV neutron equivalent (neq.) fluence (in cm^{-2})
Φ_{D}	total ionizing dose (in Gy)
e	electric elementary charge (in C)
$\hbar$	reduced Planck's constant (in J·s)
$\Phi_0 = \frac{h}{2e}$	magnetic flux quantum (in Wb)
k_B	Boltzman constant
ε	lattice strain (in %)
$\varepsilon_{0,irr}$	irreversible strain (in %) above which permanent degradation is expected
T_c	critical temperature (in K)
B_{c2}	upper critical magnetic field (in T)
$B_{c2,0}$	upper critical magnetic field at zero strain and zero temperature (in T)
I_c, J_c	critical transport current (in A) and current density (in $\mathrm{A{\cdot}m^{-2}}$)

Part I

Overview: LHC and machine protection

1 Introduction

High energy hadron accelerators and colliders such as the *Large Hadron Collider* (LHC) at CERN and it's upgrade to achieve higher luminosity, the *High Luminosity Large Hadron Collider* (HL-LHC) require superconducting magnets to provide the large magnetic fields, needed to steer and focus the particle beams at these high energies. The superconducting magnets and their components are exposed to radiation during the operation, mainly resulting from primary and secondary particles from beam losses.

Two types of beam losses occur and their effects on certain accelerator magnet components have been studied in the scope of this thesis. In the HL-LHC upgrade the beam intensity will be roughly doubled [Apo+17]. The total stored beam energy of the LHC at top energy exceeds 350 MJ and will double in HL-LHC as well. Both types of losses scale with the circulating beam intensity and need to be considered when increasing it to estimate the severity.

Firstly, fast failures can lead to parts of the beam being lost in short time. Such beam losses can lead to significant local energy deposition in the material and to thermo-mechanical stresses therein. The superconductors used in accelerator magnets, especially such as Nb_3Sn are sensitive to thermo-mechanical stresses and can permanently change their superconducting parameters, such as critical field, temperature and current. These parameters are crucial to the safe and reliable operation of the superconducting magnets and degradation of these parameters due to radiation impact would potentially require magnet replacement. Aside from the financial aspect, replacing a magnet would result in downtime of the full accelerator, limiting the availability to provide particle beams to the experiments. Special studies investigating the degradation of the superconductors due to high energetic proton beam impact are needed to evaluate the severity of potential fast failures leading to beam impact.

Secondly, there are naturally occurring steady losses into the magnet apertures. They originate from interaction of the particle beams with residual gas molecules or from particle debris in interaction or collision points and lead to accumulation of radiation doses and particle fluence in the magnet components. The energy deposition rates usually remain small in this case, but can be large enough to provoke a loss of superconductivity, a so-called quench. As the stored energy of an LHC dipole at full field is about 7 MJ [FC17], cryogenic diodes are used as part of the magnet protection systems to allow the fast and safe energy extraction of the coils in case of a quench.

During the lifetime of the accelerator magnet, there is an accumulation of radiation induced damage, e.g. in semiconductor based components used in the protection electronics such as the cryogenic diodes or in polymeric insulation materials surrounding the superconductors. In the context of HL-LHC new final focus quadrupole magnet triplets based on Nb_3Sn will be installed [Apo+17; Fer+14]. The powering layout of these magnet circuits foresees the use of cryogenic power diodes, connected in parallel to each magnet. They serve as passive protection of the sensitive coils in case of a quench, by regulating the voltages over the magnets. The triplet magnets are connected and powered in series with a maximum current of up to 18 kA and, thus, the cryogenic diodes installed in their circuits need to fulfill certain electrical requirements to ensure safe operation during their lifetime. The diodes are located inside an extension to the magnet cryostat and operated in superfluid helium, where they are hence exposed to mixed radiation fields originating from beam losses and debris from the interaction region, located in close proximity. A suitable diode type is usually found in extensive experimental irradiation programs to ensure the correct functionality during the full lifetime. In HL-LHC this means after the accumulated 1 MeV neq. fluence of $\Phi_{\mathrm{neq}} \approx 5 \cdot 10^{13}\,\mathrm{cm}^{-2}$ [Gar+18; Ler+19].

The execution and analyses of two experiments are described in this thesis.
A first experiment with beam impact on superconductors in a cryogenic environment was performed at CERN's HiRadMat facility. Three types of superconductors were tested with 440 GeV proton beams. The superconductor samples used were short wires based on the low temperature superconductors (LTS) Nb-Ti, Nb_3Sn and tapes based on the high temperature superconductor (HTS) YBCO. Afterwards, the irradiated samples were analysed for their critical transport current and critical field, as well as inspected with optical and electron microscopic methods. The experimental setup, the samples and the subsequent measurements and analysis of the beam impacted samples is described in part II of this thesis.
In a second experiment, the radiation hardness of existing LHC bypass diodes and prototype diodes, which are likely to be more radiation tolerant, was tested beyond the radiation dose expected at the location of the diodes during the lifetime of the HL-LHC. An experiment was set up, which allowed the irradiation and in situ measurements of three different types of diodes while held at cryogenic temperatures. All prototypes were analyzed for forward and reverse bias voltage characteristics and the temperature dependence while warming up. Also their thermal annealing potential could be evaluated after the irradiation program. The experimental setup, the samples and in situ measurements and analysis are described in part III of this thesis.

Part I of this thesis briefly describes the CERN accelerator complex and the two irradiation facilities at CERN where the experiments were performed. The superconducting NbTi magnets, which have been in operation in the LHC for many years, and the novel $Nb3_3Sn$-based dipole and quadrupole magnets for the HL-LHC upgrade are presented. The mechanism for fast and steady beam losses and their impact on the LHC equipment are discussed.

1.1 CERN accelerator complex and irradiation facilities

The part of the LHC accelerator complex at CERN, relevant in the scope of this thesis, is schematically shown in Fig. 1.1. The acceleration is done in steps via a linear accelerator and several synchrotron rings. The graphics shows the full chain from generation of hydrogen ions in the linear accelerator *LINAC4*, to the *Booster*, the *Proton Synchrotron* (PS), the *Super Proton Synchrotron* (SPS) and finally the LHC. The SPS allows to inject protons into the LHC via two injection lines as indicated in the figure, such that two counter-rotating beams are circulating in LHC. There are four interaction points (IPs) where beams can be brought into collision and experiments are installed to observe the collision events with large detectors. The LHC has a circumference of roughly 27 km with circular bending sections followed by longer straight sections. The maximum energy is 7 TeV per beam at a maximum magnetic field of $B = 8.3\,\mathrm{T}$, which yields a bending radius of $\rho = 2.8\,\mathrm{km}$ in the bending sections [Bru+04].

Two irradiation facilities are indicated, relevant in the scope of this thesis. HiRadMat, providing 440 GeV proton beams from the SPS to fixed targets with a focus on material testing under these

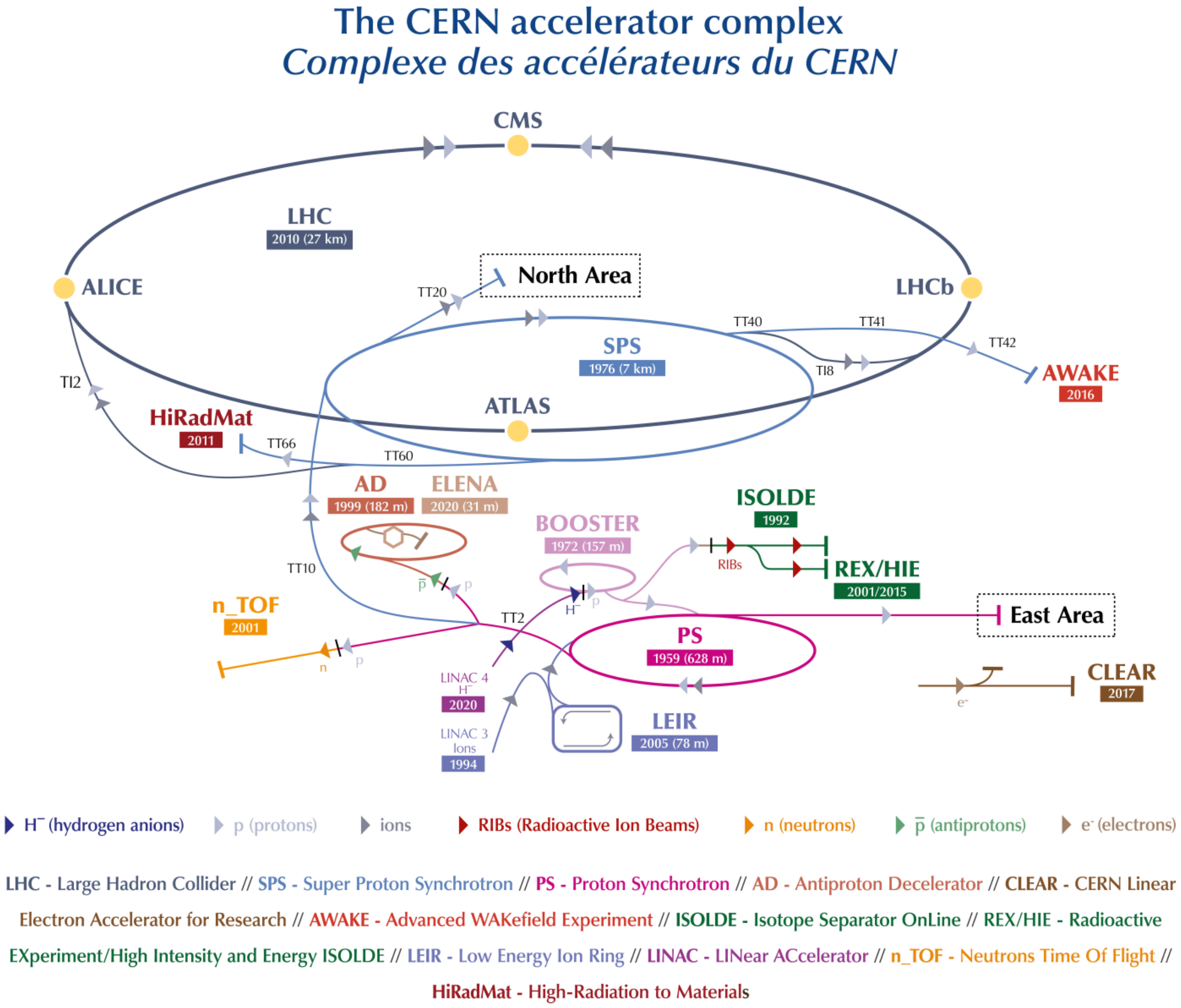

Figure 1.1 – The CERN accelerator complex. The full injector chain up to LHC for protons is shown. Two facilities relevant in the scope of this thesis are the HiRadMat facility, connected to the SPS, and the CHARM facility located at the East Area. Image from [Mob19].

extreme conditions, as well as the CHARM irradiation facility, providing mixed radiation fields for testing of electronic components by impacting a target with high energy protons from the PS. HiRadMat will be described in the following section 1.1.1 and within the context of the experiments covered in this thesis in section 5.2.3. CHARM will be described in the following section 1.1.2 and in the context of an irradiation experiment covered in this thesis in section 8.2.1.

1.1.1 HiRadMat

HiRadMat (*High-radiation to Materials*) is a unique irradiation facility at CERN, which can provide proton beam pulses with an energy of 440 GeV towards fixed targets [Eft+11; HiR; Evr+11]. As shown above, the beam is delivered from the SPS, with a maximum of 288 bunches with 25 ns bunch spacing. The number of bunches per pulse and the beam size σ can be adapted from $\sigma = 0.25$ mm to $\sigma \approx 4$ mm. Figure 1.2 shows an image of the facility, with the indicated beam axis,

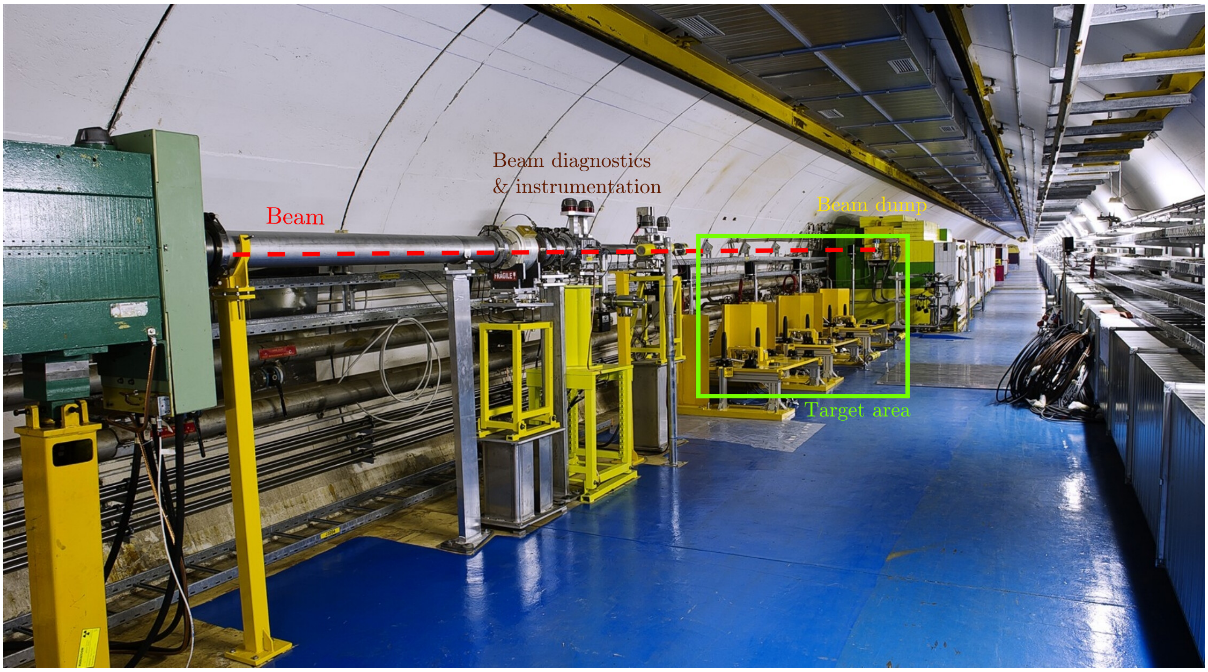

Figure 1.2 – Overview of the HiRadMat facility [Eft+11; HiR; Evr+11]. Image adapted from [Bri11].

the area for the fixed targets and the beam dump. Also indicated are the beam diagnostics and instrumentation which allow to verify the beam position after each shot [Evr+11]. This information is used online to steer and guide the incoming particle pulses accurately and repetitively with high precision to the targets. The facility is designed to verify and calibrate the beam axis with pilot bunches of low intensities and with the help of online diagnostics. Once the accelerator optics is set, the beam axis usually stays fixed and the targets are moved relative to it. The setups are mounted on experimental tables, which are placed on the sockets visible in Fig. 1.2. The experiments can be set up and tested in a laboratory above ground on the experimental tables which are then accurately installed in the facility via fiducial marks and metrological tracking. The facility is not designed to deliver large integrated doses but delivers high intensity pulsed beams to test the effects on accelerator equipment and materials [HiR]. Signal wires from online and in situ instrumentation on the target setup can be connected to a shielded neighbouring tunnel via feed-throughs where the readout electronics can be installed protected from radiation.

1.1.2 CHARM

The CERN High energy Accelerator Mixed field facility (CHARM) is an irradiation facility at CERN [Tho+16; Tho16; Inf17; CHA]. It can provide radiation fields of various composition and intensity to users. As shown in Fig. 1.1, CHARM takes proton beam pulses from the PS accelerator with an energy of 24 GeV. A central target of either solid Copper, solid Aluminum or perforated Aluminum, i.e. Aluminum with reduced effective density, is impacted by a 24 GeV proton beam from CERN's Proton Synchrotron (PS). The interaction with the different targets produces varying secondary particle spectra. Furthermore, the composition, dose and particle fluences are depending on the relative position to the target and shielding configuration. Figure 1.3 shows the facility schematics as well as an image of the inside. The different defined user positions are indicated for which the according particle spectra, doses and fluences were well studied and calculated

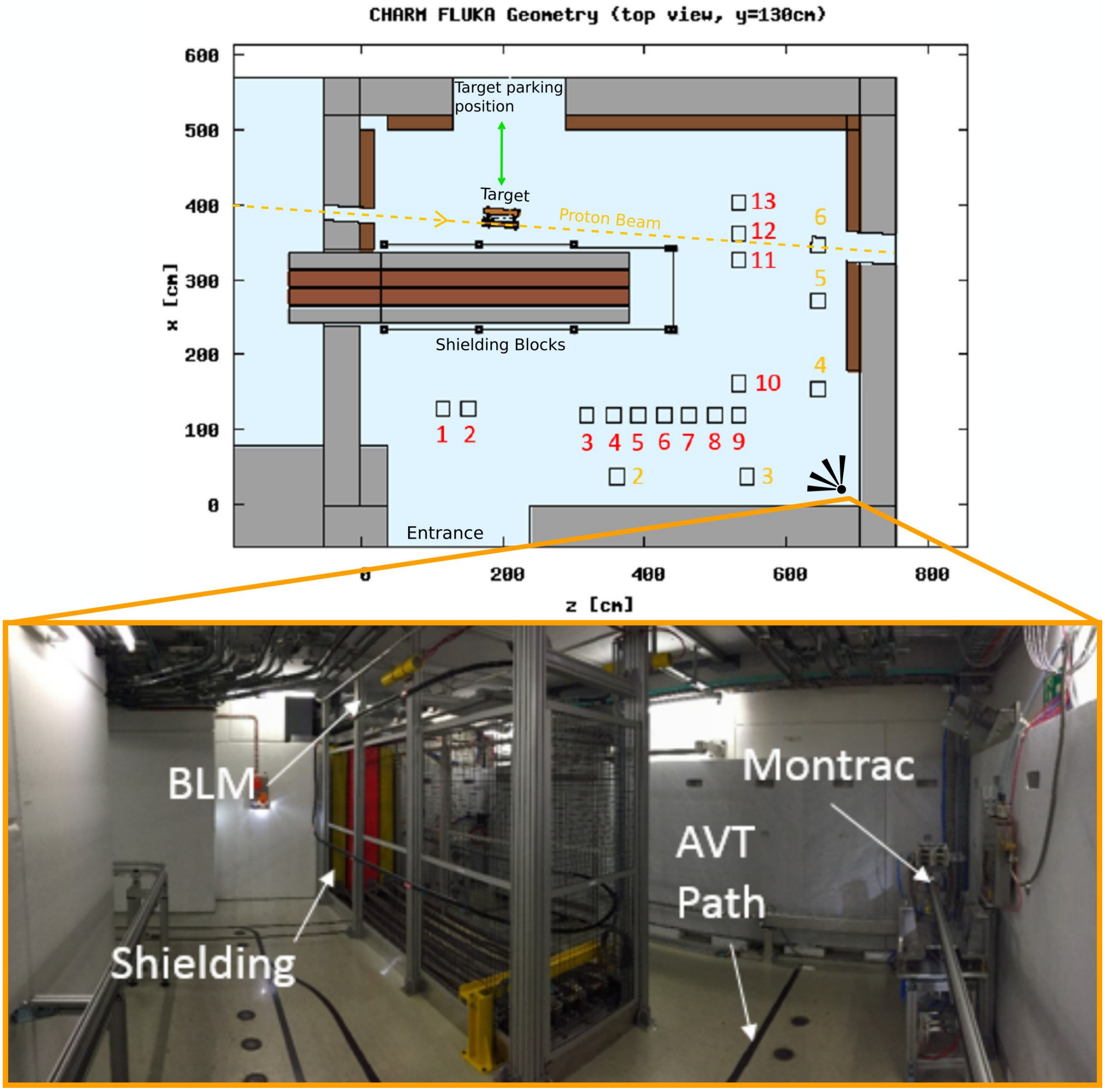

Figure 1.3 – *Top:* Geometric overview of the CHARM facility with several testing positions. The shielding blocks can be moved out. Image adapted from [Tho16]. *Bottom:* Point of view inside the CHARM facility. Image taken from [Tho16].

(see [Inf17]). The facility is accessible via a long concrete chicane for radiation protection. The control room is located above the facility. Electrical equipment can be installed there, protected from radiation. Signal wiring and cabling can be fed out via patch panels that terminate in the control room.

1.2 Superconducting accelerator magnets

There are several ways to construct multipole magnet coils. For dipole magnets the most common coil types are the $\cos\theta$ (*"cosine theta"*), the *block coil* or *Racetrack coil* and the *common coil* type [SZ19]. The most common type used in accelerator magnets is the $\cos\theta$, but future high energy hadron colliders might use the common coil design [SZ19]. This thesis will only cover the $\cos\theta$ design in the framework of LHC and HL-LHC superconducting magnets.

Given a cylindrical symmetric magnet with the symmetry axis along z in vacuum, the radial and azimuthal components of the magnetic flux density are calculated as

$$\begin{aligned} B_r(r,\varphi) &= \sum_{n=1}^{\infty} nr^{n-1}\left(C_n\cos(n\varphi)+D_n\sin(n\varphi)\right) && (1.1)\\ B_\varphi(r,\varphi) &= -\sum_{n=1}^{\infty} nr^{n-1}\left(C_n\sin(n\varphi)-D_n\cos(n\varphi)\right) && (1.2)\end{aligned}$$

with multipole coefficients C_n and D_n and multipole order n [Rus10]. The fields of multipole order n show n-fold rotational symmetry in φ. Furthermore, for constant radius $r = r_0$, the Eqns. (1.1,1.2) are identical to the Fourier series. The $\cos\theta$ design makes use of this in the way that the conductors are placed along an azimuthal shell at a distance of a certain constant radius. The current density is a distribution with a dependence on the azimuthal angle θ such that $J = J_0\cos\theta$ is approximated as close as technically feasible, to reduce the field errors.

1.2.1 The LHC superconducting main dipole and quadrupole magnets

The LHC superconducting dipoles are an example for the $\cos\theta$ design, and the magnet cross sections are shown in Fig. 1.4. The conductor cross sections are filled with Rutherford cables of an almost rectangular cross section, as will be described in more detail in section 3.2.3. The Rutherford cables are wound from Nb-Ti based wires which are discussed in more detail in section 4.2 and the LHC type wire specifically in section 4.2.3. The coils wound in this manner are enclosed by stainless steel collars and those are embedded in a magnetic yoke. The collars are pre-stressed to compensate for the mismatch in thermal contraction, when cooling down to cryogenic temperatures [Bru+04]. During powering, they additionally take the Lorentz forces from the coils, which are directed mostly outwards. Two apertures are embedded side by side to guide the two proton beams which rotate in opposite directions. Both LHC dipole and quadrupole cross sections are shown in Fig. 1.4. This assembly (the cold mass) is enclosed in a cryostat shell and the shell is wrapped in multi layer insulation. The inner cold mass is surrounded by an additional heat shield at slightly elevated temperatures and both are housed in a vacuum vessel. A total of 1232 main dipole magnets and 392 main quadrupole magnets of this type are installed in the LHC [Ros03].

1.2.2 Magnets for the High-Luminosity upgrade

In the HL-LHC upgrade of the LHC several changes and upgrades to the machine are foreseen. An important upgrade of the final focus quadrupole triplets (“inner triplets”) is foreseen as well as the installation of 11 T dipole bending magnets. These magnets will be based on Nb_3Sn wires. Superconducting wires based on Nb_3Sn are discussed in more detail in section 4.3 and the HL-LHC type RRP® wire specifically in section 4.3.2.

The HL-LHC 11 T Nb_3Sn based dipoles (MBH) are foreseen to be installed in the dispersion suppressor regions [Apo+17]. Two 11 T dipoles will replace one LHC main dipole and the additional space between the two 11 T dipole cryostats will be used to install additional collimators

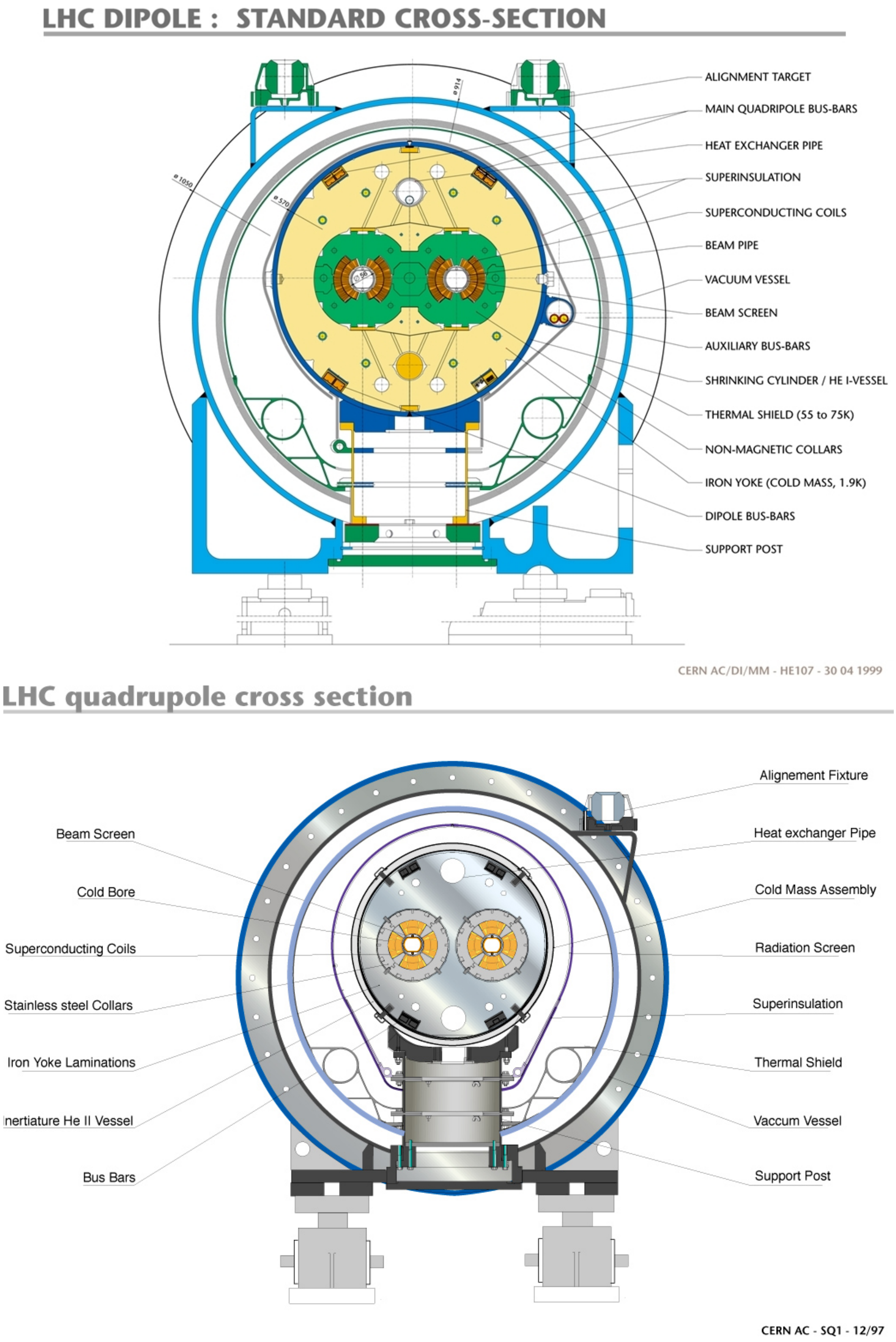

Figure 1.4 – Cross sections of the LHC dipole magnet (top, [Dai99]) and the LHC quadrupole magnet (bottom, [Car98]).

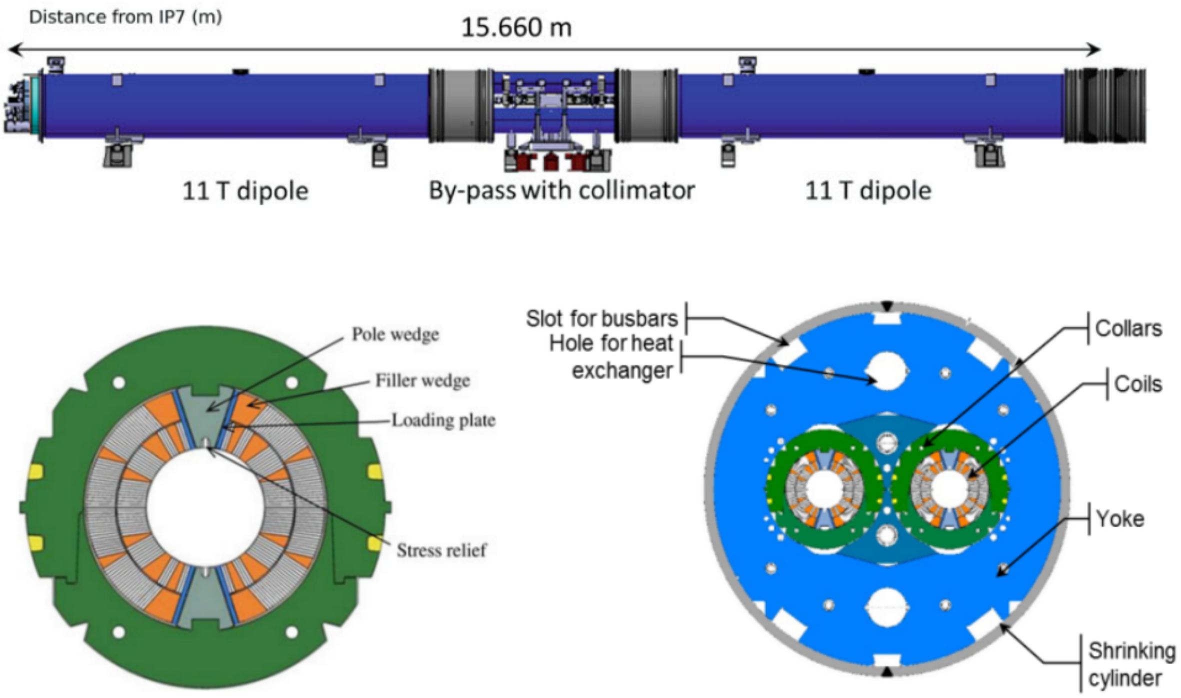

Figure 1.5 – Drawing of two 11 T dipole magnets as will be installed in the HL-LHC with the collimator in between (top, Image adapted from Fig. **9.1** in [SZ19]), the cross section with collars (bottom left, Image from Fig. **9.3** in [SZ19]) and the full cold mass assembly with yokes and shrinking cylinder (bottom right, Image adapted from Fig. **7** in [Bej15]).

to handle increased beam intensities [Apo+17]. The integrated fields of the the main bend of $(14.3\,\mathrm{m})\cdot(8.33\,\mathrm{T})\simeq 119\,\mathrm{Tm}$ needs to be matched with two 11 T dipoles and a length of about 5.417 m [Apo+17] such that $2\cdot(11\,\mathrm{T})\cdot(5.417\,\mathrm{m})\simeq 119\,\mathrm{Tm}$ is achieved but almost 3.5 m of space are gained [SZ19]. The planned installation of such a pair of MBHs with a collimator in the middle is shown in Fig. 1.5. Also the coil cross section and the collared coils in a twin aperture surrounded by a yoke and enclosed by a shrinking shell are shown.

The HL-LHC Nb$_3$Sn low β^* final focus quadrupole triplets (“inner triplets” or “MQXF”) are the most important magnetic upgrade within the HL-LHC project and enable the reduction of the beam size in the interaction points (IP) 1 and 5, where the largest experiments ATLAS [Col08a] and CMS [Col08b] are located. This reduction of beam size is directly resulting in an increase of instantaneous luminosity.

The magnet cross section with the collared coil in a single aperture surrounded by a collar and iron yoke and enclosed by an Aluminum shell all embedded in the stainless steel vessel is shown in Fig. 1.6. The planned installation of such a quadrupole triplet is shown schematically in Fig. 1.7 with the distance to the IPs and the relevant technical specifications. The electrical circuits and protection scheme will be discussed in more detail in section 7.2.

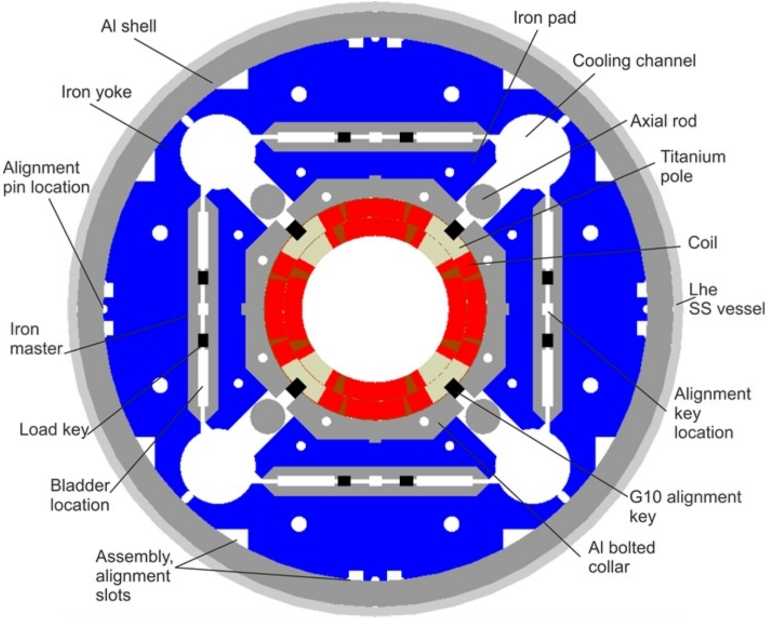

Figure 1.6 – Cross section of the inner triplet quadrupole magnets (MQXF). Image from [FA+], originally published also in [Amb15].

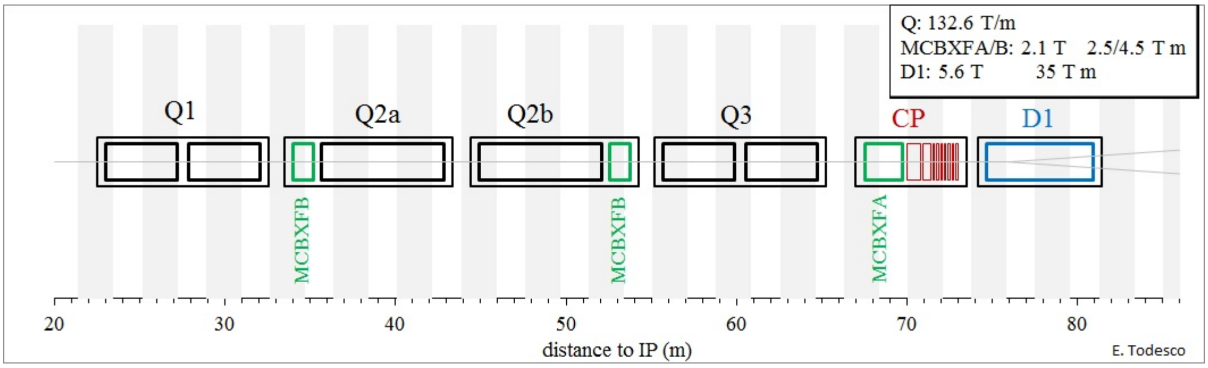

Figure 1.7 – Schematics of the layout of the inner triplet magnets Q1, Q2a, Q2b and Q3 as a function of their distance to the interaction point (IP). Image from [Tod], an altered version was originally published in [Apo+17].

2 Failures and protection of particle accelerator magnets

Failures are unavoidable during operation of complex systems like large accelerators and it is crucial to understand potential failures and their impact on the machine. Depending on the severity, they need to safely be mitigated, either by passive systems or active monitoring of machine parameters and fast intervention in case of failure detection. This chapter will cover the basics of beam-matter interaction and present some failure cases leading to interaction of high energy particles (primary or secondary) with the accelerator magnets and the superconductors as well as the cryogenic diodes used for protection of the magnets in case of a quench, as will be motivated below.

2.1 Effects of beam-matter interaction

In the following, a brief overview on the physical processes of the interaction of high energetic particles with solid matter is given. It is mostly based on the work of *Leroy* and *Rancoita* [LR16], which is suggested for further reading on the topic.

Particle matter interaction can be split in two different groups: The ionization energy loss, if an incoming particle transfers parts of its energy to atomic electrons and excites or ionizes them, and the displacement damage or simply non-ionizing energy loss (NIEL), where the energy is transferred to the atom via collisions and either the atom is displaced as a whole or the excess energy is dissipated via phonons [LR16]. Especially for charged particles the energy losses via ionization are much more prominent, resulting from the coulomb interactions with electrons. NIEL is also possible by interaction of charged particles with the charged nuclei. For neutrons the non-ionizing losses are relevant as they interact via the strong force with the nuclei. Nuclear reactions are possible, resulting in other elements or isotopes being present in the material after the irradiation as well as activation of materials, if unstable isotopes are created. Another interaction mechanism for charged particles is the radiative loss or Bremsstrahlung, when accelerated in the Coulomb field of both, electrons or the nuclei. The radiative losses are more prominent for lighter particles like electrons or positrons. For heavier particles they become relevant at much higher energies.

The displacement damage usually leads to a change of the physical properties that depend on phonons, as the crystal lattice is altered. Changes in the physical material properties, such as thermal conductivity, thermal heat capacity but also changes in the mechanical properties are the consequence, leading to swelling, embrittlement and ultimately potential mechanical failure of the material for large displacement damages [Lec18]. Especially semiconductors are sensitive to a change in the crystal lattice. The phonon properties, electrical conductivity and carrier lifetimes change significantly with an increase in displacement damage. Devices relying on these properties might alter their functionality with increasing displacement damage. Chapter 6 will further elaborate on this issue.

The ionizing energy losses are Coulomb interactions of the incident (charged) particle with the atom electrons of the impacted matter. The electrons will gain a certain kinetic energy from the collision and either be excited or detached from the atom, i.e. the atom will be ionized. The electron might likewise interact further or leave the subjected matter, which is then referred to as δ-rays [LR12]. The process leads to an energy deposition and a temperature increase of the material. The energy transfer per interaction is usually small and a high energetic incident particle will interact with many electrons before having lost all its energy [Lec18]. This electronic stopping power is relevant for smaller particle energies, or for originally high energetic particles which have already lost energy in multiple scattering events or radiative loss events.

Radiative losses, producing γ photons with large enough energy might lead to a particle cascade of electron-positron pairs (electromagnetic shower), eventually dissipating their energy via electronic ionizing losses or leaving the matter as δ-rays. Photons can also interact via Compton scattering on electrons or be absorbed (photo-electric effect).

Nuclear reactions, especially inelastic nuclear collisions occur for heavier particles at sufficiently high energies. This leads to a creation of secondary hadronic particles, like protons, neutrons, pions or kaons, which then continue to interact with the matter (hadronic showers) or decay into other particles (muons, neutrinos) or γ-photons, leading to electromagnetic shower cascades, as described above [Lec18]. Therefore, apart from the neutrons, all charged particle cascades will eventually dissipate their energy in the electronic losses. Neutrons can range far, only interacting via nuclear collisions, slowly thermalizing and eventually being captured [Lec18].

The exact type of interaction is a stochastic process, with cross sections for each possible interaction depending on the particle types and energies. The calculation is almost exclusively done via Monte-Carlo based codes, which use tabulated values for the cross sections and material properties. Both the average deposited energy and the radiation displacement damage can be evaluated in this type of software with moderate stochastic uncertainty. In the scope of this thesis, the well benchmarked and established FLUKA Monte-Carlo code [Böh+14; Fer+05] was used exclusively for this type of calculation.

The effects of beam matter interaction on accelerator magnets are different depending on the type of magnet component.
Ionizing energy deposition is usually less of a problem in metals and semiconductors as the charge neutrality can be restored simply via the mobile charge carriers. For low dose rates, the increase in temperature might be tolerable and may be simply cooled away. When many high energetic particles impact matter localized in a short timescale, the situation is very different. The material's heat conductivity might be too slow and local hot-spots and large thermal gradients occur. Large thermal strains and thermal shock waves are the consequence [SW04]. The material's structure might be altered locally, also due to diffusive processes and material phase transformations or even local melting.
On the other hand, insulating materials can build up significant charge due to the ionization. Materials, that rely on chemical bonds, such as many organic compounds commonly used for insulation (Polyamide etc.) can be severely affected, when such bonds are broken by the ionization process. They usually degrade significantly in their structural stability and suffer from degradation of the desired properties such as the insulation strength. Many of the generally used materials are tested in facilities worldwide under the influence of radiation both in large ionizing doses ranging

up to the mega-Gray level, but also exposed to large neutron or other high energy hadron fluences. In the design phase of accelerator magnet components used in radiation environments it is helpful to look up the experimental data (e.g. [GHT01]) and choose an appropriate material for the use-case. For electrical devices during operation, an induced charge might disturb the functionality. For electric components however, each device is specific and usually extensive irradiation and test programs are executed to verify the correct functionality of the device.

2.2 Steady beam losses

Steady beam losses occur in an accelerator environment during operation. A main source of steady state beam losses are scattering of the accelerated particles on residual gas in the vacuum pipes, which happens all around the accelerator. Furthermore, close to the interaction region, the radiation levels are strongly increased, resulting from the particle collisions and the subsequent scattering and interaction processes with the surrounding detector matter at the interaction points. The focusing magnets close to the interaction points see comparably large integrated doses and particle fluences during their lifetime.

The interaction of particles from the steady beam losses with the accelerator components lead to creation of other secondary particles, energy deposition into the material and radiation damage, as described above. The energy deposition due to these beam losses is usually kept small, in the order of less than $1\,\frac{\text{mJ}}{\text{cm}^3}$ [Lec18]. To allow for safe operation of the superconducting magnets, the beam losses need to be monitored and threshold levels need to be defined. In LHC, the beam loss rates are constantly monitored via ionization chambers placed all around the ring [Hol+12]. Furthermore, the energies needed to provoke a quench by impacting beam particles were well studied and the threshold values including safety factors accordingly set [Hol+12]. In case the dose rates observed exceed the threshold, the beam can be safely extracted from the accelerator before a quench occurs.

2.3 Fast failure scenarios and short time-scale energy deposition

A timescale intrinsic to each circular accelerator is the revolution time or turn-around time it takes for the particles to travel once around the full circumference. For LHC with a circumference of roughly 27 km and particles traveling roughly at the speed of light it is about 89 µs. Failures that imply drastic consequences to the machine within this time scale can't be mitigated actively, as the beam can not be extracted in time beforehand. They are called ultra fast failures [SW04]. The passive protection against these failures consists of beam absorbers and collimators. If the evolution of the fault is slower than a few revolution times, and the detection is fast enough, the beam can be extracted immediately after the detection of the failure to avoid further consequences, like losing the circulating beam to the accelerator aperture. For this reason, the machine is not fully filled with proton bunches, but a 3 µs gap is left empty. Dedicated kicker magnets are used for injection and beam extraction, which have to be ramped to maximum field during this time in order to deflect the beam either on the trajectory during injection or out of the storage ring during beam extraction.

On the other hand, the injection or extraction kicker magnets themselves can be sources of ultra fast failure. In case one or several of the 15 kicker magnets are not working properly, either by

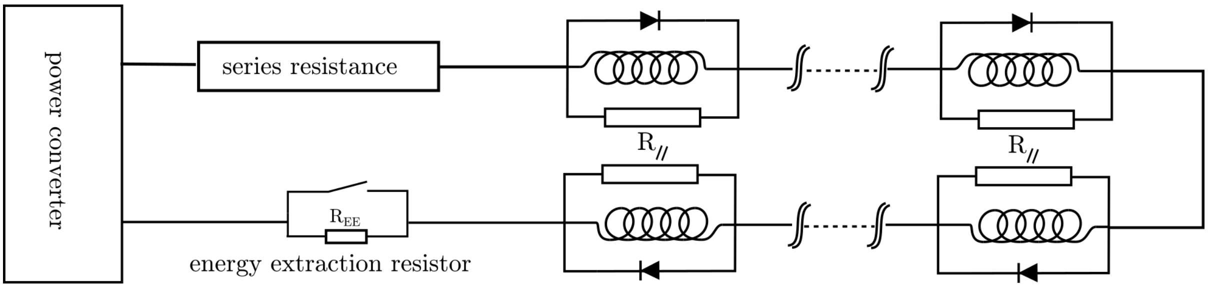

Figure 2.1 – Schematic powering circuit of several magnets in a string. In this schematics each magnet is equipped with a bypass diode, connected in parallel. Also indicated are the energy extraction switch and resistor. Image inspired by [CM09].

ramping the magnetic field at a wrong time or not ramping up at all when needed, the desired beam deflection can't be achieved. During injection, the circulating beam with an energy of 450 GeV will then be deflected on a wrong trajectory and finally be dissipated into the absorbers. The resulting secondary beam showers might reach the downstream magnets. A similar kicker failure during extraction will likewise result in a wrong particle beam trajectory, however, the beam energy during extraction is usually at maximum, i.e. 6.5 TeV in LHC. The beam stored energy and its potential to deposit into the collimators and absorbers as well as the downstream magnets is consequently much larger. In HL-LHC the beam intensities are roughly doubled and the resulting energy deposition into the accelerator equipment will scale accordingly. Especially the most sensitive parts of accelerator magnets, the superconducting coils, need to be considered when being impacted in such a failure scenario. Studies on the behaviour and damage limits of accelerator magnets and their components have been performed and are ongoing. Especially the impact of such high energy particle beams on superconductors used to construct these magnets is studied. Chapter 5 will present the first beam impact experiment on superconducting wire samples in a cryogenic environment with proton beams at an energy of 440 GeV, conducted at CERN's HiRadMat facility.

2.4 Powering circuits and protection in case of quench

Superconducting magnets in accelerator circuits need to be powered up to high currents I of several kilo amperes. With an inductance L of a few mH, the stored energy $W{=}L\,I^2$ is significant and quickly approaches a few MJ. In case of a quench, this stored energy needs to be extracted safely to not damage the superconducting coils or even the full magnet assembly.

To protect an individual magnet in case of a quench, it is important to understand the transient quench behaviour. Usually a small zone becomes normal conducting and if the current continues to flow, the Joule heating will increase the temperature of this hot-spot quickly. Heat conduction along the wire as well as to neighbouring wires and cables will let the quench propagate, increasing the normal conducting zone. If the local heating deposits the energy faster than the heat diffusion allows it to propagate further, the local temperature drastically increases and the magnet is at risk of locally burning out. Subsequent drastic consequences like Helium evaporation and explosions of the cryostat might be possible. Apart from that, the locally induced stresses might damage the superconductor already before such a drastic scenario. Hence, the deposition of the stored energy into a small localized zone should be avoided.

One common concept for that is the use of quench heaters. These are heating strips attached to the superconducting coils, which can deposit thermal energy homogeneously along the coil, in case a quench is detected. Due to the small heat capacity at the very low temperatures, a few joule are usually sufficient to lift the coil above the critical temperature of the superconductor. As a result the stored energy is dissipated more evenly along the full magnet, which is now in a completely quenched or normal conductive state. Another concept developed more recently, is the CLIQ system [Rav15]. Large AC pulses are injected in addition to the DC powering current in order to lift the superconductor above its critical current. The advantage of this system is, that it also works at elevated temperatures, independent of the material's heat capacity. On the other hand, it can only be used with the superconductor in a powered state rather close to its maximum critical current, as the injected current pulse amplitude can not be realized arbitrarily large.

Furthermore as mentioned above, several magnets might be powered in a string as shown in Fig. 2.1. The power converters are usually slow compared to the quench velocity and in case of a quench cannot be turned off fast enough, also due to the large inductive load with multiple magnets in series. A common concept is the use of bypass diodes, connected in parallel to each magnet individually in the string. The magnets are represented in Fig. 2.1 as an inductance (the superconducting coil), a parallel resistance (the copper matrix of the cables) and the diodes in parallel to each coil. As can be seen, these diodes are bypassing the current in case one magnet coil is quenching and the resulting voltage drop across the quenched coil due to the copper matrix resistance becomes larger than the turn-on or onset voltage of the diode. Consequently, only a tiny fraction of the current will flow through the quenched magnet and most of it will be conducted through the diode. In this state, the magnet will dissipate its own stored energy into the cold mass, as described above, but the external current flowing in the circuit will be safely bypassed around it. Once the quench is detected, the power converter can be ramped down, which might take several seconds or up to minutes, due to the inductance of the remaining coils in the string. An energy extraction dump resistor can be connected in series, such that the stored energy of the remaining powered coils can safely be burned off there. The diodes need to be special power diodes that can handle large currents and the resulting energy deposition due to Joule heating.

While larger equipment such as power converters can be placed away from the accelerator ring, shielded from radiation, the quench protection electronics and passive protection systems like the bypass diodes are usually placed in close proximity, to allow a direct and short current route. Especially the bypass diodes are often located inside the magnet cryostat, immersed in liquid Helium, not far away from the circulating beam. Chapter 6 explains the theoretical implications of radiation damage on power diodes, chapter 7 shows the explicit use-case of such diodes in LHC and HL-LHC.

The radiation damage to the magnet electronics accumulates gradually over time. Since the steady losses can in general not be avoided, their effects need to be understood and the equipment installed in the high radiation areas of accelerators need to be characterized to reliably function during their lifetime. The losses scale with beam intensity and in high luminosity machines, such as the HL-LHC, the increase in beam intensity by a factor of two will also lift the radiation levels to the machine components. Experimental irradiation programs where the devices are tested under the influence of radiation up to the foreseen integrated dose and particle fluence levels are a necessary tool to achieve this. Chapter 7 shows the details of cryogenic diodes used in LHC and HL-LHC circuits. Chapter 8 presents an irradiation program conducted to qualify cryogenic diodes which are to be used in the HL-LHC final focus quadrupole triplet magnet circuits.

Part II

Damage mechanisms in superconductors due to instantaneous proton beam impact

3 Introduction to superconductors

3.1 Theory of superconductivity

In the following, a brief overview on superconductivity is given. It is mostly based on the detailed work of *Tinkham* [Tin04], which is suggested for further reading on the topic.

Superconductivity is describing a phenomenon of a material's vanishing electrical resistance, when cooled down below a critical temperature T_c. Besides the critical temperature, there are two more parameters that limit the superconductivity, the critical magnetic field B_c and the critical current density J_c. If at least one of the parameters lies on or above the critical value, superconductivity breaks down. Two types of superconductors were identified, called *type I* and *type II* superconductors. Type I superconductors expel an external magnetic field, both in case the field was present before the onset of superconductivity and also if the field is applied to the superconductor already in the superconducting state. Type I superconductors are ideal diamagnets, i.e. supercurrents are induced, exactly compensating the external field. The field is not expelled completely but enters the surface and decays exponentially into the superconductor with a characteristic length, the so-called London-penetration depth λ_L [LL35]

$$\lambda_L = \sqrt{\frac{m_s}{\mu_0 n_s q_s^2}} \tag{3.1}$$

and the mass m_s, charge q_s and density n_s of superconducting charge carriers. Type II superconductors act as type I superconductors up to a certain critical field B_{c1}, the lower critical field. Above B_{c1} the flux lines partially enter the superconductor and normal conducting zones are formed around them (mixed state). The flux lines are quantized to contain exactly one flux quantum and a super-current around the entered flux line is induced. Superconductivity is still maintained for the largest parts of the superconductor. Above a – usually much higher – upper critical field B_{c2} superconductivity finally breaks down.

Ginzburg and Landau proposed an empirical description, in analogy to any other phase transitions of second order. The wave function $\Psi(\vec{r}, t)$ of all charge carriers in the superconducting state is the order parameter in this phase transition. Hence, $|\Psi|^2 = n_s$ is the density of superconducting charge carriers. It is zero above the critical parameter values and non zero below, where the superconducting state is present. The Gibbs free energy functional in the superconducting state can be expanded in a Taylor series taking into account the free energy in the normal conducting state and several terms accounting for the energy gain by expulsion of the magnetic field and also by the energy gain due to the surface energy when allowing the partial penetration of flux. Besides the London penetration depth in Eq. (3.1), a second length scale was found: the Ginzburg-Landau superconducting coherence length

$$\xi_{GL} = \sqrt{\frac{\hbar^2}{2 m_s \alpha}} \tag{3.2}$$

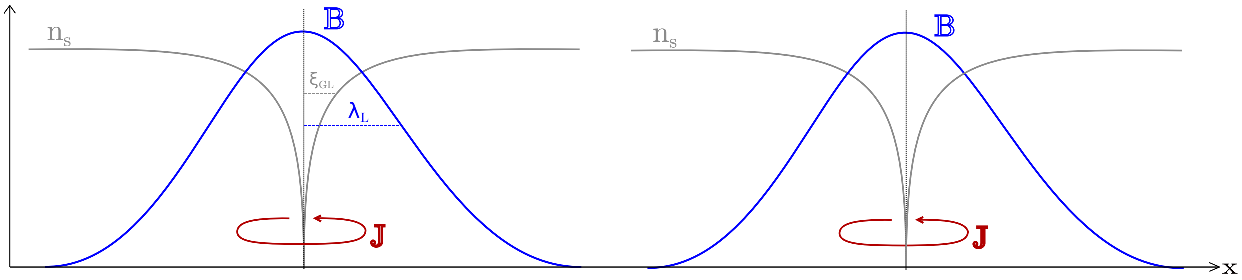

Figure 3.1 – Abrikosov vortices around the penetrating flux line. The magnetic flux density B decays exponentially on a length scale of λ_L, the density of superconducting charge carriers n_s decays on a length scale of ξ_{GL}.

where α is a temperature dependent parameter from the Ginzburg-Landau free energy functional (discussed in detail in e.g. [Tin04]). While the London penetration depth λ_L gives the length scale of the depth up to which the external magnetic field penetrates into the superconductor, the Ginzburg-Landau coherence length describes the length scale on which the superconducting order parameter varies and hence also the density of superconducting charge carriers. The Ginzburg-Landau parameter, defined as

$$\kappa = \frac{\lambda_L}{\xi_{GL}}, \tag{3.3}$$

determines the type of superconductor. If $\kappa < \frac{1}{\sqrt{2}}$, the superconductor is of first type, if $\kappa > \frac{1}{\sqrt{2}}$ it is of second type. For superconductors of type II, flux lines can penetrate the material, whereby the zone of penetration becomes normal conducting and the field decays on the length scale of λ_L into the material. Vortex supercurrents are induced around the flux line and the superconducting charge carrier density n_s is varying on the length scale ξ_{GL} from zero in the flux core to n_s further away. A representation is shown in Fig. 3.1.

If a transport current is applied, the penetrating flux lines are subjected to a Lorentz force and start to move through the superconductor. The phenomenon is often referred to as flux flow or flux jumping. A moving magnetic flux line on the other hand implies an inductive voltage drop, hence a finite resistivity and dissipation of energy. Flux movement should be suppressed in case the superconductor shall be used for current transport or else the superconducting state might break down. This is usually referred to as flux pinning. The volumetric flux pinning force is calculated from the measured critical current density as

$$\vec{F}_p(T,B) = \vec{J}_c(T,B) \times \vec{B}. \tag{3.4}$$

The maximum of the pinning force is determined by the pinning mechanisms, the pinning centers and their spacing. The peak indicates at which field the flux line spacing ideally matches the pinning center distribution, so that flux is pinned ideally. Depending on the fabrication process and the pinning mechanism, the superconductor parameters can be changed in a way to favor pinning at a field region of interest, i.e. where the superconductor is supposed to be operated. If this is not possible, the superconductor will have an intrinsic maximum at a given field and might not be ideally operable in an arbitrary external field. Matching the pinning center spacing to the penetrating flux lattice at a given field is an important factor for high field applications. Abrikosov calculated the distance a between flux lines as a function of the magnetic flux density, when the flux lines are spaced as [Abr57]

$$a = \sqrt{\frac{\Phi_0}{\mu_0 H}} \tag{3.5}$$

with the magnetic flux quantum Φ_0. This holds true for a square lattice, but the energetically favourite solution is the hexagonally spaced one where the above equation has to be multiplied by $\left(\frac{4}{3}\right)^{0.25} \simeq 1.075$ [Tin04]. The stronger the external magnetic field H, the smaller becomes the distance between the penetrating flux lines. For high magnetic field applications it is therefore beneficial to have high pinning center densities, i.e. small spacing between the pinning centers to match the flux line vortex lattice. For a magnet operated at a magnetic flux density of $B = \mu_0 H = 10\,\mathrm{T}$ one finds for example

$$a \simeq \sqrt{\frac{2.06 \cdot 10^{-15}\,\mathrm{Wb}}{10\,\mathrm{T}}} \approx 14\,\mathrm{nm}. \tag{3.6}$$

The mechanism of flux pinning is described later in more detail in sections 4.2.1 and 4.3.1 for selected materials.

The BCS theory predicts the existence of bosonic states of pairs of bound electrons where the attractive net force is mediated via phonons [BCS57]. Two electrons with opposite momentum and opposite spin (according to the Pauli exclusion principle) form such a Cooper-pair below a certain temperature, as soon as it is energetically more favourable. In the bound state, they obey Bose-statistics and loss-less current transport is possible. The charge of the superconducting carriers is then $q_s = -2e$. The critical temperature depends on the electronic density of states at the Fermi energy $N(E_f)$ and the coupling potential of the electron-phonon interaction V as well as the Debye phonon frequency ω_D [BCS57]

$$k_B T_c = 1.14\,\hbar\omega_D\,\exp\left(-\frac{1}{N(E_f)V}\right) \tag{3.7}$$

The electronic density of states has a gap $\pm\Delta$ symmetrically around the Fermi energy, with a width of [BCS57]

$$2\Delta(T) = 3.2\,k_B T_c\,\sqrt{1 - \frac{T}{T_c}} \tag{3.8}$$

and depends on T_c, i.e. the critical temperature at which the superconducting phase transition occurs. The binding energy is very small, in the order of milli-electron-volt which is the reason for the very low critical temperatures for most of the classic superconductors. If the (thermal) excitation energy is greater than the binding energy, the cooper pairs break up. Furthermore, for the critical magnetic field a proportionality

$$H_c(T) \simeq H_c(0)\left(1 - \left(\frac{T}{T_c}\right)^2\right) \tag{3.9}$$

was approximated [BCS57]. Eliashberg could relate an electron-phonon-coupling constant λ to the phonon density of states, quantifying the phonon mediated attractive potential and finally allowing to calculate and predict the critical temperatures. A review of Eliashberg theory can be found e.g. in [PI13]. Equation (3.7) was found to be the weak coupling limit with a dependency $\propto \exp\left(-\frac{1}{\lambda}\right)$ and for the strong coupling limit with $\lambda \gg 1$

$$k_B T_c \propto \hbar\omega_D \sqrt{\lambda}, \tag{3.10}$$

which indicates that there is no theoretical upper limit of T_c [PI13].

The BCS theory describes the low temperature superconductors well and cooper pairing of two electrons with opposing momentum and spin (so-called *s*-wave pairing) is considered to be the mechanism behind the net attractive potential and hence the superconductivity [PI13]. For high temperature superconductors there is no established theory, yet. Mechanisms like *d*-wave pairing are considered [PI13] but are yet to be fully confirmed.

3.2 Superconducting wires and cables

Superconductors for technical applications are barely used in pure, stoichiometric form, but embedded in well conducting materials like aluminum or copper in case of most LTS conductors or deposited on a support substrate such as Hastelloy in case of (Re)BCO HTS. Furthermore the crystalline structure is often not ideal and due to production processes the exact chemical composition might vary locally. Compounds other than the pure superconducting phase might be present next to it, which can be both beneficial for flux pinning or troublesome for mechanical stability. Sections 4.2, 4.3 and 4.4 will describe the specific mechanisms for the materials investigated in this report in more detail. This section shall give some general considerations how the behavior of the technical superconductors is altered with respect to the ideal superconducting theory.

The resistivity of a superconductor as a function of the applied current density is described empirically as

$$\rho_{sc} = \rho_c \left(\frac{J}{J_c}\right)^{n-1}. \tag{3.11}$$

By convention, the exponent is written here as n-1, such that the evolution of the electrical field over the superconducting wire as a function of the applied current density is described by a power law of the form

$$E = J\,\rho_{sc} = J\,\rho_c \left(\frac{J}{J_c}\right)^{n-1} = E_c \left(\frac{J}{J_c}\right)^{n} \tag{3.12}$$

with the critical current density J_c and the critical electrical field $E_c = \rho_c\, J_c$.

3.2.1 Copper matrix and thermal stability

Superconductors used to build accelerator magnets are often embedded in a metallic matrix with high conductivity such as copper or aluminum to protect them in case of a quench and also to allow for an easier connection to current leads by regular soldering. These solder joints are often normal conducting ohmic connections and need to be of high quality to keep Joule heating sufficiently low. This is why low resistivity copper of high quality and purity is commonly used. A certain amount of the current will flow through the copper close to the joints until it transits into the superconductor. The so called current transfer length can be centimeters or more, and is purely given by the transversal resistances between the superconducting layers, the surrounding protection layers (Nb or Silver for example), and the copper layer in which it is embedded [Eki78; Zho+14]. In a circuit representation, this corresponds to the superconducting filaments connected in parallel to copper shunt resistors and coupled via the transversal resistances. According to the Kirchoff law, the current path will be determined by the balance of voltages over all the filaments. Due to the non-negligible transverse resistance and the relatively low resistance of the copper matrix, the copper might carry significant portions of the current before it finally enters the superconductor. This part of the current transport - being ohmic and not superconducting - is measurable as it results in a non-zero voltage and energy dissipation along the wire.

The resistivity of copper at low temperatures is mainly defined by scattering of the electrons on impurities and lattice defects. It differs strongly between the different grades of copper, while the resistivity at room temperature usually differs very little. Therefore, the copper matrix resistivity is often simply expressed via the *Residual Resistivity Ratio* (RRR), which is usually defined as the ratio of the copper resistivity at 293 K and 4.2 K

$$RRR = \frac{\rho_{\mathrm{Cu}}(293\,\mathrm{K})}{\rho_{\mathrm{Cu}}(4.2\,\mathrm{K})}. \tag{3.13}$$

It can range up to well above 300 and more. The RRR is higher for high purity grades of copper as well as for copper that has been thermally annealed and hence has very little lattice defects and dislocations. Strain hardening on the other hand, introducing dislocations in the crystal lattice, lowers the RRR. If the RRR of the superconductor's copper matrix is to be measured experimentally, it is more practical to define it as the ratio of the resistivity at room temperature and at the resistivity at the critical temperature of the superconductor

$$RRR = \frac{\rho_{\mathrm{Cu}}(293\,K)}{\rho_{\mathrm{Cu}}(T_c)}. \tag{3.14}$$

In this thesis the definition according to Eq. (3.14) will be used, if not stated otherwise.

The heat capacity of most materials decreases significantly with decreasing temperature, resulting to values of $\ll 1\,\frac{\mathrm{J}}{\mathrm{kg\,K}}$. Therefore, the thermal stability of practical superconductors is largely reduced when operated at these low temperatures. Small energy fluctuations can result in relatively large temperature increase, potentially lifting the superconductor above its critical temperature. When powered or exposed to an external magnetic field, the thermal margin of the superconductor with respect to the critical surface is furthermore reduced. Therefore, the energy required to quench a superconducting wire during operation can be expressed as a function of its operating current, temperature and magnetic field to which it is subjected. This formulation, often referred to as the *Minimum Quench Energy (MQE)*, was described by Wilson and Wolf [WW97] for LHC type Nb-Ti wires and Rutherford cables but the concept is generally applicable. It describes the thermal balance between Joule heating and conduction cooling along the wire as well as cooling due to the liquid Helium bath in which it is immersed during operation or during critical current measurements. A small zone which quenches does not necessarily lead to a quench of the full wire, if the equilibrium can be restored quickly. The MQE gives this critical value in terms of energy, up to which the wire can be operated in a thermal equilibrium. Important is the dependence on the copper-matrix resistivity at the cryogenic operation temperature $\rho_{\mathrm{Cu}}(4.2\mathrm{K})$

$$\mathit{\Delta}_{\mathrm{MQE}} \propto \frac{1}{\sqrt{\rho_{\mathrm{Cu}}(4.2\mathrm{K})}} \propto \sqrt{RRR}. \tag{3.15}$$

According to equation above, a reduction of the RRR leads to a reduction of the MQE, i.e. the thermal stability of the wire. A copper matrix with high RRR is thus preferable for safe operation and thermal margin.

3.2.2 Critical transport current and magnetization measurements

In a practical wire, the critical properties are not uniform but rather a distribution. The transition does not happen at one sharp critical current but over a certain region, where the electrical field starts to rise with increasing applied current as described by Eq. (3.12). The exponent n is commonly called the n-value and can be determined by a fit of the form Eq. 3.12 on the measured voltage signals. The n-value can be taken as a reference to describe the steepness of the superconducting transition. In a practical application, the critical current density is not defined by fit, but at a certain electric field criterion. Commonly used are 1 $\mu\mathrm{V\,m^{-1}}$ or 0.1 $\mu\mathrm{V\,m^{-1}}$ and authorities such as NIST or the IEC have standardized the measurement procedures [Eki06; GF82; IEC].

However, in case significant portions of the current are flowing through the copper, the additional ohmic contribution should be considered in the powerlaw dependence of Eq. (3.12) to describe the superconducting transition

$$E = \rho \cdot J = E_c \left(\frac{J}{J_c}\right)^n + J\rho_{\text{Shunt}}. \tag{3.16}$$

The ohmic contribution can be determined by fit and the measurement signal can be corrected for it. Section 3.2.2 will further elaborate on the critical current measurement techniques.

In transport current measurements with applied transport currents of $\gg 100\,\mathrm{A}$, a significant self field is induced by the current carrying filaments onto each other. The maximum field within the wire is found on the outer filaments. For a long straight wire, the calculation reduces to the magnetic field of an infinitely long line current density evaluated at the radial position of the outermost layer of filaments [God+13]. The self field B_{self} is proportional to the applied current I according to the Biot-Savart law

$$B_{\text{self}} = \frac{\mu_0 I}{2\pi R} \tag{3.17}$$

For the Nb_3Sn based RRP® type wire as presented below, the outermost filaments are at a radius of 0.375 mm. The self field correction results in

$$B_{\text{corr.}} = B + I_c \cdot 0.533\,\frac{\mathrm{T}}{\mathrm{kA}}. \tag{3.18}$$

The magnetization of a slab of superconducting material in an alternating external magnetic field was firstly described by Bean [Bea62; Bea64] and Kim et al. [KHS63]. More detailed calculations were performed subsequently for superconductors of different geometries. Bean showed, that the difference in the magnetization of such a slab, while undergoing a hysteresis loop is proportional to the critical current density of the superconductor. For a long cylinder geometry one finds for example

$$\Delta M = \frac{4R}{3\pi} J_c. \tag{3.19}$$

When measuring superconducting wires and cables, the magnetization is measured per volume of the sample and the above equation needs to be corrected by the copper to superconductor ratio

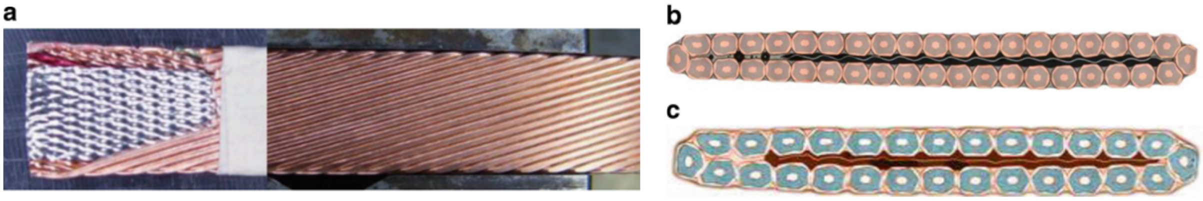

Figure 3.2 – "Nb3Sn Rutherford cables: (a) large face view of cable with stainless-steel (SS) core; (b) cross-sections of 40-strand cable; and (c) 28-strand cable with SS core" [SZ19]. Image from [SZ19], Fig. 2.10 (p. 39), published under the terms of the Creative Commons Attribution 4.0 International License.

as the copper matrix does not contribute to the magnetization. Measuring the small changes in magnetization with changing applied magnetic field requires a good resolution and is usually done with SQUIDs. The sample to be measured is inserted in a solenoid magnet and the current is ramped to measure a full hysteresis loop.

3.2.3 AC losses, Eddy currents, Rutherford cables

If alternating currents (AC) are applied to a superconductor, resistive losses are observed. Two mechanisms are responsible for that: hysteresis losses and coupling currents both between filaments within a wire and between wires if several wires are in contact (e.g. in cables). A time varying magnetic field induces an electric field and hence a dissipation of energy, i.e. no loss-free current transport.

The hysteresis losses can be understood as the energy needed to regroup the pinned penetrating flux lines as the magnetic field pattern changes with varying magnetic field [Oom00] (compare Eq. (3.5)). This effectively changes the magnetization of the sample – an irreversible process – and hence the name hysteretic losses. As mentioned above in Eq. (3.19), the magnetization is described by Bean's model and is proportional to the diameter of the superconducting filaments. Therefore, in practical superconducting wires it is favorable to reduce the filament size as much as possible. In high-field magnets, a magnetic field is naturally the self field of the coil onto its own conductors. Especially for high inductance magnets this can become an issue during current ramps where large values for $\frac{\mathrm{d}\vec{B}}{\mathrm{d}t}$ are possible.

The coupling currents are similar to eddy currents in normal conductors, i.e. circular current loops induced by the time-varying magnetic field according to Lenz's rule. As the current path is mostly along the filaments and only closes transversally via the copper matrix, the resistance is very small and the decay time of these eddy currents is very large. Furthermore, as the current loop formed in this way can become very large (up to twice the sample length), the enclosed magnetic flux can become likewise very large and due to the Lenz's rule of induction, the induced current might exceed the critical current of the filament [Oom00]. To avoid this, the filaments can be twisted with a twist pitch length L_p [Wil96]. The enclosed current loops are then changing sign on a length scale of the filament twist pitch. The net current along each filament cancels. On each of the loops the effective amount of trapped flux is much smaller. Subsequently the inductive current and the resistive losses due to the transverse matrix resistance and also the decay time of the eddy currents are reduced. An increased matrix resistance is also beneficial to suppress these eddy currents and filament coupling losses but is not desired for thermal stability during DC operation and magnet protection in case of a quench, as mentioned above. The principle of twisting the conductors is likewise applied when manufacturing cables from several wires. There, the individual wires are twisted to form so-called Rutherford cables as shown in Fig. 3.2. The contact resistance between the wires defines the wire-coupling losses accordingly. In the cabling process mechanical reinforcement can be inserted and the full wire is usually insulated with Polyimide or glass fiber insulation [SZ19].

In synchrotron accelerators, such as the LHC, the magnetic field is ramped while the beam is circulating and the beam energy is increased. It is important to suppress the AC losses to avoid quenches and specifically the eddy currents during the current ramp to ensure a good field quality, as eddy currents might lead to erroneous multipole field harmonics.

4 Superconductors for accelerator magnets: Nb-Ti, Nb_3Sn, (Re)BCO

4.1 Critical current scaling laws for Nb-Ti and Nb_3Sn

The critical current density is usually described by scaling laws as a function of the applied magnetic field or flux density, the temperature and the lattice strain. A variety of scaling laws exist in literature. To mention are the Bottura scaling for Nb-Ti based wires [Bot00] as well as the MAG scaling law for Nb_3Sn, after Mentink, Arbelaez and Goedeke [Men08], which itself is a simplification of the scaling relations of Ekin [Men14; Eki80] and Summers [Sum+91]. Many more models were suggested, but they are essentially variations in the amount and dependence of several of the fit parameters and no fundamental difference in the underlying physics is taken into account. The widely accepted MAG scaling will therefore be discussed exclusively in this thesis. Overviews on the other models for Nb_3Sn can be found in various publications [Eki80; BB09].

The MAG scaling relation [Men08; Men14] describes the following dependence of the critical current on temperature T, the externally applied magnetic field B perpendicular to the wire and the strain ε

$$J_c(T,B,\varepsilon) = C_1 \cdot (1-t^2)^{\mu} \cdot b^{\,p-1} \cdot (1-b)^q \tag{4.1}$$

with scaling constant C_1 and the free fit parameters μ, p and q, where often $\mu \sim 1$ is assumed. The reduced temperature t and reduced magnetic field b are derived as

$$t = \frac{T}{T_c(\varepsilon)}, \qquad b = \frac{B}{B_{c2}(T,\varepsilon)}. \tag{4.2}$$

Mentink showed, that the different scaling relations are almost identical within large ranges of temperatures and fields [Men14]. Especially if the critical properties, such as the critical temperature T_c and the upper critical field B_{c2} are not constant but a rather inhomogeneous distribution within the wire. Then, a parametrization via the fit parameter μ in Eq. (4.1) is sufficiently accurate, without taking into account the exact distribution [Men14]. He furthermore showed, that this scaling relation can also be used for Nb-Ti with the exception of the temperature dependence of the upper critical field B_{c2}. As opposed to the Ginzburg-Landau dependence (compare Eq. (3.9)) the exponent differs for different materials. For Nb-Ti it is found [Lub82]

$$B_{c2}(T,\varepsilon) = B_{c2}(0,\varepsilon) \cdot (1-t^{1.7}). \tag{4.3}$$

For Nb_3Sn the implicit Maki-deGennes relation describes the dependence of upper critical field on temperature, but it is reasonable to use a still very accurate approximation of the form [God06]

$$B_{c2}(T,\varepsilon) = B_{c2}(0,\varepsilon) \cdot (1-t^{1.5}). \tag{4.4}$$

Hence, the two descriptions for Nb-Ti and Nb_3Sn are very close, but differ in this regard. With this distinction, the MAG relation can be used and fitted onto measured data to describe accurately the critical current of Nb_3Sn and Nb-Ti based wires as a function of temperature and magnetic field.

The strain dependence is hidden in this formulation, intrinsically within the dependence of critical field and temperature on the strain as indicated in Eq. (4.2) and Eqs. (4.3, 4.4). The nomenclature used in the following where not stated otherwise is

$$\begin{aligned} T_{c,0} &:= T_c(\varepsilon{=}0, B{=}0), && (4.5)\\ B_{c2,0} &:= B_{c2}(T{=}0, \varepsilon{=}0). && (4.6) \end{aligned}$$

The dependence of the critical parameters on strain is usually expressed via a strain dependent function $s(\varepsilon)$. The dependence of T_c on strain is of the form

$$T_c(\varepsilon) = T_{c,0} \cdot s(\varepsilon)^{\frac{1}{3}}. \tag{4.7}$$

For B_{c2} the dependence is found to be

$$B_{c2}(T, \varepsilon) = B_{c2}(T) \cdot s(\varepsilon) \tag{4.8}$$

or by using Eqs. (4.3) and (4.4) respectively, one can express the full dependence as

$$B_{c2}(T, \varepsilon) = s(\varepsilon) \cdot B_{c2,0} \cdot (1 - t^{\omega}) \qquad \text{with } \omega \begin{cases} 1.7 & \text{for Nb-Ti} \\ 1.5 & \text{for Nb}_3\text{Sn} \end{cases}. \tag{4.9}$$

B_{c2} shows a direct dependence on the function $s(\varepsilon)$ while the dependence of the critical temperature T_c on this function is much weaker. T_c is only proportional to $s(\varepsilon)^{\frac{1}{3}}$. The function $s(\varepsilon)$ is normalized and ranges from one to zero, where the maximum is not necessarily at zero strain. Both large positive (tensile) and negative (compressive) strains eventually lead to a degradation of the superconductor. Therefore, $s(\varepsilon)$ tends to zero in both cases, but is not necessarily symmetric around the maximum. At zero temperature the strain dependent function can be concluded from the critical magnetic field or the critical temperature as

$$\frac{B_{c2}(0, \varepsilon)}{B_{c2}(0, \varepsilon{=}0)} \equiv s(\varepsilon) \equiv \left(\frac{T_c(\varepsilon)}{T_c(\varepsilon{=}0)}\right)^3. \tag{4.10}$$

If the strains are not too large, the dependence of T_c on strain can also be considered small and for a fixed temperature

$$\frac{B_{c2}(T, \varepsilon)}{B_{c2}(T, \varepsilon{=}0)} \approxeq s(\varepsilon) \tag{4.11}$$

is a good approximation.

Wires are produced at room temperature and slightly above. Therefore, they are intrinsically strain free at this temperature. When cooling down to the operation temperature the difference in thermal contraction between different materials often leads to an axial compressive pre-strain on the superconductor [God+06]. The strain can be expressed as

$$\varepsilon = \varepsilon_a + \varepsilon_m \tag{4.12}$$

with the externally applied strain ε_a and the pre-strain ε_m resulting from the different thermal contraction. If the applied strain equals the pre-strain, the superconductor is essentially strain free and the superconducting properties are at a maximum, i.e. the strain dependent function is maximal and equal to one. The strain dependent functions are different for the different materials and will be discussed later.

The volume pinning force F_p is calculated following Eq. (3.4) and using the critical current scaling law Eq. (4.1), which yields

$$F_p(T, B, \varepsilon) \propto b^{\,p} \cdot (1-b)^q \tag{4.13}$$

in the units of Nm^{-3}. Assuming the parameters p and q are constant and the only degradation due to strain is in the upper critical field B_{c2} and the critical temperature T_c, the relative maximum of the above formula is not altered. Hence, the relative maximum of the normalized flux pinning force is usually independent of the strain. Other mechanisms that provoke a change in the pinning behaviour, e.g. changes in the nano- and microstructure will result in a change of the exponents p and q.

The Kramer representation of the critical current allows to conclude B_{c2} from measurements of the critical current by extrapolation, if the critical current was measured in applied fields well below B_{c2}. Especially for Nb_3Sn with a critical field of about 30 T, the Kramer form is a helpful way to conclude B_{c2} even from measurements in fields $\lesssim 20\,\mathrm{T}$. Using the MAG scaling law Eq. (4.1), the functional dependence

$$f_K(T, B, \varepsilon) = J_c(T, B, \varepsilon)^{\frac{1}{q}} \cdot B^{\frac{1-p}{q}} \quad \propto \quad (1-b) \tag{4.14}$$

is directly linear in the applied magnetic field and is zero at the upper critical magnetic field $B_{c2}(T, \varepsilon)$, i.e. where $b = 1$. A linear fit on this formulation and a subsequent extrapolation up to B_{c2} can be more accurately performed and is less prone to errors than a direct fit of the scaling law as in Eq. (4.1).

For Nb_3Sn it is often suggested, that $p = 0.5$ and $q = 2$, and the Kramer form becomes simply

$$f_K(T, B, \varepsilon) = J_c(T, B, \varepsilon)^{0.5} \cdot B^{0.25}. \tag{4.15}$$

As stated in Eq. (4.11), knowledge of the upper critical field allows also to conclude the value of the strain dependent function $s(\varepsilon)$.

4.2 Nb-Ti based wires

Nb-Ti is one of the most commonly used superconductors in technical applications, such as superconducting magnets for high energy physics, nuclear fusion, NMR systems for material analysis and also medical devices like MRI magnets. In this section the micro and nano-structure of Nb-Ti based wires for technical applications is discussed in more detail. Finally, the LHC type Nb-Ti based superconducting wire, as used for example in the more than 1200 superconducting dipole magnets of the LHC, is presented in more detail.

4.2.1 Production and microstructure

In the optimization process of Nb-Ti based wires, a variety of studies was performed in order to optimize the wires with respect to the critical current for the field regions of interest. The upper critical field and temperature both vary with the stoichiometry. The most commonly used stoichiometry is Nb 47wt-%Ti. A maximum in the upper critical field of 14.5 T and a critical temperature of $\sim 9\,\mathrm{K}$ was found for this composition [Osa93]. The pinning centers were identified to be α-Ti precipitates [LL03] that form in triangular grain boundaries, during a heat treatment of $\approx$400 °C for several hours [LML88]. As mentioned before, the flux pinning can be optimized by managing the spacing of the precipitates and their density within the superconducting Nb-Ti phase. This was found to be possible by (cold) rolling the wire under a certain strain, which leads to formation of very fine ribbons of α-Ti with a thickness of few nano meters and a spacing of $\lesssim 10\,\mathrm{nm}$ [MLL89]. Even though the spacing is about half the spacing of the Abrikosov vortex lattice [LML88], as calculated above (compare Eq. (3.5)), it was found to be the optimum for these type of wires.

A specific recipe of dedicated heat treatment to form the precipitates in the desired size and quantity, followed by a cold rolling process with plastic strain can be found to optimize the Nb-Ti wires for each use-case. It makes this type of wire very flexible in its application range. Since it is a ductile alloy, the winding process of coils is similar to resistive copper-conductor based coils. Both points have lead to Nb-Ti being widely used in a variety of scientific and industrial applications.

4.2.2 Strain dependence of the critical current

Nb-Ti is a ductile alloy and shows a very weak dependence on strain, so weak that there exists no established model for the strain dependent function $s(\varepsilon)$ in literature. It is however measured and well studied [Eki87], so that if needed, the values can be taken from tabulated data. The degradation due to strain is usually small enough to not be of significance for technical applications, so that strains present even in high field magnets impose no significant degradation in Nb-Ti based wires. The observed degradation is usually smaller than 5% for strains below one percent and only significant in the field regions close to the critical field or for high strains of 2-3% [Eki87]. Furthermore, Nb-Ti was found to show almost no irreversible degradation. After the wire was unloaded, the original critical current was restored up to few percent [Eki87]. This explains also the good training behaviour of superconducting Nb-Ti based magnets. Even when de-training occurs over time, the magnet can be re-trained.

4.2.3 LHC dipole type wire

For the LHC main magnets two types of wires were used to produce Rutherford cables. For the fabrication of the dipole magnets a 1.065 mm diameter wire with a copper to superconductor ratio of 1.65 was used in the inner layers and a 0.825 mm diameter wire with a copper to superconductor ratio of 1.95 in the outer layers [Bru+04]. The superconducting quadrupoles were fabricated from the second type exclusively. The filaments within the wires have a twist pitch of 18 mm and 15 mm respectively. Other magnet types such as the dispersion suppressor quadrupoles, the matching quadrupoles, separator dipoles, the final focus quadrupoles and the correctors all use different variations of this wire type with different amounts of filaments, outer diameters and copper to superconductor ratios. The general layout and production mechanism is identical for the other wire types and diameters, the variation is purely geometric. Figure 4.1 shows an optical microscopy image of the cross section of the the 1.065 mm wire. The single filament diameter of all the wire types ranges between 6-10 µm [Bru+04] and several filaments are grouped to a bundle with a diameter of $\gtrsim$ 50 µm (compare right hand side of Fig. 4.1). Many of such bundles are embedded in the surrounding copper matrix separated by few micrometers of copper. The view on the substructure is also shown in the image and gives a rough view on the fine α-Ti ribbons embedded in the Nb-Ti phase and optimizing the pinning behaviour as described above. Finally, the wire is coated with a Tin-Silver layer on the outside, during a last heat treatment step to reduce the contact resistance when producing Rutherford cables [Ada+99]. This final heat treatment also results to strain annealing of the copper matrix, which is beneficial for a high RRR [Ada+99]. The LHC dipole type wires have been studied in detail and the critical current measurement data was published in literature so it can be used as a reference [Bou+06; God+09].

4.3 Nb_3Sn based RRP® wires

After about 60 years of research, a variety of ways to produce Nb_3Sn wires has been found. The general concept is similar between the different fabrication routes. Due to the brittle nature of the Nb_3Sn phase, wires need to include only ductile constituents in a first step, such as pure niobium, copper, tin or bronze (Cu-Sn), or tubes filled with tin-rich powders such as Nb_2Sn. This allows the cold drawing of billets to a final wire diameters of $\lesssim$ 1 mm and sufficiently long lengths. The magnet coil needs to be wound with this un-reacted but ductile wire and once in place, the Nb_3Sn phase is formed in a heat treatment procedure. During this heat treatment at temperatures of well above 600°C, the Tin diffuses through the copper and reacts with the niobium to form the desired Nb_3Sn in the A15 crystal lattice structure. The exact Tin-content strongly affects the superconducting properties such as the critical field and temperature and subsequently the critical current density. The tin-content ranges from 18-25 at.-% [SZ19] and the optimum in terms of the critical parameters is found very close but slightly below the ideal stoichiometry of 25 at.-% [Men14]. The three dominating production methods are the bronze-route, the powder-in-tube and the internal-tin processes. Overviews on the history of Nb_3Sn based wires and the various production methods are explained in detail elsewhere [San17; God06; SZ19]. The most promising candidate for high-energy physics applications, such as high-field accelerator magnets is a specific kind of internal-tin process, the so-called Restack Rod Process ® (or short RRP®). In the HL-LHC upgrade this type of wire is used and the specifics of this wire type will be discussed in the following.

4.3.1 Production, reaction and micro-structure

The RRP® process is an internal Tin process patented by Bruker[1]. Hexagonally shaped filaments are stacked in a hexagonal geometry and are embedded in a round copper tube. Each filament is surrounded by a Niobium or Tantalum diffusion barrier layer. Figure 4.2 shows the schematics of such a filament. Niobium rods are stacked in a shell orientation surrounding a pure tin-core. The so-called copper channels in between the niobium rods are important to allow the Tin to diffuse

---

[1] Bruker Energy and Supercon. Technologies (BEST) `https://www.bruker.com/best`

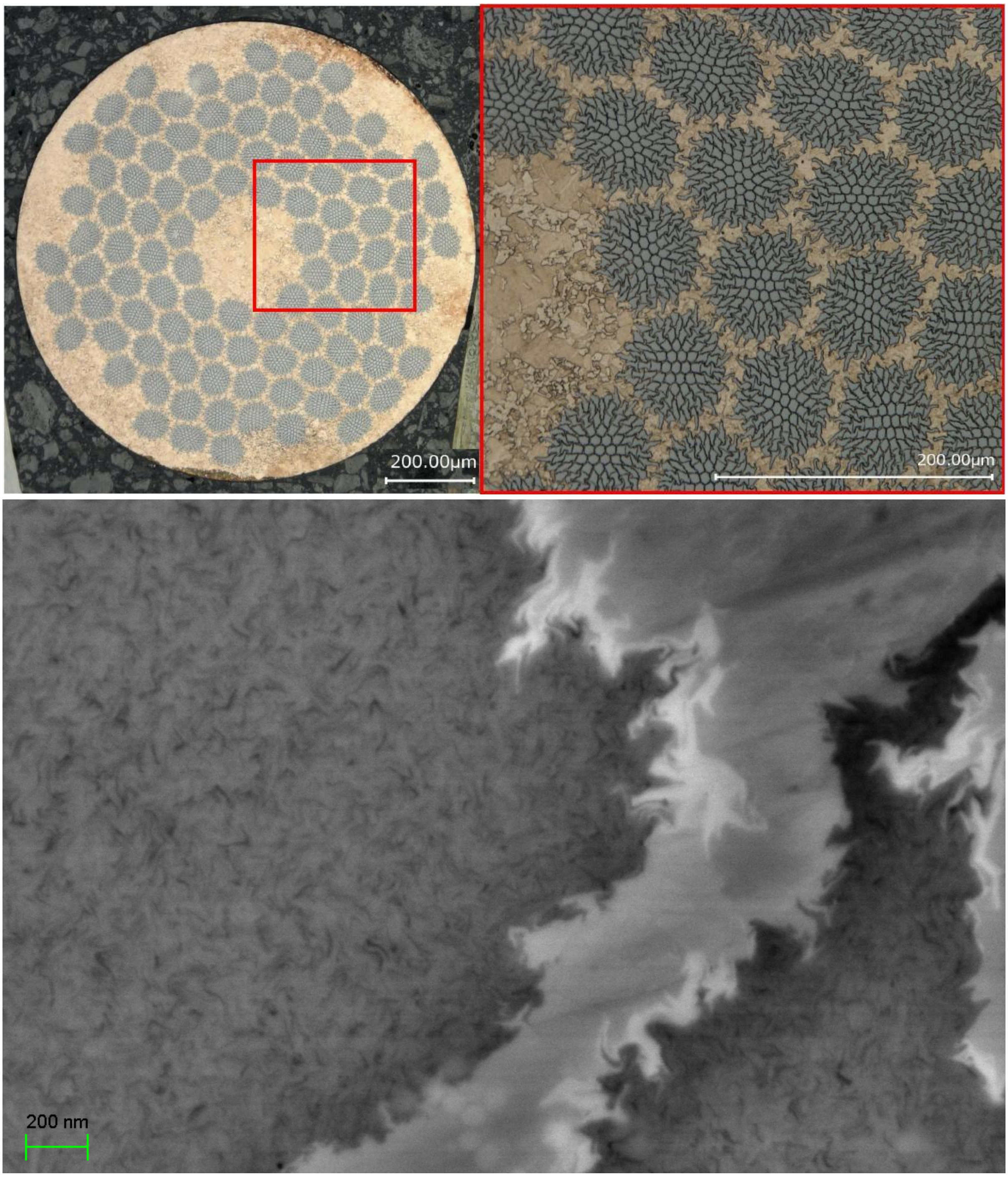

Figure 4.1 – Cross section of a Nb-Ti LHC dipole type wire. *Left:* Full cross section, where the bundles of Nb-Ti filaments with a diameter in the order of a few tens of micrometer are visible embedded in the surrounding copper matrix. *Right:* Zoomed view on the filament bundles that reveal the fine Nb-Ti filaments with diameters of few micrometers. The sub-structure of these filaments can not be resolved by optical microscopy as it is in the range of several nanometers. The image below shows a BSE electron microscopic view on sub-filaments and parts of the copper matrix. Within the Nb-Ti phase of the filament (dark gray) the sub-structure of α-Ti ribbons (black) is visible surrounded by the partial pure Nb-barrier (light-gray) and the copper matrix (gray) around the filaments. Image courtesy of M. Meyer [Meya].

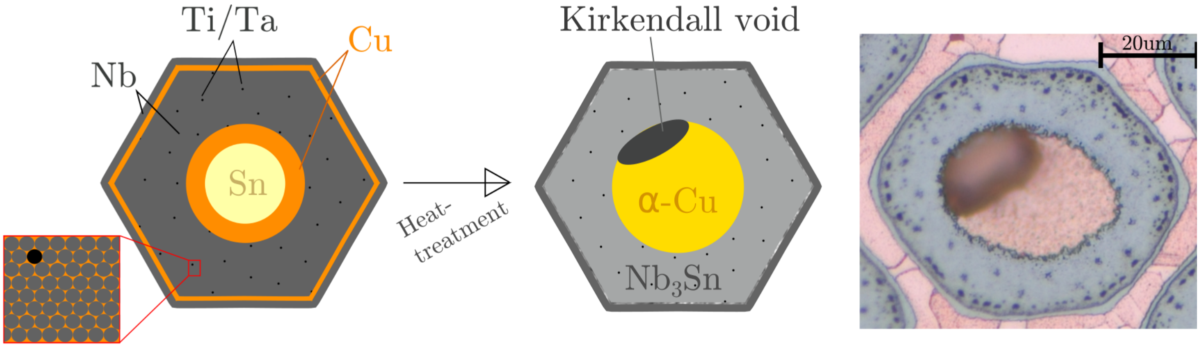

Figure 4.2 – Subfilaments of RRP® wires before and after the heat treatment. In a first step the hexagonal shape is formed in the stacking process. After the heat treatment, a shell of Nb_3Sn is formed surrounded by a Nb diffusion barrier layer. In the center region, Kirkendall-voids have formed in the remaining α-Cu phase.

and surround the rods optimally during the heat treatment [San17]. Some of the niobium rods can be replaced by titanium or tantalum to enhance flux pinning. Dwells at several temperatures during the heat treatment are usually performed before the final Nb_3Sn reaction temperature of $\approx 650°C$ is applied and kept for more than hundred hours typically. These dwells shall enable the tin to diffuse all around the copper matrix (so-called Cu-Sn-mixing [San17]). The first dwell should be just below the melting point of tin at 227°C to allow for a diffusion of the tin into the surrounding copper without it leaking out [SZ19] and is kept for a few days. Once the Cu-Sn phase with a higher melting point is formed, the temperature is increased to around 400°C and kept again for a few days [SZ19]. In this step the tin finally diffuses all around the sub-filament rods, again avoiding the liquid phase and potential tin-leaks [SZ19]. In the final step, the superconducting Nb_3Sn phase is formed. The temperature and duration of this step determine the micro- and nano-structure such as the grain size. In Nb_3Sn, the grain boundaries are considered the main flux-pinning centers. The grain size typically is found to be in the order of 100 nm [God06; San17], much bigger than the ideal Abrikosov lattice spacing as mentioned above in Eq. (3.5). Fine grains are preferred in the production and large grain areas do not significantly contribute to the current transport [San17]. Artificial pinning centers can be introduced by irradiation with very large particle fluences of Neutrons or Protons to create lattice defects (see e.g. [Bau13] and sources therein for a detailed overview). The fluences needed are in the order of $10^{18}\,\mathrm{cm}^{-2}$ (1 MeV neq. fluence) [Bau13] which can usually be achieved only in special neutron irradiation facilities, nuclear reactor- or fusion environments.

Due to the Sn-diffusion, Kirkendall-voids are left in the center, next to an α-Cu phase. Other porous phases close to the outer niobium barrier are also visible in the microscopic image of a reacted filament in Fig. 4.2. Furthermore, on the inner part of the Nb_3Sn phase, a ring of a large grain phase separates the Nb_3Sn from the inner α-Cu.

4.3.2 The HL-LHC type RRP® wire

The wire chosen for the HL-LHC magnets is of RRP® type and has 108 filaments. The wire diameter is either 0.85 mm or 0.7 mm in the non-reacted state at room-temperature. Figure 4.3 shows the cross section of such a wire in the reacted state. The 108 filaments are arranged or stacked hexagonally. The official nomenclature reads as RRP® 108/127, indicating, that the full hexagonal stack has 127 positions but only 108 of which are actually populated with filaments, while the inner 19 slots are just filled with copper. The copper to superconductor ratio is around

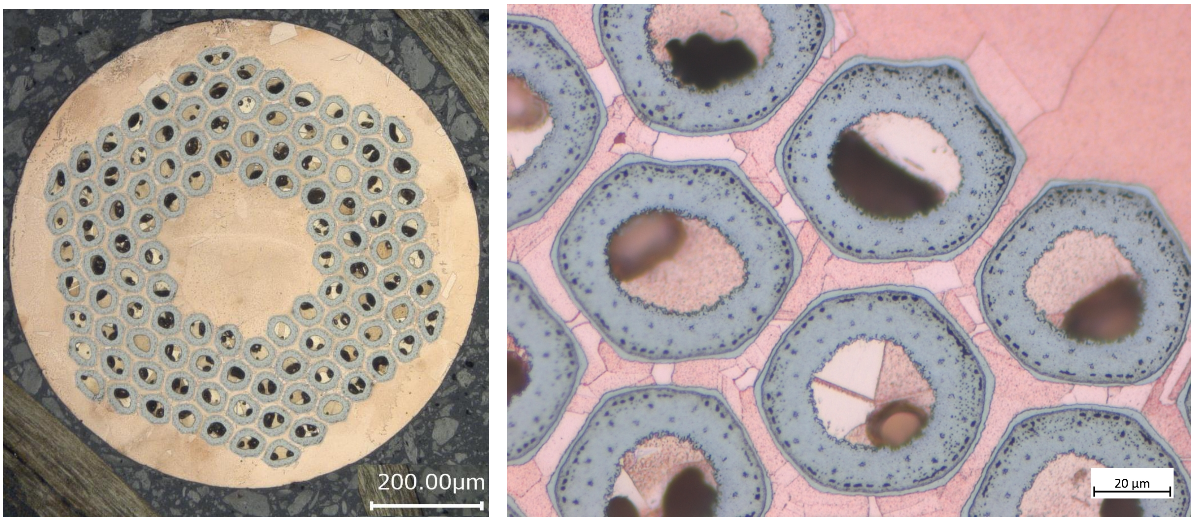

Figure 4.3 – Cross section of a reacted 108/128 RRP® wire with a diameter of ∼0.85 mm and zoomed view on the filaments. The gray areas are the Nb_3Sn phases that have formed after the heat treatment. The outer filament phase boundary around each filament is a pure Nb layer acting as a diffusion barrier. Large voids in the center of the filaments are a result of the reaction process, where Sn from the center diffuses outwards to form the Nb_3Sn layer. These voids are very irregular but an unavoidable intrinsic result of the reaction process. Image courtesy of M. Meyer [Meya].

1.15 and the RRR after the heat treatment should be above 150 [SZ19]. An overview of the wire and cable properties specified for the HL-LHC inner triplet quadrupole magnets, as well as critical transport current measurement results can be found e.g. in [FA18].

4.3.3 Strain dependence of the critical current

Several models for the strain dependent function $s(\varepsilon)$ have been published over the many years, during which Nb_3Sn has been studied. The originally proposed laws were mostly of empirical nature, describing the measured strain dependent function, which were found to be approximately inverse parabolas. The powerlaw formulation by Ekin [Eki80; Eki06] describes the strain dependence empirically in the case of uniaxial applied strain as

$$s(\varepsilon) = 1 - a_{\pm} \left|\varepsilon\right|^{u} \tag{4.16}$$

with ε as in Eq. (4.12) and the coefficient $a_{\pm}$ for the tensile and compressive strain and an exponent $u \approx 1.7$. This empirical law describes the strain dependence accurately for not too large strains. The advantage is the simplicity, with only two free parameters.

A model which addresses the underlying physics was introduced by ten Haken, Goedeke *et al.* [tGt95; God+06], assuming a dependence on the second strain invariant, i.e. accounting for the three dimensional strain and was refined by Arbelaez *et al.* [AGP08]. It reads as [God+06]

$$s(\varepsilon) = \frac{C_{a1} \cdot \left(\sqrt{\varepsilon_h^2 + \varepsilon_{0a}^2} - \sqrt{(\varepsilon - \varepsilon_h)^2 + \varepsilon_{0a}^2} \right) - C_{a2} \cdot \varepsilon}{1 - C_{a1} \cdot \varepsilon_{0a}} + 1 \tag{4.17}$$

with

$$\varepsilon_h = \frac{C_{a2} \cdot \varepsilon_{0a}}{\sqrt{C_{a1}^2 - C_{a2}^2}} \tag{4.18}$$

and ε as in Eq. (4.12). Another model was proposed by Bordini *et al.* and relates the strain to the strain invariants in an exponential form [Bor+13]

$$s(\varepsilon) = \frac{1}{2} \left(e^{-C_1 \frac{J_2+3}{J_2+1} J_2} \quad + \quad e^{-C_1 \frac{I_1^2+3}{I_1^2+1} I_1^2} \right) \tag{4.19}$$

with

$$I_1 = (1-2\nu)\varepsilon_a + \varepsilon_{l0} + 2\varepsilon_{t0} \tag{4.20}$$

$$J_2 = \frac{1}{3}(\varepsilon_{l0} - \varepsilon_{t0} + (1+\nu)\varepsilon_a)^2 \tag{4.21}$$

and the longitudinal and transversal strains ε_{l0} and ε_{t0} as well as the Poisson ratio ν where it can also be written as [Bor+13]

$$\varepsilon_{t0} = -\nu \; \varepsilon_{l0} + 0.1. \tag{4.22}$$

Other empirical models were proposed by e.g. [Mar08; TH05].

The physically correct approach is to calculate the electron density of states (DOS) of the superconducting material's lattice, when subjected to strain, and then to conclude the change of superconducting properties, such as T_c and subsequently B_{c2} via microscopic theory as explained in section 3.1. This was done first by Markiewicz [Den04a; Mar04; Mar08]. Mentink later found the origin of the strain sensitivity of Nb_3Sn to be related to the sub-lattice distortion of the Nb-chains in the Nb_3Sn A15 lattice [Men14]. He related the lack of strain sensitivity in Nb-Ti to the same origin, i.e. there are no such sub-lattices in this type of material and hence no significant change in the DOS when subjected to strain. The calculations of this type are not straightforward and require numerical integrations, i.e. they have no direct analytical solution. Therefore, no general, analytic correlation of arbitrary strain states to the change in superconducting properties was found. Each scenario would result in a (re-)computation of the DOS and the subsequent correlation to the superconducting properties via microscopic theory.

For a practical application, any of the presented empirical models can be used, if it has been fitted to experimental data within the strain range of interest and therefore serves as a good interpolation with few percent uncertainty. For extrapolations, the physically motivated models are more suitable. This is however not more than an academic exercise, since the regions of large tensile strain are in any case not relevant for practical applications as will be explained in more detail in the following subsection.

4.3.4 Irreversible degradation and filament breakage

Nb_3Sn is a brittle chemical compound. It has a linear isotropic strain response to applied stress with an E-modulus of 120 to 140 GPa, depending on the orientation of the crystal axis [Sch+15]. After the maximum applied stress, i.e. the maximum induced strain, the material fractures and is permanently damaged. In a composite wire, consisting of the ductile copper matrix, the brittle Nb_3Sn filaments and several other constituents, such as bronze and pure niobium, the response to applied stress is complex. Tensile tests on full wires as well as extracted filaments have been performed at both room temperature and cryogenic temperatures of 4.2 K [Fer18; Sch+15] and show a non-linear behavior with slight residual strain after stress relieve. It is therefore not justified to assume a perfect linear behaviour in this composite wires, as opposed to the pure bulk Nb_3Sn.

Furthermore, cracking of filaments within the wires has been observed when applying bending strain [Jew08] and tensile strain [Bar+18]. At the same time, the critical current has been observed to decrease permanently and irreversibly when straining the wire above a certain value, the so called irreversible strain limit often referred to as ε_{irr}. Degradation in this context means, that after unloading a strained wire under test and re-measuring its critical current, the original value is not reached anymore. If the wire has not been exposed to a strain larger than ε_{irr} the original critical current can be reached after unloading. Since "the degradation of [the critical current] I_c can be gradual, dramatic or abrupt, depending on the nature of fractures" [Goo+11], a standardized method to measure the irreversible strain including a common definition for it have been proposed by *Goodrich, Cheggour et al.* [Goo+11]. The irreversible strain in this definition is given in the context of the amount of irreversible degradation of e.g. 1%, 2% or 5% [Goo+11] of the original I_c. The observed value of ε_{irr} is dependent on the wire type, the heat treatment and the addition of other materials such as Tantalum or Titanium [Che+10]. When straining above the irreversibility limit, the critical current continues to degrade significantly with increasing strain down to zero. The onset of permanent degradation published in literature range within all values up to about $\varepsilon_{irr} \approx 0.4\%$ [Che+19]. These values are usually also corrected for the intrinsic strain ε_m according to Eq. (4.12). It is only useful, to assume values individually for each type of wire subjected to specific heat treatments, when detailed studies for this combination have been performed or have been published already. Magnet designers and builders at CERN have found empirically, that the stress limit during assembly at room temperature of the Nb_3Sn coils, using the HL-LHC type RRP® wire, should stay well below $\sigma_c = 150\,\text{MPa}$ [Ebe+18].

Some magnets built from Nb_3Sn based wires have been found to degrade significantly after few thermal cycles. The reason for this is not fully understood to date, but very likely a results of irreversible stress and strain due to thermal differences, present during the thermal cycle. In this case the strain is intrinsic, due to thermal contraction, and not due to the Lorentz-/inductive forces. Due to the large E-modulus, large thermal stresses above the stress limit can be reached easily in a confined wire with thermal gradients as small as

$$\Delta T = \frac{\sigma_c}{\alpha E} \sim \mathcal{O}(100\,\text{K}) \tag{4.23}$$

for an axial E-modulus in the order of 140 GPa at room temperature [Sch+15] and a coefficient of linear thermal expansion in the order of $1.4 \cdot 10^{-5}\,\text{K}^{-1}$ [XTG95]. This is a challenge for large magnets during a quench and during thermal cycles and needs to be monitored precisely at all times, as one single event can permanently and irreversibly damage the coil.

4.4 High temperature superconductor: (Re)BCO

Rare Earth Barium Copper-Oxide (or ReBCO) superconductors are a group of cuprate superconductors that have the highest observed critical temperatures ranging up to more than 100 K and critical fields at zero temperatures well above 100 T. One of the most commonly used elements is yttrium and the superconductor is referred to as YBCO. The chemical stoichiometric composition is $YBa_2Cu_3O_{7-\delta}$ with possible variation in the oxid content indicated by the δ [Uso+18]. The crystal has two-dimensional planes where the supercurrent is flowing and hence the critical properties vary with the orientation of the field with respect to the crystal axis $\vec{c}$. YBCO has a critical temperature of ~95 K and a critical field at zero temperature of about 120 T for $\vec{B} \perp \vec{c}$ and 250 T for $\vec{B} \parallel \vec{c}$ [Sek+04]. Some empirical scaling laws exist (for example [Sen+15]) but are not discussed in this thesis, as the evaluation of the critical current measurement was not finished by the time of the submission. This thesis will only cover the mechanical and visual damage observed immediately after the experiment.

Several commercial suppliers are present on the market. In this thesis, the Bruker 2g HTS tapes were used and are exclusively discussed. The production process is described briefly in the following according to [Uso+19]. HTS coated conductors are usually produced in a sequence of steps. A substrate tape of Cr-Ni stainless steels such as *Hastelloy®* with a typical thickness of 100 µm or 50 µm serves as a base. The width of this tape is in principle free to choose but most vendors offer widths of 4 mm or 12 mm. The length is – to date – usually limited to few 100 m. In a first step, a "bi-axially textured yttria-stabilized zirconia (YSZ) buffer layer, typically 2-3 µm thick" [Uso+19] is deposited onto the cleaned substrate tape. Then a double disordered YBCO superconducting layer is deposited via *Pulsed Laser Deposition (PLD)* [Uso+19]. Doubled disordered means that disorder is introduced both through intrinsic disorder due to a local variation in stoichiometry and extrinsic disorder by adding foreign atoms and elements, both resulting in crystal defects that act as pinning centers [Uso+18; Abr+15]. Finally, the tape is coated with a ~ 2 µm thick silver layer to protect the superconductor. Depending on the application, an additional coating of copper with several tens of micro-meters thickness is applied to enhance protection against excessive normal conducting current and heating in case of a quench, similar to the copper matrix in LTS conductors. Figure 4.4 shows the schematics of such an HTS tape as well as a short sample of tape with 4 mm width and 60 mm length, as used in this experiment.

Due to the geometry of the tape and due to the fact that the substrate is the dominant part, with substrate to superconductor ratios of up to 100, the mechanical stability in longitudinal (axial) direction is usually defined solely by the substrate properties. With a very large E-modulus of about 218 GPa and an ultimate tensile strength of about 800 MPa at room temperature [Has], the material is significantly more resistant to stress than Nb_3Sn and more than an order of magnitude more strain resistant to stress than annealed copper as usually present in the LTS copper matrices. The Hastelloy will take the longitudinal stresses which avoids large strains on the superconductor itself. The resulting irreversible critical strain is found in the order of 0.7%, however the stress needed to achieve this strain is in the order of 700 MPa [BMS15] compared to the 150 MPa for Nb_3Sn [Ebe+18]. Transversal pressure, perpendicular to the tape face, can result more quickly to damage of the YBCO crystal lattice as the stress cannot be taken anymore by the substrate. Cable stacks impregnated in epoxy resins are less prone to this effect, as the epoxy will take the strain, resulting to critical transverse stresses of a few hundreds of MPa [Ott+15].

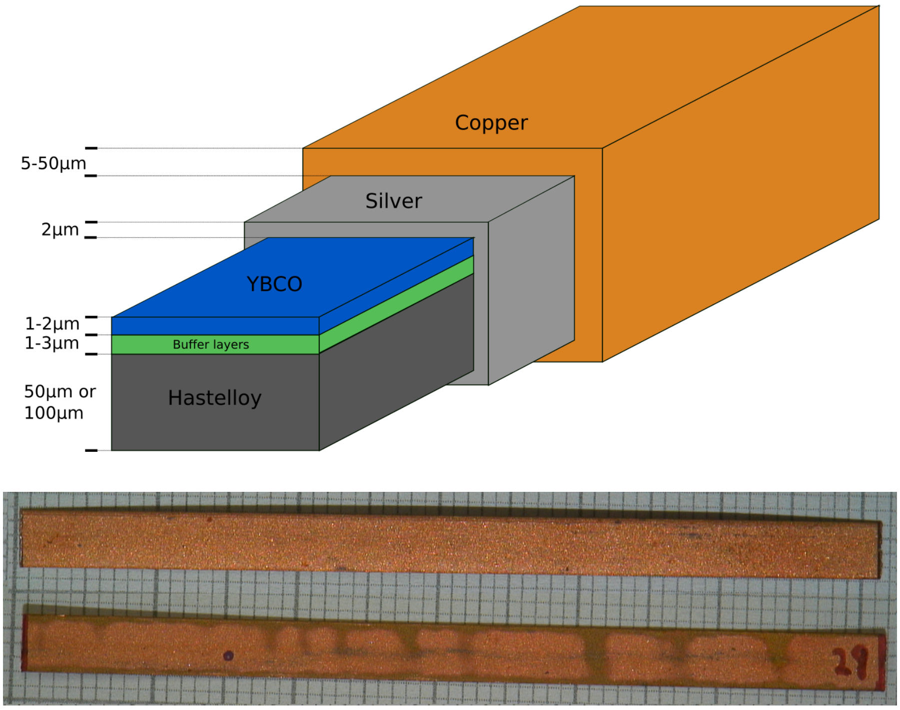

Figure 4.4 – Top: Schematic cross section and layered structure of YBCO tape as produced by Bruker HTS GmbH. Image inspired by [Uso+19], where the tape structure is described as: "*[..] Stainless steel (or Hastelloy) used as a substrate material, [..] buffer layer deposited via ABAD, [..] buffer cap layer deposited via PLD. DD-YBCO: double disordered superconducting layer [..] based on $YBa_2Cu_3O_{7-\delta}$ deposited via PLD. Ag: silver protection layer deposited by thermal vacuum evaporation, Cu: copper layer deposited via galvanic plating.*".
Bottom: HTS tape provided by *Bruker HTS GmbH* with a width of 4 mm and a Cu-layer-thickness of 2x50 µm, cut to pieces of 60 mm length.

5 Beam impact experiment of 440 GeV protons on superconductors in a cryogenic environment

This chapter presents the results obtained in a first "cryogenic beam on superconductor impact" experiment, which was performed in the scope of this thesis. The experimental setup is presented in section 5.2, the analysis of the different superconductors Nb-Ti, Nb_3Sn and YBCO are shown in sections 5.3, 5.4 and 5.5 and the conclusion on the damage mechanisms is given in 5.6. Beforehand, in section 5.1, the results of a preceding beam impact experiment at room temperature (compare [Rag18]) will be briefly summarized.

5.1 Results of previous studies

In a previous beam impact experiment, HRMT31 [Rag18; Rag+18], wire samples based on Nb-Ti as well as Nb_3Sn have been impacted with 440 GeV proton beams at CERN's HiRadMat facility, at room temperature in an Argon atmosphere. The results of that previous beam impact experiment are discussed in detail by V. Raginel [Rag18]. The samples used were the Nb-Ti LHC dipole type wire and various types of Nb_3Sn wires, including the CERN HL-LHC RRP® type wire. This section will briefly summarize the results of the characterizations of both CERN Nb-Ti LHC dipole type wire and the CERN Nb_3Sn HL-LHC RRP® type wire. The same type of wires was also used in the subsequent beam impact experiment, which is the basis of this thesis.

5.1.1 Nb-Ti LHC type wire

Magnetization measurements were performed on the impacted samples to derive the critical current density. No degradation was observed up to peak temperatures of 879 K [Rag18]. The main damage mechanism was found to be a change in the nano- and microstructure due to diffusive processes. This is in agreement with experiments observing degradation of Nb-Ti based wires due to exposition to elevated temperatures on longer timescales of up to several seconds [Rag+17; Sch+10], where microscopic analyses confirmed this hypothesis. It was observed, that Ti diffused into the copper, strongly altering the originally present α-Ti/Nb-Ti substructure in the filaments (compare section 4.2.1). A change in the pinning behaviour was observed as the maximum of the pinning curve was shifted. This is also in agreement with the change of the spacing of the normal conducting α-Ti phases, that determines the magnetic field at which the pinning force is maximal according to the ideal Abrikosov lattice spacing.

In general, a diffusive process follows Arrhenius law and therefore both peak temperature and exposition time are important. In the beam experiment, degradation was found to start from higher peak temperatures compared to the heating experiments at longer timescales, which is in agreement with the hypothesis.

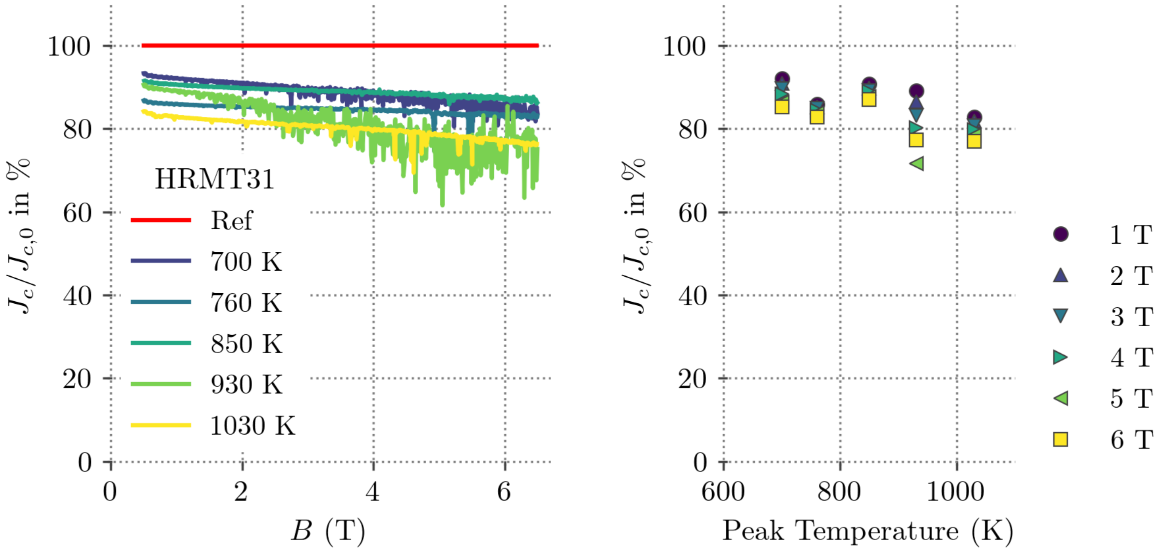

Figure 5.1 – Results from the magnetization measurements at a temperature of 10 K of Nb_3Sn wire samples from the HRMT31 experiment. The data was taken from measurements performed by V. Raginel [Rag18]. *Left:* Relative degradation of the scaled critical current density as a function of the applied magnetic field. *Right:* Relative degradation of the scaled critical current density at selected magnetic fields, as a function of the peak temperature.

5.1.2 Nb_3Sn RRP® wire

The magnetization of the beam impacted Nb_3Sn RRP® type wires was measured for fields from 0 T to 6.5 T and at temperatures of 2 K, 4 K, 10 K and 15 K (see [Rag18]). The critical current density was scaled using Eq. (3.19). The relative loss of critical current density is presented in Fig. 5.1 as a function of the applied magnetic field (left hand plot) and as a function of the calculated peak temperature for selected applied magnetic fields (right hand plot), both measured at a temperature of 10 K, as an example. A degradation was observed in all of the exposed samples, where the lowest peak temperature in the experiment was about 700 K. A clear dependence of this degradation on the peak temperature is not found, as the degradation seems rather similar in all of the samples.

A Kramer fit analysis (compare Eq. (4.15)) was performed for all samples at all measured temperatures to conclude the critical surface $B_{c2}(T)$, The results are presented in Fig. 5.2. The resulting curve was fitted to a function of form Eq. (4.4) and the fit-results for $B_{c2,0}$ and T_c are given in the legend of the plot. A modest degradation of $B_{c2,0}$ and effectively no degradation of T_c are observed, as the change of T_c is within the uncertainty of the fit.

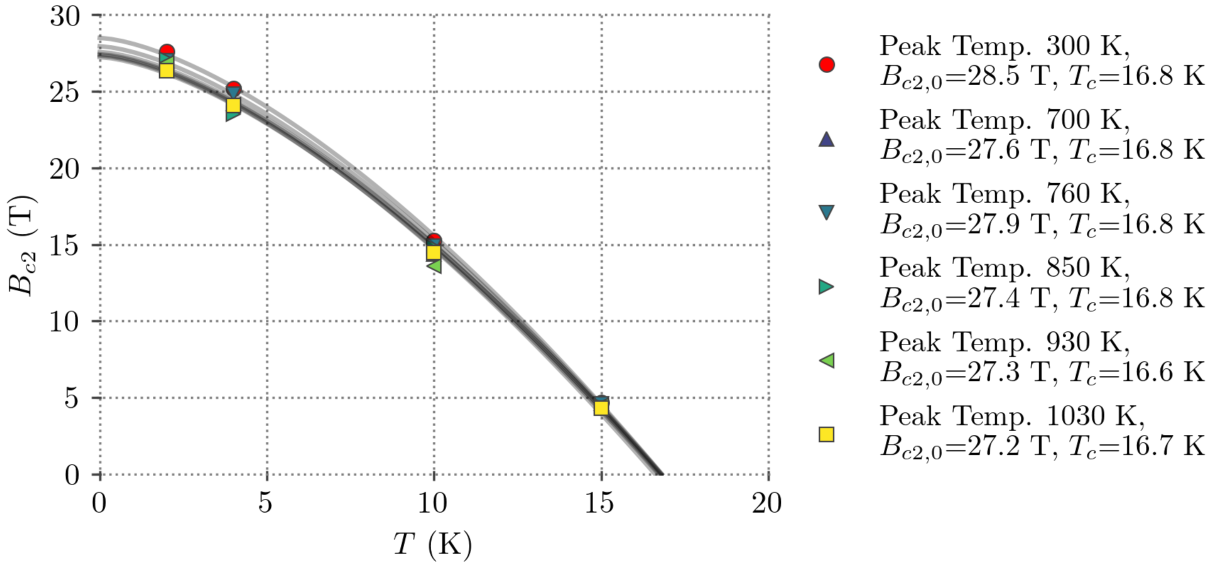

Figure 5.2 – Critical surface $B_{c2}(T)$ of the beam impacted Nb_3Sn wires from the HRMT31 experiment. The raw data was taken from measurements performed by V. Raginel [Rag18]. The critical field was determined by Kramer fit analyses of the magnetization measurements at various temperatures. The resulting values were fitted with a function of the form as in Eq. (4.4), to conclude $B_{c2,0}$ and T_c. The resulting fitted curves are represented with gray lines and the fit parameters are noted in the plot legend.

5.2 The HRMT37 cryogenic beam-impact experiment

This section summarizes the execution and analysis of the results of the “HRMT37” beam impact experiment performed in August 2018 in CERN’s HiRadMat facility. The setup and some of the results have been presented already elsewhere in conference proceedings and publications [Wil+19; Wil+20b]. A partial overlap with these publications and results therein is unavoidable. For better readability, detailed citation marks were omitted. The technical details of the experimental system and setup in the Irradiation facility including an error analysis of the measured quantities were summarized by A. Oslandsbotn [OWW18] as part of a technical studentship supervised in the context of this thesis. The relevant points are recapped briefly in the following.

5.2.1 Samples and sample holder

The samples used were the Nb-Ti LHC dipole type wire and the RRP® HL-LHC type Nb_3Sn wire as well as YBCO based HTS tapes, as presented in sections 4.2,4.3 and 4.4. Two sample holders were used in this experiment, one for the round LTS wires and another one for the HTS tapes. Each one consisted of sheets of copper stacked together, allowing easy sample mounting. The sheets of the first sample holder had slits adapted to the tape geometry of the HTS tapes. The sheets of the second sample holder had grooves to house the Nb-Ti and Nb_3Sn LTS wires. Figure 5.3 shows the fully assembled sample holder for the LTS wires as well as one individual sheet separately. It housed 50 short wire samples with a length of 50 mm each, split into five batches (B1-5 in Fig. 5.3) of 10 samples each. In total, three batches of Nb_3Sn samples and two batches of Nb-Ti samples were mounted in the LTS sample holder. The samples of one batch were installed along the beam axis, i.e. all samples of one batch were impacted simultaneously by one beam pulse. They were oriented to be impacted perpendicular to the wire axis and approximately in the longitudinal center. The spacing between different batches was chosen large enough, to avoid an impact by the beam pulses on neighbouring batches. The HTS sample holder was designed to mount a total of six batches with seven tape samples, i.e. 42 HTS tape samples with a length of 60 mm and a width of 4 mm. Due to the tape geometry two options of beam impact were of interest, one perpendicular and one parallel to the flat tape surface. The grooves in the sample holder were accordingly adapted to test both options. Batches B1 to B4 were oriented with the tape surface parallel to the beam axis, B5 and B6 were oriented with the tape surface perpendicular to the beam axis.

The energy deposition in the sample holder was calculated using FLUKA[1]. Figure 5.4 shows the nominal energy deposition along the beam axis for one beam pulse assuming a beam sigma of 1.1 mm and $3.1 \cdot 10^{12}$ protons. As a reference, the energy deposition was scaled to the corresponding peak temperature reached in an equivalent block of pure copper by numerical integration of the copper heat capacity data. The results are shown in the lower graph in Fig. 5.4. The sample spacing along the beam axis was chosen to result in a variation between 300 K and 1200 K with an incremental peak temperature increase of about 100 K between the subsequent samples. The sample placement is shown in Fig. 5.4 for the LTS samples. As the beam impact happened within 600 ns the energy deposition is assumed to be instantaneous. The peak temperatures were calculated with the full energy deposition and neglecting thermal diffusion, which is very small on these time scales.

While the HTS tapes and the Nb-Ti samples could be prepared and mounted to the sample holder without further preparation, the Nb_3Sn samples had to undergo the designated heat treatment before mounting (see section 4.3.1). The wires were put in quartz glass tubes during the heat treatment to assure a perfect sample straightness as well as to provide protection against mechanical forces after the heat treatment and during the transports. The dedicated HL-LHC heat treatment [Bor] with dwells at 210 °C, 400 °C and a final reaction temperature of 665 °C was applied. They were then cut to pieces of 50 mm length and mounted in the sample holder.

5.2.2 Cryostat system

The left part of figure 5.5 shows the experimental cryostat without the vacuum vessel and thermal shields. The system is cryogen-free, based on a two-stage Sumitomo cryo-cooler[2] and provides a large copper interface plate on the second stage. This second stage provides sufficient cooling power to reach temperatures down to about 3 K and served as the mounting point for the sample holders for the experiment. Both sample holders were attached with bolts to this interface plate to withstand the thermal shock during the beam impact and allow for a good thermal contact and homogeneous thermalization of the whole assembly. Vacuum grease was applied to the contact faces to further enhance the thermalization. A thermal shield that fully surrounded the second stage was connected to the first stage. The first stage was used exclusively to cool this thermal shield and as a heat sink for instrumentation wires, but could likewise be used for sample mounting at elevated temperatures up to about 77 K. The compact system has a height of about

---

[1] FLUKA particle physics Monte-Carlo simulation software Böh+14; Fer+05.

[2] Sumitomo RP-082B2 4K pulse tube cryocooler https://www.shicryogenics.com/

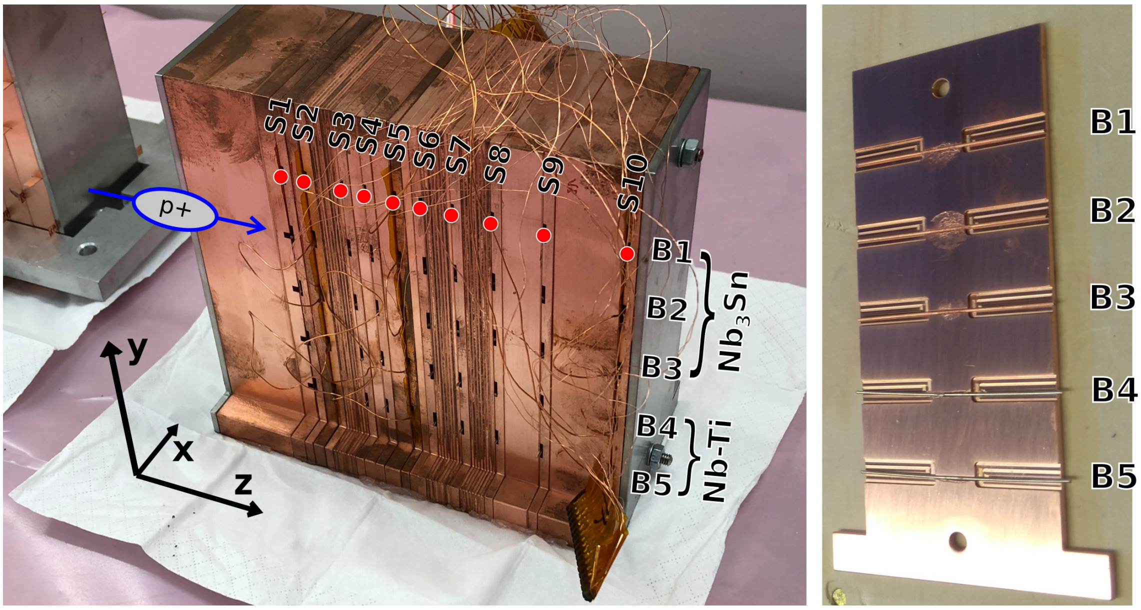

Figure 5.3 – *Left:* Side view of the assembled LTS sample holder used in the HRMT37 experiment [Wil+19]. The setup consists of different blocks of copper and the sliced structure is visible. The red circles indicate the sample positions S1 to S10. The blue arrow indicates the proton beam direction. Originally published in [Wil+19].
Right: Slice of the sample holder with grooves for LTS samples. The samples are held in place with vacuum grease.

0.9 m, including the cold head, and a diameter of about 0.6 m. The vacuum vessel and thermal shields were designed of Aluminum which leads to a low energy deposition of the 440 GeV proton beam into the vessel, making it almost transparent to the beam. Beam windows were omitted for this reason, as the beam could penetrate anywhere through the vessel walls making the full cryostat volume available for beam impact experiments. A detailed metrological evaluation of the system with mounted sample holders was performed before the closing of the vessel. Two fiducial marks on the top plate were used as a reference, accessible also when the vessel was closed. They allowed for accurate positioning of the cryostat in the beam impact facility.

5.2.3 Experimental setup in the HiRadMat facility

The experiment was performed in the HiRadMat facility at CERN, presented earlier in chapter 1.1.1. The cryostat with the samples was moved between the different shots by vertical and horizontal stages, as the beam axis was kept fixed to avoid shot to shot variations. A detailed view on the technical aspects of the experimental setup in the facility, the execution of the experiment and the accuracy of the measured online data are given in a dedicated report elsewhere [OWW18]. The right part of figure 5.5 shows the installed setup on the HiRadMat facility experimental tables. To achieve the desired energy deposition in the samples mentioned above (compare Fig. 5.4), the beam size at the sample position was chosen with a standard deviation of $\sigma = 1.1$ mm. During the experiment a total of 11 beam pulses of 24 bunches with about $1.3 \cdot 10^{11}$ protons per bunch were impacted on each of the batches. An intensity of $(3.1 \pm 0.06) \times 10^{12}$ protons per pulse was recorded. The beam parameters and the temperatures of the sample holders were monitored and recorded during the experiment. As the energy deposition heated up the full second stage to about 35 K after each beam pulse, a re-cooldown to about 4.5 K and a good thermalization of interface

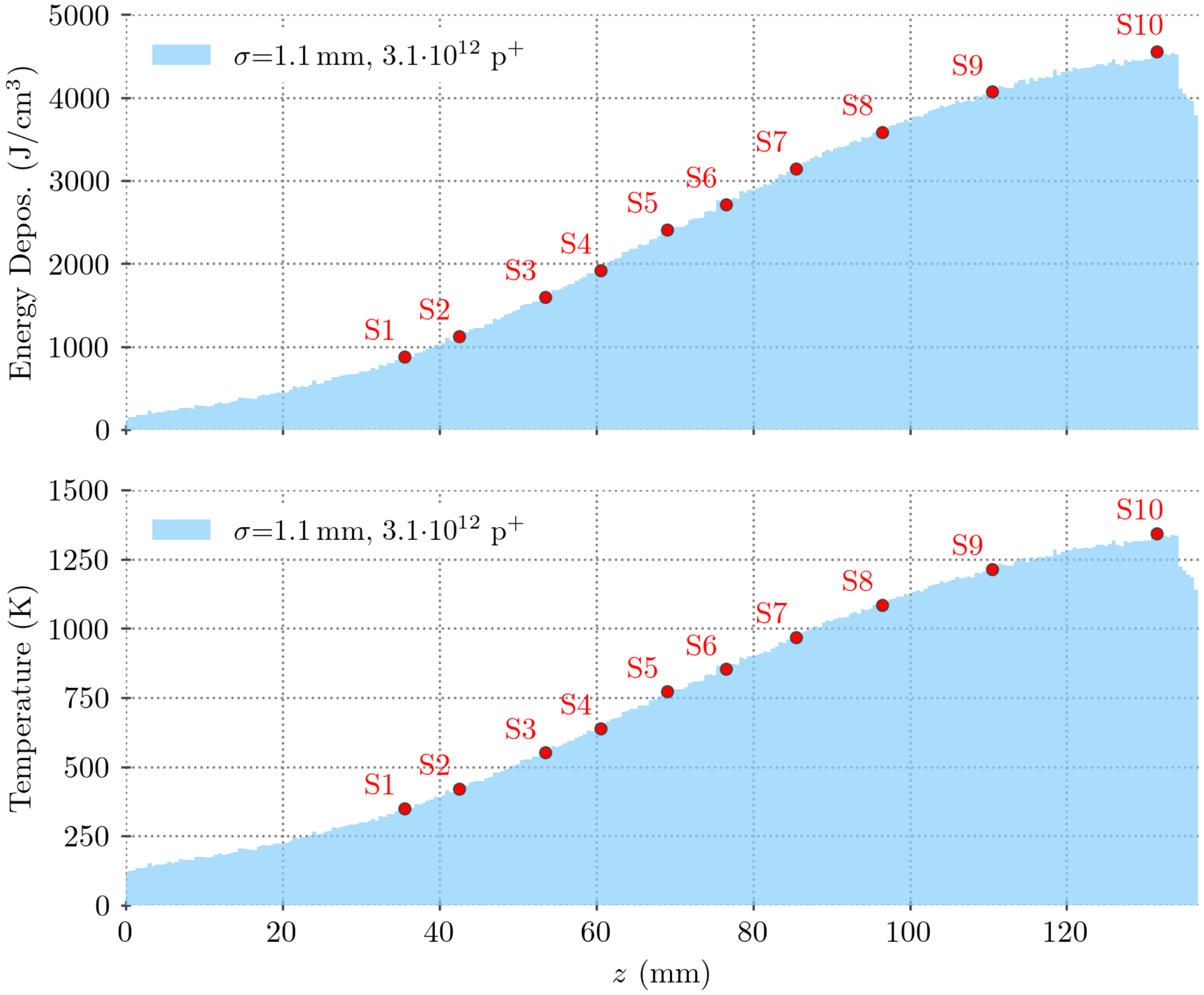

Figure 5.4 – *Top:* Peak energy deposition in the sample holder in the HRMT37 experiment as seen in Fig. 5.3, along the beam axis (z), calculated with FLUKA [Böh+14; Fer+05].
Bottom: The corresponding peak temperatures reached in copper, by scaling the energy deposition with the temperature dependent heat capacity of copper [Dav11]. The red dots indicate the position of the Nb-Ti and Nb_3Sn LTS wire samples.

and sample holders was ensured before impacting the next batch by waiting for about 45 minutes in between subsequent shot. The beam size and position in the facility as well as the beam intensity were reproducible during the full length of the experiment.

5.2.4 Post-irradiation visual inspection

After the experiment, a visual inspection was performed while extracting the samples from the sample holder. The impact marks left by the beam on several pieces of the sample holder were analyzed using a digital optical microscope. The offsets between beam impact and the sample were determined from the measured distance to the edges of the block sheets [OWW18]. The principle of the evaluation of the beam impact positions is shown in Fig. 5.6. A systematic vertical offset between 1 mm and 1.2 mm from the expected impact positions was observed for the LTS samples. A slight misalignment, resulting in a rotation of the sample holder around the beam

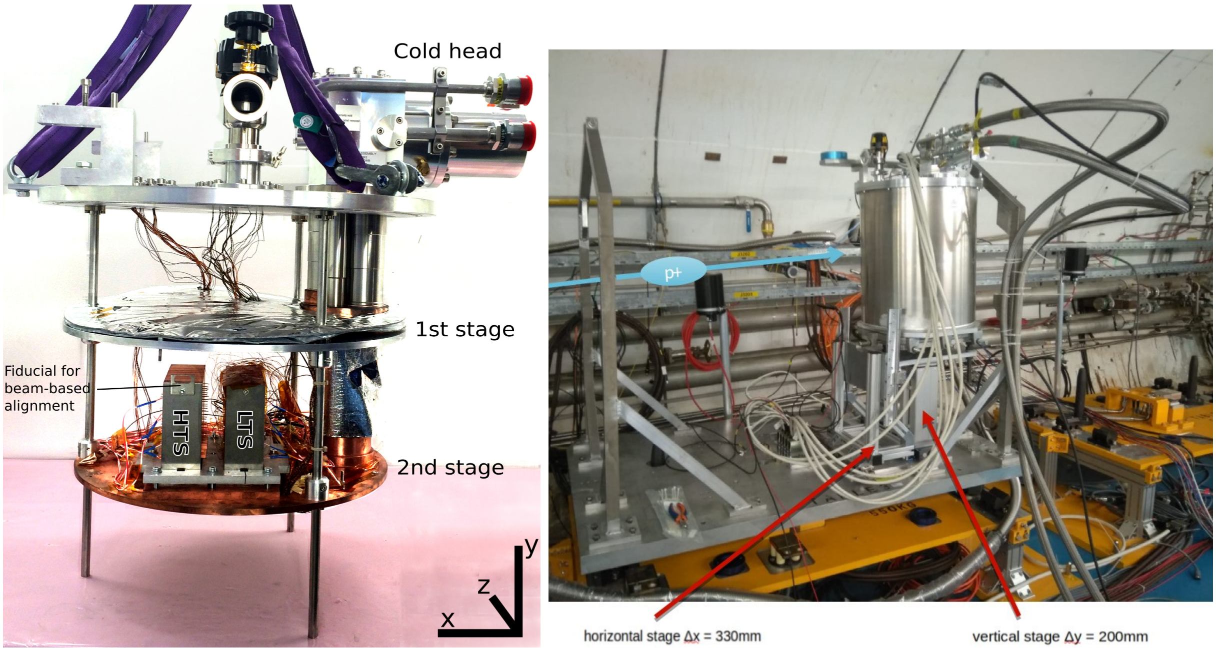

Figure 5.5 – *Left:* Opened cryostat without the thermal shields as used in the HRMT37 experiment. The setup consisted of a two-stage cryocooler and interface plates attached to each stage. On the second stage, the two sample holders were mounted. The first stage was used to cool the thermal-shields. Originally published in [Wil+19]. *Right:* Cryostat system installed on an experimental table in the HiRadMat facility.

axis of few degrees was observed as well (compare blue and red dashed lines in Fig. 5.4). This misalignment is negligible and shows no significant effect on the beam impact. The method of determining the offset positions as well as a detailed error analysis are given in [OWW18]. The overall uncertainty of this method was estimated to be ±300 µm [OWW18]. The vertical beam offset for the HTS samples was observed to vary a lot in between the batches due to an operator error in the vertical positioning of the stages. It was around 0.5 mm for HTS batches B1 to B3 and up to 2 mm for batches B4 to B6. The tapes of the HTS batches B5 and B6 were oriented with the flat side perpendicular to the beam axis so the beam still impacted within the 4 mm wide tape surface even for comparatively larger offsets.

5.2.5 Achieved energy deposition and peak temperatures

Refined simulations in FLUKA were performed to calculate the energy deposition in the samples for each shot taking into account the respective offset. The equivalent temperatures at the respective positions are shown in Fig. 5.7 perpendicular to the wire axis (y-axis) and along the wire central axis (x-axis for $y = 0$) for the LTS wire samples of Batch B2 which had the lowest observed offset of y_0=1 mm. Due to the offsets, the peak temperatures are lower than originally foreseen, reaching from about 290 K to 1200 K. The temperature gradients within the wires, perpendicular to the wire axis, are larger as a result. The gradients along the wire axis on the other hand are not significantly altered due to the offset, when compared with the ideal impact without offset.

Table 5.1 summarizes the calculated peak temperatures (T_{max}) for all LTS batches and samples with their according offsets y_0. Due to the large temperature gradient perpendicular to the wire axis, the lower value of the temperature on the line perpendicular to the wire axis (T_{min} as indicated in the

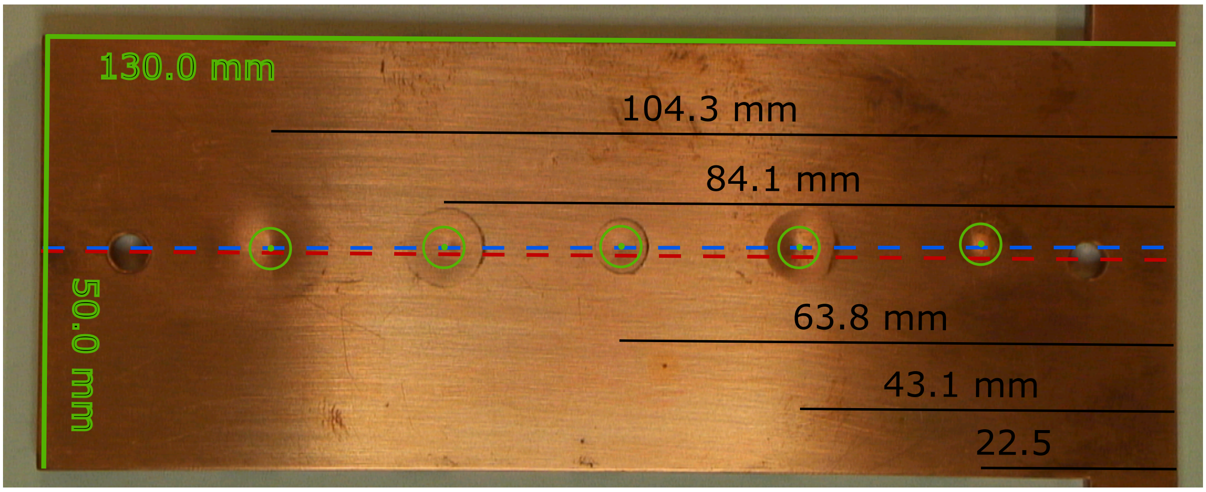

Figure 5.6 – Extracted copper slice from the LTS sample holder (as seen in Fig. 5.3) after the beam impact. The beam impact positions are clearly visible. They are marked as measured with a digital optical microscope. Image and analysis from A. Oslandsbotn [OWW18].

left plot of Fig. 5.7) is given in addition to the peak temperature. The perpendicular temperature gradient can thus be estimated as

$$\frac{\mathrm{d}T}{\mathrm{d}x} \approx \frac{T_{max} - T_{min}}{0.85\,\mathrm{mm}} \tag{5.1}$$

and ranges from about 130 K/mm in Sample S1 to more than 400 K/mm in Sample S10. Due to the uncertainties in the beam intensity and the beam offset, the simulated temperatures show an uncertainty of $\sim$ 10%.

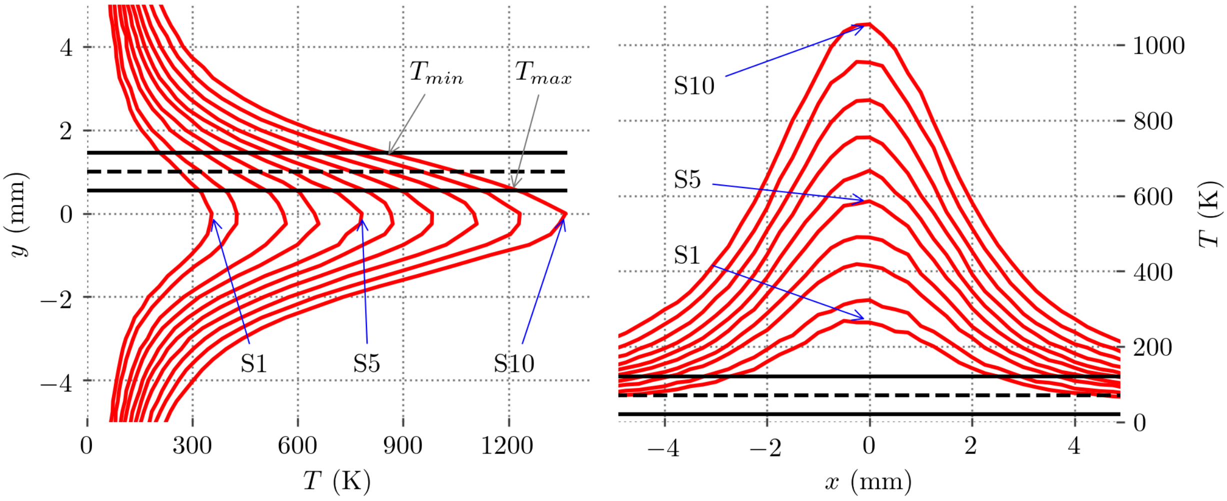

Figure 5.7 – Simulated peak temperature equivalent reached in copper in the sample holder in the HRMT37 experiment during the beam impact at the 10 sample positions. The sample is indicated by black solid lines and the wire central axis with an offset of 1 mm is indicated by a black dashed line.. *Left:* Temperature dependence transversal to the wire, with an exemplary offset of 1 mm as experienced during the experiment for Batch B2. *Right:* Temperature dependence longitudinally along the wire center axis. In both plots the wire is indicated

Table 5.1 – Simulated peak temperatures reached in copper in the sample holder used in the HRMT37 experiment at the different sample positions. Maximum and minimum temperatures T_{max} and T_{min} are the values along the transversal axis of the wire (compare left side of Fig. 5.7).

Batch B1				Nb$_3$Sn,	y_0=1.2 mm					
Samples	**S1**	**S2**	**S3**	**S4**	**S5**	**S6**	**S7**	**S8**	**S9**	**S10**
T_{max} (K)	290	350	460	550	630	720	820	930	1030	1130
T_{min} (K)	190	230	290	340	400	460	520	590	680	760
E_{max} $\left(\frac{\text{kJ}}{\text{cm}^3}\right)$	0.66	0.89	1.26	1.59	1.88	2.21	2.58	2.99	3.37	3.75
Batch B2				Nb$_3$Sn,	y_0=1.0 mm					
Samples	**S1**	**S2**	**S3**	**S4**	**S5**	**S6**	**S7**	**S8**	**S9**	**S10**
T_{max} (K)	310	380	500	580	680	770	870	980	1100	1200
T_{min} (K)	200	250	320	380	450	510	580	660	750	830
E_{max} $\left(\frac{\text{kJ}}{\text{cm}^3}\right)$	0.75	1.0	1.41	1.72	2.08	2.42	2.78	3.2	3.62	4.01
Batch B3				Nb$_3$Sn,	y_0=1.1 mm					
Samples	**S1**	**S2**	**S3**	**S4**	**S5**	**S6**	**S7**	**S8**	**S9**	**S10**
T_{max} (K)	300	370	480	570	660	750	850	960	1070	1170
T_{min} (K)	190	240	310	360	430	490	550	630	710	800
E_{max} $\left(\frac{\text{kJ}}{\text{cm}^3}\right)$	0.71	0.95	1.34	1.66	1.99	2.33	2.7	3.12	3.52	3.9
Batch B4				Nb-Ti,	y_0=1.0 mm					
Samples	**S1**	**S2**	**S3**	**S4**	**S5**	**S6**	**S7**	**S8**	**S9**	**S10**
T_{max} (K)	310	380	490	580	680	770	860	970	1090	1190
T_{min} (K)	200	250	320	380	450	510	570	650	740	830
E_{max} $\left(\frac{\text{kJ}}{\text{cm}^3}\right)$	0.74	0.99	1.39	1.7	2.06	2.39	2.75	3.17	3.59	3.96
Batch B5				Nb-Ti,	y_0=1.1 mm					
Samples	**S1**	**S2**	**S3**	**S4**	**S5**	**S6**	**S7**	**S8**	**S9**	**S10**
T_{max} (K)	300	370	480	570	660	750	850	960	1070	1170
T_{min} (K)	190	240	310	360	430	490	550	630	720	800
E_{max} $\left(\frac{\text{kJ}}{\text{cm}^3}\right)$	0.71	0.95	1.34	1.66	2.0	2.33	2.7	3.12	3.52	3.91

5.3 Damage mechanisms in Nb-Ti

5.3.1 Critical current measurements and analysis

The critical transport current of the first batch of Nb-Ti samples was measured for sample S5 to S10 and the reference sample at the University of Geneva [Uni] and the results are shown in Fig. 5.8. The measured samples S5 to S10 showed a reduction in thermal stability when large transport currents were applied, i.e. at low applied magnetic fields. The critical current of samples S5 and S6 could only be measured at applied fields of 5 T and above. For sample S7 and S8 the minimum applied fields needed to allow a stable measurements were even larger with 6 T and 8 T respectively. For samples S9 and S10 with the highest exposed energy deposition, the critical current could only be measured at fields of more than 9 T. This is very close to the upper critical magnetic field of $B_{c2}(4.2\text{K}) \approx 10.7\,\text{T}$ of Nb-Ti at 4.2 K. Samples S5 and S6 broke in half at the beam impacted area

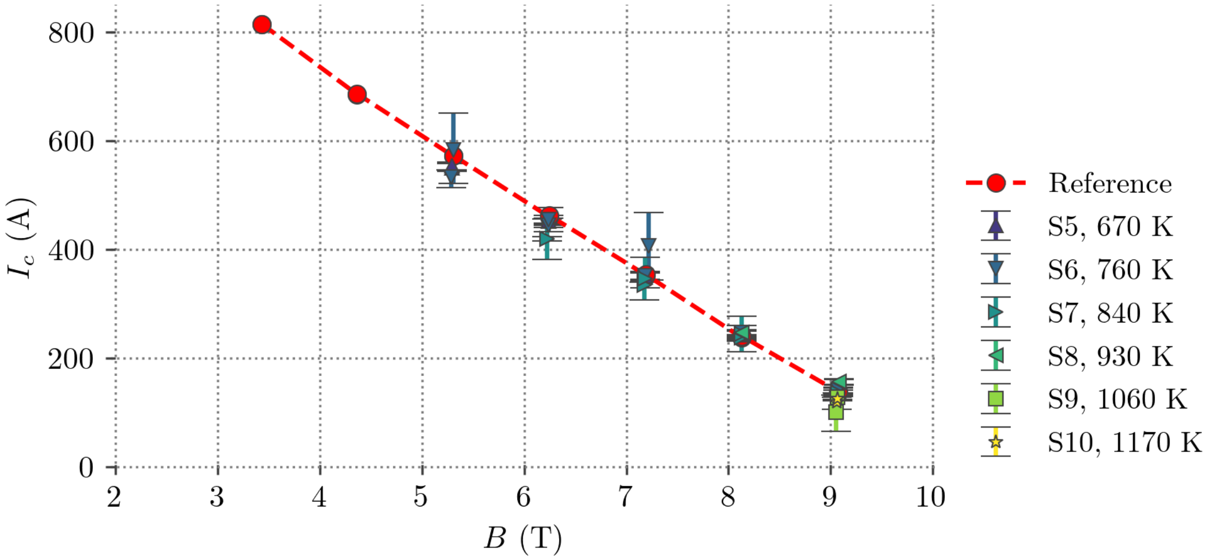

Figure 5.8 – Measured critical transport current I_c, for Nb-Ti wire samples S5 to S10 of Batch B4 and the reference sample from the HRMT37 experiment. Data originally published in [Wil+20b].

during the un-soldering from the critical current measurement setup and could not be used for the subsequent analyses described below. On the other hand, for fields where the wire could be measured, the critical transport current showed no significant reduction in any of the examined samples. These results are in agreement with beam impact experiments on Nb-Ti wires at room temperature [Rag+18], where the critical transport current had been determined via magnetization measurements, and thermal instability is not of importance. The modest observed degradation of few percent in the previous beam impact experiment for comparable peak temperatures are well within the uncertainty of the presented experiment.

5.3.2 RRR measurements and implications on thermal stability

A potential reason for the observed thermal instability could be a weakening in the copper matrix due to the thermo-mechanical stresses during the beam impact. Due to strain dislocations are introduced and an indicator can be the RRR. Therefore, the RRR was measured on all remaining intact samples S1-4 and S7-9. The results are shown in Fig. 5.9 indicated by red dots and marked as "Full wire" values. A reduction of the RRR with increasing energy deposition can be seen from around 220 for the reference sample down to 155 for sample S9. These values marked as "Full wire" were determined by measuring the wire resistance over the full sample length by applying a small transport current at a temperature just above the critical temperature and measuring the voltage over the sample. Due to the beam impact, the resistance should only increase close to the beam impact point with a width of about the beam size of $\sigma = 1.1\,\text{mm}$. A Gaussian resistivity profile with a degraded zone similar to the beam profile was assumed and the resulting resistance as well as the RRR were calculated as the integral along the wire. The RRR was matched to the "Full wire" value by varying the maximum of the degraded zone of the resistivity curve. This results in a "minimum RRR" as plotted in Fig. 5.9. The error bars assume a 2% error on the resistivity measurements and a 50% uncertainty of the width of the damaged region. The minimum quench energy (MQE) is proportional to the the square root of the RRR as shown in

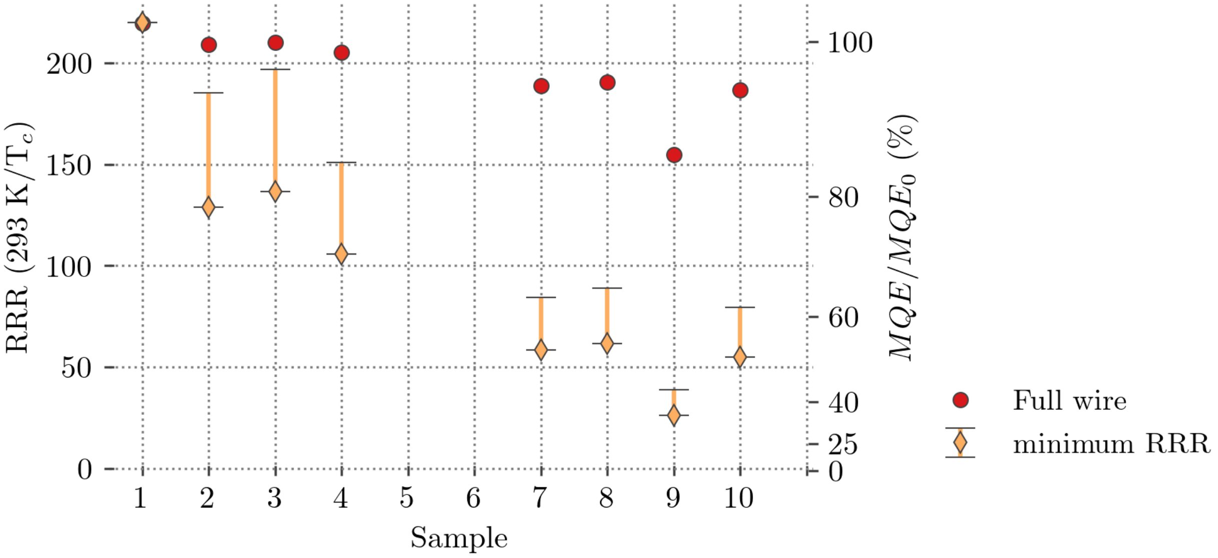

Figure 5.9 – Measured RRR between room temperature and the critical temperature T_c of the Nb-Ti wire samples of batch B4, and derived minimum RRR values at the beam impacted zone. The right axis shows the corresponding remaining fraction of the minimal quench energy. Data originally published in [Wil+20b].

Eq. (3.15) and, therefore, the local reduction of MQE in the wire can be directly derived from the minimum RRR as calculated at the beam impact center

$$\frac{\mathrm{MQE}}{\mathrm{MQE}_0} \propto \sqrt{\frac{\mathrm{RRR}}{\mathrm{RRR}_0}} \tag{5.2}$$

The right hand axis of Fig. 5.9 shows the relative reduction of MQE calculated in this way. For samples S7 to S10, the calculated MQE is reduced to below 60% of the reference value at the beam impact. This can explain the observed thermal instabilities of the samples.

5.4 Damage mechanisms in Nb_3Sn

5.4.1 Visual inspection after beam impact

A first visual inspection was performed after the extraction of the samples from the cryostat. A sharp kink of the wires around the longitudinal center was observed for samples S6 and above. Since the samples had been reacted in quartz glass tubes, the deformation originated from the beam impact. The kinks were detected when trying to re-insert the wires into the glass tubes. This was no longer possible for the samples, where such a kink was present, even if small and not directly visible by eye. Figure 5.10 shows Sample S8 from Batch B2, with contour lines representing the simulated peak temperatures in copper. The contour lines were aligned by the previously determined beam offset with respect to the edges of the wire. The original sample position is indicated by red lines.
Furthermore, a clear imprint of the sample holder into the sample's copper matrix was observed in some of the samples with higher peak temperatures, most prominent for samples S7 and higher.

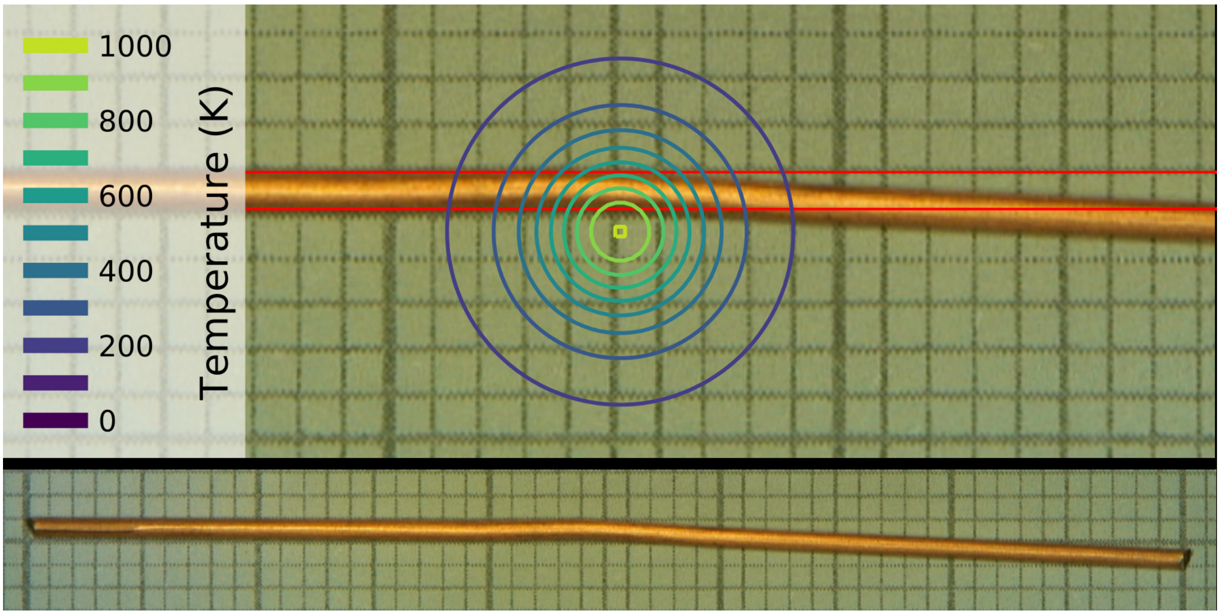

Figure 5.10 – Nb_3Sn sample S8 from Batch B2 after the beam impact. A clear sharp kink is visible around the beam impact center. The circles indicate the simulated temperature reached immediately after the beam impact. Red lines indicate the wire position found via the visual inspection of the beam imprint marks on the sample holder.

This originated from the thermal expansion of the sample holder inside the gap, pressing onto the samples. A more detailed discussion will follow in section 5.4.3.
For some of the samples S8 and above, the copper matrix was partially cracked open. In one case longitudinally, in the other a transversal crack was observed.

5.4.2 Critical transport current measurements and analysis

The critical transport current of the samples was measured at the University of Geneva [Uni]. The measurements were performed in a liquid helium bath cryostat in applied magnetic fields up to $B = 19\,\mathrm{T}$. Two pairs of voltage taps were soldered on each wire, with distances of 12 mm and 24 mm, symmetrically around the beam impact. The wires were soldered onto copper molds (compare Fig. 5.11) to protect them against the significant Lorentz-forces during the measurements at large currents and magnetic fields. The raw voltage signal in the critical current measurement showed a contribution proportional to the applied current. The origin is the copper, serving as a shunt resistor in parallel to the superconductor. Due to the large copper to superconductor ratio, as well as due to the rather short samples, compared to the current transfer lengths, parts of the current will flow through the copper matrix and copper mold. Especially the voltage tap with a 24 mm distance showed significant contributions. These voltage taps are in proximity to the large end faces, where the current enters the mold and therefore, the current is not yet fully in the superconductor. The voltage signal was fitted using Eq. (3.16), allowing to substract the linear part from the measured signal. The measured voltage originates essentially from a very localized degraded zone in between the voltage taps, where the beam impacted the wire. Hence, the electric field is non uniform and can't simply be determined by measuring the voltage over this zone.

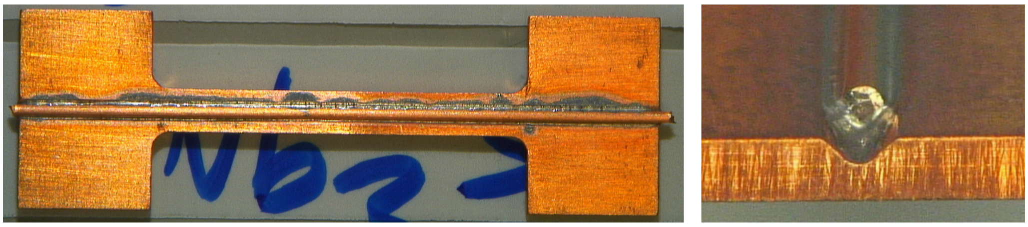

Figure 5.11 – Copper mold with soldered sample. Originally published in [Wil+20b].

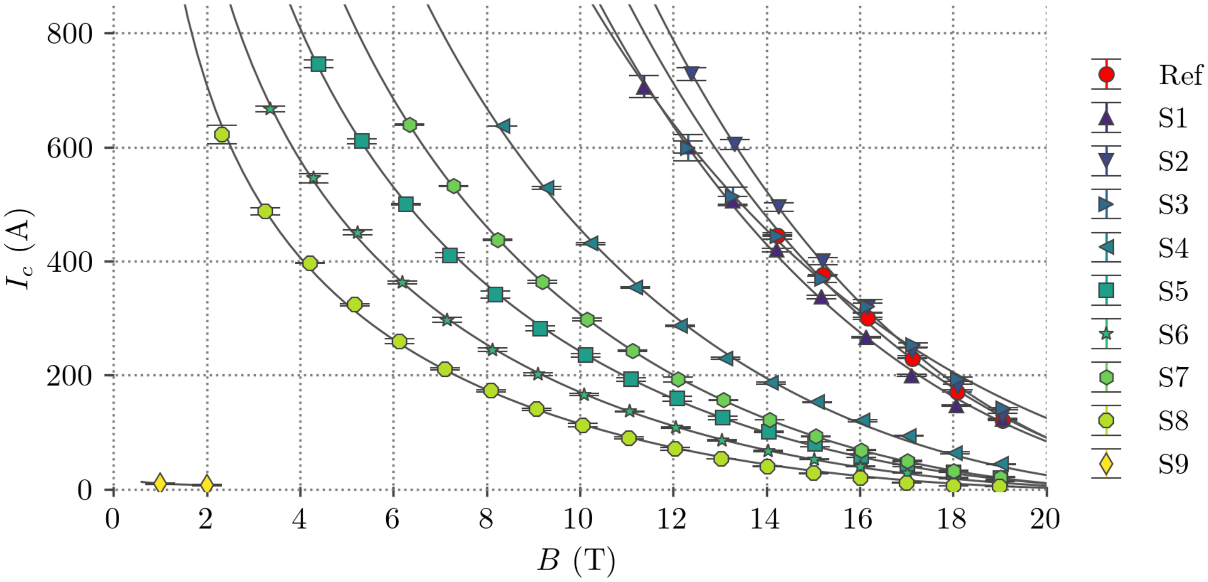

Figure 5.12 – Critical transport current measurement results of the first batch B1 of the Nb_3Sn wire samples of the HRMT37 experiment. The sample labeled *Ref* is the reference sample, that originates from the same lot of wires and has undergone the same heat treatment before the experiment but was not subjected to beam. The critical current was determined at a criterion of E_c=0.1 µV cm^{-1}. The error bar represents the mean and variance of the signal measured on two pairs of voltage taps, one with 12 mm separation and one with 24 mm separation, spanning over the wire center. Data originally published in [Wil+20b].

Therefore, it was chosen to take the absolute voltage signal as a criterion instead of the electric field as commonly used for long homogeneous wires (compare section 3.2.2). The fit then becomes

$$U = U_c \left(\frac{I}{I_c}\right)^n + I \cdot R_{\text{Shunt}}. \tag{5.3}$$

and gave very consistent results for the two pairs of voltage taps, independently of their spacing, as they covered the same degraded zone of the wire.
Figure 5.12 shows the results of the first batch of samples as an example of the analysis which was performed for all batches. The measurements are assumed to have an uncertainty on the absolute value of the critical current of $\lesssim 5\%$. The error-bars in the figure indicate the standard deviation from the mean of the critical current values obtained from the two different voltage taps. It can be seen, that the variation between the two voltage taps is marginal except for sample S3 in the field region below 13 T, where a slightly larger difference was observed. This might be due to a bad solder joint on one of the taps. A functional dependence of the form Eq. (4.1) was fitted to the measured values. Sample S1, S2 and S3 group together, along with the reference sample. Sample S4 is the first of the samples to show a strong degradation over the full field range. With an exception of sample S7, the degradation is stronger with an increasing sample number, i.e. peak temperature. For the fits, the reduced critical temperature was fixed to $\frac{T}{T_c} = \frac{4.2\,K}{16.8\,K}$ and the constants C_1 and $B_{c2}(\varepsilon)$ were fitted for each of the samples. The fit-results are indicated in the plot by gray lines. Figure 5.13 shows the relative degradation of the critical current as a function of the peak temperature for selected applied fields. The observed critical transport current of sample S4 was degraded down to about 40% of the reference value. The samples with peak temperatures above were degraded even further, with sample S8 to $< 10\%$ of the original critical current. Samples S9 and S10 showed no measurable critical transport current. The plot also shows the n-value from the fit as in Eq. (5.3). Plotted is the mean n-value for measurements at various fields and the error bars indicate the variance of the mean. The n-value correlates with the onset of the strong degradation, pointing to an onset of filament cracking. The degradation of the strongly degraded samples shows at best a very small correlation to the applied magnetic field, which again points to filament cracking as the main cause. According to the strain scaling relation Eq. (4.1) and therein Eqs. (4.7,4.8), the degradation should be field dependent, if strain is the dominant mechanism of degradation. In case of filament breakage, a certain part of the wire cross section is not contributing to the current transport, independent of the field. The critical transport current is reduced to the fraction of the remaining cross section for the full field range.

The relative degradation of all measured wires as a function of the peak temperatures reached in the experiment is shown in Fig. 5.14 for two fields 15 T and 19 T. The values are consistent between the batches. Samples S1, S2 and S3 show no significant degradation or seem to have slightly improved, from samples S4 on, a strong degradation to less than 40% of the original value is observed and samples S9 and S10 were broken in all batches.

The normalized magnetic flux pinning force was calculated as

$$\hat{F}_p = \frac{I_c \cdot B}{max(I_c \cdot B)}, \tag{5.4}$$

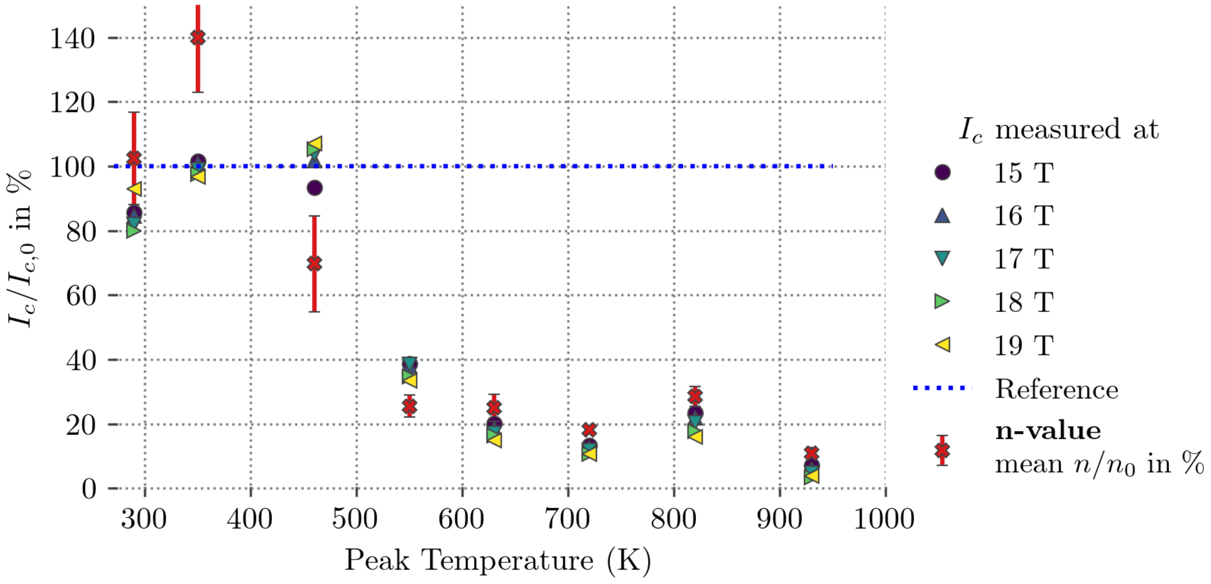

Figure 5.13 – Relative degradation of the measured critical transport current for samples of batch B1 of the HRMT37 experiment (compare Fig. 5.12), mesaured at various fields between 15 T and 19 T, plotted over the sample peak temperature (compare Table 5.1). The red crosses mark the mean n-values including the variance for measurements from 15 T to 19 T.

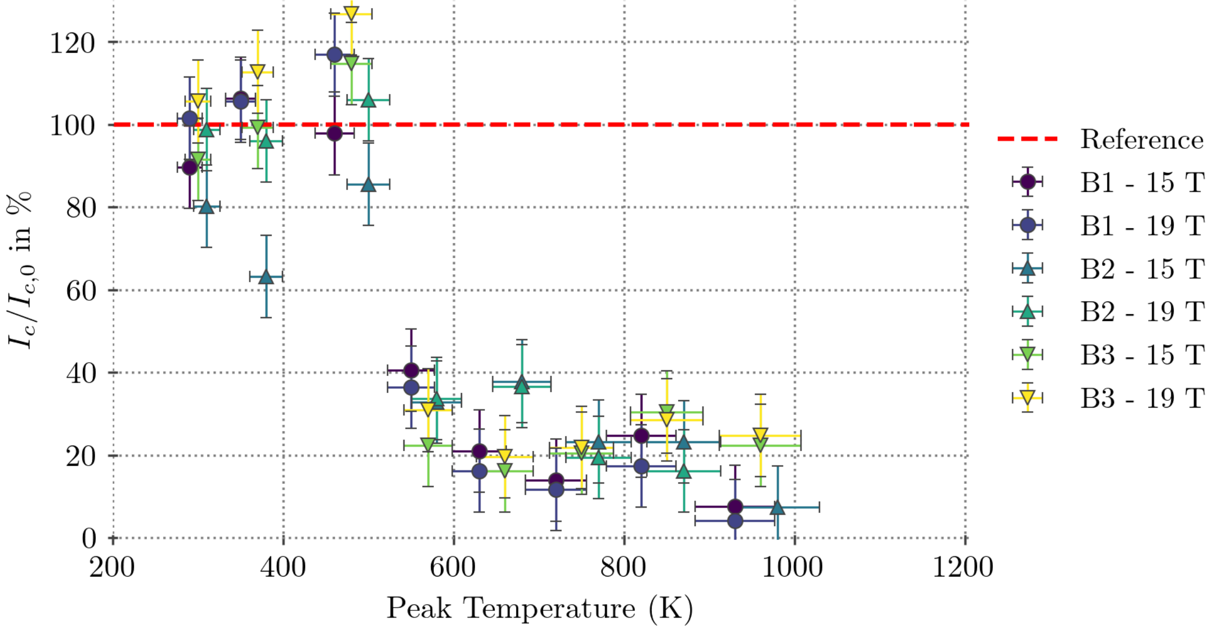

Figure 5.14 – Relative degradation of the measured critical transport current for samples of all impacted batches B1, B2 and B3 of the HRMT37 experiment at two selected fields 15 T and 19 T, as a function of the calculated peak temperature. A strong degradation is visible from around 500 K on.

and plotted over the reduced applied magnetic field b as in Eq. (4.2), where B_{c2} was determined by fit of the form Eq. (4.13). The results are shown in Fig. 5.15. The points lie on the normalized master curve independent of the peak temperature. A significant change in the pinning mechanism is therefore not visible. This is in agreement with the findings from the previous beam impact experiment. Measurements of the grain size distribution and of the tin content in the Nb_3Sn phase showed no change e.g. due to diffusive processes during the beam impact and the local heating due to the energy deposition [Kul18; Rag18]. The absolute value of the pinning force is also reduced by the amount of conductor cross section which is no longer actively contributing, e.g. due to filament breakage. To analyze the relative loss of pinning force as a function of the magnetic field, this was corrected for by normalizing the values with respect to the scaling constant C_1 found by fit for each of the samples. The relative degradation of the pinning force with respect to the reference sample was then calculated as a function of the magnetic field and is plotted in Fig. 5.16. The resulting fitted functions are also shown and extrapolated up to the upper critical field as found in the fit for each sample. Sample S3 was omitted, as a non-physical divergence was observed in the calculation, due to the non-physical kink in the I_c measurement, described above. The relative loss of pinning force shows a strong field dependence between 10 T and 19 T as measured and above 20 T as indicated by the extrapolation. For samples with higher energy deposition, the strain degradation is gradually stronger. The filaments which are still intact are also strongly strained in these regions. Below 10 T the relative loss in pinning force is smaller than 10% and the main mechanism of degradation is the pure loss of active conductor cross section due to filament breakage. The strain degradation seems to play a minor role in these low field regions, in accordance with the strain scaling laws.

Linear fits on the Kramer representation as in Eq. (4.14) were performed to conclude B_{c2}. The Kramer form and fits are shown in Fig. 5.17. The curves are indeed linear, with the exception of sample S3, that shows a curved shape in the Kramer representation with a rather strange kink around $B = 16\,\mathrm{T}$. Nevertheless, a linear fit to this curve was performed, but the result is questionable leading to an extrapolated B_{c2} of more than the theoretical B_{c2} of the non degraded wire. A detailed analysis for this sample is shown in appendix A.2. If only the high field part with $B \geq 16\,\mathrm{T}$ is considered in the fit, a physically reasonable value of 25.6 T is found.

The results for the fitted B_{c2} of all samples are shown in Fig. 5.18. With the exception of the mentioned sample S3, a clear reduction of B_{c2} with the increasing peak temperature is observed for samples above sample S3. The obtained fit value for sample S3 for $B \geq 16\,\mathrm{T}$ is marked in gray alongside the other fit-results. Furthermore, the corresponding approximated value of the strain dependent function $s(\varepsilon)$ is shown on the right hand axis, calculated according to Eq. (4.11). It suggests degradation due to strain of up to 17% for sample S8.

5.4.3 Coupled transient thermo-mechanical simulations

The energy deposition calculated with FLUKA was used as an input for the FEM tool ANSYS®[3]. In a first step, the thermal behaviour in the wires during and after the beam impact was calculated in ANSYS®. For this purpose the energy deposition calculated with FLUKA was scaled to a heating rate via the pulse length of the beam impact of 600 ns. The transient mechanical behaviour of the

---

[3] ANSYS - FEM mechanical and multiphysics simulation software, see ANS.

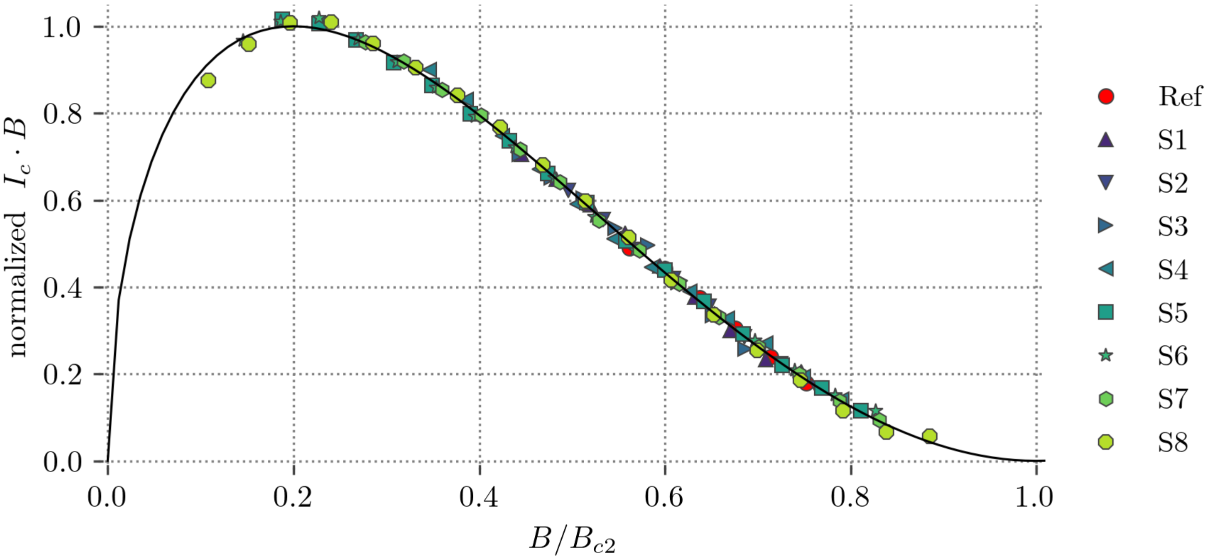

Figure 5.15 – Normalized product of critical current and absolute field $I_c \cdot B$ of samples from batch B1 plotted over the reduced field B/B_{c2}, where B_{c2} was determined from a fit of form Eq. (4.13). Data originally published in [Wil+20b].

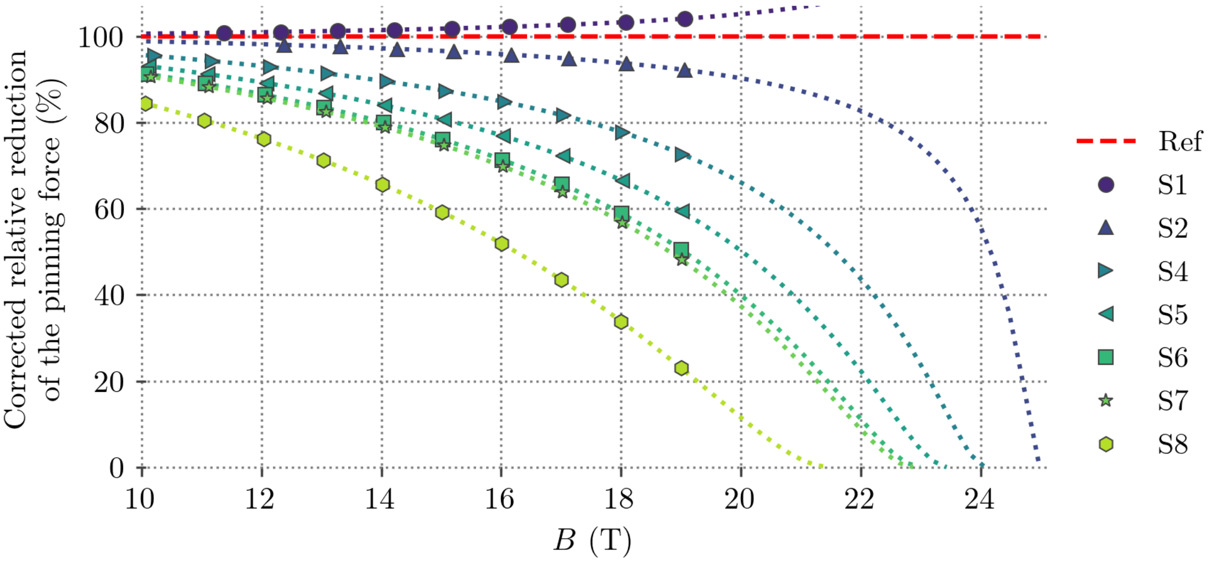

Figure 5.16 – Normalized relative reduction in pinning force for samples of batch B1, corrected for the absolute loss in active conductor cross section. The lines indicate the extrapolation of a fit of the measurement data to a function of the form as in Eq. (4.13).

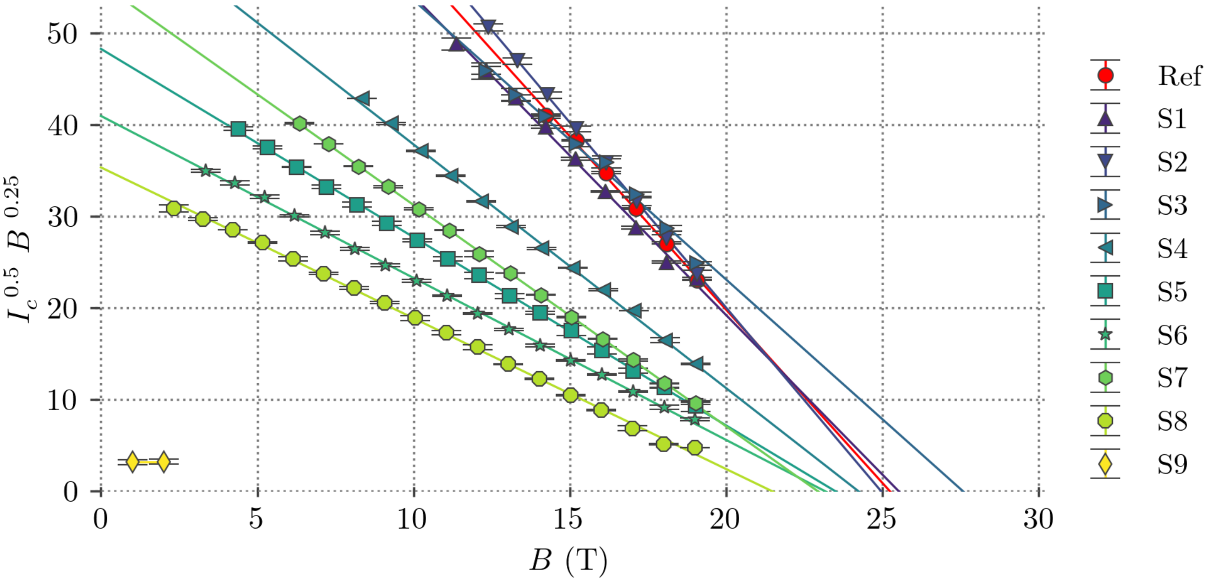

Figure 5.17 – Critical transport current measurement results of samples from batch B1 as in Fig. 5.12, shown in the Kramer representation as in Eq. 4.15, including linear fits to each data set. Data originally published in [Wil+20b].

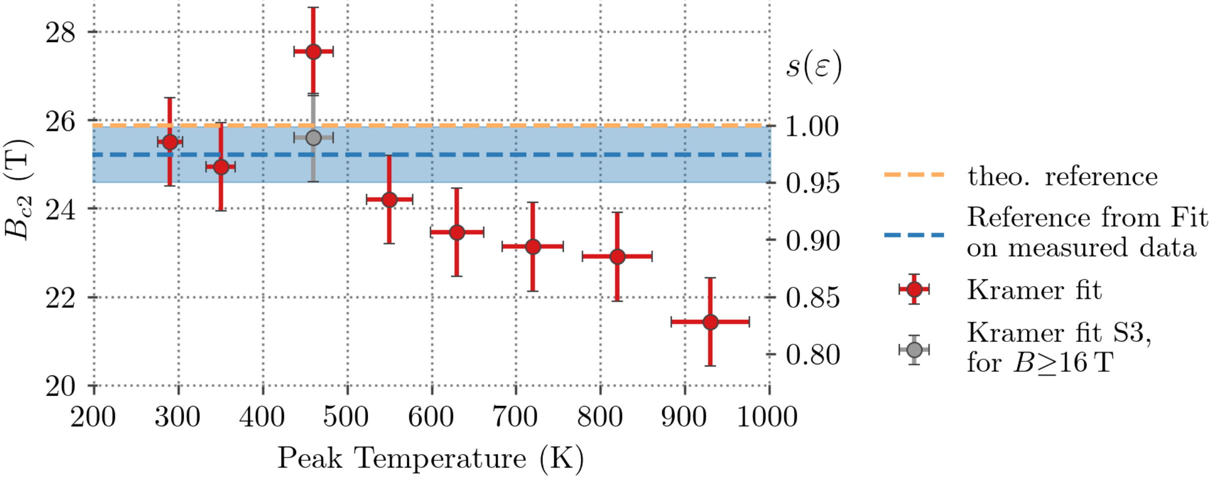

Figure 5.18 – B_{c2} obtained from linear fits on the measured critical transport current in the Kramer representation as in Fig. 5.17. The approximate value of the strain dependent function $s(\varepsilon)$ according to Eq. (4.11) is shown on the right hand axis.

wires was subsequently simulated with the mechanical solver, i.e. the evolution of the mechanical deformation of the wires and the sample holder as well as the residual strain after the beam impact were studied. Material properties were used from literature where available and from internal material databases or measurements [Sch+15; Fer18; Dav11; LG17; Mit05; WR96; SDR92; Prz68].

The mechanical simulations in ANSYS® were performed by J. Schubert and documented in the form of a Bachelor thesis[Sch20], which was supervised within the context of this thesis. This section gives an overview on the relevant points, necessary to discuss the post processing of the obtained results in the following.

A simplified wire geometry was assumed. The Nb_3Sn phase was modeled as a cylindrical shell of a mixture of Nb_3Sn and copper. The individual filaments were not modeled in detail, but the cylinder shell covered the filament region fully. The material properties of this shell were chosen to be a mixture of materials, representing the local copper to superconductor ratio in that region. Material properties from tensile tests which showed a semi-plastic behavior for the Nb_3Sn phase [Fer18] were used. Finally, the Von-Mises-equivalent residual or plastic strain within the cylinder shell was evaluated and is used in the following analysis.

The sample holder was modeled as a laminated block of copper including the grooves, where the wire samples were located. The imprint marks and damage of the copper matrix, which were found in the visual inspection could be traced back to originate from thermal expansion of the sample holder and samples, and hence a compression of the samples due to the sample holder in the grooves, starting from sample S4 and higher. The copper matrix of the Nb_3Sn wires is considered to be significantly softer than the cold worked copper of the sample holder.

The kinks in the wires could be traced back to originate from transversal oscillations of the wire around the beam impact center. Due to large thermal gradients and the resulting imbalance in thermal expansion after the beam impact, the wire starts to oscillate as the hotter side of the wire expands stronger longitudinally than the cooler side. After the re-cooldown a certain kink is left, due to plastic strain, in agreement with the observed bent samples, as shown in Fig. 5.10.

The simulated residual strain distribution in the wire cross section at the central point of the beam impact area is shown in Fig. 5.19 as an example for Sample S4, which was observed to be the first sample to be significantly degraded. Furthermore, the cross section perpendicular to the beam, in the xy-plane, is shown in Fig. 5.20. In both plots the Von-Mises-equivalent residual strain is shown. The wire diameter and the filament positions are shown just as indication. Due to the beam offset during the experiment, a clear and strong gradient is visible. Strain values range from 0.23% to more than 5%. The simulations do not take into account physical fracturing, therefore the very high values of strain are purely hypothetical. In section 5.4.5 it will be shown, how the problem of filament cracking due to excessive strain is modeled in a post processing step. The pre-strain is not simulated, so the simulated strains are understood as relative changes and need to be corrected for ε_m according to Eq. (4.12). The uncertainty of the obtained strain values were estimated to be around 16% [Sch20], taking into account the uncertainties in the energy deposition due to the uncertainty of the wire positioning as well as the material properties uncertainty and uncertainties due to the FEM mesh and geometric approximations of the real sample holder geometry.

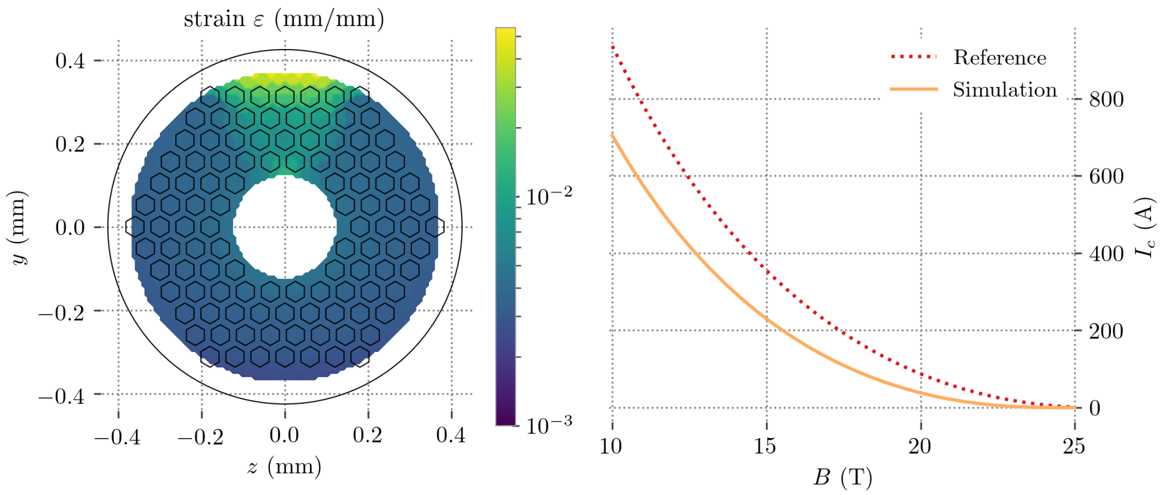

Figure 5.19 – *Left:* Schematic central wire cross section of the Nb_3Sn RRP® wire and simulated local residual strain for sample S4 with the assumed beam-offset of $y_0 = 1.1$ mm as obtained in thermo-mechanical simulations [Sch20]. The filament positions are indicated by hexagons (compare Fig. 4.3).
Right: Critical current for a wire with that strain distribution obtained by scaling the local critical current density according to the strain dependent scaling law in Eq. (4.1) and integrating over the full cross section to obtain the absolute critical current. The simulated value is compared to the theoretical reference for this type of wire, both at 4.2 K.

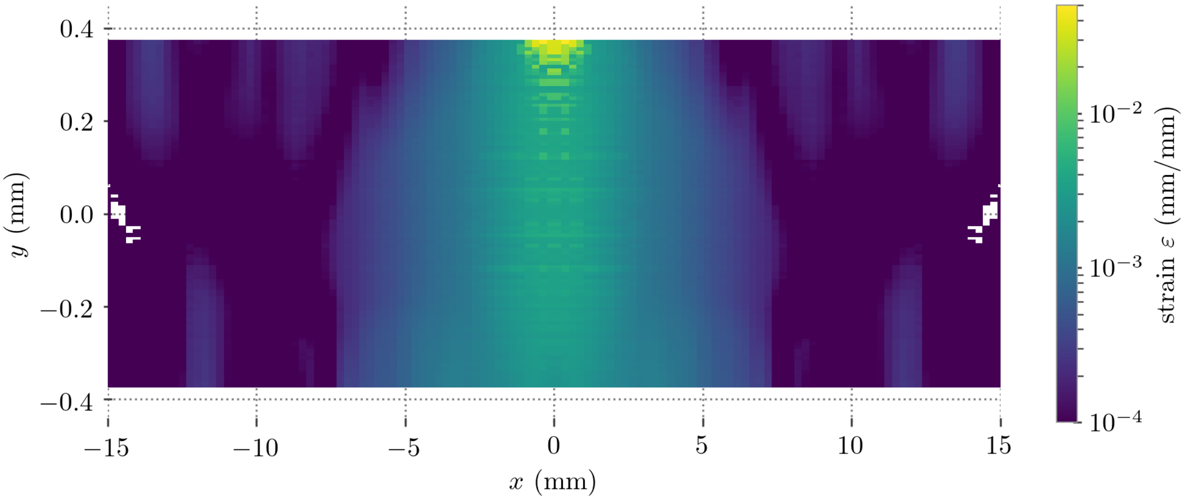

Figure 5.20 – Simulated local residual strain in the Nb_3Sn RRP® wire at sample position S4 with the assumed beam-offset of $y_0 = 1.1$ mm. The cross section perpendicular to the beam direction is shown.

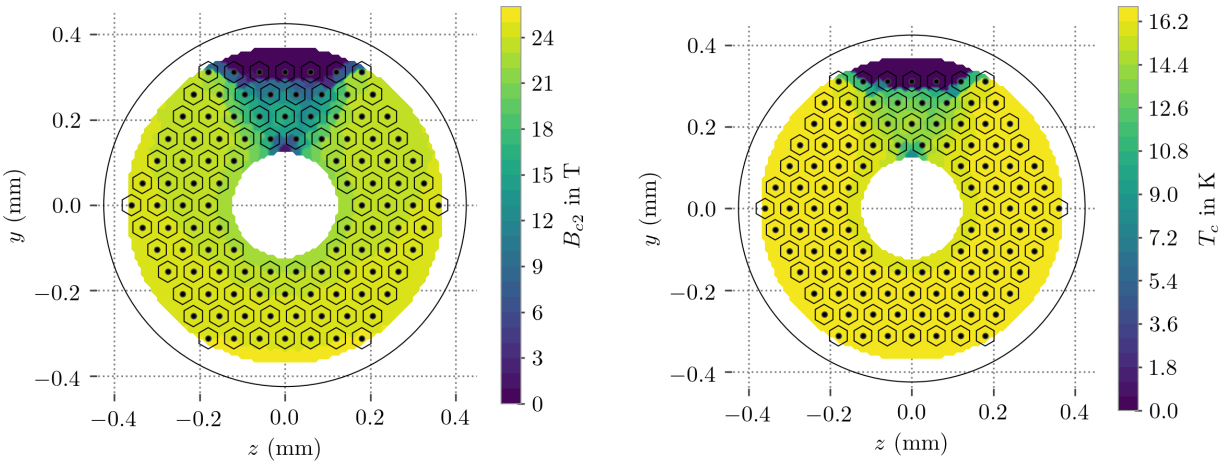

Figure 5.21 – Local B_{c2} (left) and T_c (right) for sample position S4, calculated with the simulated local residual strain as shown in Fig. 5.19. The strain dependent function $s(\varepsilon)$ was assumed to be of the form as in Eq. (4.17) with parameters as in Table 5.2.

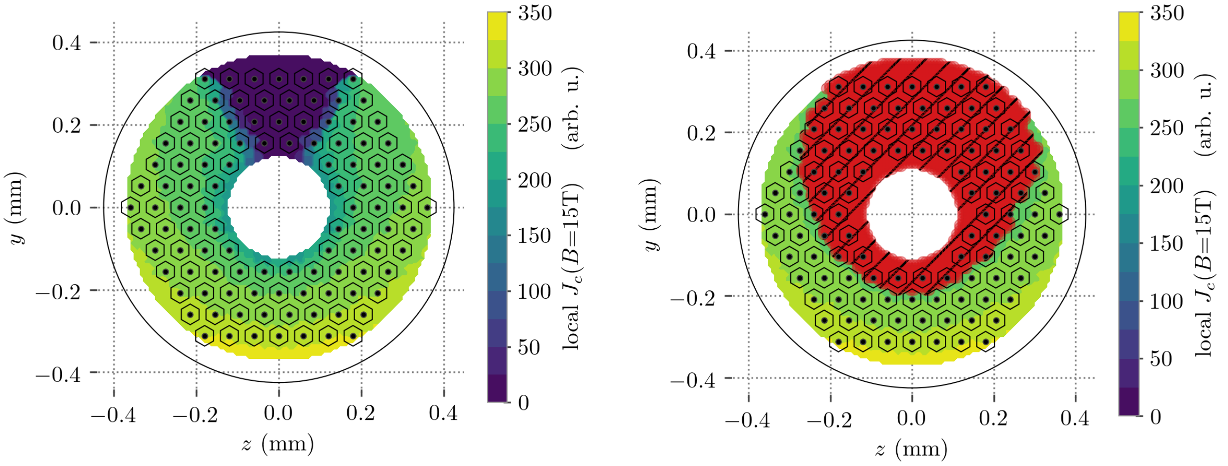

Figure 5.22 – Calculated local critical current density of the Nb$_3$Sn RRP® wire at sample position S4 with the simulated lattice strain as shown in Fig. 5.19 assuming the strain dependent scaling law in Eq. (4.1). The red patches on the right hand side plot indicate areas where the van-Mises-equivalent strain exceeded $\varepsilon \geq 0.57\%$ during the beam impact, indicating filament breakage.

5.4.4 Applying microscopic models to simulation results

Given the residual plastic strain distribution over the filament center cross section, several post processing steps have to be performed. Firstly, the critical temperature T_c and critical upper magnetic field $B_{c2}(4.2\,\mathrm{K})$ need to be calculated on each node, according to Eqs. (4.7,4.9). The results are shown in Fig. 5.21 for Samples S4. In a next step, the local critical current density needs to be calculated for each node, using the scaling law in Eq. (4.1) and the strain dependent function as in Eq. (4.17). The scaling parameter C_1 in Eq. (4.1), which determines the absolute value of the critical current, is evaluated by fit on reference measurement data. For the RRP® wire the scaling

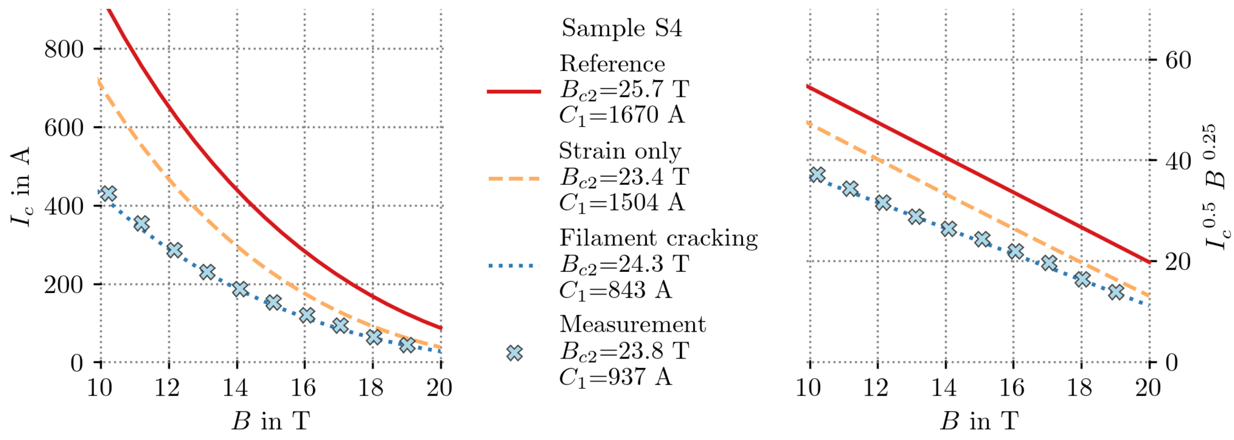

Figure 5.23 – Simulated critical transport current (left) and Kramer representation (right) of the Nb_3Sn RRP® wire at sample position S4. The different curves represent the original undegraded I_c (red solid line), the degradation by strain only (dashed yellow line) and the irreversible strain limit model with $\varepsilon_{0,irr} = 0.57\%$ (blue dotted line) found by a best fit to the measured I_c for Sample S4 of Batch 1. The legend indicates the resulting values for B_{c2} when performing a linear fit to the Kramer representation of the simulated data.

parameters are taken from literature, where this exact type of wire has been characterized under axial and transverse strain [NIA08]. The scaling parameters are shown in table 5.2 and are used in this thesis.

Table 5.2 – Scaling parameters of the strain dependent function as in Eq. (4.17) for the HL-LHC RRP® wire from [NIA08].

C_{a1}	C_{a2}	ε_{0a}	ε_{max}
59.36	23.91	0.309%	-0.11%

The result of the critical current scaling is shown on the left hand side of Fig. 5.22 for an applied magnetic field of 15 T. The local values represent the hypothetical critical transport current of the full wire if it was subjected homogeneously to that strain value. To derive the critical transport current of the full wire with such an inhomogeneous strain distribution, the integral of the critical current density is calculated over the area of interest, i.e. the cylinder shell area where the filaments are located. This can be done for all temperatures and fields.

Figure 5.23 shows the resulting calculated critical transport current as a function of the applied magnetic field from 10 T to 20 T and at a temperature of 4.2 K. A degradation with respect to the original reference curve is seen but the measured value is clearly below the calculated curve. When taking into account the irreversible strain, i.e. filament fracturing, and therefore certain areas no longer participating in the current transport, a good agreement can be found between measurement and simulation. The method will be described in the next section. On the right hand side of Fig. 5.23 the resulting Kramer representation is plotted. As opposed to the absolute critical current, the resulting critical magnetic field from the fit is already very similar to those values from fits on the measured data, even without taking into account filament cracking.

Table 5.3 – Minimum (ε_{min}), maximum (ε_{max}) and average strain (ε_{avg}) from the simulation for Samples S1 to S8. Additionally the critical strain ($\varepsilon_{0,irr}$) as found by a best fit of the critical current model on the measurement data are presented.

Sample Nr	$\varepsilon_{0,irr}$ (%)	ε_{min} (%)	ε_{max} (%)	ε_{avg} (%)
1	–	0.105	0.218	0.160
2	–	0.156	0.283	0.216
3	–	0.226	0.411	0.310
4	0.577	0.226	5.437	0.511
5	0.748	0.138	20.050	2.123
6	0.756	0.315	3.314	0.649
7	1.033	0.168	6.180	1.087
8	1.208	0.264	41.924	6.037

5.4.5 Irreversible strain by Fit

As described above, the upper strain value in the simulation is not limited, i.e. the material does not fracture. Therefore a certain threshold has to be defined. The so called critical or irreversible strain is however not easy to determine as it varies substantially between wires. It was chosen to determine a threshold value $\varepsilon_{0,irr}$ by fit. An irreversible strain $\varepsilon_{0,irr}$ is defined above which the filament is assumed to be fractured and therefore no longer contributes to the integral of the critical current density. Then, the resulting critical transport current can be calculated in an analogous manner as before. The result is shown on the right hand side of Fig. 5.22. The red area indicates strain values of more than $\varepsilon_{0,irr} = 0.57\%$. This area was assigned a critical current density of zero in the surface integral. The resulting critical transport current is given in Fig. 5.23. The value $\varepsilon_{0,irr} = 0.57\%$ was found by a best fit of the calculated critical current to the measured critical current, by adapting the threshold value $\varepsilon_{0,irr}$.

Accordingly all simulated data were fitted to the measured critical current data of Batch 1. The found irreversible strain is given in Table 5.3. No consistent irreversible strain could be found between the samples. The reason for this is, that in reality the threshold value is rather a distribution and not a fixed value. Furthermore, a crack might not necessarily degrade the filament fully. The minimum and maximum strains as well as the average strain over the cross section are shown as well. The highest strain in sample S3 can give an indication for the threshold, as S3 was the last sample which did not show degradation.

Figure 5.24 shows the results of the calculated critical currents, taking into account the irreversible strains found in the best fit to the measurements, as listed in Table 5.3. This shows, that reasonable agreements can be found by fitting the irreversible strain. An exception was sample S8, which was less degraded in the measurement, than the simulation predicted. On the right hand side, the Kramer representation of the calculated critical currents (lines) and fitted critical currents (markers) is shown. The critical magnetic fields can be concluded from linear fits on the Kramer form as before, and are shown in Fig. 5.25 along with the measurement data. A reasonable agreement is found. For the samples that have seen higher energy deposition, the simulation without the strain cracking model predicts much stronger degradation than observed in the measurements. When the irreversible strain found by a best fit to the measured critical current data is included in the critical current calculation, a good agreement is found. In the critical transport current measurements, only the parts which are not affected by strain fracturing are contributing. Naturally, the parts of

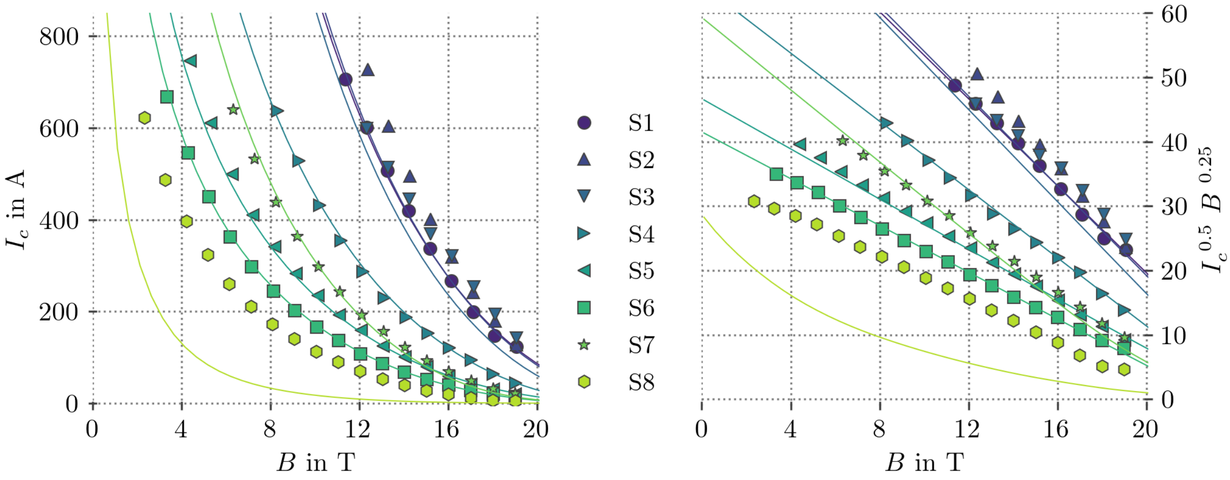

Figure 5.24 – Simulated critical transport current (lines), assuming the critical strain values ε_c as listed in Table 5.3. The critical strain values were found by a best fit to the measured data, which are represented by the symbols in the plot.

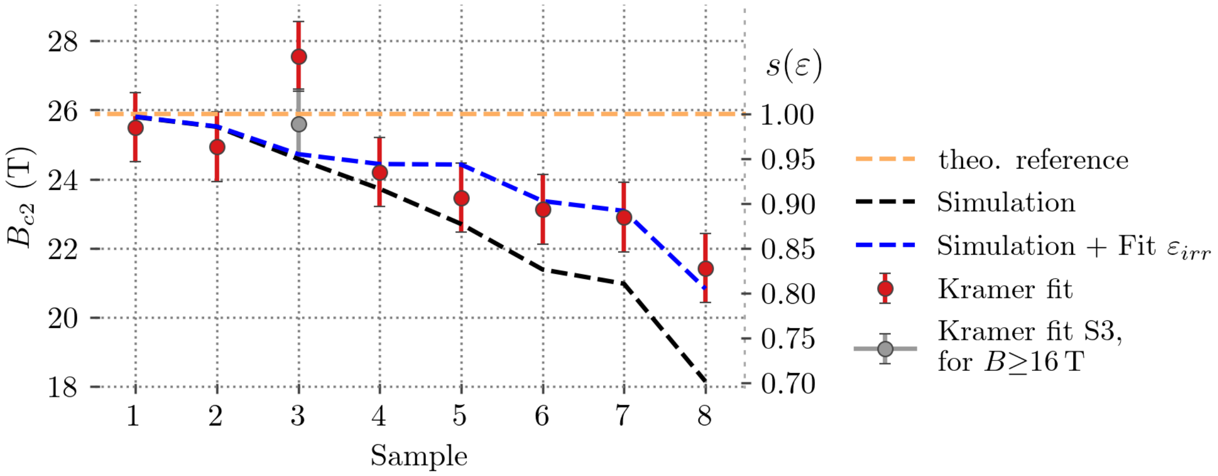

Figure 5.25 – B_{c2} obtained from linear fits on the simulated critical current in the Kramer representation as in Fig. 5.24 for the two simulation models both with and without the strain cracking model. $\varepsilon_{0,irr}$ was found by fit. Alongside the results from the fit on the measured data as in Fig 5.18 is shown.

the wire which are heavily degraded due to strain would also result in a lower B_{c2} but those region are likewise most likely to exceed the irreversible strain limit and, therefore, not contributing to the measurement. Thus, the remaining "active" filaments of the wire show a lower average degradation and relatively higher B_{c2}.

The model is only a simplified approach. In reality, the fracturing is observed over a region of strain rather than at one exact value [Jew08]. A more sophisticated model could include the degradation due to strain cracking accordingly as a distribution. However, this introduces the width of the distribution as another fit parameter and furthermore the general shape of this distribution is not clear (Gaussian or a more skewed type like a Maxwell-Boltzmann distribution). The approach has been tried an showed reasonable results (compare [Sch20]) but for the present type of study, the amount of available measurement data is too thin. The irreversible critical strain within this scope is treated as a numerical parameter to model the underlying physics adequately but its absolute value should not be payed too much attention.

5.4.6 Parameters for degradation due to inhomogeneous strain

A valid way to quantify the degradation is to perform extensive thermo-mechanical simulations. However, it is of interest to find other quantities that might indicate the onset or threshold for strong degradation potentially being more easily accessible from simulations. For example, taking into account only the peak temperature reached during the experiment is not generally representative. The physical origin of degradation is excessive strain and hence filament cracking. From the simulation the minimum, maximum and average strain can be extracted for each of the simulated samples and compared to the respective measured critical current degradation. The result is shown in Fig. 5.26. The minimum strain is not a good quantity, as both strongly degraded samples and weakly degraded samples show minimal strains in the same order of magnitude. For the maximum strain the situation is different. Samples that have been strongly degraded show a very large (and also nonphysical) maximum strain. The gap between the maximum strain in the non-degraded samples and the strongly degraded ones is huge and hence the maximum strain is neither a good measure for degradation. Only for sample S3, the maximum strain can allow for a quantitative analysis, as this was the sample with highest maximum strain which was not found to be degraded in the critical current measurements. Its maximum strain of $\varepsilon_{max} = 0.411\%$ can therefore be a indication of the maximum allowable strain. Finally, the average strain shows a very good correlation with the strong degradation of the critical current. In the region of $\varepsilon_{avg} = 0.31\%$ to $\varepsilon_{avg} = 0.51\%$, i.e. between samples S3 and S4, the strong degradation is observed to start, wich also matches the value of the maximum strain of sample S3.

As a second measure the temperature gradient is compared to the degradation of the critical current. In a first order, the strain should be directly proportional to the temperature gradient and hence could give a good indication of the degradation. The results are shown in Fig. 5.26. A fairly good correlation is observed, very similar to the peak temperature. A critical region of $\Delta T = 200 \ldots 250\,\mathrm{K/mm}$ is observed, where the critical current was observed to start degrading strongly.

Both measures can be used to estimate the onset of strong degradation (i.e. filament fracturing) in the wire. The average strain is more difficult and extensive to calculate via a coupled thermo-mechanical solver, which needs the preceding energy deposition simulation. However it is the correct approach based on the underlying physics model of degradation and showed rather good results in predicting the degradation when applying the scaling laws from literature. On the other hand, the beauty of using only the energy deposition and subsequent scalings such as peak temperatures and temperature gradients, lies in the simplicity of these type of simulations with respect to the full thermo-mechanical problem. As the peak temperature itself might not be generally representative, the temperature gradient could be a more adequate measure to indicate the order of degradation.

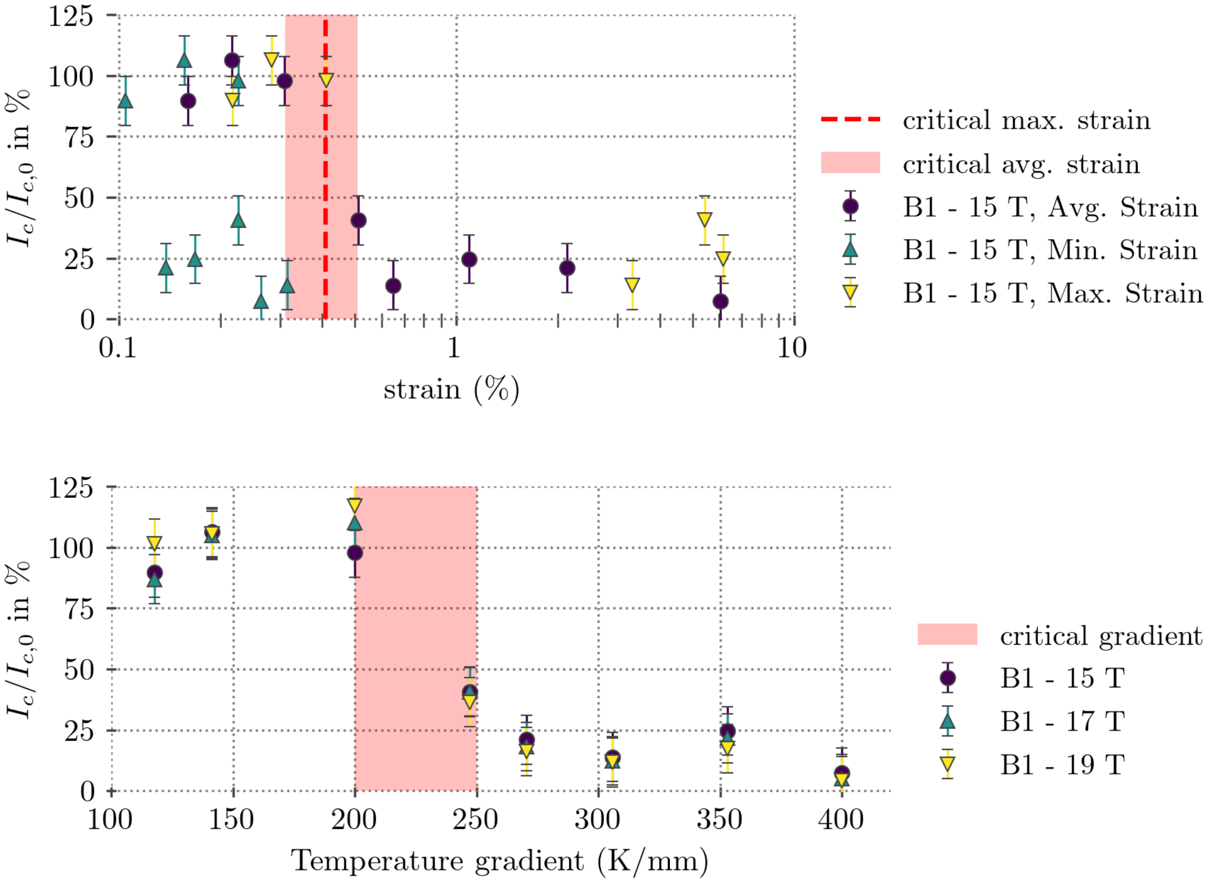

Figure 5.26 – Relative degradation of the critical current for all measured samples of batch B1, plotted over the simulated minimum, maximum and average strain in that respective sample (top) and plotted over the simulated temperature gradient in that respective sample (bottom).

5.4.7 Strain annealing experiment

An annealing experiment was performed to support the hypothesis of residual strain due to deformation of the copper matrix. Two of the beam impacted samples were heated to 300 °C for several hours, one sample with large degradation (sample S8 from batch B1) and one with full degradation beyond the reversible limit (sample S9 from batch B1). After this heat treatment, the critical transport current was measured again.

The results of the two measurements of Sample S8 are shown in Fig. 5.27. The critical transport current was improved; At 15 T from 7.5% to 15% of the original critical current. This is a clear indication for the residual strain contributing to the degradation of the critical current, as filament breaking cannot be reversed by such a heat treatment. The measured value of the critical current at $B = 19\,\mathrm{T}$ was surprisingly almost equal to the value at $B = 18\,\mathrm{T}$, as it was probably below the resolution limit of the critical transport current measurements for the short samples. At these small current values, the stabilizing copper and dog-bone sample holder can take the current and it is very difficult to determine the critical current. For this reason, the value was not taken into account in the Kramer-fit. The fit shows an improvement of B_{c2} in agreement with the strain dependent critical current model. No improvement was found for the permanently degraded sample S9, which was assumed to be damaged fully due to filament breakage.

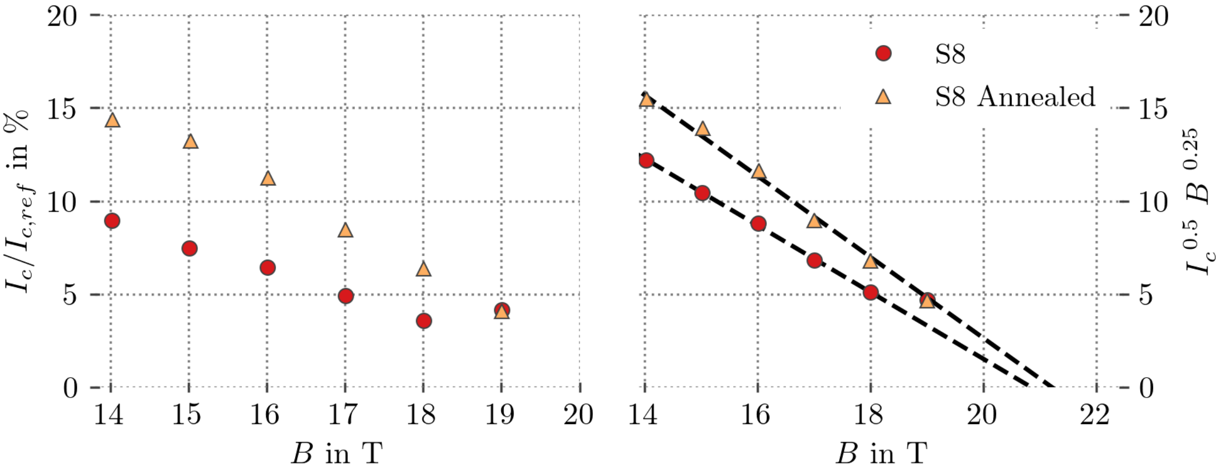

Figure 5.27 – Results of the critical transport current measurements of the Sample S8 of the first batch, normalized to the reference sample. The measurements after the beam impact as well as after an annealing heat treatment of 300°C for several hours to fully anneal the copper matrix from residual strain are shown.

5.4.8 Magnetization measurements

Three beam impacted samples S3, S6, and S8 from batch B2 as well as a reference wire were chosen to undergo magnetization measurements. Small sections of about 5 mm length were cut out, with the beam impacted area in the center. Measurements at temperatures of 2 K, 4 K, 10 K and 15 K were performed each at fields up to 6.5 T. According to Eq. (3.19), the magnetization is proportional to the critical transport current density. The relative degradation of the critical current density was calculated and is shown in Fig. 5.28. Two effects are visible:

Firstly, even sample S8, which has been observed in the critical transport current measurement to be strongly degraded, shows very little degradation in the magnetization measurements. This shows the nature of magnetization measurements. The ramping magnetic field induces localized current loops according to the Bean model. These might be even inter-granular in the Nb_3Sn grains with extents of around 100 nm, and hence on spacial scales much smaller than the dimensions of the cracks in the filaments. Furthermore, as the name says, they are current loops. Local degradation does therefore not act as a bottle neck of the full wire's transport current. Magnetization measurements rather give an volumetric averaged critical current density. This is very much opposed to the critical transport current, where a bottle neck, like a crack in the filament center, is the most important source of degradation for the full length of the wire as the current can no longer pass along. The reason for the observed small degradation is the sample size. With the 5 mm long pieces and a beam size of 1.1 mm the edge regions of the sample have little degradation and the full average of the sample's critical current density is, therefore, also less affected. A solution could be to take much smaller pieces capturing only the beam impact center. However, this imposes technical problems in sample preparation.

Secondly, Sample S3 and S6 show an improvement in the critical current. For sample S3, the improvement is in the order of more than 10%, while for S6, the improvement is marginal. As shown in Eq. (4.12), the Nb_3Sn based wires are intrinsically pre-strained. It is therefore fair to assume, that in sample S3, the measured improvement is real and originates from the induced

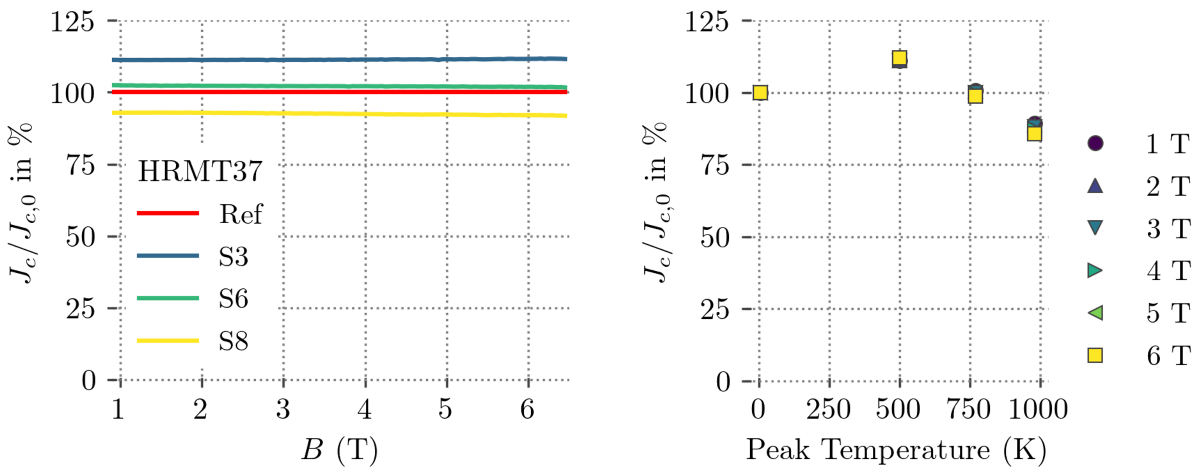

Figure 5.28 – Results from the magnetization measurements performed at a temperature of 10 K on the beam impacted Nb_3Sn RRP® wire samples from batch B1. *Left:* Relative degradation of the scaled critical current density as a function of the applied magnetic field. *Right:* Relative degradation of the scaled critical current density at selected magnetic fields, as a function of the peak temperature.

strain compensating the pre-strain. For the same reason as above, the total volumetric average has to be considered for sample S6. The observed measured critical current density is a result of the sum of some regions being largely strained and degraded in the central parts and the edge regions with small enough strain to compensate the pre-strain. The sum then results to a small overall average improvement. To support this hypothesis, an edge part of the tested wires was measured for sample S3 and that part of the sample behaved similarly to the reference sample.

The analysis on the Kramer form was also performed for these samples. The result of the fitted values for $B_{c2}(T)$ is shown in Fig. 5.29 for the four measured samples at the four measured temperatures. Moreover, the data was fitted to a function of the form as in Eq. (4.4) to conclude $B_{c2,0}$ and T_c. The difference is very small and no significant degradation could be determined between the samples. The reason is similarly the nature of the magnetization measurements. The deduction of critical parameters from this type of measurements via the critical current scaling is not accurate for this type of samples with highly irregular strain distributions.

5.4.9 Critical Temperature measurements

The sample pieces described above were subjected to a small magnetic field of $B = 1\,\mathrm{mT}$. The magnetization was measured during a temperature sweep from 4 K to 20 K. As described in section 3.2.2, the change in magnetization with temperature gives a representation of the critical temperature distribution in those sample pieces. The resulting numerical derivations from the measured magnetization curves are plotted in Fig. 5.30. A pronounced tail towards lower values of T_c is found for samples with higher energy deposition (S6, S8), originating from largely strained areas in the sample. From the simulations of the volumetric strain distribution in the 5 mm long segments, the theoretical critical temperature, field and current distribution can be derived according to Eqs. (4.1, 4.7, 4.9). In the reference measurement in Fig. 5.30 it is visible that the wire has an intrinsic T_c distribution which does not result from strain but from natural Sn-composition

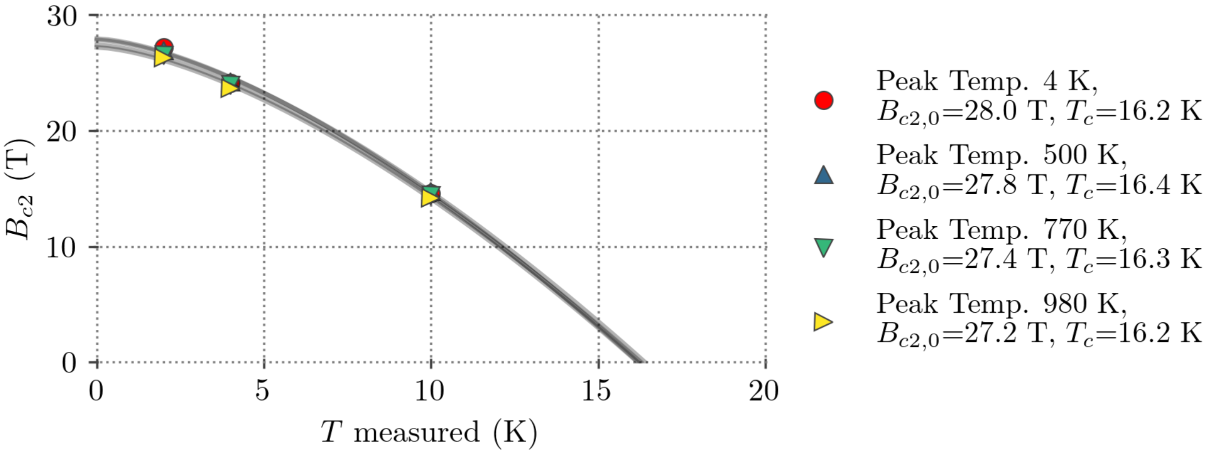

Figure 5.29 – Critical surface $B_{c2}(T)$ of the beam impacted Nb$_3$Sn RRP® wire samples from batch B1. The upper critical field was determined by Kramer fit analyses of the magnetization measurements at various temperatures. The resulting values were fitted with a function of the form as in Eq. (4.4), to conclude $B_{c2,0}$ and T_c. The results of these fits are given in the plot legend.

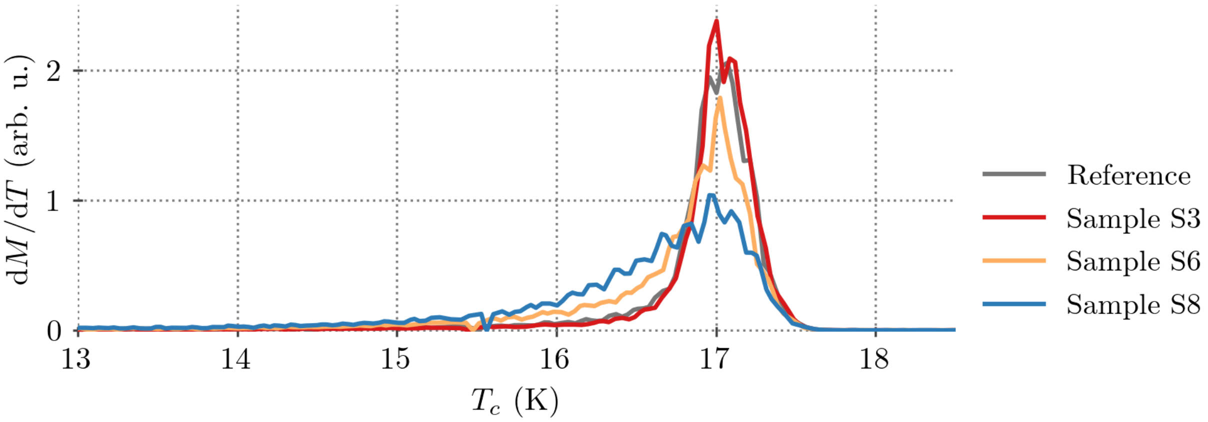

Figure 5.30 – Critical temperature T_c distribution for three different samples of Batch 1. The change in magnetization was measured during a temperature sweep from 13 K to 20 K with an applied magnetic field of $B = 1\,\mathrm{mT}$.

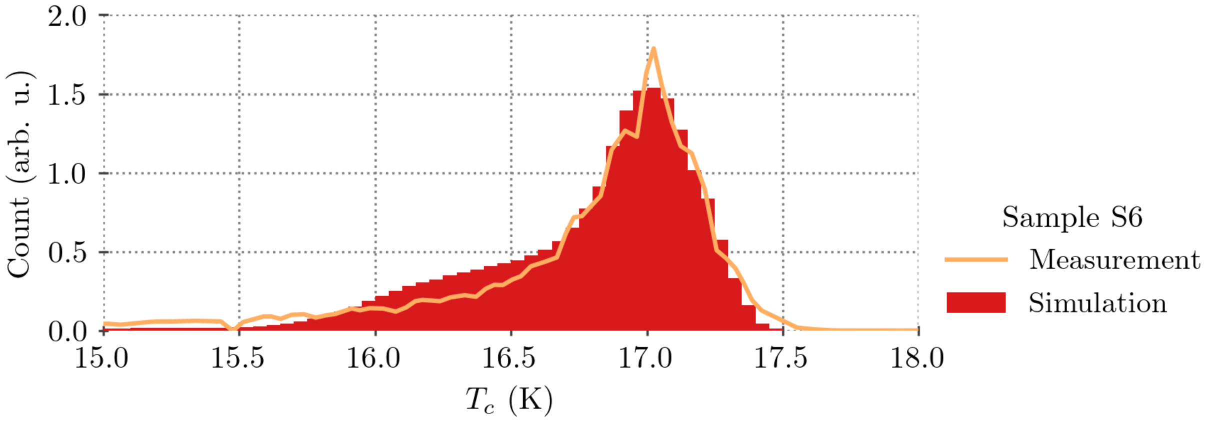

Figure 5.31 – Critical temperature T_c distribution as calculated from the simulated volumetric strain distribution in sample S6 from batch B1. In addition the line shows the measured change in magnetization of Sample S6 of batch B1 during a temperature sweep from 15 K to 20 K with an applied magnetic field of $B = 1\,\mathrm{mT}$ as shown in Fig. 5.30.

gradients within the Nb_3Sn filaments [4]. To calculate the critical parameters it was chosen to assign a Gaussian distribution of critical values for T_c to each simulation node rather than fixed ones. The Gaussian distribution with a mean at $T_{c,0} = 16.9\,\mathrm{K}$ and a width of $\sigma_{Tc} = 0.1\,\mathrm{K}$ was used to match the measured distribution of the reference sample. Similarly, this was done for B_{c2} with a mean at $B_{c2,0} = 29.5\,\mathrm{T}$ and a width of $\sigma_{Bc2} = 0.5\,\mathrm{T}$. The distribution was calculated for each simulation node within the volume of the size of the measured sample (approximately $\pm 2.5\,\mathrm{mm}$ around the beam impact center) and strain dependent critical parameter degradation was derived from the strain scaling laws Eqs(4.17,4.7). A comparison between the volumetric distribution of simulated and measured critical temperatures for sample S6 is shown in Fig. 5.31. Simulation and measurements show good agreement. Especially the long tail towards lower values of T_c, originating from highly strained regions, is well reproduced in the simulations.

The resulting distributions of T_c and $B_{c2}(4.2\mathrm{K})$ for all simulated samples are shown in Fig. 5.32. A step-wise shift to lower values of T_c and B_{c2} is visible with increasing sample number, i.e. increasing energy deposition. The influence on B_{c2} is much stronger due to the direct proportionality of B_{c2} on the strain dependent function $s(\varepsilon)$, and values as low as 20 T are observed.

5.4.10 Microscopical analysis

Both electron microscopical and optical microscopical have been performed on Nb-Ti and Nb_3Sn samples at the the CERN EN-MME-MM Microscopy laboratory under supervision of M. Meyer [Meya]. Secondary emission microscopy (SEM), back scattered electron (BSE) analysis as well as energy dispersive X-ray (EDX) analysis have been performed on the samples. While the regular SEM gives a topological representation in its contrast, images obtained via he BSE analysis show a proportionality of the brightness to the atomic number, i.e. heavier elements have a brighter signal in the image. In EDX, elements are identified by their characteristic X-ray spectral lines and furthermore the stoichiometric amount can be quantified by comparing the signal strengths. It

---

[4] for a detailed analysis of Sn-composition gradients see [Pfe20] and references therein

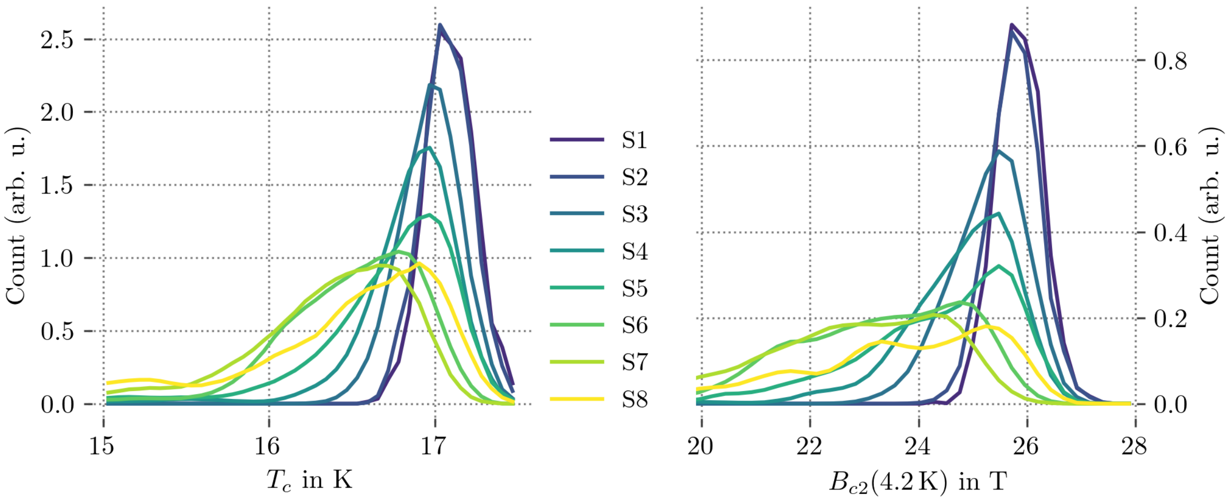

Figure 5.32 – Simulated critical temperature T_c and critical field B_{c2} distribution, calculated from the simulated volumetric strain distribution in samples S1 to S8.

is therefore possible to evaluate the chemical composition with this method more quantitatively. The results have been summarized in dedicated reports [Meyb]. The relevant points will briefly be shown in the following.

An optical microscopic analysis has been performed to evaluate the cracking behaviour in the samples. They were polished transversally to the wire axis down to about half the wire radius, i.e. the cross section along the central wire axis could be observed. Figures 5.33 and 5.34 show the overview of Samples S1 to S8 with the exception of samples S3 and S7 which were not available for this analysis.

Strong cracking of the filaments is observed from sample S5. In this sample, clusters of cracks are visible, both transversal and longitudinal to the filaments. In Sample S6 the cracks are wider and networks of large cracks range over almost the full width. Finally, samples S8 is broken in half with only a small connection left in the outer region of the copper matrix, which is in agreement with the findings of the visual inspection (compare section 5.4.1). However, this sample was examined in the thermal annealing study beforehand and large areas, where diffused tin has entered the copper matrix, are visible on the outer parts of the wire. Due to this rather special and extensive treatments it can not be excluded, that this wire was broken to the visible extent only after the heat treatment, with the subsequent critical current measurements. The damage beforehand was probably already strong enough to weaken the wire extensively and eventually forming this breaking point.

In general, occasionally very fine cracks are visible even in the reference sample and other lesser degraded samples. They are however much finer and mostly singular and not forming any kind of network. They lie outside the beam impacted area and it can be concluded that they do not originate from it. Besides, the samples in which only these fine cracks were visible were not observed to be significantly degraded in their critical current.

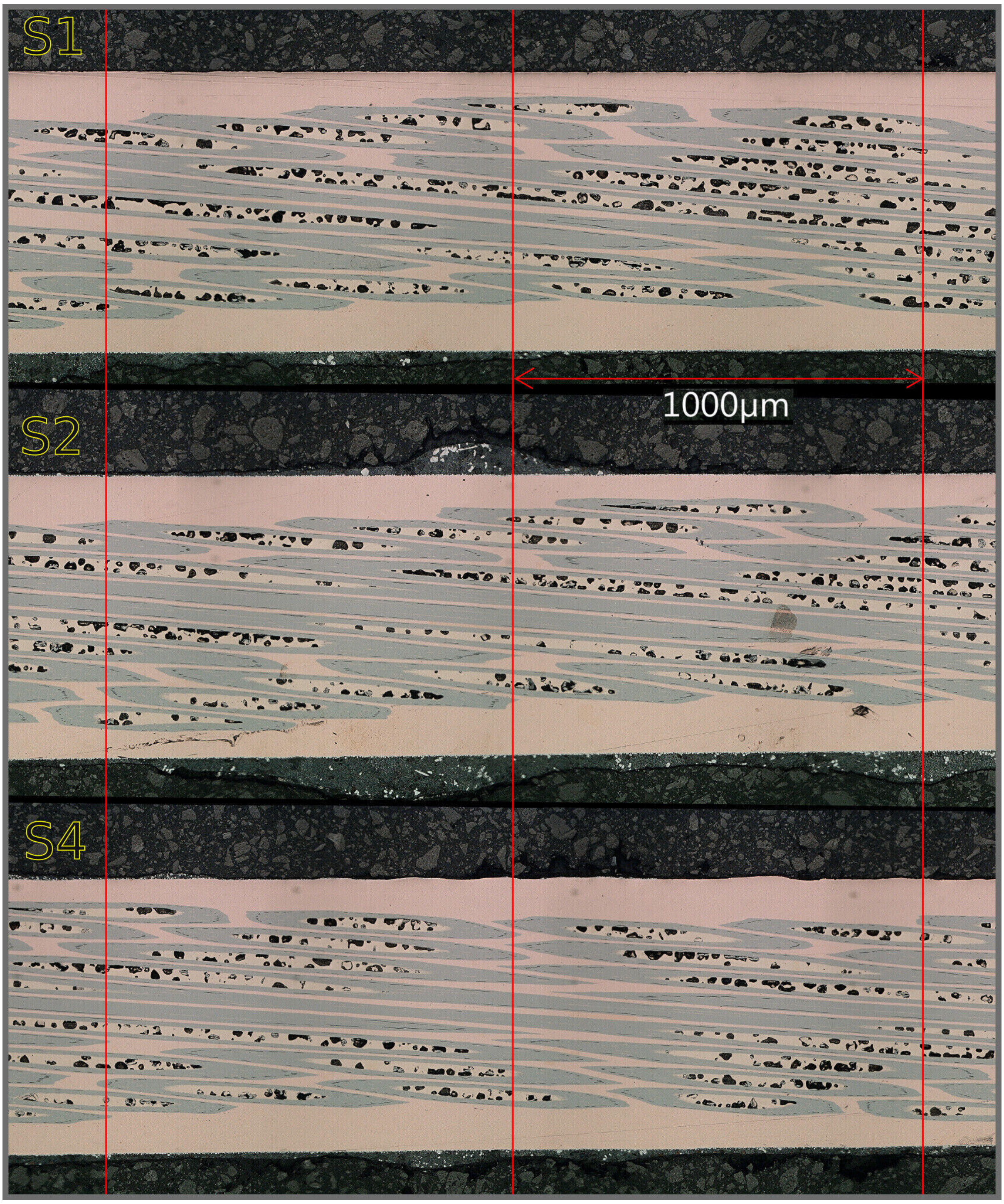

Figure 5.33 – Nb_3Sn samples S1, S2 and S4 of batch B1 polished such that the longitudinal plane in the wire center is visible, and observed with an optical microscope. The red lines indicate the estimated center and a spacing of ±1 mm, i.e. about the main beam impacted area. Image courtesy of M. Meyer, CERN microscopy lab [Meyb].

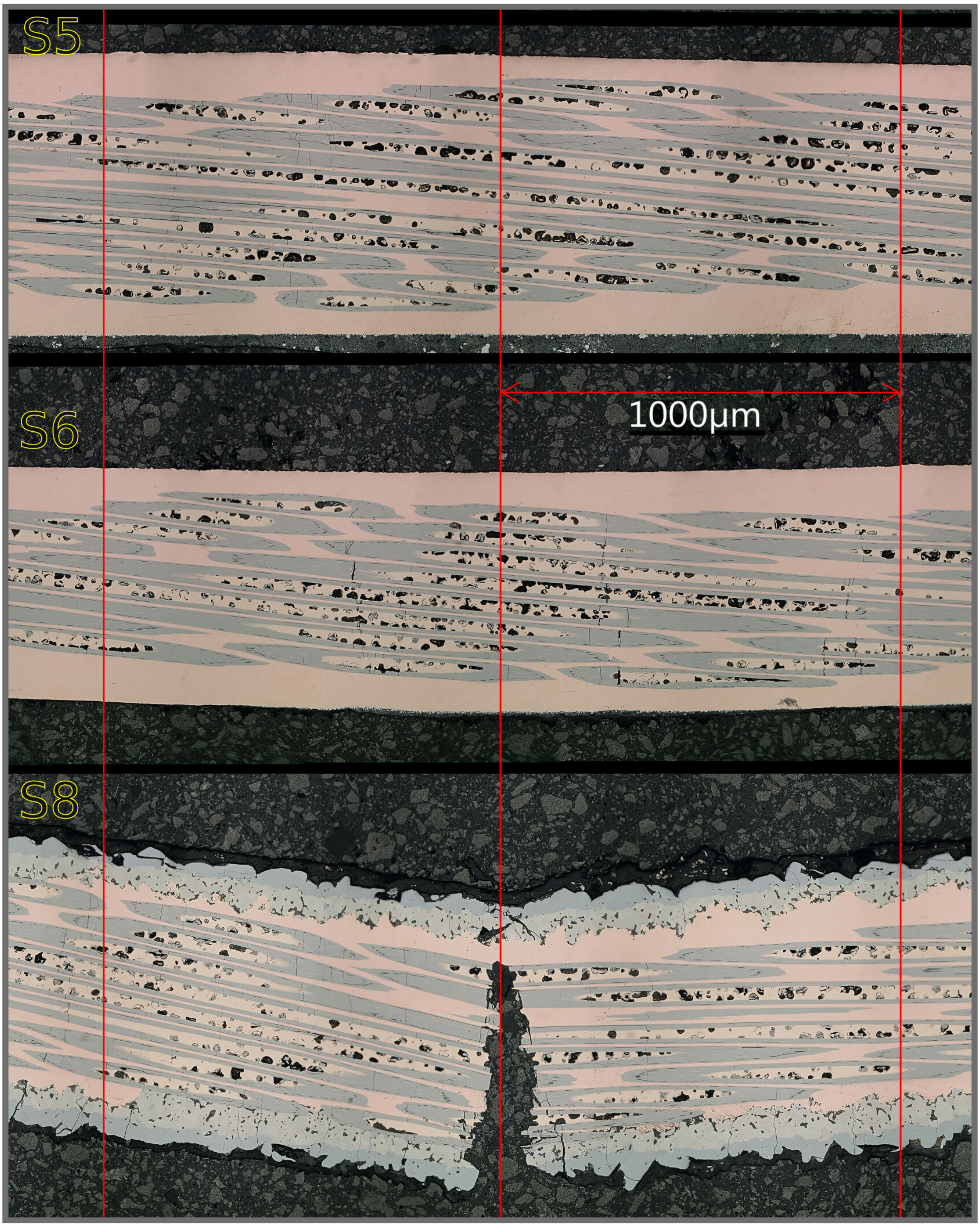

Figure 5.34 – Nb_3Sn samples S5, S6 and S8 of batch B1 polished such that the longitudinal plane in the wire center is visible, and observed with an optical microscope. The red lines indicate the estimated center and a spacing of ±1 mm, i.e. about the main beam impacted area. Sample S6 seems to be smaller in radius, as it was polished down further than the wire center due to misalignment in the sample mold. Sample S8 shows strong signs of diffusion on the outer edges which originate from the long heat treatment during the strain annealing experiment (compare section 5.4.7). Cracks are visible for Sample S5 and higher. Image courtesy of M. Meyer, CERN microscopy lab [Meyb].

SEM, BSE and EDX electron microscopic analysis were performed as well on the same samples. The observation of the EDX showed no change in chemical composition on the length scales that are resolvable and also the BSE method showed no significant change of the (chemical) microstructure, both in agreement with previous findings [Kul18; Rag18]. In contrast to the optical analysis, higher resolved images could be obtained with the SEM. Two images of the center regions of samples S5 and S6 are shown in Fig. 5.35. The copper matrix was etched away such that only the Nb_3Sn filament tubes remained. The fine crack network in sample S5 and the more severe cracks in sample S6 are visible in a close up image. In sample S6 it can be seen that the filaments are still partially held together by the ductile Nb-barrier surrounding them even though the crack clearly separates the full filament (compare lowest and second to bottom filament).

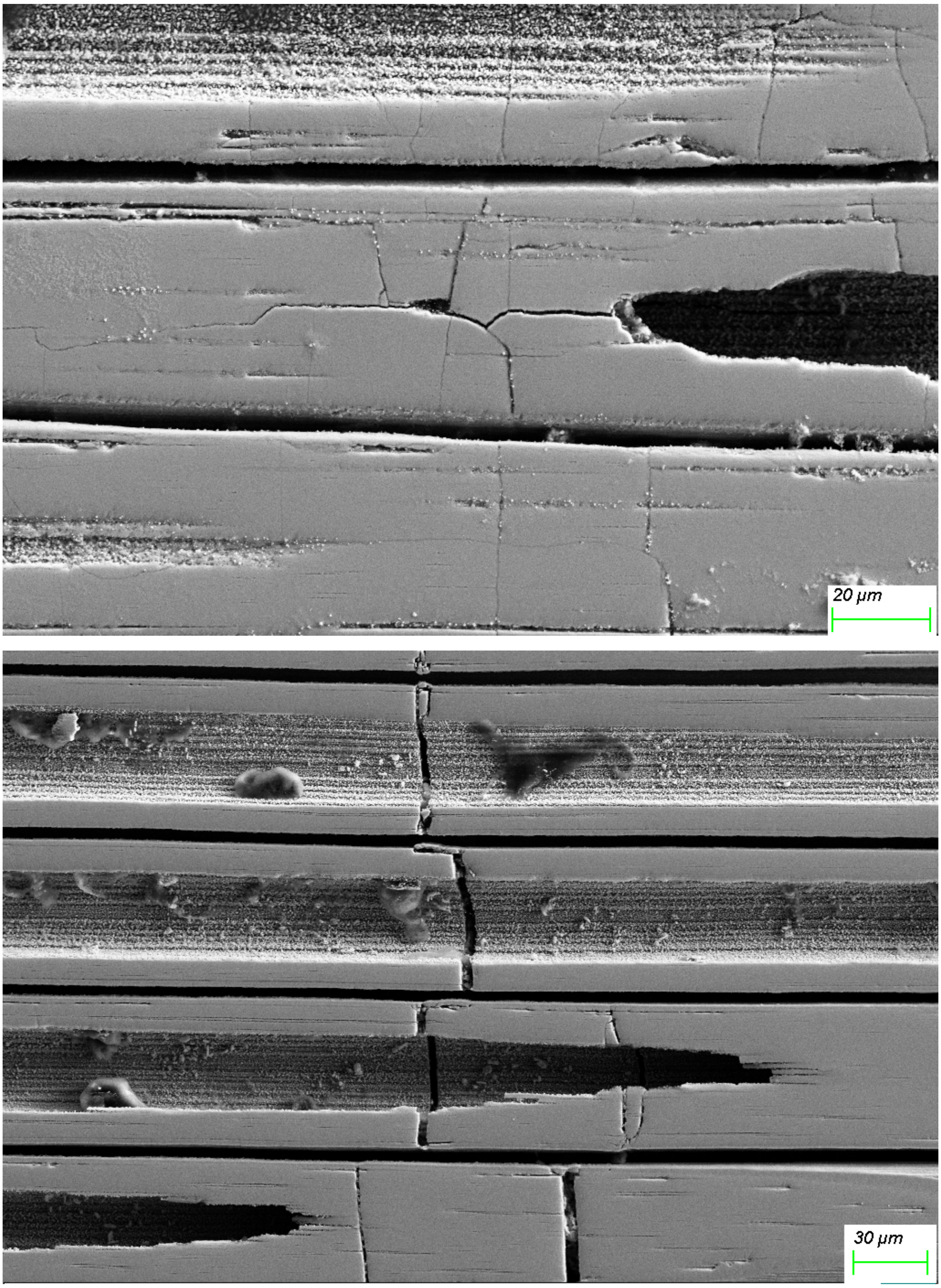

Figure 5.35 – Nb_3Sn samples S5 (top) and S6 (bottom) of batch B1 polished such that the longitudinal plane in the wire center is visible, and observed with with an electron microscope. The copper matrix was etched to leave the filaments exposed. Image courtesy of M. Meyer (CERN microscopy lab) [Meyb].

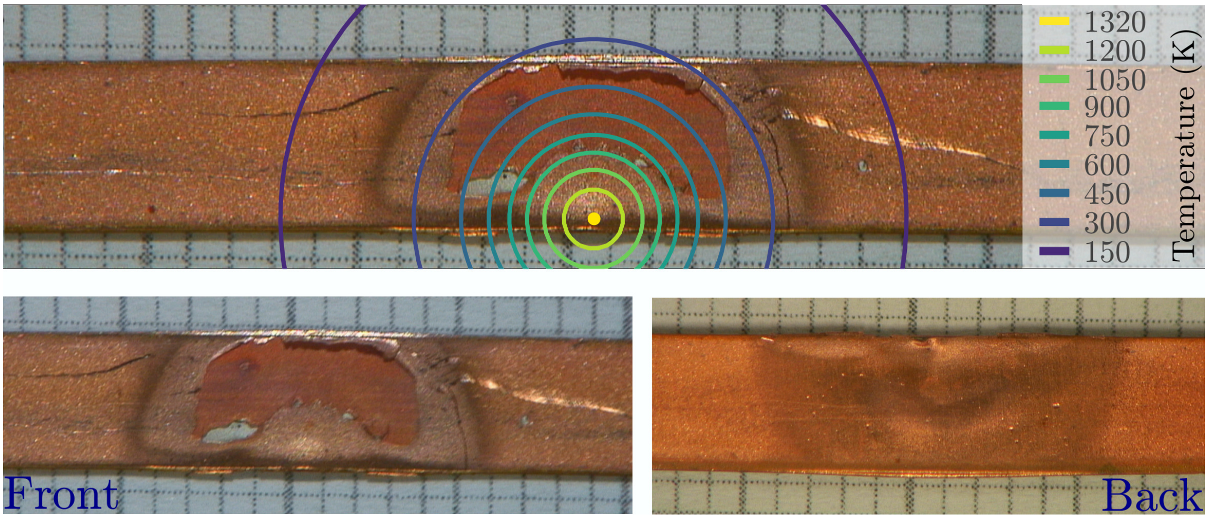

Figure 5.36 – HTS tape sample S7 from HTS Batch B5 with visual decoloration due to the beam impact. The simulated temperature profiles are indicated and overlap well with the visual damage.Furthermore, the front side with superconducting layer partially visible due to de-lamination (bottom left) and the back side, where the copper was not de-laminated but clearly shows a decoloration (bottom right) are shown.

5.5 Damage mechanisms in (Re)BCO tape

As the investigation of the HTS samples was still ongoing and not completed by the time of submission of this thesis, only a short excerpt of the visual inspection is presented in the following. The evaluation of the I_c measurements is not within the scope of this thesis. A detailed overview of the experiment, energy deposition and full visual inspection can be found elsewhere [OWW18]. The visual inspection revealed clear decoloration on the copper surface of the tapes except for samples S1 and some of the samples S2 with peak temperatures $\lesssim$400 K. The original copper plating had a high surface roughness but after the beam impact, at the position of the beam, the surface seemed much smoother. Furthermore de-lamination of the tapes was observed for very high peak temperatures of $\gtrsim$900 K at samples that were oriented such that the surface was perpendicular to the beam axis, whereas the samples with a flat orientation did not show signs of de-lamination. As an example, sample S7 from HTS Batch B5, which was oriented with the surface perpendicular to the beam axis, is shown in Fig. 5.36. De-lamination is visible on the front side, which is the side where the superconducting layer is deposited on the substrate. The back side shows clear imprint marks, inducing a color and surface roughness change on the copper layer but no de-lamination. The simulated temperature profiles are indicated as well; a maximum sample temperature of 1320 K was calculated. The beam offset of 1.5 mm as found in the visual inspection of the sample holder after the experiment [OWW18] was used to overlay the temperature lines with a graphic manipulation program to get the correct spacial scaling and positioning. The equi-temperature lines overlap well with the visual damage.

5.6 Summary and conclusion on damage mechanisms

Conclusion on damage mechanisms in Nb-Ti

In agreement with the previous beam impact experiments, Nb-Ti based wires were found to degrade very little in the ultra-short time scale of beam impact experiments, even when high peak temperatures were reached. The time scale is too short for significant diffusive processes to take place in the nano-structure, at least for peak temperatures up to 1170 K as reached in this experiment. The observed degradation of the copper matrix however can be of importance for the operation of an accelerator magnet but is not necessarily an issue. Especially high field magnets are usually operated rather close to the critical field and hence at lower applied currents. At low currents, all impacted wires still showed the non-degraded critical current similar to the reference wire and thermal instabilities were not observed. Nevertheless, a general statement can not be made, as the result depends on the deposited energy density, the position of the beam impact in the coil (high field region or low field region), the load line of the wire in the coil as well as the operating point of the magnet with respect to the critical surface of the superconductor. An increased RRR on the other hand implies reduced AC-losses during ramping due to a reduction of filament coupling losses, but more importantly also results in a reduced thermal margin in case of a quench and more resistive heating in the normal conducting state, localized around the degraded zone. A local burn-out of the wire might be the consequence. Therefore, a degradation of RRR should be avoided as the risk of damaging the magnet is enhanced.
A significant reduction in the thermal stability was found for samples S5 and above, with peak energy depositions of $\gtrsim 2\,\frac{\mathrm{kJ}}{\mathrm{cm}^3}$ and peak temperatures of $\gtrsim$680 K should be avoided.

Summary and conclusion on damage mechanisms in Nb_3Sn

In the previous experiments only magnetization measurements were performed on beam impacted wires and the degradation was found to be relatively small with only around 20% even for high achieved energy depositions and resulting peak temperatures of up to 1000 K. The wires exposed to proton beam at cryogenic temperatures evaluated in the experiment described in this thesis were investigated for both their critical transport current in fields up to 19 T at 4.2 K and in magnetization measurements at various temperatures up to 15 K and fields up to 6.5 T. The degradation observed in the critical transport current measurements was significant, ranging from no degradation for samples S3 with peak temperatures of 460-500 K to about 60% degradation for samples S4 with peak temperatures of 550-580 K and finally 100% degradation in samples S9 and above with peak temperatures of 1030-1100 K. In terms of energy deposition achieved, the highest value recorded with no observed degradation in the critical transport current was sample S3 of batch B2 with 1.41 $\mathrm{kJ/cm^3}$. The magnetization measurements revealed systematic differences to the critical transport current measurement. The degradation observed in sample S8 in magnetization measurements at 6 T and at 4 K showed little degradation of $\lesssim$20%, while the critical current measurements showed a degradation of more than 85% at 6 T.

The main damage mechanisms were identified as the fracturing of superconducting Nb_3Sn filaments. A modest degradation of the upper critical field was observed in Kramer fits, which pointed to a second mechanism of degradation: the residual plastic strain in the copper matrix after the beam impact, which strained the superconducting Nb_3Sn phase. The strain sensitivity of Nb_3Sn is well documented in literature and common scaling laws were used to compare the found

degradation of the upper critical field to the strain dependent function from theory. The strain levels needed to achieve the observed degradation in the upper critical field were not large enough to explain the overall severe degradation of the critical transport current. It was concluded that in the critical transport current measurements the filament fracturing is the dominating effect and the fractured regions limit the absolute transport current for the full wire, while the magnetization measurements showed very little sensitivity to filament fractures and the observed degradation corresponded well to the degradation due to strain only. At the same time, the volumetric average critical properties were measured in the magnetization measurements, such that the regions of strongest degradation were not the limiting factor and sufficiently small samples close to the beam impact would need to be measured for accurate results.
Two strongly degraded samples S8 and S9 of batch B1 were heated to 300°C for a thermal annealing of the copper matrix and their critical transport current was re-measured afterwards. Sample S8 showed strong degradation before but the critical transport current was still measurable. Sample S9 was already degraded to 100% after the beam impact and before the thermal annealing. In sample S8 a slight improvement of the critical current and the upper critical field were found after the thermal annealing while for sample S9 no improvement was observed. In full agreement with the assumption, the strain dependent degradation of the critical transport current in sample S8 could be annealed by annealing the copper matrix from strain. Sample S9 was fully degraded due to filament fracturing and the annealing showed no effect.

Finally, thermo-mechanical simulations of the beam impact could give a good understanding of the plastic strain evolution in the wires. The strain scaling laws could be used to calculate the resulting critical transport currents of the wires. The critical currents were greater than observed in the measurements and the difference was concluded to be due to filament fracturing, which was not modeled in the simulation. Hence, an irreversible strain was found by fit to the measured data such that the theoretical model would represent the absolute critical transport current well. From the simulations, the parameters indicating strong degradation could be concluded. Besides the peak temperatures mentioned above, also the temperature gradient was evaluated and strong degradation was found to start for gradients between 200-250 K/mm. Furthermore, the calculated critical average strain was observed to be between 0.31% to 0.51%. The maximum calculated strain present in sample S3, which did not show significant degradation was 0.41%, also indicating the limit for irreversible and strong degradation. Both values, when corrected for the pre-strain of -0.11%, lie well in the order of magnitude seen in literature for the irreversible strain.

Part III

Radiation tolerance of cryogenic diodes used for HL-LHC magnet circuits

6 Silicon based power diodes in a radiation environment

This chapter gives an overview on the relevant semiconductor physics of silicon based power diodes and the implications of radiation and high energy particle irradiation on the device characteristics. It is mostly based on several books about Silicon material and wafer fabrication and characterization [Sch06; BP18], general (power) semiconductor device physics [Bal19; BP18; Sch06] as well as the radiation effects in semiconductor (power) devices and particle detectors [LR16; LR12; HA01; VU77; Har17], which are suggested for further reading on the topic.

6.1 Silicon semiconductor physics

Semiconductor physics assumes perfect crystal lattices to calculate the physical properties. To achieve ideal device properties, the base material should be an ideal single-crystal with little to no defects or impurities. In practice high purity silicon melts are used to grow silicon crystals from the molten phase by slowly pulling a seed crystal out of the molten mass, which is called Czochralski or CZ process. This results in relatively good crystal properties but causes a large impurity concentration, mainly due to oxygen. An improved way of fabricating silicon ingots is the float-zone (FZ) process, where a poly-crystalline rod is locally heated by moving an RF induction coil along the rod. The impurities with a lower solubility are pushed along the edge of the heated phase and the single-crystal is formed along the molten zone. Both methods result in a cylindrical rod with diameters of up to a few tens of centimeters and lengths in the order of a meter. Thin disks with a few hundreds of micro meters, the so called *wafers* are then cut from the rod. These wafers form the basis for all further semiconductor devices.

Silicon properties

The intrinsic free carrier density in pure silicon is a strong function of temperature

$$n_{\text{int}} \propto \exp\left(-\frac{E_g}{k_B T}\right), \tag{6.1}$$

where E_g is the energy gap between conduction and valence band, with $E_g = 1.12\,\text{V}$ for silicon at room temperature. The free carrier concentration can largely be enhanced by doping atoms that act as donors (n-type) or acceptors (p-type) of free electrons. In n type silicon, the electrons are the majority carriers and holes are the minority carriers, the opposite is the case for p type silicon. The resistivity of silicon depends on the free carrier concentration n and p of electrons and holes. In the presence of an electric field the charge carriers are accelerated to a statistically distributed mean drift velocity and are scattered on phonons or impurities and defects along their way, which results in a resistivity. The resistivity of a doped semiconductor can be written as

$$\rho = \frac{1}{\frac{e^2}{m_e} n\tau_e + \frac{e^2}{m_h} p\tau_h}. \tag{6.2}$$

with the contributions of electrons and holes

$$\frac{e^2}{m_e}\tau_e \, n \;=\; \rho_{0,e}^{-1} \;=\; e\mu_e n, \qquad \frac{e^2}{m_h}\tau_p \, p \;=\; \rho_{0,h}^{-1} \;=\; e\mu_h p. \tag{6.3}$$

and the carrier or drift mobilities $\mu_{e/h}$, effective masses $m_{e/h}$ and the charge densities n and p of electrons and holes respectively [BP18]. The scattering lifetimes of electrons and holes τ_e and τ_h describe the average time between scattering events on phonons, crystal defects or impurity atoms, when the electrons or holes are drifting through the material. Due to the different effective mass of electrons and holes as well as the different charge densities, the contribution of the two lifetimes can differ significantly, i.e. the mobilities of electrons and holes are different. As the carrier mobilities are a function of temperature and the local doping concentration, the resistivity of a silicon wafer varies strongly as a function of those parameters. The resistance can be derived as the integral over the wafer thickness

$$R_s = \int_0^{w_d} \frac{\rho(x)}{A} \mathrm{d}x, \tag{6.4}$$

assuming the constant wafer area A and the wafer thickness w_d. The dependence of $\rho(x)$ on the local doping profile along the wafer structure needs to be taken into account. Tabulated values for carrier mobilities can be used to calculate the silicon resistance along a given doping structure by evaluating Eqs. (6.2,6.3).

In addition to the drift currents, diffusion currents flow where there are gradients in free carrier concentration, for example due to the gradients in dopant concentrations. The total electron and hole diffusion current is expressed as

$$\vec{J} = eD_e\nabla n - eD_h\nabla p, \tag{6.5}$$

with diffusion coefficients $D_{e/h}$. The Einstein relations relate the diffusion coefficients to temperature and mobility

$$D_{e/h} = \frac{k_B T}{e}\mu_{e/h}. \tag{6.6}$$

For minority carriers a characteristic time $\tau_{d,e/h}$ can be introduced, which is the average diffusion time through the material before the minority carriers recombine. The associated diffusion length is defined as

$$L_{e/h} = \sqrt{D_{e/h}\tau_{d,e/h}}. \tag{6.7}$$

Shockley-Read-Hall Theory

Silicon is an indirect semiconductor and direct band-to-band generation and recombination of excited electrons or holes are largely suppressed. It mainly works via intermediate energy levels (“deep levels”) that are located within the band gap and are introduced via impurities and crystal defects or dislocations. Such impurities or dislocations are referred to as generation-recombination centers or traps. The inverse of the generation/recombination lifetime τ_r is proportional to the impurity concentration N_t [Har17]

$$\tau_r \propto \frac{1}{N_t}. \tag{6.8}$$

The impact on the semiconductor properties will be described in more detail in the following sections.

6.2 Power diodes: $p(\nu)n$ structures

A diode consists of a pn-junction, which is realized by bringing in contact highly p and n doped semiconductors. If there is a weakly doped n structure between the highly doped n and p region it is referred to as a p^+nn^+ or $p\nu n$-Diode, where the ν stands for a lightly doped n region in the center, with dopant concentrations in the order of $< 10^{14}$ cm^{-3}. This region is referred to as the base, or the n-base of the diode in this case. Other types of bases, such as lightly doped p type or intrinsic silicon are also used, but will not be discussed further. The widely used nomenclature is *pin* in case of an intrinsic base, $p\pi n$ for a lightly doped p type base and $p\nu n$ for a lightly doped n type base [LR16].

The $p\nu n$ structure can be realized by implanting dopants on the two sides of a wafer of low n-type impurity concentration followed by a thermal diffusion drive. The length of the diffusion drive determines the resulting junction depths. The junction depths are defined as the depth in the diode, where the implanted doping concentration is equal to the intrinsic doping concentration of the wafer before doping. The difference between the two junction depths, i.e. the resulting width of the central n region is often called the *base-width*. These type of diodes are referred to as diffusion diodes, as opposed to epitaxial diodes, where the crystal structures are grown directly onto each other with epitaxial processes.

At the junction of p and n type silicon, diffusion currents flow due to the large gradients in carrier concentration. When the majority carriers on each side flow over the junction, a charge builds up due to the leftover ionized (immobile) dopant atoms. This results in an electric field and a drift current, opposing the diffusion current. A space charge zone is built up until both drift and diffusion current cancel out, resulting to a zero net current over the junction in the equilibrium. The total current can be written as

$$\begin{aligned}\vec{J} &= e(D_e\nabla n - D_h\nabla p) \;+\; (e\mu_e n + e\mu_h p)\vec{E} \\ &= e(D_e\nabla n - D_h\nabla p) \;+\; \frac{e\vec{E}}{\rho}.\end{aligned} \tag{6.9}$$

The built up space charge region implies a built in voltage over the junction. In the center of the junction region, a zone depleted from majority carriers remains.

6.2.1 Forward characteristics $U_f(I_f)$

The equilibrium can be disturbed when biasing the diode by applying a voltage. In case the bias voltage opposes the built in voltage, the drift current will be reduced while the diffusion current rests unaltered. A net current will start to flow, the diode is in forward operation. Holes from the p^+ region will be injected in the n-base where they are minority carriers. Depending on the amount of injected carriers, the behaviour is altered. For low injection levels, when the amount of injected minority carriers is smaller than the intrinsic carrier density n_{int}, the result is a diffusion current with exponential decay into the n-base with the diffusion length as in Eq. (6.7). The minority carriers will recombine along the way with the timescale $\tau_{d,e/h}$, latest when they arrive in the n^+ region. The recombination takes place via traps, impurities or in general at generation-recombination centers as mentioned in the section above. The forward current is a contribution of diffusion and recombination current

$$J_f = \frac{e\, n_{\text{int}}^2}{N_d}\sqrt{\frac{D_h}{\tau_{d,h}}}\left(\exp\left(\frac{eU_f}{k_B T}\right) - 1\right) + \frac{e\, n_{\text{int}}\, w}{\tau_r}\exp\left(\frac{eU_f}{2k_B T}\right) \tag{6.10}$$

with the effective recombination lifetime τ_r, donor concentrations in the base N_d, the width of the depleted zone w and Boltzmann constant k_B. The diffusion current is dominating for higher injection levels. In real diodes the approximation

$$J_f \approx J_{s,eff}\ \exp\left(\frac{eU_f}{lk_B T}\right) \tag{6.11}$$

is generally used with the ideality factor l and $J_{s,eff}$, for example determined by fitting measured data.

For very high injection levels the diode characteristics is dominated finally by the resistance, given in Eqs. (6.2, 6.4). The characteristics is then more or less purely ohmic. The Shockley equation [Sho49] defines the full voltage U_f over a diode, when a current I is flowing, as

$$U_f(I) = IR_s + \frac{lk_B T}{e}\ln\left(\frac{I}{I_s} + 1\right), \tag{6.12}$$

taking into account the ohmic behaviour. Besides the case of very high injection levels, the first ohmic term can also dominate for moderate injection levels if the series resistance is large. The saturation current I_s follows from the Eqs. (6.10,6.11).

Turn-on voltage U_{to}

The ideal diode is a rectifying device, i.e. above a certain threshold voltage, it starts to conduct abruptly and the current rises steeply. Below the threshold voltage no current should flow. The diode equation, intended to approximate the real diode behaviour as shown in Eq. (6.12), indicates that this is not true for real diodes. A small current will always flow for non-zero voltages, however largely suppressed for small voltages and exponentially rising with the applied voltage. The definition of a turn-on voltage can therefore be chosen by defining a current level at which the diode is considered to be conducting, depending on the technical use-case. A value depending on the application should be chosen, such that currents below the turn-on value can be safely regarded as small compared to the currents expected in the conducting state. For example, superconducting magnets are powered with currents of $\mathcal{O}(10\,\text{kA})$. In such circuits currents of $100\,\text{mA}$ can be considered small (i.e. a precision of 10^{-5}) and the turn-on voltage could safely be defined as the voltage when the diode conducts a current of $100\,\text{mA}$. Below that voltage, the diode is considered to be in the non conducting state, above it is considered to be conducting. Once conducting, the diode wafer will heat up due to resistive heat generation. The forward voltage in the low level injection regime, such as U_{to}, is decreasing with increasing temperature from cryogenic to room temperature. For a diode in cryogenic operation, the heat generation when turning on can therefore quickly and significantly decrease the forward voltage resulting in a quick rise in current. This is in fact a beneficial property in the use-case of current bypass diodes which allows to quickly take and re-distribute the current via the diode while also decreasing the resistive losses.

Temperature dependence

The temperature dependence is not only given by the prefactor lk_BT/e in Eq. (6.12) but also hidden in the saturation current, which depends on the intrinsic carrier concentration n_{int}. For Phosphorous doped n type silicon at low temperatures it is found to be

$$n_{\text{int}}(T) \propto \exp\left(-\frac{E_C - E_D}{2k_BT}\right) \tag{6.13}$$

where the difference $E_C - E_D$ of conduction band energy and the donor level energy is in the order of 45 meV [LR12]. The carrier concentration is tending heavily to zero for temperatures $T \lesssim 50\,\text{K}$, the so-called carrier freeze-out regime [LR12]. In this regime, the conduction can be heavily prevented if defects or impurities acting as traps are present [LR16]. Until they are filled with injected carriers, no current will flow and then abruptly and very steeply rise once the traps are filled [LR16].

Furthermore a temperature dependence of the resistivity part has to be considered as the carrier mobilities are temperature dependent. For low injection levels, the overall voltage-temperature dependence is almost linearly negative down to the freeze-out regime. The dependence is no longer trivial to calculate, when the series resistance plays a significant role. This is the case for high injection levels or due to heavy decrease of scattering lifetimes due to crystal defects and dislocations, e.g. from radiation damage. Then, the voltage drop will also be increased in the higher temperature range, where the contribution due to series resistance is more prominent. The voltage increases both for very low temperatures and for high temperatures will result in a voltage minimum in intermediately low temperature ranges.

6.2.2 Reverse bias characteristics $U_r(I_r)$

When applying a bias voltage to the diode such that the built in voltage is enhanced, the depleted zone will be enlarged and the electric field will build up. Carriers generated via generation-recombination centers in the depleted zone are swept out towards the junctions, resulting in a leakage current. As mentioned above, the generation lifetime is inversely proportional to the density of such generation-recombination centers N_t and so the leakage current is directly proportional to them [Bal19]

$$I_r = Aw_d\, e\frac{n_{\text{int}}}{\tau_r} \propto VN_t, \tag{6.14}$$

where w_d is the width of the depletion zone, A the wafer area and hence $V = Aw_d$ the volume of the depletion zone. The leakage current linearly increases with the absolute number of defects VN_t in the depleted zone. It is strongly temperature dependent around room temperature due to its dependency on n_{int}. It can be suppressed strongly by cooling to low temperatures even for high defect densities. Usually temperatures way above the cryogenic region, i.e. $< 0°\text{C}$ are already sufficient to suppress the leakage current for most technical applications.

Breakdown voltage

The diode is only able to block currents up to finite reverse voltages. Above the reverse blocking voltage U_b a strong exponential increase in reverse current is observed. The mechanism is avalanche multiplication of charge carriers that are accelerated in the strong electric fields and achieve a large enough drift velocity so that the impact ionizes exponentially more charge carriers, which then themselves are accelerated in the electric field. A cascade of ionized and accelerated charge carriers quickly produces a strong current. Two factors influence the maximum reverse blocking voltage. The maximum electric field silicon can support before the drift velocity of the charge carriers becomes too large, is determined by the resistivity. The breakdown voltage increases with resistivity as

$$U_b \propto \rho^k \tag{6.15}$$

and $k < 1$ is found empirically [VU77]. Weakly doped base regions with high resistivity have a higher blocking voltage. For the absolute voltage the integral of the electric field along the drift region has to be taken into account

$$U = \int_0^{w_d} E(x)\mathrm{d}x \tag{6.16}$$

Assuming the full drift region is subjected to an electric field of almost the critical electric field E_c it follows, that a larger drift region supports a higher blocking voltage $U_b \lesssim E_c w_d$.

Another limiting factor originates from the wafer fabrication. When cutting the wafers from the ingot, the edges are often microscopically damaged [Bal19]. Especially in reverse bias operation, the large voltages can lead to breakdowns via those edge regions for voltages below the theoretical breakdown voltage. The edge regions are beveled to improve the electric field distribution and sealed either by insulating layers such as Polyimide/Polyamide or silicon dioxide [Bal19]. This process is usually called *passivation*.

The power deposited in reverse bias operation can become significant even for small leakage currents, due to the large voltages

$$P_r = U_r I_r. \tag{6.17}$$

The deposited energy can lead to heating of the wafer and the strong increase of leakage current with temperature can in return further enhance the leakage current quickly: the wafer is at risk of being burnt out. Maintaining a small leakage current is substantial in applications where large reverse bias voltages are expected and the diode should be in a blocking state. For superconducting magnet circuits with cryogenic diodes, the maximum voltage in the circuit needs to be well defined and a suitable diode needs to be selected. If the diodes are exclusively operated at very low temperatures, where leakage currents are largely suppressed, it is usually not a problem in those circuits. It is sufficient to consider the blocking voltage U_b where avalanche breakdown occurs, with a reasonable safety margin. The leakage current for voltages below the blocking voltage can then be neglected.

6.3 Radiation displacement damage in Silicon

The primary atom which is impacted by an incident particle is called the primary knock on atom (PKA). In silicon, an energy of 25 eV is needed on average to knock an atom out of its lattice position [Har17]. In case the energy transfer to the PKA exceeds ≈ 5 keV, the PKA can lead to a cascade of further atom displacements, resulting in a cluster defect [Har17]. The amount of energy that can be transferred to the PKA is dependent on the incident particle type. Heavier particles like protons or neutrons can transfer enough energy to the recoil atom to create point defects, if their kinetic energy exceeds 185 eV, while electrons need at least 225 keV [Har17]. To create cluster defects, protons or neutrons need at least 35 keV and electrons 8 MeV of kinetic energy [Har17]. Charged particles interact preferably via the electromagnetic force and low energy transfers such that point defects are more prominent, while neutrons can knock on several atoms consecutively creating cluster defects [Har17]. High energy photons, such as γ-radiation can interact with atomic electrons via Compton scattering. In accelerator environments the ^{60}Co decay is usually very prominent due to activated impurities in several steel alloys. The photons emitted in this decay have energies of 1.17 MeV or 1.33 MeV. Hence, the ionized electrons from Compton scattering processes can have sufficient energy to create point defects but not enough to create cluster defects [Har17].

The displacement damage in materials is described by [Har17; LR16]

$$D(E) = \sum_i \sigma_i(E) \int f_i(E, E_R) P(E_R) dE_R \tag{6.18}$$

where the sum counts over all possible interaction cross sections σ_i, the integral integrates over the recoil energy E_R transferred from the incident particle with energy E to the lattice atom. The function $f_i(E, E_R)$ is the probability of this energy transfer for that specific process and $P(E_R)$ is the Lindhard partition function, that accounts for the fraction of the recoil energy actually going into the atom displacement [Har17]. In mixed radiation fields the incident particle beam is non-uniform, i.e. consists of several types of particles with an energy distribution described as $\phi(E)$ (in the units of cm^{-2} MeV^{-1}). According to the NIEL-scaling hypothesis, the displacement damage is independent of the incident particle type and Eq. (6.18) is only dependent on the particle energy and the energy transfer. With this assumption in mind, it is a convention to compare the incident particle fluence with an equivalent fluence of only neutrons with an energy of 1 MeV

$$\Phi_{\text{neq}} = \frac{\int D(E)\phi(E)\mathrm{d}E}{D_{\text{n}}(1\,\text{MeV})} \tag{6.19}$$

with the displacement damage of 1 MeV neutrons [Har17]

$$D_{\text{n}}(1\,\text{MeV}) = 95\,\text{MeV mb}. \tag{6.20}$$

This scaling postulates a 1 MeV neutron equivalent (neq.) fluence needed to achieve the same amount of displacement damage as with the original particle fluence $\Phi = \int \phi(E)\mathrm{d}E$ and allows to compare displacement damages from completely different radiation environments. The above equations can be solved for example with numerical Monte-Carlo codes such as FLUKA [Böh+14; Fer+05].

A general assumption for the defect density N_t is an exponentially damped growth, with the original defect density $N_{t,0}$ and the damage coefficient K

$$N_t = N_{t,0} + N_\infty \left(1 - e^{-K\Phi_{\text{neq}}}\right) \approx N_{t,0} + K_1\Phi_{\text{neq}} \ + \mathcal{O}(\Phi_{\text{neq}}^2) \tag{6.21}$$

which increases approximately proportional to the fluence for low defect densities or small fluence levels.

6.4 Effects of radiation damage in Si-based power diodes

6.4.1 Increase in the n-base resistance

With an increasing amount of displacement damage in the crystal structure, scattering of charge carriers becomes more likely on the created defects. The inverse scattering lifetimes were found to degrade proportional to the displacement damage, i.e. the amount of defects, and therefore in first order linearly with 1 MeV neq. fluence Φ_{neq} [HA01]

$$\frac{1}{\tau_{e/h}} = \frac{1}{\tau_{0,e/h}} + K_\tau\Phi_{\text{neq}}, \tag{6.22}$$

with the damage coefficient K_τ as a proportionality factor. Inserted into Eq. (6.2), the resistivity can be derived as

$$\rho = \frac{1}{(\rho_{0,e} + K_{\rho,e}\Phi_{\text{neq}})^{-1} + (\rho_{0,h} + K_{\rho,h}\Phi_{\text{neq}})^{-1}} \tag{6.23}$$

If one of the lifetimes is dominant, like in strongly doped structures of only one kind (i.e. $n \gg p$ or $p \gg n$), or if one of the two lifetimes has degraded significantly stronger due to exposed fluence, the resistivity growth can be expected linear and hence the resistance grows linearly with Φ_{neq} as well

$$R_s \approx R_0 + K_R\Phi_{\text{neq}}. \tag{6.24}$$

In case of the $p\nu n$ structure, the integral in Eq. (6.4) has to be evaluated according to the doping profile. Only the total series resistance will be measured. As a simplification, it is assumed, that the three different regions have step-function like doping profiles and the resistance as a function of fluence is then found to be approximately

$$R_s = \frac{1}{(R_{0,e} + K_{R,e}\Phi_{\text{neq}})^{-1} + (R_{0,h} + K_{R,h}\Phi_{\text{neq}})^{-1}}. \tag{6.25}$$

with degradation coefficient $K_{R,e}$ and $K_{R,h}$ for electrons and holes in units of Ωcm^2.

We assume a lightly doped central region ν in a $p\nu n$ structure. With the dependence of Eq. (6.3), it becomes clear, that the central lightly doped region will have the largest influence on the total resistance of the diode in the integral of Eq. (6.4). Hence, when subjected to radiation, its resistivity growth will likewise dominate the increase in resistance. However, the increase of the resistance can simply be reduced by the influence of the geometric properties. A thinner base width for example automatically yields a smaller absolute resistance for the same local resistivity, when calculating the integral. On the other hand, for a given base width, the resistance is likewise smaller for a larger diameter wafer.

Wafer thermal transient behaviour under current loads

The heat generation during a current pulse will mainly be affected by the dynamic series resistance of the diode. It is the highest for large forward currents and decreasing with temperature as described above. The maximum acceptable temperature of the wafer during a current pulse or ramp is usually defined and limited in order not to destroy it. While the current ramps are usually set in a given application, the maximum temperature reached varies, as the series resistance grows with radiation and so does the deposited energy. In LHC the maximum allowable temperature for the main dipole magnet's cold diodes was set to 430 K [Bru+04]. The evolution of the series resistance should be closely monitored and a reasonable limit for the maximum allowed series resistance should be set such that this temperature limit is never exceeded.

It is common practice to express the thermal load on ohmic devices in terms of the so-called *MIIt*, which corresponds to the integral of the square of the transient current ramp $I(t)$

$$M = \int I^2(t)\mathrm{d}t, \tag{6.26}$$

and is often expressed in the unit of $10^6\mathrm{A}^2\mathrm{s}$. The deposited energy W follows by multiplying M with the resistance R of the device. For diodes, the resistance is a strong function of current. As the current is a function of time in the above representation, the diode resistance is also dependent on time, as current and temperature vary during a ramp. As an upper limit, the deposited energy W can also be estimated by this formalism, taking into account the maximum diode series resistance $R_{s,\mathrm{max}}$

$$W = \int R(t)I^2(t)\mathrm{d}t \;\leq\; R_{s,\mathrm{max}} \cdot M. \tag{6.27}$$

As M stays constant, the change in deposited energy can be estimated by knowing the series resistance evolution.

Wafer burn-out due to inhomogeneous irradiation

In case the wafer is irradiated inhomogeneously, the resistivity of the wafer changes inhomogeneously within the wafer area A. The integral in Eq. (6.4) has to be adapted. The consequence is an inhomogeneous distribution of forward voltage which results in an inhomogeneous current distribution and heat generation across the wafer. It can be seen as several diodes connected in parallel with different forward characteristics. Diodes connected in parallel are an unbalanced system due to the negative temperature dependence of their forward current, i.e. the diode with the lower forward voltage will take more current according to Kirchhoff's law. As it heats up, the forward voltage decreases further resulting to even more current flow. In an inhomogeneously irradiated wafer the parts with less degraded forward voltage will accordingly take more current than the regions with high degradation ("current crowding" [Dre19]). In case some parts of the diode are heavily damaged, the effective conducting cross section is reduced and – against the intuition – the less degraded zones are at risk of burning out as they are forced to take significantly more current. Unfortunately, the whole diodes turn-on behaviour will still be determined by the least degraded part and measurements of this kind might not reveal the inhomgeneous degradation. This has happened in accelerators where cryogenic power diodes have been installed in close proximity to the beam pipes, where the radiation field gradients are strongest [Dre19]. Ideally, the wafers have to be put in regions of homogeneous radiation fields to avoid this erratic behaviour and allow safe operation.

6.4.2 Saturation current and reverse leakage current

The saturation current in forward (I_s) and reverse bias operation (leakage current, labeled I_r in this thesis) is mainly influenced by the generation-recombination centers. While in forward operation they serve as traps for the charge carriers and reduce the forward saturation current, in reverse bias operation charge carriers are generated enhancing the leakage current significantly.

The leakage current under reverse bias depends on the generation lifetime, which is the time between two carrier generation events. It is shorter if more generation centers are present, as more generation events occur. Under the assumption, that the amount of generation centers increases linearly with the 1 MeV neq. fluence Φ_{neq}, the inverse of the generation lifetime $\frac{1}{\tau_r}$ increases linearly with Φ_{neq}[LR16] as

$$\frac{1}{\tau_r} = \frac{1}{\tau_{r,0}} + K_{\tau,r}\Phi_{\text{neq}}, \tag{6.28}$$

following Eq. (6.8). Consequently the reverse leakage current increases linearly with fluence

$$I_r(\Phi_{\text{neq}}) = I_{r,0} + K_I \cdot \Phi_{\text{neq}}, \tag{6.29}$$

with the damage coefficient K_I and the Wafer active volume V. In literature the damage coefficient is usually normalized by the volume V of the depleted zone as

$$\alpha_I = \frac{K_I}{V}, \tag{6.30}$$

Especially for particle detectors used in large experiments at particle colliders, the leakage currents are the main concern and the detector depletion zones have substantially different volumes this allows to transfer the measured results easily between different detector designs. The values found are very consistent all over the literature and scale in the order of $\mathcal{O}(\alpha_I) = 10^{-17}\,\text{A/cm}$. In this thesis, the nomenclature α_I or K_I will be used in strict accordance to Eqs. (6.29) and (6.30).

The saturation current in forward direction shown in Eq. (6.10), consists of the contributions of diffusion and recombination current. At low temperatures, where n_{int} is small, the term proportional to n_{int}^2 is negligible compared to the one proportional to n_{int}. The inverse of the recombination lifetime or trapping time τ_r was found to be proportional to the density of recombination centers or traps. The saturation current can be assumed to decrease linearly with Φ_{neq} in first order

$$I_s(\Phi_{\text{neq}}) = I_{s,0} - K_I\Phi_{\text{neq}}, \tag{6.31}$$

with the original saturation current $I_{s,0}$ and the damage coefficient K_I.

The turn-on voltage is affected by the decrease in saturation current. From the Shockley equation as in Eq. (6.12), the voltage for small currents follows by taking into account only the logarithmic term

$$U_{to} := U_f(I_{to}) \approx \frac{lk_BT}{e}\,\ln\left(\frac{I_{to}}{I_s} + 1\right). \tag{6.32}$$

A second effect originating from the increasing amount of trapping centers is the delay in onset of conduction, as already mentioned above. Due to the small amount of free carriers at very low temperatures in the freeze-out regime, the time until all traps are filled can become significant, when carriers are injected [LR12; LR16]. If used in an accelerator magnet circuit, the diode should be able to switch to the conducting state fast enough to allow a re-routing of the current before damage happens in the superconductor. The transient quench behaviour and the resulting voltage rise rates over the coils have to be known. Both the absolute value of the turn-on voltage and the delay in conductivity on-set should be smaller than the expected voltage rise rate in order for the magnet protection to work. Radiation damage might change these properties during the lifetime and either good knowledge of the evolution of the properties with increasing radiation damage or constant surveillance of the diode's properties over the lifetime is essential. Monitoring of the diode's properties might not always be possible, once installed and included in a large circuit and inside magnet cryostats, which is why irradiation and measurement programs are an essential part of R&D for this kind of accelerator technology.

7 Cryogenic power diodes in accelerator circuits

Most of the content of this chapter was taken from [Wil+20a] in an only slightly modified form. For better readability, detailed citation marks were omitted.

7.1 LHC main dipole and quadrupole magnet circuits

The LHC main dipole and quadrupole magnet circuits are powered in long strings, connecting for example 154 dipole magnets in series. There are a total of 8 main dipole and 16 main quadrupole circuits and they are each powered by a single 13 kA power converter. To protect the magnets from excessive currents in case of a quench, bypass diodes are installed in parallel to each magnet. The protection scheme of bypass diodes was described in more detail in section 2.4. The diodes in the LHC main dipole and quadrupole magnet circuits are mounted in a stacked assembly as shown in Fig. 7.2, which is housed in a small extension of the magnet helium vessel, in proximity to the magnet coil to allow short current routes. This stack ensures a suitably low contact resistance by a Cu-Be spring washer, that presses the diodes with a force of 40 kN to the current lead connections. The stack has two half-moon shaped connectors where it can be mounted in the cryostat vessel connecting the diodes in parallel to the magnet coils. The stack for quadrupole magnets looks very similar but houses two diodes as the four sub-coils are connected in pairs of two to one diode each. The diode wafers are embedded in a capsule as shown in Fig. 7.1. The capsule houses the wafer embedded in several bounding layers and two large copper pole pieces, which are used as an electrical connection interface. The two pole faces are nickel plated to further reduce the electrical contact resistance. The capsule side walls consist of an insulating ceramic. Voltage taps are attached on each of the pole face's sides to allow for electrical measurements when the diode capsule is installed.

Due to their proximity to the beam axis, the diodes are impacted by secondary particle debris from interaction of the beams with residual gas molecules and by collision debris from the interaction region (compare section 2.2). Therefore, the assessment of the radiation tolerance of such diodes is of high importance, to ensure that the operational parameters stay within the specification during the lifetime of the circuit. A suitable diode type has been identified and qualified in several test campaigns [Gha+04; DH00; Den04b]. The LHC cold diodes are diffusion type power diodes with a n-base width of 10 µm [Gha+04]. They have been successfully used during the nearly ten years of LHC operation (see [Wil+15]). The expected total ionizing dose (TID) Φ_D and the 1 MeV neutron equivalent (neq) fluence Φ_{neq} for the diodes of the LHC dipoles over the machine lifetime was estimated to be $\Phi_D = 200$ Gy and $\Phi_{neq} = 1.2 \times 10^{12}\,\mathrm{cm}^{-2}$ [DH00]. Extensive studies have been performed, exposing these diodes to $\Phi_D = 2\,\mathrm{kGy}$ and $\Phi_{neq} = 3 \times 10^{13}\,\mathrm{cm}^{-2}$ [Den04b] and evaluating the behavior under the influence of radiation, at cryogenic temperatures. The same type of diode had later been qualified for the FAIR project, to $\Phi_D = 1.2\,\mathrm{kGy}$ and $\Phi_{neq} = 2.2 \times 10^{14}\,\mathrm{cm}^{-2}$. The irradiation was performed at 77 K, some diodes were warmed up to room temperature after each irradiation step, and testing was done up to a maximum current of 7.5 kA [Flo+07].

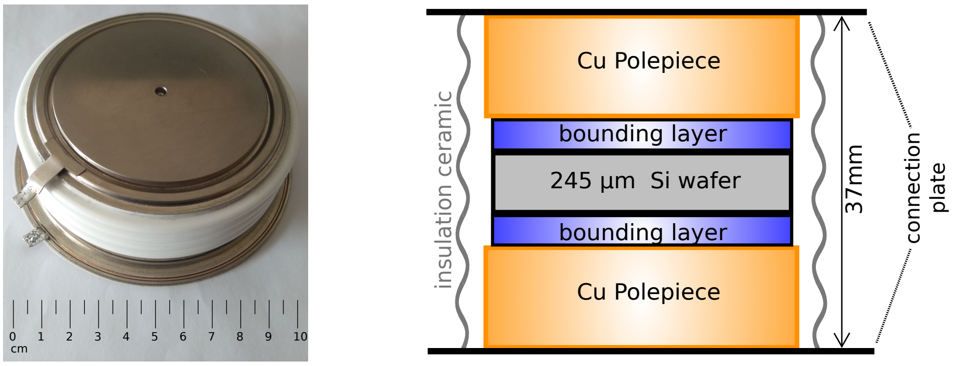

Figure 7.1 – *Left:* Diode Capsule as used in LHC and to be used in HL-LHC. Two voltage taps are attached to the top and bottom. The current flows perpendicular to the circular wafer, the conducting faces are from nickel plated copper.
Right: Schematic drawing of the inner structure of the diode capsule. Image originally published in [Wil+18]. The 245 µm thin wafer is bonded on copper pole pieces. The outer shell consists of ceramic, the capsule is filled with a mixture of Nitrogen and Helium gas.

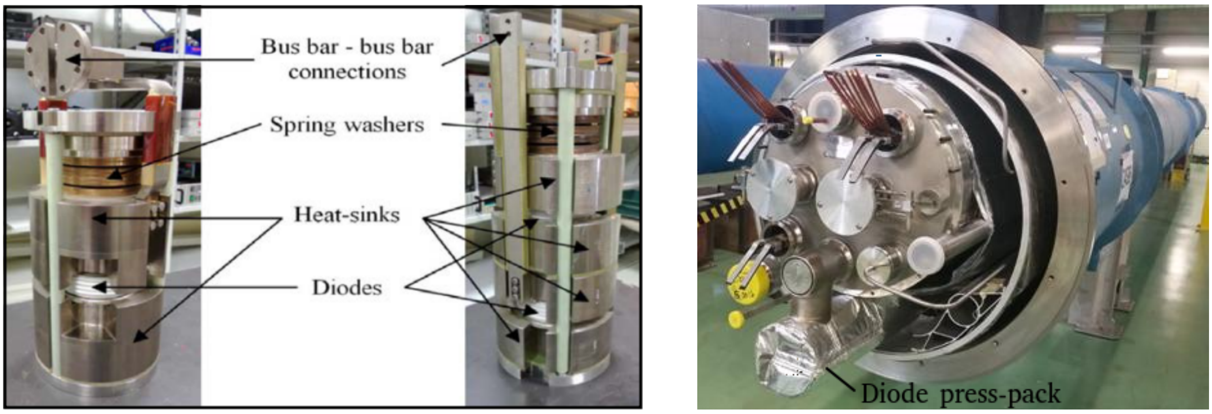

Figure 7.2 – Diode press-packs as installed in LHC superconducting dipole (left image, stack on the left) and quadrupole magnets (left image, stack on the right). The diode capsules are pressed with a Cu-Be spring washer to guarantee a low thermal and electrical contact resistance. The heat sinks in the press-packs are many times larger than the diode capsule's internal heat sinks as shown in Fig. 7.1. The image on the left was taken from [Wil+15]. The opened LHC main dipole cryostat is shown on the right image with the wrapped and enclosed diode press-pack module connected to the cryostat. The image on the right was taken from [CER].

7.2 HL-LHC final focus quadrupole magnet circuits

Cryogenic diodes are foreseen in the powering scheme of the new final focus quadrupole magnets for HL-LHC, the so-called inner triplets. The inner triplet magnets were presented earlier in section 1.2. The diodes for these magnets will be located in an extension to the cryostat close to the separation dipole D1 (compare Fig. 1.7), immersed in superfluid helium where they are exposed to radiation induced by the collision debris from the interaction point as well as by secondary particles, resulting from steady beam losses. A dose of 12 kGy and a 1 MeV neq. fluence of $\Phi_{neq} = 5 \cdot 10^{13}\,\text{cm}^{-2}$ was estimated with FLUKA at the foreseen position for the lifetime of the HL-LHC [Gar+18; Ler+19]. The expected radiation levels in these cryogenic diodes will exceed the ones of the existing LHC cryogenic diodes by one order of magnitude. The electric circuit corresponding to the schematic circuit diagram of Fig. 1.7 is presented in Fig. 7.3. As shown, the cold diodes will be installed in parallel to the quadrupole magnets Q1, Q2a, Q2b and Q3. The operating conditions as well as the electrical requirements for the diodes to be used in this circuit are listed in Table 7.1. During their lifetime, the turn-on voltage should never exceed 15 V and the series resistance at maximum current should stay well below 0.5 mΩ. The reverse blocking voltage U_b, defined at a reverse current of 1 mA, should stay below 200 V. Moreover the value of U_b contains a large safety factor of about 2.5 allowing to choose diodes also with comparably low blocking capabilities.

The quench protection system was designed to force a quench in all magnets in case one of the coils quenches spontaneously. Therefore, the diodes will function as voltage regulation elements, protecting the magnets against excessive transient voltages during a non-uniform quench process rather than acting as bypass diodes. The maximum current they will have to carry is specified to be 7 kA. Since the maximum current in the magnet circuit is 18 kA, the diodes should nevertheless be tested up to this level.

Table 7.1 – HL-LHC operational conditions and electrical requirements for cryogenic diodes in the HL-LHC inner triplet circuits [Wil+20a] as shown in Fig. 7.3.

Operational conditions	
Operating temperature	1.9 K
Maximum thermal load	$4.9 \cdot 10^6\,\mathrm{A^2s}$
Lifetime Dose	12 kGy
Lifetime 1 MeV neq. fluenceΦ_{neq}	$5 \cdot 10^{13}\,\mathrm{cm^{-2}}$
Maximum current to diode during quench	7 kA
Maximum current in circuit	18 kA
Electrical requirement	
Turn-on voltage at 1.9 K	<15 V
Diode series resistance at max. current	<0.5 mΩ
Reverse blocking voltage U_b at 1.9 K for I_r=1 mA	≥200 V

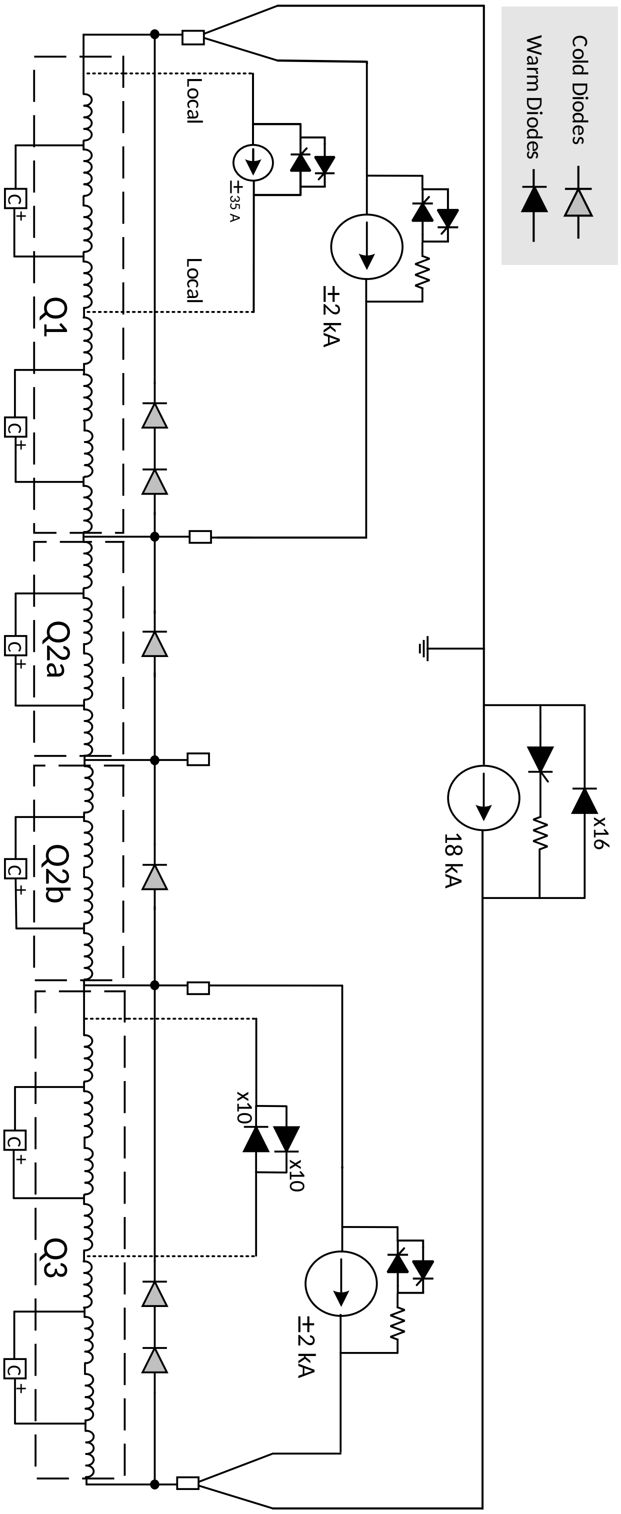

Figure 7.3 – Circuit layout of the HL-LHC inner triplets for IP1 and IP5. The drawing shows the quadrupoles Q1, Q2a, Q2b, Q3, the main, and trim power converters with their crowbars, the Coupling Loss Induced Quench protection systems (C) [Rav15] and the cold diodes. Image adapted by courtesy of CERN's Magnet Circuit Forum (MCF) and originally published in [Wil+20a].

8 In situ characterization of cryogenic diodes in a mixed radiation field to be used in HL-LHC circuits

This chapter summarizes the results and the subsequent analysis of an irradiation program, launched in 2018 at CERN, based on the experience of the LHC cryogenic testing programs. The goal of this study was to qualify the radiation tolerance of LHC type bypass diodes and two new prototype diodes up to fluence levels expected in the new HL-LHC inner triplet circuits. The setup and some of the results have been presented already elsewhere in conferences proceedings and publications [Wil+20a; Wil+18; Wol+19]. Most of the data shown in sections 8.3 and 8.4 was published in a different form in [Wil+20a]. A partial overlap with these publications and results therein is unavoidable and for better readability, detailed citation marks to these publications were omitted. Design of the setup, the installation in the irradiation facility as well as the execution of some of the measurements was done in collaboration with teams of the CERN sections TE-MPE-PE and TE-MPE-EE.

8.1 New prototype diodes for HL-LHC

The prototype diodes for HL-LHC have been chosen to be of the same form factor as the ones installed in LHC. This allows for easier integration in the existing infrastructure. The new diode capsules are thus identical to the ones shown in Fig. 7.1, while the doping profiles of the diode wafers differ. The wafers have a diameter of 65 mm i.e. a surface of $A = 33.18\,\mathrm{cm}^2$. The dominant factor for the increase of forward voltage with increasing displacement damage is the increase in n-base resistivity as described above. The resistance and hence the forward voltage (compare Eq. (6.12)), scales with the inverse of the wafer area A^{-1} and the n-base width w_n. Therefore, to keep the increase in resistance small for a given wafer diameter it is beneficial to reduce the base width. The manufacturer defined the base width as the difference of the n^+ and the p^+ junction depths. The junction depth itself is defined as the intersection of the n^+ or p^+ doping concentration curve with the original n-type concentration level in the Si-wafer of about $9 \cdot 10^{13}\ \mathrm{cm}^{-3}$, before the implantation of phosphorous and boron. Figure 8.1 illustrates the doping profiles and the junction depths. The diodes used were prototypes of diffusion diodes with an elongated Boron p^+ diffusion drive. The length of the diffusion drive defines the junction depth, resulting to different base widths. When the p^+ junction depth is overlapping the n^+ junction, the base width in this definition becomes negative, as can be seen for the *very thin base* prototype in Fig. 8.1. Figure 8.1 shows also the approximate resistivity, calculated as a function of the dopant density by using tabulated values from [Van11]. The main contribution to the resistance originates from the region around the n-base width, as the resistivity drops quickly for dopant concentrations of 10^{16} and higher.

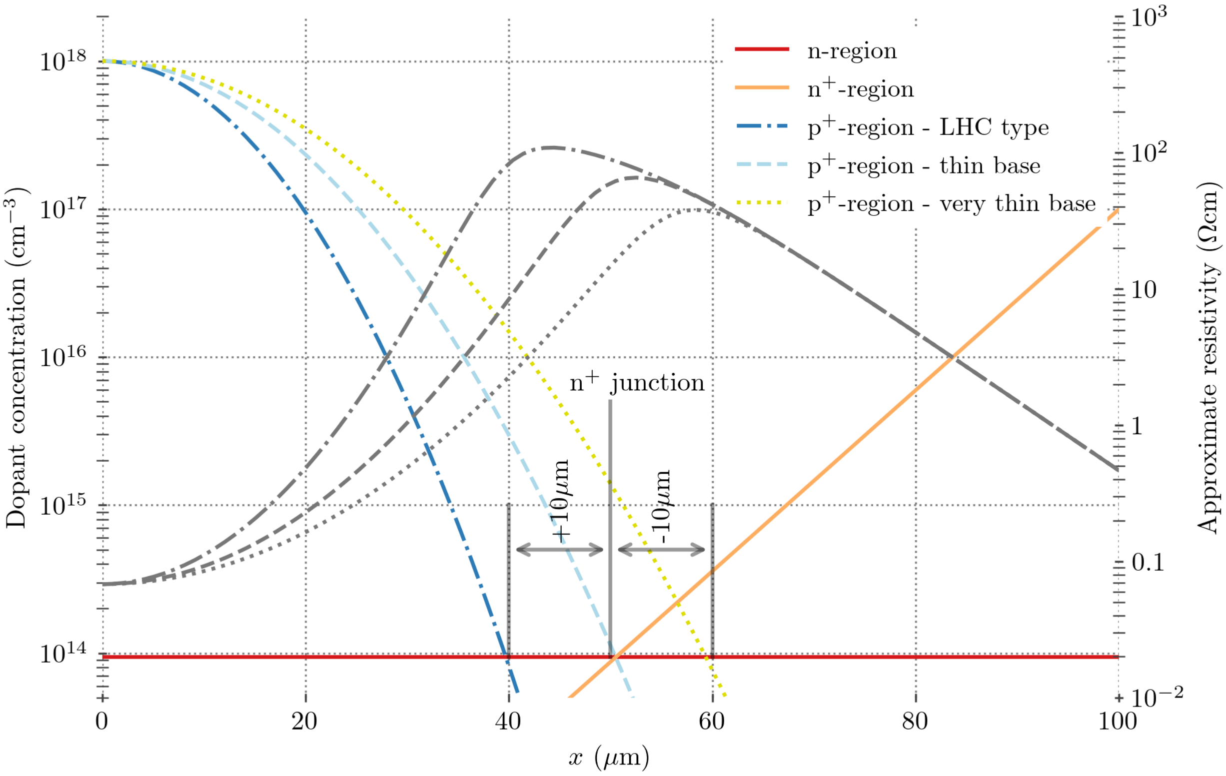

Figure 8.1 – Schematic doping profiles for the three diode types [Rou18]. The distance between the n^+ and p^+-junctions at a doping concentration of about $9 \cdot 10^{13}$ defines the base width. The values are for illustration only and do not represent measured data. The gray lines indicate the approximate resistivity at room temperature. It was calculated using tabulated values for the resistivity as a function of dopant concentration from [Van11]. The main contribution to the resistance originates from the *n*-base region.

All diode types were produced by Dynex Semiconductor Ltd. [Dyn]. Two new prototypes were tested, with base widths of 0 ± 5μm (*thin base*) and -10 ± 5μm (*very thin base*) according to the definition above. Neither U_{to} nor $U_f(I)$ of these virgin prototype diodes are affected by the base-width, while the reverse blocking voltage U_b decreases with decreasing *n*-base width. Table 8.1 provides an overview of the parameters of the different diodes used in the experiment as well as the naming convention.

8.2 Experimental Setup

To study the effects of mixed field irradiation on the new prototype diodes and to verify their radiation tolerance, the irradiation program was intended to represent the conditions for such diodes during the life cycle of HL-LHC. The particle spectra and fluence as well as the total dose were supposed to be representative with a stronger focus on the 1 MeV neq. fluence rather than the dose. Furthermore, the diodes were tested in situ during the irradiation period without intermediate warm up, similar to their operation in a superconducting magnet. The temperatures of main interest to perform the measurements were 4.2 K and 77 K. This allows a comparison to previous measurements, performed in liquid helium and liquid nitrogen. Those temperatures can be conveniently achieved with commercial cryostat systems. A temperature of 1.9 K is harder to

Table 8.1 – Parameters of diode prototypes and their corresponding labels. The temperatures at which the in situ characterization was performed is indicated.

Diode label		**Measurement Temperature**	**n-base width**	**U_{rev}**
LHC reference	D1	77 K	10±5 µm	520±10 V
	D8	4.2 K		
thin base	D2	77 K	0±5 µm	400±5 V
	D7	4.2 K		
very thin base	D3, D4	77 K	-10±5 µm	250±20 V
	D5, D6	4.2 K		

reach and no significant change of the diode properties is expected as will be discussed and shown later. The characteristics at other temperatures up to room temperature was of interest as well, e.g. to determine the temperature dependence and to assess the annealing capabilities during thermal cycles.

Lastly, as access to irradiation facilities is usually very limited, during the several months long irradiation program, the system had to be controlled remotely with distances of a few tens of meters from the control room to the cryostat. This concerned instrumentation and signal wires, high current leads and the cryogenic supply lines to the cryostat.

8.2.1 Cryostat System and in situ measurements

A cryostat system was designed following the requirements described above as well as the constraints given by the CHARM irradiation facility. It consists of a two stage pulse tube cryocooler[1] with two interface plates, where the first stage can be operated at temperatures from around 40 K up to more than 77 K and the second stage at around 3.5 K and above. Furthermore, both stages allow to individually set an exact temperature within this range, using stage heaters and a PID control feedback loop. The absence of large quantities of helium as well as the closed cycle operation permits a safe remote operation over long term, while the compressor unit can be set outside of the radiation zone.

Figure 8.2 shows the opened cryostat, where the vacuum vessel and thermal shields have been removed. Two stacks of four diodes each were attached to the two stages. The stacks were equipped with two *very thin base* diodes with -10 µm base width on the position closest to beam (D3 and D4 as well as D5 and D6), one *thin base* diode with 0 µm base width below (D7, D2) and one *LHC reference* type diode at the bottom (D1 and D8), with the largest distance from the beam.

Copper spacers were put between the diodes. They served as thermal mass, stabilizing the temperature in the system while acting as mounting points for the temperature sensors. The temperatures were continuously monitored on three heat sinks within each stack - the two outermost heat sinks on the top and bottom as well as the central one (compare left side of Fig.

---

[1] Sumitomo RP-082B2 4K pulse tube cryocooler https://www.shicryogenics.com/

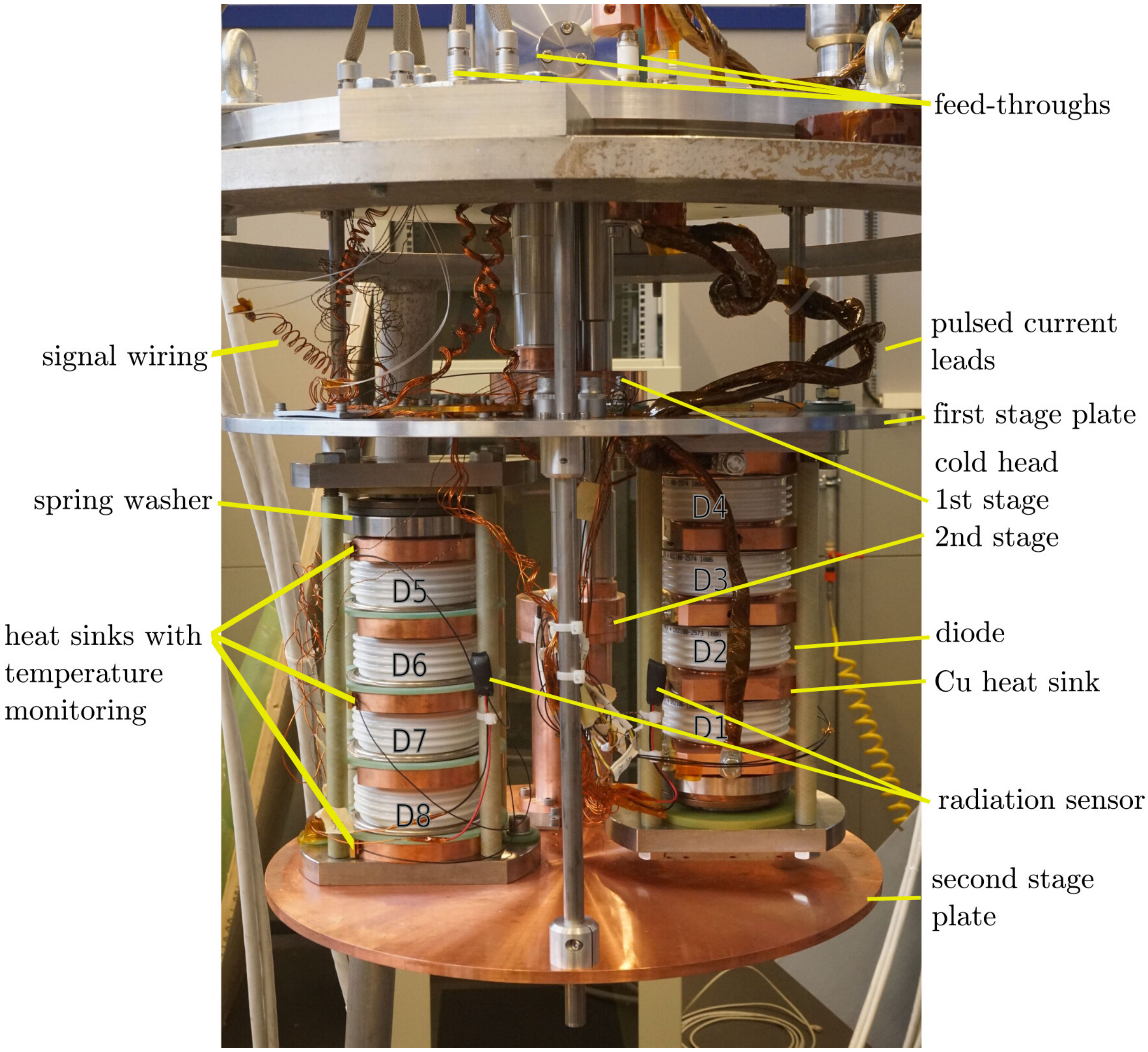

Figure 8.2 – Cryostat system without heat shields and opened vacuum chamber. The two diode stacks with four diodes each are visible. The two stages are thermally decoupled, so both stacks can be held simultaneously at different temperatures. The diode stack with diodes D1-D4 is coupled to the first stage plate and operated at 77K, the diode stack with diodes D5-D8 is coupled to the second stage plate and operated at 4.2 K. Image originally published in modified form in [Wil+20a].

8.2), and on each of the stage plates. The temperature of each diode could be monitored and set with a precision of $\pm 0.1\,\mathrm{K}$ by using the PID controller for the stage heaters with feedback from the temperature sensors on the stacks. Furthermore, the temperature gradient along the stack could be interpolated from the three measurement points.

Each diode was equipped with two voltage and two low-current leads, allowing individual four-point measurements of currents up to 2 A and voltages up to about 600 V. Those leads were directly connected to the taps on the diode housing (compare Fig. 7.1). The diodes attached to the 77 K stage, were connected in series within their stack. Two current leads allowed to apply current pulses of few milliseconds duration and with amplitudes of up to 18 kA. The diodes in the stack attached at the 4.2 K stage were insulated from each other. Three quantities were measured to evaluate the degradation of the diode characteristics as a function of absorbed dose and the 1 MeV neq. fluence. Two of them could be recorded on both stacks at all available temperatures:

- The turn-on voltage U_{to} was measured by applying a linear voltage ramp with a defined ramp rate of 50 and $100\,\mathrm{V\,s^{-1}}$ while the current flowing through the diode was recorded simultaneously. The voltage ramp rate was matched to the ramp rates observed in the LHC main dipole magnets during a quench, which is in the order of $50\,\mathrm{V\,s^{-1}}$.
- The leakage current under reverse bias voltage was measured by applying a logarithmic current sweep from 1 µA to 1 mA and measuring the voltage drop over the diode at each current step. A reverse bias current limit of 1 mA ensured, that the reverse characteristics of the diode could be safely measured up to reverse breakdown, without damaging the wafer. The reverse blocking voltage U_b was defined as the voltage at a leakage current of 1 mA.

Two current leads connected to the first stage allowed to test the full forward characteristics of the diodes $U_f(I)$ as a function of the applied current up to 18 kA. This was done by applying half-sinusoidal current pulses of various amplitudes, with a pulse width of few milliseconds. The measured voltage drop across the diodes at the pulse maximum was recorded, where $\frac{\mathrm{d}I}{\mathrm{d}t} = 0$, in order to suppress the inductive component in the measured voltage signal. The voltage drop across each diode in the stack was measured simultaneously during such a pulse, which is why the diode temperatures could not be set individually in this type of measurement. Instead, the measurements were performed with the central heat sink set to a temperature of $77 \pm 0.1\,\mathrm{K}$. Section 8.2.2 shows a detailed evaluation of the temperature gradients in the diode stack and the temperature evolution during the high current pulses as well as the implications on the measurement results.

Setup in the CHARM irradiation facility at CERN

The CHARM facility at CERN, as introduced in chapter 1.1.2, was found to be a suitable irradiation facility for the envisaged test program. The beam passes at a height of 130 cm in the facility. The cryostat with a height of approximately 1 m was well below the main beam cone. A position was evaluated for the cryostat to be situated very close to the target. The position was optimized to achieve high integrated fluences and to minimize the dose and fluence gradient within the stack (compare [IFK18]). The shielding configuration doesn't affect the spectrum at the position of the cryostat significantly. A geometrical overview of the irradiation zone with the cryostat position is shown in Fig. 8.3 as well as an image of the installed setup in the facility. Furthermore, as the cryostat was to be installed for the full run of 2018, the position guaranteed, that users at the other positions were not affected by its presence. Helium supply lines and high-current leads were attached to the shielding wall (compare Fig. 8.3) and fed outside the irradiation zone, such that

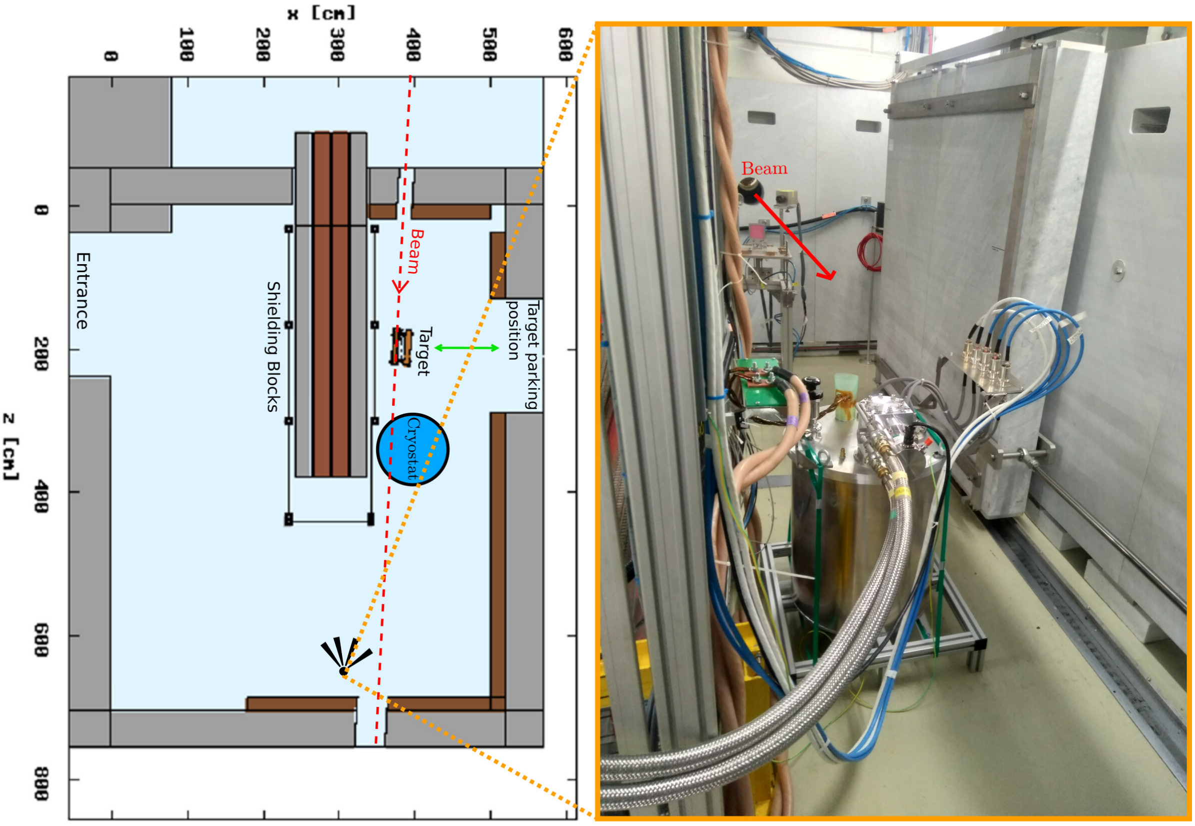

Figure 8.3 – *Left:* Geometric overview of the CHARM facility with the indicated cryostat position. Image adapted from [Tho16]. *Right:* Image of the installed cryostat system in the CHARM facility. The proton beam is indicated schematically (not to scale). The beam passes at a height of 130 cm, well above the cryostat. The point of view, where the image was taken in the facility is indicated in the schematics on the left.

both the compressor unit and the high-current pulse generator could be placed next to the control room for easy access and protected from radiation.

8.2.2 Thermal simulations

During the commissioning of the cryostat system, a base temperature of 33 K was reached at the first stage. The diodes in the stack attached to this stage could reach a minimum temperature of 43.6 K for D4 to 44.3 K for D1. The thermal gradient was assumed to originate from the heat load due to the high current leads, which were directly connected to the stack without intermediate heat-sinking. The second stage reached a minimum temperature of 2.9 K. The diodes in the stack attached to this stage reached a temperature of 3.5 K for D8 up to 3.8 K for D5. Thus, the margin in cooling power was sufficient and allowed the diode temperatures to be set accurately within the stack, using the stage heaters with feedback from the temperature sensors on the heat sinks within the stack.

In addition to the temperature measurements, a 3D thermal model for FEM simulations in COMSOL [COM] was created to evaluate the thermal gradients in the diode stacks when in thermal equilibrium, to allow an interpolation of the temperature in between the measurement

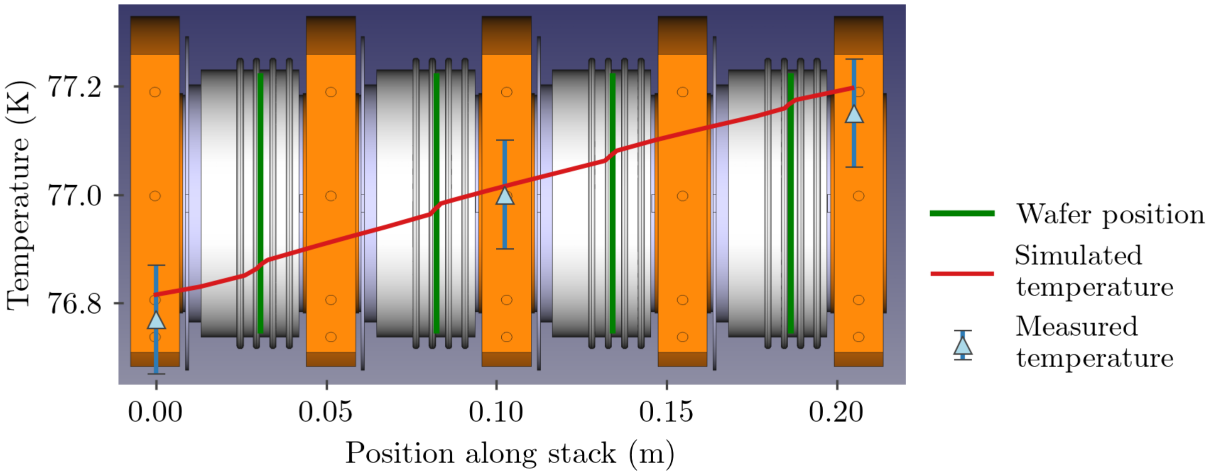

Figure 8.4 – Results of the FEM simulations in COMSOL[COM] to evaluate the temperature gradient in the 77 K diode stack. As a comparison, the measured temperatures on the different heat sink positions are indicated. A 3D scheme of the diode stack assembly is shown in the background.

points, as well as the transient thermal behaviour during the high current pulses. The model represented the stage plates with cold head and the according cooling capacity of the cryocooler [Sum], as well as heat flow through instrumentation and pulsed current wires and the diode stacks with the diode capsule's internal layered structure. The stage heater load resistor was modeled accordingly as a variable heat source. A non-uniformity in heating up the interface was expected, as the heater is small compared to the stage interface.

The gradient in thermal equilibrium on the 77 K stack originated mostly from the large cross-section current leads going from ambient temperature directly to the diode stack. As the cross section and heat conduction of copper are well known quantities, the equilibrium simulations were used as a benchmark. The temperature gradient within the stacks could be measured with the temperature sensors on the heat sinks and a comparison between measurements and simulation allowed fine-tuning of the simulation. The results are shown in Fig. 8.4. The simulations agreed well with the measurements. It showed, that the temperature within any given position of the stack could be assessed by interpolating linearly between the measured values of the three temperature sensors. The temperature controller in the cryostat made use of this information, when setting temperature values to specific diodes on positions between the temperature probes.

The transient thermal behavior during the high current pulses was of interest, as the self heating of a diode is a function of its forward voltage and, thus, changes with radiation. All current pulses were applied at a starting temperature of 77 ± 0.1 K, measured on the central heat sink. The current pulses had a duration of few milliseconds, with the current peak reached after about 800 µs. Nevertheless, the energy deposited into the wafer was not negligible, increasing with rising current amplitudes. Due to the negative temperature dependence of a diode's forward voltage, the measured voltage drop would be slightly smaller if self heating during the current pulse raised the wafer temperature.

Therefore, the wafer temperature during a current pulse was evaluated in a transient thermal simulation of the full diode stack. The large copper pieces are considered to not heat up significantly due to their low resistance and it was chosen to simulate the diode wafer as a current dependent

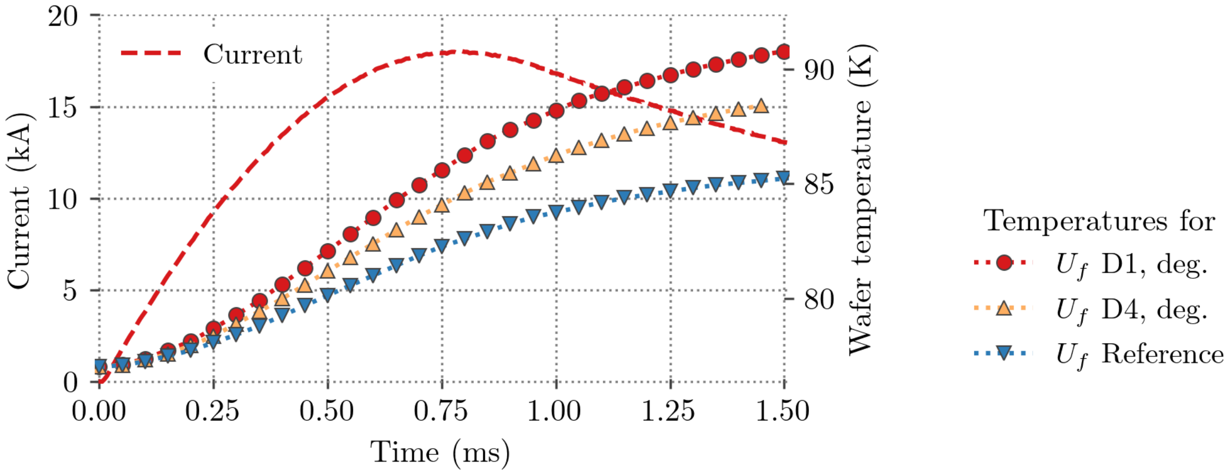

Figure 8.5 – Results of the FEM simulations in COMSOL[COM] to evaluate the temperature rise in the diode wafer during a current pulse with peak current of 18 kA. The simulated temperature evolution in the wafer center is shown along with the current pulse. The current peak is reached at about 0.75 ms. In a measurement, the voltage value at that time would be recorded.

heat source. The power P_{Pulse} deposited in the diode during the time dependent current pulse $I(t)$ was calculated as

$$P_{\text{Pulse}} = U_f\left(I(t), T, \Phi_{\text{neq}}\right) \cdot I(t) \tag{8.1}$$

where U_f is the measured forward voltage of the diodes

$$U_f = \begin{cases} U_{f,Ref}(I, T{=}77\text{ K}, \Phi_{\text{neq}}{=}0\,\text{cm}^{-2}) & \text{measured Reference} \\ U_{f,D1}(I, T{=}77\text{ K}, \Phi_{\text{neq}}{=}2.09 \cdot 10^{14}\,\text{cm}^{-2}) & \text{as measured for D1} \\ U_{f,D4}(I, T{=}77\text{ K}, \Phi_{\text{neq}}{=}2.28 \cdot 10^{14}\,\text{cm}^{-2}) & \text{as measured for D4.} \end{cases} \tag{8.2}$$

The temperature dependent parameters of the diodes were fixed to the measured values at 77 K. Due to the negative temperature dependence of diodes, as mentioned above, this yields a conservative maximum estimation of the simulated wafer temperatures.

Figure 8.5 shows the simulated transient temperature in the center of the diode wafer along with the current pulse. In the measurements, the forward voltage was always recorded at the peak of the current pulse. There, the simulations yielded wafer temperatures of about 84 K, when assuming the degraded forward voltage of D4, and about 87 K, when assuming the degraded forward voltage of D1, both measured at 77 K and at the end of the irradiation program.

The temperature dependence of the forward voltage drop after the irradiation was measured during a controlled warm-up, as described in a following section. From the measurements, the derivative $\frac{\mathrm{d}U}{\mathrm{d}T}$ was determined and the temperature rise could be scaled accordingly to an equivalent decrease in voltage. For diode D1 at 18 kA, this results in a total decrease in forward voltage of about 200 mV, which corresponds to an under-estimate of 8% of the measured voltage signal at this current level. For simplicity, it was decided not to correct each measured value for this shift but to rather consider it as an absolute systematic error, as indicated for example by the error-bars in Figs. 8.7 and 8.8. For currents below 12 kA the self heating is negligible and was not considered.

8.2.3 Dosimetry

The TID and 1 MeV neq. fluence were calculated [IFK18] using FLUKA. In the simulation both dose and fluence could be scored at each wafer position individually, taking into account the diode capsule and the diode stack geometry embedded in the cryostat system within the CHARM facility. The simulation yielded calibration factors for each diode to calculate dose and 1 MeV neq. fluence per proton on the target in CHARM and for each shielding and target configuration. To verify the simulated results a calibration run was performed in the CHARM facility before the irradiation program. Two pin-diodes inside the cryostat and two RADMON detectors [RGM05] on the cryostat walls – up and down-stream with respect to the beam – were used to validate the simulation results.

Table 8.2 summarizes the total ionizing dose and the 1 MeV neq. fluence accumulated for each diode at the end of the irradiation program. The difference between the diodes can be explained by their geometrically different position with respect to the beam axis. From the calibration run an uncertainty of 20% was estimated on the calculated scaling factors. The measured value of protons on target has an uncertainty of 10%. As both factors affect the result linearly and are not correlated, a Gaussian propagation of uncertainties can be performed which yields an uncertainty of about 25% on the absolute values of the 1 MeV neq. fluence given in Table 8.2.

Table 8.2 – Dose and 1 MeV neq. fluence at the end of the irradiation program for the diode prototypes. The uncertainty is 25%.

Diode	**D1**	**D2**	**D3**	**D4**
1 MeV neq. fluence Φ_{neq} (10^{14} cm^{-2})	2.09	2.15	2.27	2.28
Dose (kGy)	10.40	11.17	11.06	10.24
Diode	**D5**	**D6**	**D7**	**D8**
1 MeV neq. fluence Φ_{neq} (10^{14} cm^{-2})	1.74	1.75	1.70	1.66
Dose (kGy)	11.00	11.02	12.20	9.75

8.3 Measurement program - results and analysis

During the irradiation program, weekly measurements were taken. This corresponded to increases in dose of about 0.5 kGy and $\Phi_{\text{neq}}=1 \cdot 10^{13}$ cm^{-2}. This section presents the measurement results as well as the analysis and theoretical models to explain the results.

8.3.1 Forward characteristics $U_f(I_f)$

Figure 8.6 shows the absolute and relative increase of the measured forward voltage U_f as a function of the absorbed 1 MeV neq. fluence for diodes D1, D2, D3 and D4 for currents from 1 kA to 18 kA. The absolute value of U_f for the virgin diodes ranged from 1.14 V at 1 kA to 1.72 V at 18 kA and was similar for all diodes independent of their base width. With a wafer area of roughly 33 cm^2, a current of 18 kA corresponds to a current density of 540 $\frac{\text{A}}{\text{cm}^2}$, which is considered to be in the high-level injection regime. The lowest measured pulsed currents of 0.5 kA correspond to 15 $\frac{\text{A}}{\text{cm}^2}$. A steep increase upon radiation of the forward voltage was observed for currents above

2 kA. The increase reached about 43% at the end of the irradiation program for diode D4 at a forward current of 18 kA. Below a forward current of 2 kA the total increase stayed below 15% for diode D4. For diode D1 an increase of the forward voltage of about 83% at 18 kA was observed. Above a 1 MeV neq. fluence of about $5 \cdot 10^{13}$ cm^{-2}, the original steep increase flattened out. Starting from a 1 MeV neq. fluence of about $1 \cdot 10^{14}$ cm^{-2}, the increase became almost linear. Qualitatively, the other diodes showed the same behaviour as can be seen in Fig. 8.6. The slope of the linear part differed significantly between the diode types with the largest slope for diode D1.

The relative change of U_f with the accumulated 1 MeV neq. fluence at 18 kA is shown in Fig. 8.7 for the diodes D1, D2, D3 and D4. Diodes D3 and D4 with the smallest n-base widths showed the lowest increase of U_f of about 40% and behaved very similar in general. U_f increased up to 83% for the LHC reference diode D1. Diode D2 showed an increase of 58% and ranked in between the two other types. As expected, the lower degradation of the forward voltage correlated with the reduction of base width for this high level injection regime.

Comparison to previous studies

The results of the LHC type diode were compared with results of those previously obtained in the LHC irradiation programs [Den04b] and the FAIR irradiation program [Flo+07]. The results are shown in Fig. 8.8. The forward voltages measured at a current of 12 kA (LHC irradiation program) and 7.4 kA (FAIR irradiation program) at a temperature of 77 K are compared to the results presented in this thesis. Both are plotted as a function of the 1 MeV neq. fluence. The values of the FAIR irradiation program were obtained from the original publication and the error bars indicate the uncertainty in reading the values. The measured forward voltages in the previous LHC program and the FAIR program agree well with the measurements presented above.

8.3.2 Dynamic series resistance R_d increase

The dynamic or differential series resistance R_d is defined as

$$R_d = \frac{\mathrm{d}U_f}{\mathrm{d}I_f}. \tag{8.3}$$

From the measurement data it was determined numerically via the discrete gradient on the measured $U_f(I_f)$ forward characteristics using the *numpy.gradient*[2] function in *Python*. The values at the end of the irradiation program are shown as a function of the current in Fig. 8.9 for diode D1, D2 and D4. The yellow squares indicate the calculated series resistance from the forward characteristics as measured in the experimental setup before irradiation. The red circles indicate the calculated values from reference measurements performed in a different setup where the diodes were immersed in liquid nitrogen. The increase in resistance with increasing fluence was found to be less than 0.12 mΩ for all diodes. The specified upper limit of 0.5 mΩ, as mentioned in Table 7.1, was not exceeded for any of the diodes, currents or fluence levels.

---

[2] Python *gradient* function from the Python package *numpy*, see numpy.gradient documentation webpage

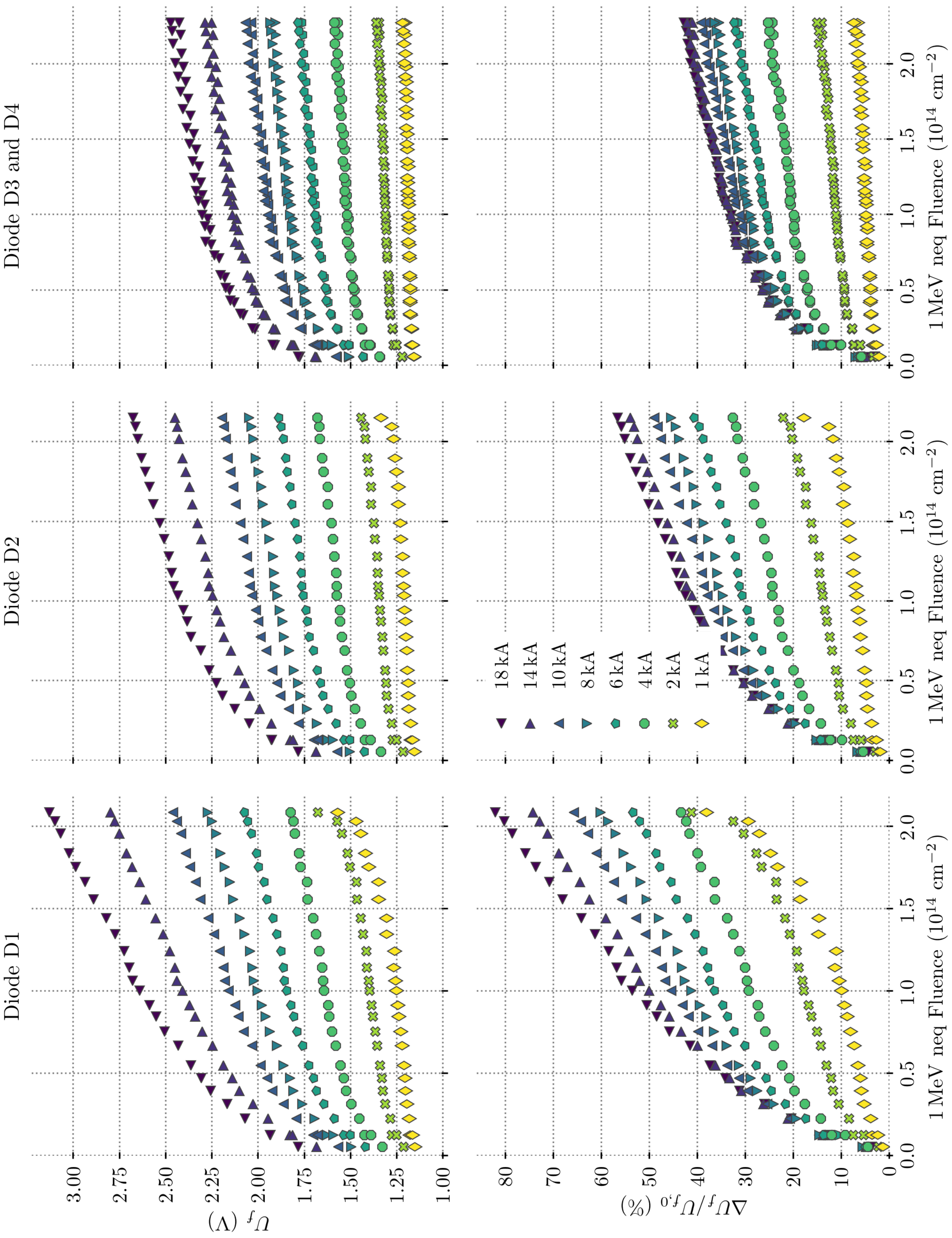

Figure 8.6 – Measured relative increase of the forward voltage U_f in diode Diode D1 as function of the accumulated 1 MeV neq. fluence, for currents from 1 kA to 18 kA.

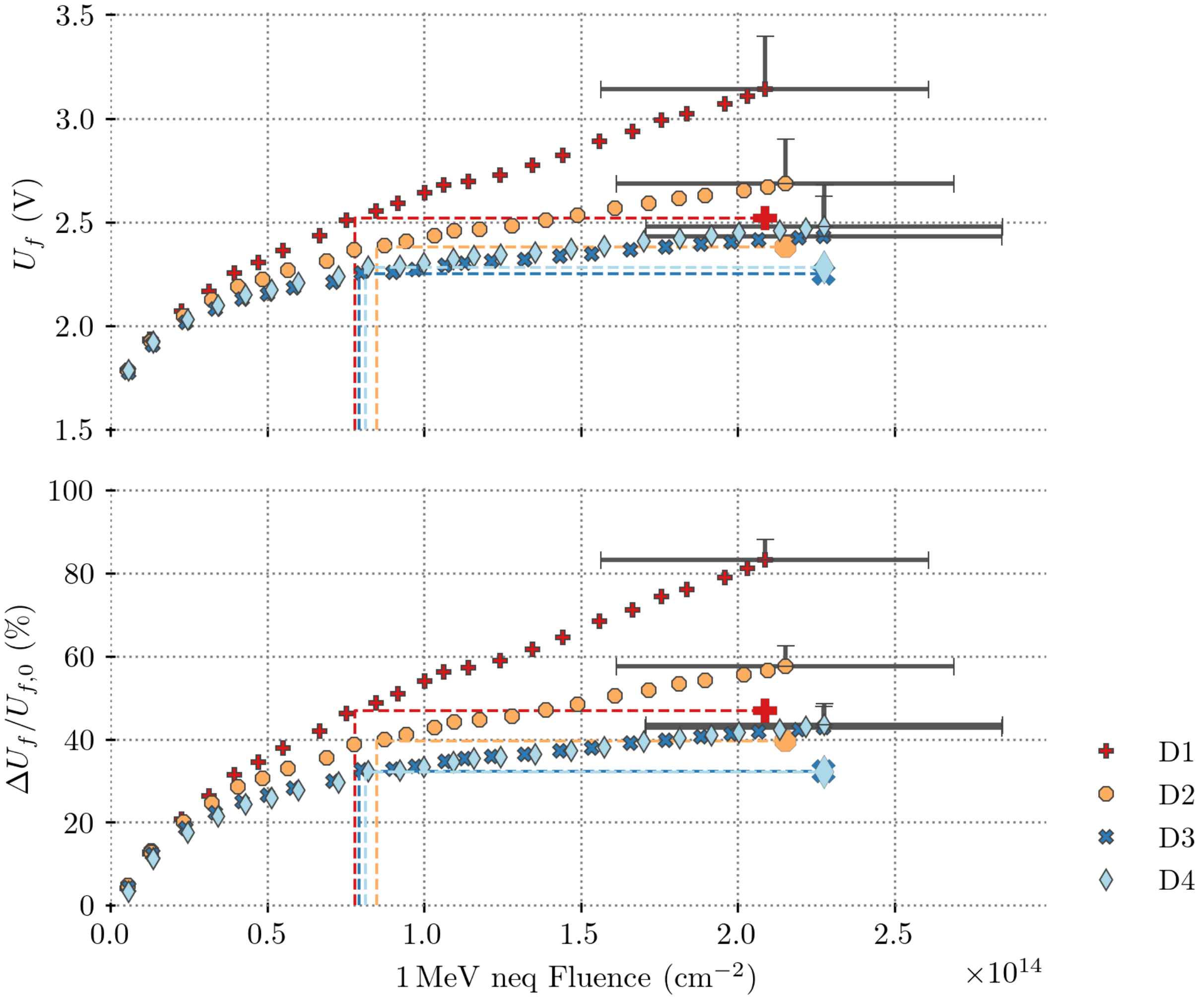

Figure 8.7 – Absolute (top) and relative change (bottom) of the forward voltage U_f of the diodes D1, D2, D3 and D4 as a function of the accumulated 1 MeV neq. fluence at a forward current of 18 kA. The last offset measurement points of each diode indicate the value of U_f after a thermal cycle up to room temperature. The dotted lines indicate the equivalent accumulated fluence levels for these U_f values. The error bars indicate an uncertainty of ±25% in the 1 MeV neq. fluence and an error of +8% in the forward voltage due to self heating. Data originally published in [Wil+20a].

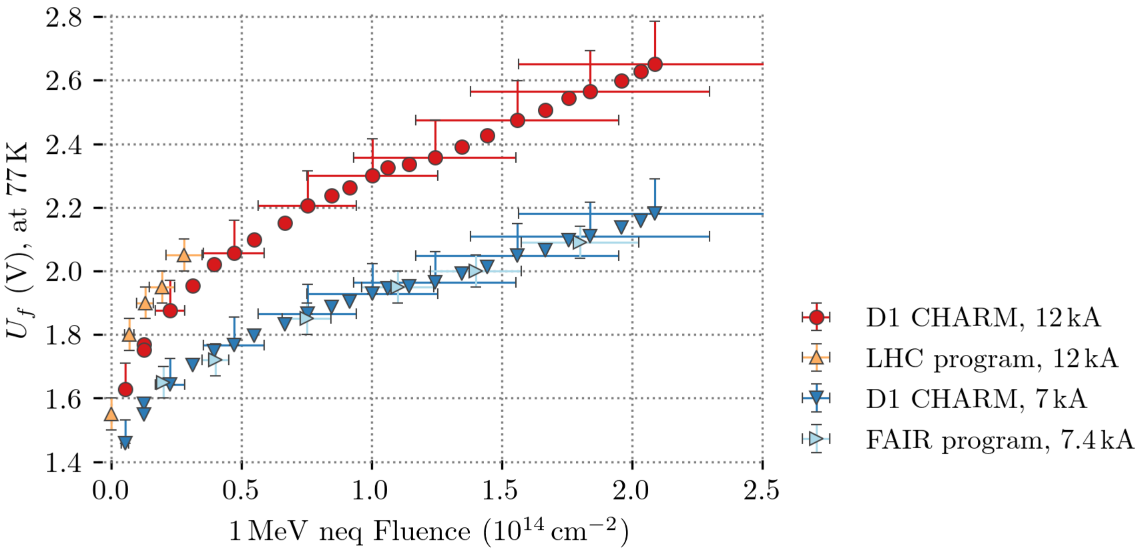

Figure 8.8 – Comparison of the LHC type diode's forward voltages measurements of the LHC irradiation program [Den04b], FAIR irradiation program [Flo+07] and the irradiation program presented in this thesis. The forward voltages were measured at a current of 12 kA (LHC irradiation program) and 7.4 kA (FAIR irradiation program) at a temperature of 77 K. They are shown as a function of the 1 MeV neq. fluence and dose.

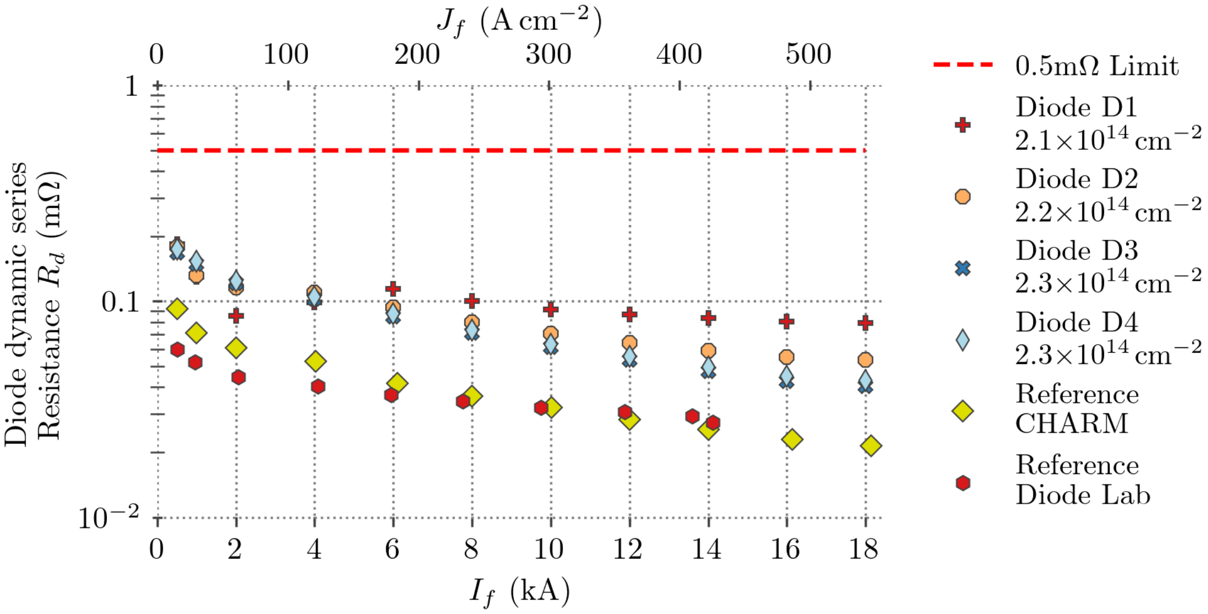

Figure 8.9 – Dynamic series resistance R_d of diodes D1 to D4 as a function of the current. The series resistance was calculated as the gradient to the forward characteristics measured at the end of the irradiation program. The reference values are from a measurement in a different system before the irradiation program (red dots) as well as from the calibration run in CHARM (yellow diamonds). Data originally published in [Wil+20a].

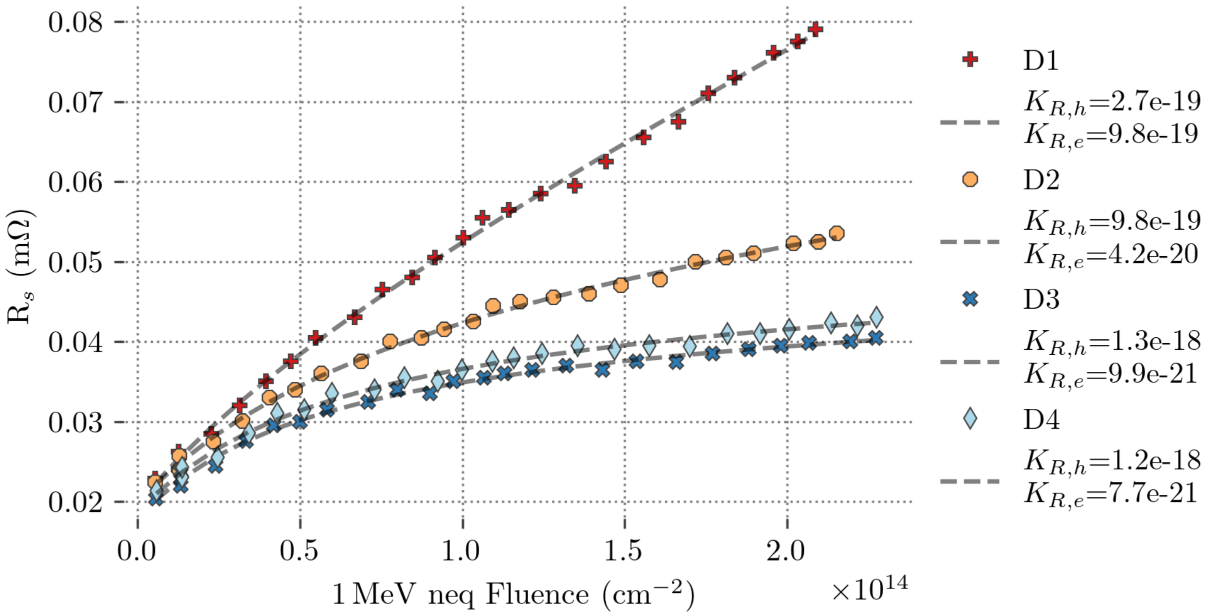

Figure 8.10 – Schockley series resistance extracted from the forward characteristics of the diodes, as a function of the exposed 1 MeV neq. fluence. A fit using a functional dependence in the form of Eq. 6.25 was performed on the data. The resulting fit coefficients are mentioned in the legend. Data originally published in [Wil+20a].

8.3.3 Increase of the *n*-base resistance R_s

According to Eq. (6.12) in the limit of high injection the dynamic series resistance should correspond to the *n*-base resistance. Hence, the *n*-base resistance R_s was extracted in the analogous manner as the dynamic series resistance, but taking into account the gradient of the measured $U_f(I_f)$ curves only for the highest measured current levels, between 16 kA and 18 kA. Figure 8.10 shows the increase of this resistance as a function of the 1 MeV neq. fluence for diodes D1 to D4. A fit on the measured series resistances using a function of the form as in Eq. (6.25) was performed. The resulting fit coefficients $K_{R,e}$ and $K_{R,h}$ were determined and are given in Fig. 8.10. The contribution of the two lifetimes differ significantly, due to the different effective mass of electrons and holes. The degradation coefficients show different orders of magnitude. A linear growth of resistance can be assumed as long as one of the two lifetimes is dominating (see Eq. 6.25). This is the case in the regime above a 1 MeV neq. fluence of about $1 \cdot 10^{14}$ cm^{-2}.

8.3.4 Theoretical model and fits

The Schockley equation as shown in Eq. (6.12) was fitted to the measured data. It has seven free fit parameters, considering the dependencies in Eq. (6.25). The resistance as a function of the 1 MeV neq. fluence, as presented in Eq. (6.25), was extracted directly from the measured data, as described above. The ideality factor l and the saturation current I_s remained as free fit parameters. For I_s it is usually assumed to decrease linearly with exposure to 1 MeV neq. fluence, as described in Eq. (6.31). The fits on the full measured data-set $U_f(I_f, \Phi_{\text{neq}}, T{=}77\,\text{K})$ using this model are shown in Fig. 8.11 for D1, D2 and D4. The trends of the measurement are represented well by the fit model. Especially the onset of non-linear growth of voltage in the lower current regime $\lesssim$2 kA can be clearly seen. The mathematical origin for this behaviour is the decrease of I_s with increasing 1 MeV neq. fluence, leading to a divergence in the logarithmic part of Eq. (6.12). The linear decrease as in Eq. (6.31) is assumed to only be valid until I_s approaches zero. Close to zero, the linear behaviour is no longer valid and is more likely to flatten out and to approach zero asymptotically. Within the measured range of 1 MeV neq. fluence of about $2 \cdot 10^{14}$ cm^{-2}, the linear model stays valid as it can represent the measured data well.

For further extrapolations to higher 1 MeV neq. fluence levels, an exponential decaying saturation current model was assumed when approaching $I_s = 0$

$$\begin{aligned} I_s(\Phi_{\text{neq}}) &= I_{s,0} \cdot \exp(-K_I \Phi_{\text{neq}}) && (8.4) \\ &\approx I_{s,0} - K_{I,1}\Phi_{\text{neq}} + \mathcal{O}(K_{I,2}\Phi_{\text{neq}})^2. && (8.5) \end{aligned}$$

The expansion in a Taylor series for low regimes of damage, i.e. $K_I \Phi_{\text{neq}} \ll 1$ (see Eq. (8.5)) yields exactly Eq. (6.31) in the first order. Fits were performed also with the exponential model. Fig. 8.12 shows the results, including the extrapolation for the exponential and linear models, for a current of 18 kA. The divergence of the linear model can clearly be seen, compared to the finite increase for the exponential model. For diode D1, the divergent behaviour starts just after the maximum measured fluence value. For the other diodes, the linear and exponential models coincide for a longer range, before the divergence in the linear model separates the two curves abruptly. Future measurements have to show if the proposed model is valid for those levels of 1 MeV neq. fluence.

8.3.5 Turn-on behaviour U_{to}

The turn-on voltage U_{to} was measured at a temperature of 77 K for D1, D2, D3 and D4 and at 4.2 K for D5, D6, D7 and D8, both at a current of 200 mA. This corresponded to a current density of $6 \cdot 10^{-3}$ Acm^{-2}. Figure 8.13 shows the values of U_{to} as a function of the accumulated 1 MeV neq. fluence. U_{to} increased by between 30% or 1.8 V in case of D5 and D6 to about 46% or 2.7 V in case of D8. This is in agreement to measurements of the change of U_f, where the *LHC reference* diode type D1 showed the strongest and the *very thin base* type D3 and D4 showed the least degradation. As it was identified earlier, the increase of base resistance was the main source for the increase of forward voltage at elevated current densities and, therefore, a significant difference was observed for the different base width diodes. At the very low current levels for the turn-on voltage this effect played no significant role and the difference in degradation of the turn-on voltage between the diode types was observed to be accordingly much smaller. The measured turn-on voltage at 77 K did not significantly alter with exposed 1 MeV neq. fluence for D2, D3 and D4. The results of the measurements are shown in Fig. 8.13. Diode D1 showed an irregular increase starting from around a 1 MeV neq. fluence of $1 \cdot 10^{14}$ cm^{-2}. This is similar to the non-linear increase of the forward bias voltage at lower currents ($\lesssim 2$ kA) mentioned above.

Turn-on delay at low temperatures

The onset of conduction was observed to be significantly delayed with increasing 1 MeV neq. fluence. Figure 8.14 shows the transient behaviour of diode D6 during a turn-on voltage measurement for different fluence levels. The linear voltage ramp with 50 Vs^{-1} was applied and the recorded current is shown as a function of time (left hand side) and as the voltage-current characteristics. The transient signal for the non- and lightly irradiated diodes show a gradual onset of current

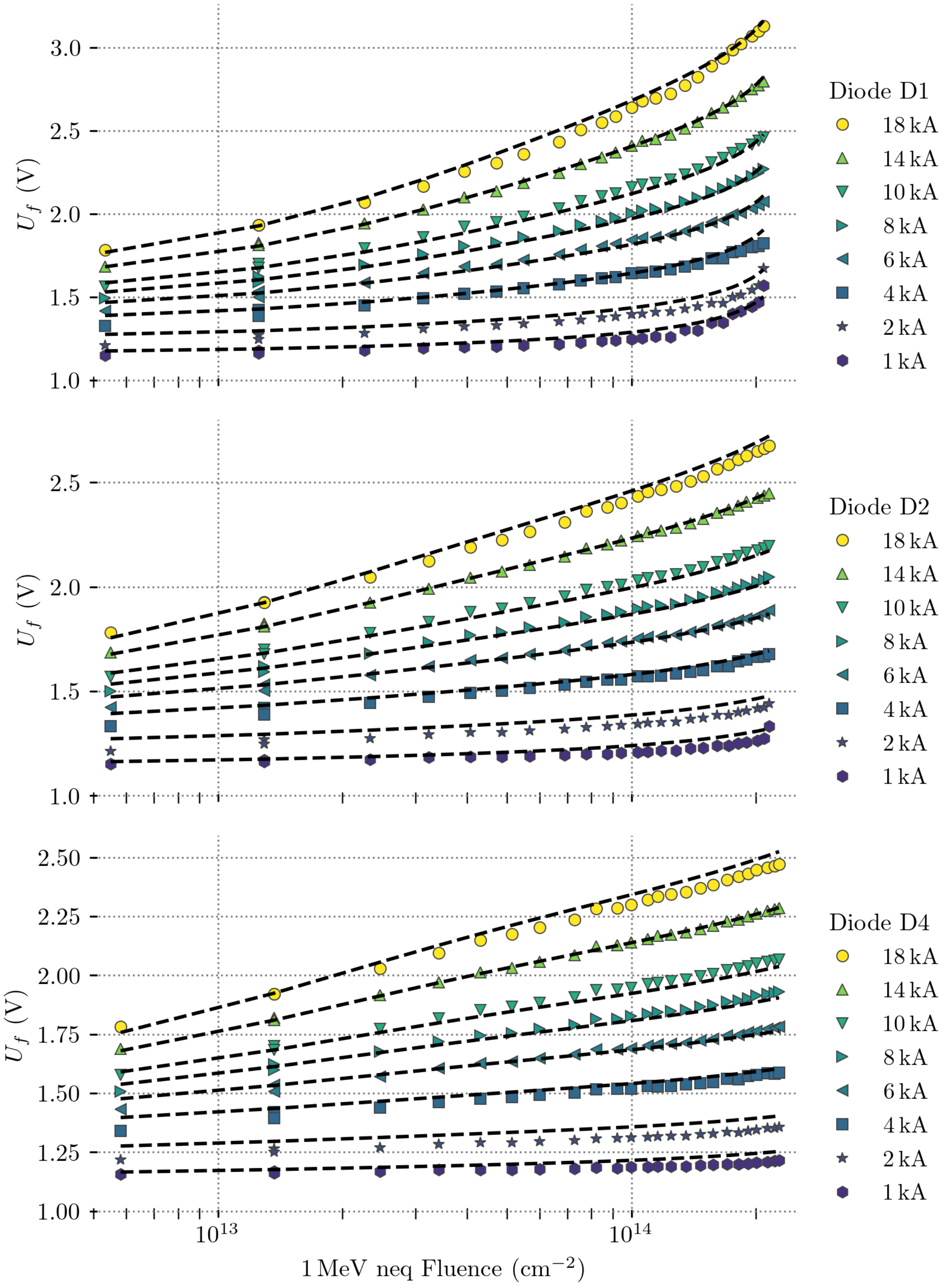

Figure 8.11 – Schockley equation fit on the full data-set $U_f(I_f, \Phi_{\mathrm{neq}}, T{=}77\,\mathrm{K})$ for Diodes D1 and D4 using the linear model for I_s. Data originally published in [Wil+20a].

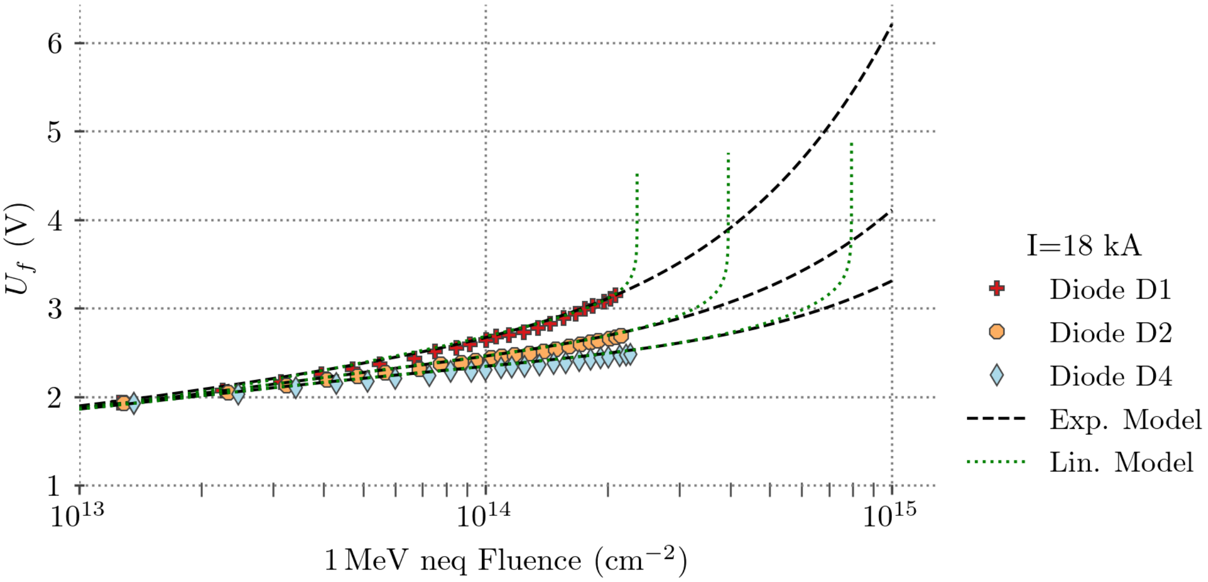

Figure 8.12 – Extrapolations using the fitted models of the forward voltage U_f at 18 kA for diodes D1,D2 and D4. The linear and exponential model for the saturation current are plotted as a comparison. The divergence of the linear model is visible, while the exponential model stays finite. Data originally published in [Wil+20a].

conduction with increasing voltage over time while the heavily irradiated diode at the end of the irradiation program very abruptly starts to conduct. The right hand side plot emphasizes this behaviour. The applied voltage was significantly overshooting first, and once the diode started to conduct, it falls back to a lower value: the actual turn-on voltage. As described above, this behaviour is very likely due to large presence of traps which have to be filled with injected carriers first, before the diode finally starts to conduct. The delay in turn-on time needs to be considered to still match the voltage development during a magnet quench but apart from that is not an issue, as the absolute increase in turn-on voltage was detected to be well within the requirements.

8.3.6 Reverse blocking voltage U_b

The leakage current under reverse bias was measured for all diodes at various fluence levels. Due to the low temperature no significant increase of the leakage current levels were observed during the irradiation program. The reverse blocking voltage U_b was defined as the voltage required to drive a current of 1 mA through the diode under reverse bias, as described above. This was well in the avalanche breakdown regime but still safe to operate. Figure 8.15 shows U_b at $I_r = 1\,\text{mA}$ for all diodes as a function of the accumulated 1 MeV neq. fluence. An increase of up to 20% was observed, which is beneficial in the foreseen use-case. As mentioned above, the increase can be explained by the dependency of the avalanche breakdown voltage on the base resistivity increase as in Eq. (6.15). The diodes of the same type showed a very similar behaviour of U_b, independent of their operating temperature of 4.2 K or 77 K.

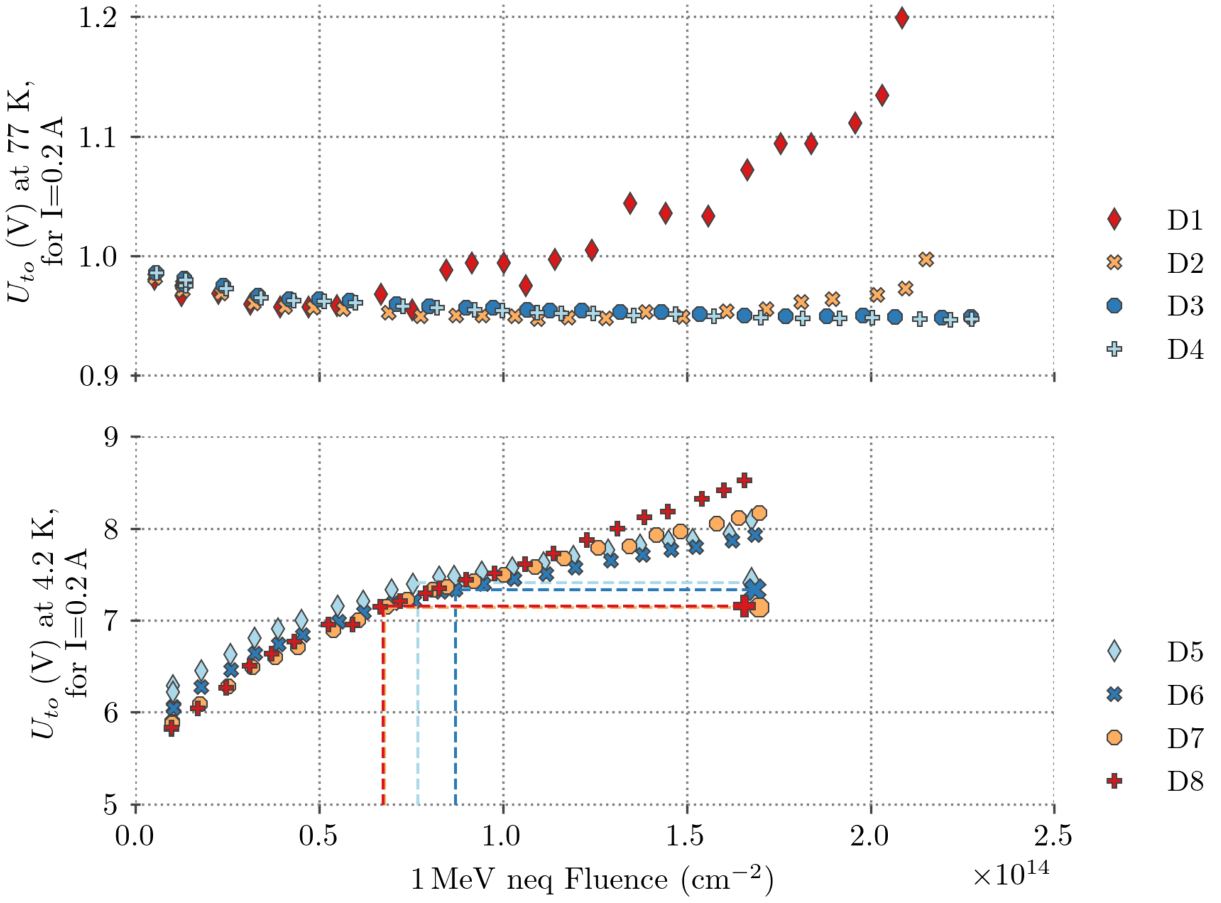

Figure 8.13 – *Top:* Turn-on voltage U_{to} of D1, D2, D3 and D4 as a function of the accumulated 1 MeV neq. fluence measured at a current of $I = 0.2$ A at 77 K.
Bottom: Turn-on voltage U_{to} of D5, D6, D7 and D8 as a function of the accumulated 1 MeV neq. fluence measured at a current of $I = 0.2$ A at 4.2 K. The last offset measurement points of each diode indicate the value of U_{to} after a thermal cycle up to room temperature. The dotted lines indicate the equivalent accumulated fluence levels for these U_{to} values. Data originally published in [Wil+20a].

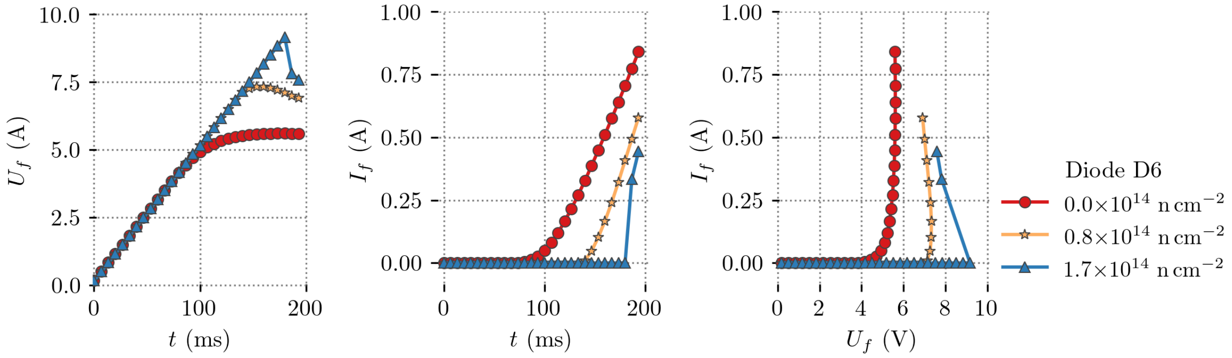

Figure 8.14 – Measured turn-on voltage of diode D6 for different irradiation states. *Left:* Applied voltage ramp. *Center:* Diode current as a function of time. A sudden jump in current was recorded for the heavily irradiated diode while for low and intermediate irradiation states, the conduction started more gradually. *Right:* Current-voltage characteristics during the turn-on voltage measurement. The applied voltage overshot the expected value on the heavily irradiated diode and then dropped abruptly once the current started to conduct. The measurement points are connected by lines as a guide for the eye in the order of the time they were recorded.

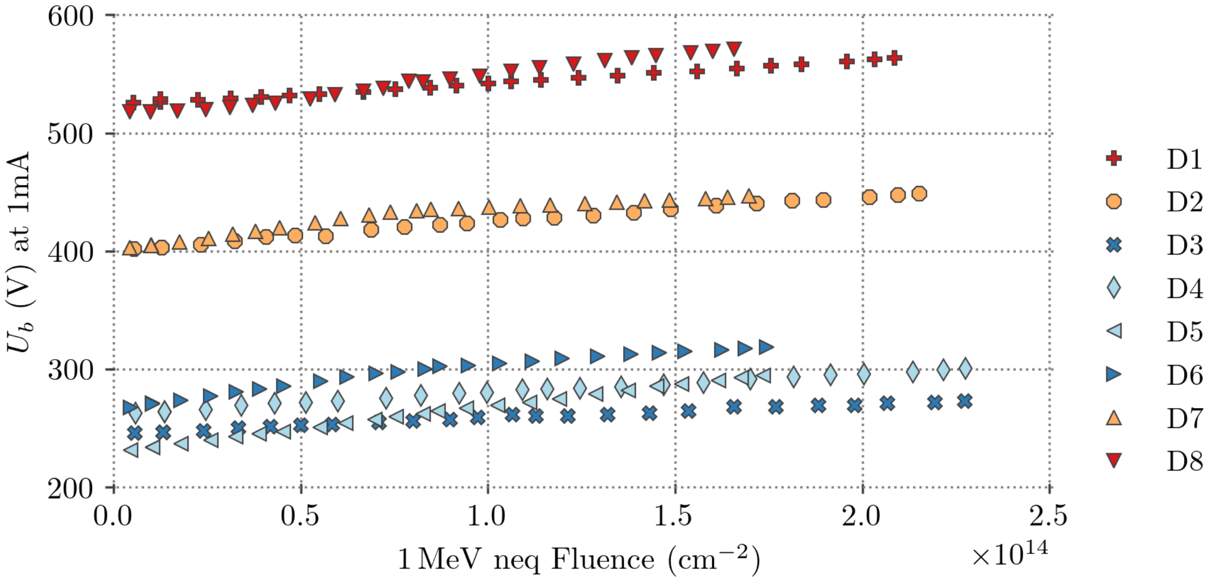

Figure 8.15 – Reverse blocking voltage U_b of all measured diodes, defined at a reverse current of $I_{rev} = 1$ mA, shown as a function of the accumulated 1 MeV neq. fluence. Data originally published in [Wil+20a].

8.4 Annealing study - results and analysis

An annealing study was performed after the irradiation campaign had ended. The diodes were warmed up to 293 K and temperature dependent measurements were performed on various temperature levels. In a subsequent cooldown, the diode properties at cryogenic temperatures were measured and compared to the values at the end of the irradiation program. In HL-LHC two scenarios of warm-up are foreseen. Firstly, during a quench the diode temperature could rise up to room temperature when conducting the large circuit currents. Secondly, a regular warm up for even longer timescales of weeks or months can be expected during long shutdowns of the accelerator, needed for maintenance. Two such long shutdowns are foreseen during the lifetime of HL-LHC. Therefore, it is of interest to evaluate and quantify the annealing capability of the diodes during and after such a thermal cycle.

8.4.1 Temperature dependence of U_{to} and U_f

The temperature dependence of U_{to} of diode D5 is shown in Fig. 8.16, from 3.9 K to room temperature. The measurements were performed during the first thermal cycle after the irradiation program. U_{to} is almost constant in the temperature range of 3.9 K to 5 K. Between the operational temperature of the cold diodes in HL-LHC of 1.9 K and 3.9 K no significant increase of U_{to} is expected, as indicated in the zoomed view in Fig. 8.16. Above about 5 K U_{to} decreases rapidly down to about 1.2 V at 30 K and finally to about 1 V at 50 K from where it decreases linearly to 0.3 V at room temperature. The other diodes in the experiment showed a similar behavior while they differed in the residual final value at the very low temperatures, as indicated before in Fig. 8.13. Figure 8.17 shows the dependence of U_f on temperature for Diode D4, from 65 K to room temperature for several constant current levels. The values were measured during the first

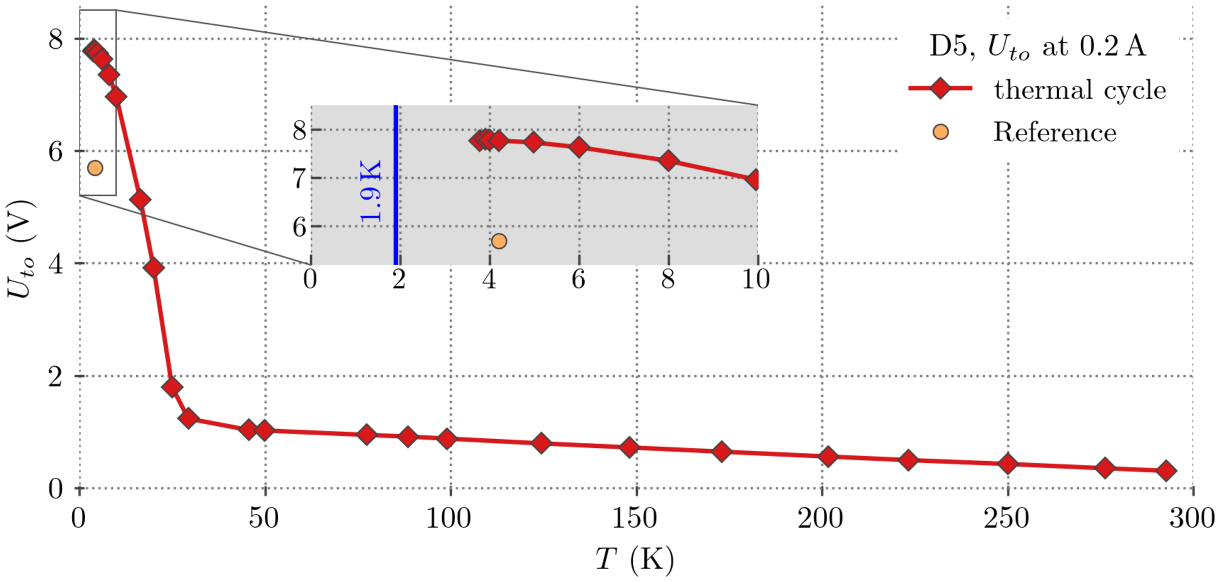

Figure 8.16 – Turn-on voltage U_{to} of diode D5, shown from 3.9 K to room temperature and including a zoomed view between 0 and 10 K, where the HL-LHC operating temperature of 1.9 K is highlighted. Data originally published in [Wil+20a].

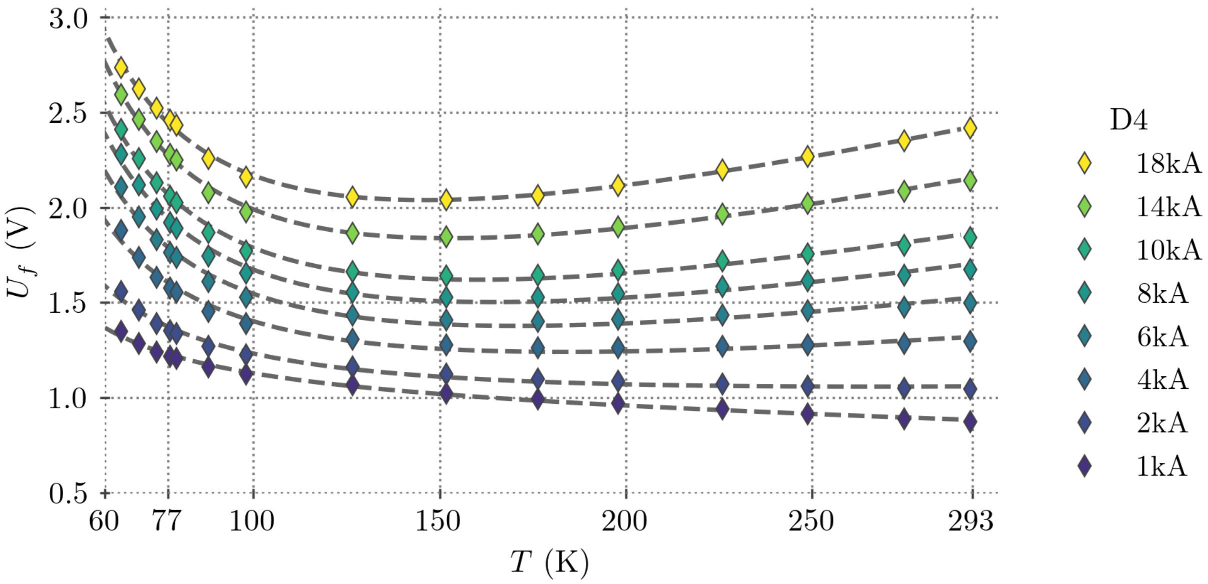

Figure 8.17 – U_f of diode D4 from 65 K to room temperature for different current levels. Data originally published in [Wil+20a].

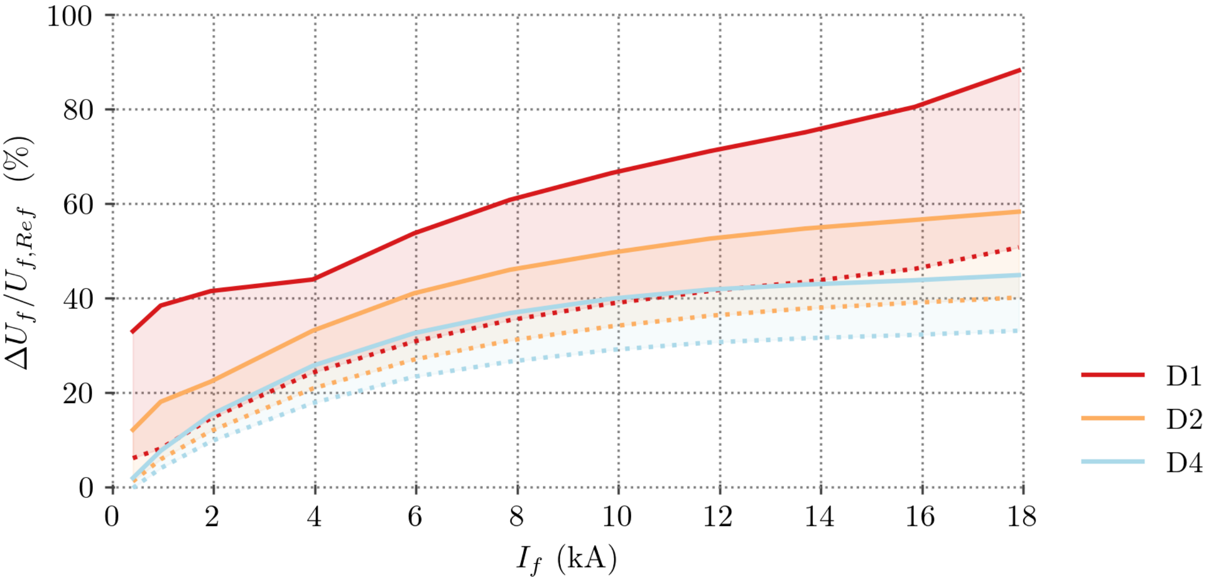

Figure 8.18 – Relative increase of the diodes' forward voltages as a function of the current. The values correspond to measurements taken at the end of the irradiation program (solid lines) and after the thermal cycle (dotted lines). The measurements were performed at 77 K. D3 was omitted in this plot for better visibility, however it behaves very similar to D4. Data originally published in [Wil+20a].

thermal cycle performed after the irradiation program. The diode characteristics originally showed a negative temperature dependence. For currents higher than about 2 kA, the voltage drop over the base resistance becomes significant, finally inverting the negative temperature dependence and resulting in an increase of the forward voltage for temperatures above about 150 K. The curves were fitted assuming a dependence of the form

$$U_f = C_1(I) \cdot e^{\frac{T_0}{T}} + C_2(I) \cdot T + C_3(I), \tag{8.6}$$

with fit coefficients C_1, C_2, C_3. The exponential term originates from the temperature dependence of the base resistance and T_0 was set to 50 K, the carrier freeze out temperature, as mentioned above in Eq. (6.13). The term with a linear temperature dependence originates from the Shockley Equation (6.12). The fits correspond well with the measurements. They might be used for circuit modeling or thermo-electric simulations, where analytical formulations are required.

8.4.2 Annealing of U_f and U_{to}

Measured turn-on and forward voltage anneal after a thermal cycle, as indicated in Figs. 8.7 and 8.13. In both figures, the voltage values after annealing and an interpolation back to the corresponding 1 MeV neq. fluence levels are indicated. The amount of annealed voltage is slightly different for all diode types. In case of the forward voltage, shown in Fig. 8.7, the 1 MeV neq. fluence levels correspond very well. This can be understood as the annealing is a thermally driven process, and should in theory anneal a similar amount of defects in all prototypes.

The relative annealing potential as a function of the current is shown in Fig. 8.18 for diodes D1, D2 and D4. The measured relative increase of U_f at the end of the irradiation program for all

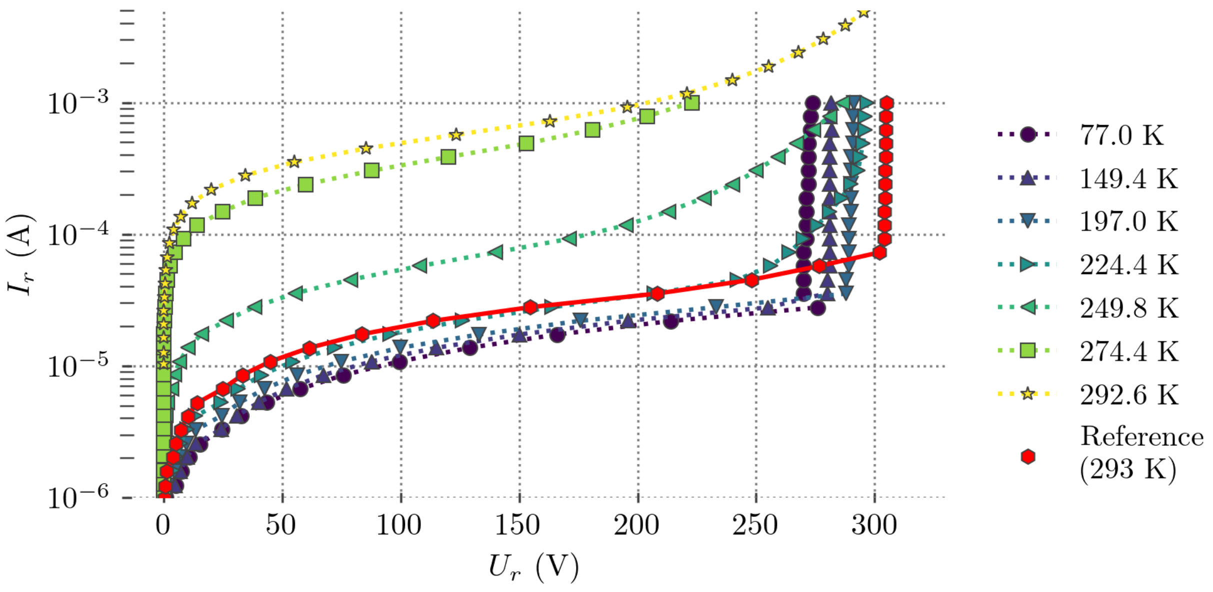

Figure 8.19 – Leakage current under reverse bias, measured for diode D3 during the first thermal cycle up to 293 K. The red hexagons show the reference measurement of that diode at 293 K before irradiation. Data originally published in [Wil+20a].

measured current levels as well as U_f after one thermal cycle are plotted. Diode D3 is omitted for better visibility, but behaves similar to diode D4. The above mentioned non-linear increase in forward voltage at lower currents results in the bump on the curve of diode D1 at low currents in Fig. 8.18. After the thermal cycle, this damage seems to fully anneal, as the bump is no longer visible on the annealed curve. The reason for this annealing, as was observed experimentally, is not known.

8.4.3 Leakage current increase

Figure 8.19 shows leakage current measurements on diode D3 under reverse bias for selected temperature values. The measurements were performed during the first thermal cycle after the end of the irradiation program. As expected, the leakage current under reverse bias shows a strong temperature dependence between around 250 K and room temperature, whereas at temperatures <200 K the change in leakage current with temperature is negligible, the measured curves overlap. A comparison of the leakage current at room temperature before the irradiation and after the irradiation at the end of the first thermal cycle (compare red hexagons with yellow stars in Fig. 8.19) reveals an increase of two orders of magnitude.

The damage coefficient K_I for the leakage current as described in Eq. (6.29) was calculated from the leakage current measurements of the diodes D1 to D4. The results are shown in Fig. 8.19. The damage coefficient $\alpha_I = K_I/V$ was also calculated and is shown below. However, the diode wafer active volume cannot be easily estimated, due to the overlapping doping profiles. The maximum value for the volume was assumed to be half the wafer volume and the minimum volume was assumed to be a slice with a thickness of 10 µm, similar to the base width. The results of the calculations for K_I with these assumptions are plotted in Fig. 8.20 as a function of the reverse bias voltage. The colored bands correspond to the range of values obtained with minimum and

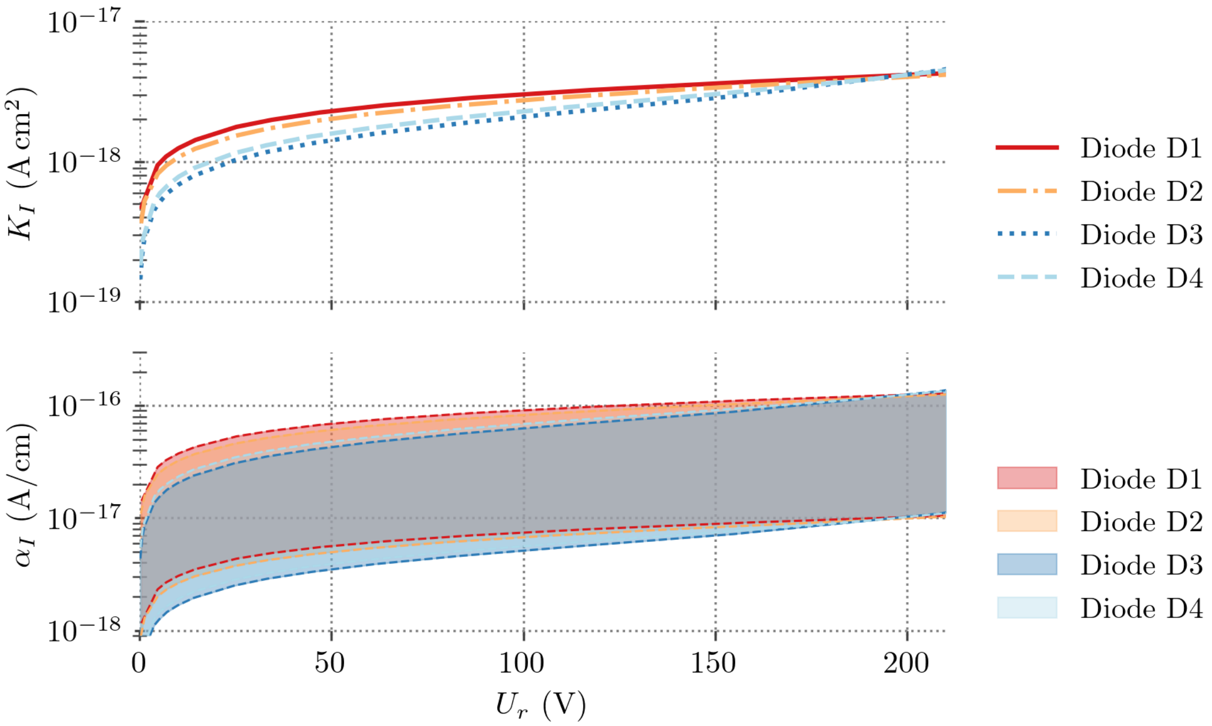

Figure 8.20 – Voltage dependence of the damage coefficients K_I and α for the leakage current increase under reverse bias for diodes D1, D2, D3 and D4. Data originally published in [Wil+20a].

maximum volume assumptions. As an example, the damage coefficient of diode D4 for negative bias voltages from aournd 10 to 200 V scales in the range

$$\alpha_I = (2.6\ ^{+5.1}_{-2.3}) \cdot 10^{-17}\,\mathrm{A\,cm^{-1}} \tag{8.7}$$

which agrees well with literature values usually in that order of magnitude. As no intermediate warm ups were performed, the exact dependency of the room temperature leakage current on the 1 MeV neq. fluence was not measured. For the use of the diodes in the HL-LHC triplets, this increase in reverse leakage current is not an issue. The scenario of a quench and a warm-up of the diodes to more than 200 K implies a forward bias operation of the diodes and hence the leakage current is irrelevant. In other scenarios, where the diodes blocking capabilities are of concern, the operating temperature is well below 200 K, where the leakage current is largely suppressed and as long as the operational requirements stated in table 7.1 are not exceeded, reverse breakdown of the diodes is not an issue either.

8.5 Summary and conclusion

Three types of diodes have been irradiated to a 1 MeV neq. fluence of about $2 \cdot 10^{14}$ cm^{-2} and a dose of more than 10 kGy, while held at cryogenic temperatures of 4.2 K and 77 K. The diodes were of *LHC reference* type and two new prototypes with reduced *n*-base widths, the so called *thin base* and *very thin base* diode. In situ measurements were performed to probe the forward and reverse bias characteristics as a function of the absorbed dose and fluence. After the end of the irradiation program, the diodes were heated up to room temperature and the characteristics was measured on several temperature steps. In a subsequent cool-down, the values before and after such a thermal cycle were compared, and hence the annealing capabilities of the diodes were assessed. In the non-irradiated state, all diodes show similar forward voltage characteristics, while the reverse blocking voltage decreases with decreasing base width. The analysis of the measurements showed the expected correlation of the base width and radiation hardness, i.e. the increase in forward voltage with absorbed fluence increases with increasing base-width. The LHC type diode showed the highest degradation in forward voltage (ca. 83% increase at $I_f = 18\,\mathrm{kA}$), the *very thin base* prototype the lowest increase (ca. 43% increase at $I_f = 18\,\mathrm{kA}$), and the *thin base* type lies in between (ca. 57% increase at $I_f = 18\,\mathrm{kA}$).

The Schockley model was fitted on the measured data, including radiation damage models for the increase in n-base resistivity due to a decrease of carrier scattering lifetimes, as well as a decrease of the saturation current in forward direction resulting from a decrease of the effective doping concentration, due to trapping of carriers in defect trap states. The increase in base resistance was observed to be the major influence on the overall increase in forward voltage, especially at the higher current levels. The fitted models can be used whenever analytical formulations are needed. This is the case in thermo-electric simulations of the circuits and can be useful to evaluate and model the electrical characteristics also for diodes in an irradiated state. The models were extended to be able to extrapolate up to a 1 MeV neq. fluence of $1 \cdot 10^{15}\,\mathrm{cm}^{-2}$.

The reverse blocking voltages of all tested diodes were measured at 4.2 K and 77 K. They behaved similarly, as a small increase was observed with absorbed TID and 1 MeV neq. fluence. During the annealing study, the reverse bias leakage current was measured at room temperature after the irradiation and compared to the original value. From the measurement, the reverse current damage coefficient could be estimated and compared to literature values which agreed well.

Based on the results and analysis of this irradiation program the *very thin base* diode type has been chosen to be used for the HL-LHC final focus quadrupole magnet triplet circuits.

Summary and outlook

The protection of high energy particle accelerators against the effects of primary and secondary particles from beam losses is important to ensure safe operation. Especially the superconducting magnet systems with large stored energies and sensitive superconducting wires need to be protected and the severity of such failure cases needs to be evaluated. Two relevant parts of superconducting accelerator magnet systems were investigated in the scope of this thesis: the superconductors themselves and cryogenic diodes, used for magnet protection in case of a quench. While the superconductors are sensitive to short timescale energy deposition, which can happen during ultra fast beam losses, the cryogenic diodes suffer from an accumulation of radiation damage due to steady particle losses, which are largest close to the interaction points. In the scope of this thesis the design, execution and the subsequent analysis of two experiments, conducted in 2018 at CERN, dedicated to these two subjects, were presented and discussed.

The first cryogenic beam impact experiment at CERN's HiRadMat facility was performed, impacting samples of three superconductors, Nb-Ti, Nb_3Sn and YBCO at 4.2 K with 440 GeV proton beam pulses. The samples were embedded in a copper sample holder block, allowing batches of 10 samples of Nb-Ti and Nb_3Sn and 6 batches of 7 samples of YBCO to be irradiated such that the energy deposition within the samples of each batch was increasing from $0.66\,\frac{\mathrm{kJ}}{\mathrm{cm}^3}$ to $4\,\frac{\mathrm{kJ}}{\mathrm{cm}^3}$ resulting in peak temperatures in the samples of 290 K to 1200 K and temperature gradients of $120\,\frac{\mathrm{K}}{\mathrm{mm}}$ to $400\,\frac{\mathrm{K}}{\mathrm{mm}}$. The beam impacted samples of Nb-Ti and Nb_3Sn were analysed subsequently for their critical transport current and microscopic analyses were performed. The YBCO based samples are not part of this thesis, the study is ongoing. The individual results and conclusions on the damage mechanisms can be found in sections 5.3 for Nb-Ti and in section 5.4 for Nb_3Sn.
Especially for Nb_3Sn limits for the peak temperature and temperature gradients were determined to be around 460-500 K and 200-250 K/mm, above which strong permanent degradation due to filament cracking was observed. Moreover, thermo-mechanical FEM simulations were performed and the application of theoretical scaling models for the critical parameters could reproduce the measured critical transport current well. The calculated critical average strain for the onset of permanent degradation due to filament cracking was found between 0.31% to 0.51%.
For Nb-Ti the results confirmed the ones previously obtained in a room temperature experiment. No significant degradation in terms of the critical parameters were found, but a weakening of the copper matrix, i.e. its RRR and hence a reduction in thermal stability were observed.
The limits found for both superconducting wire types will allow to estimate the severity of potential failure cases in terms of the single wire conductor performance. Extrapolation to the damage provoked in full magnet coils by using the simulation model is possible but will need to be verified in future beam experiments. A successor experiment is planned for the upcoming experimental period of the HiRadMat facility.

The second experiment characterized the radiation tolerance of cryogenic power diodes, to be used in the final focus quadrupole triplet magnet (*inner triplets*) circuits of the HL-LHC. This kind of diodes is used to protect magnets in case of a quench, either as by-pass diodes as in the LHC main dipole magnet circuits, or as voltage limiting devices as in the HL-LHC inner triplet magnet circuits. The experiment aimed to emulate the mixed field radiation and to yield comparable accumulated dose and 1 MeV neq. fluence levels as the diodes will see during their lifetime in HL-LHC. Both LHC type diodes and two new prototypes with smaller base widths were tested in-situ at 4.2 K and 77 K for their forward bias and reverse bias characteristics. Finally the accumulated 1 MeV neq. fluence reached was about $\Phi_{\mathrm{neq}} = 2 \cdot 10^{14}\,\mathrm{cm}^{-2}$, largely exceeding the foreseen lifetime fluence in HL-LHC of $\Phi_{\mathrm{neq}} = 5 \cdot 10^{13}\,\mathrm{cm}^{-2}$, giving good confidence in the obtained results with large margin. Moreover, the annealing capability of the diodes was tested after the irradiation program by several thermal cycles to room-temperature. The experimental setup, the measurements and the results were discussed in chapter 8 and the conclusion and summary is given in chapter 8.5.

Due to the obtained results, one of the new prototype diodes with the smallest base-width was chosen to be used in the HL-LHC inner triplet circuits. As the achieved 1 MeV neq. fluence exceeded the projected lifetime values of HL-LHC, future accelerators such as the FCC-hh might benefit from the results of the irradiation program.

Acknowledgements

This work was only possible due to the input and support of many people and I am sincerely grateful for it.

The doctoral student position was funded by the *Wolfgang Gentner Program* of the German Federal Ministry of Education and Research (BMBF) for which I am very grateful. The research was conducted at CERN, my supervising home-university was the Karlsruhe Institute of Technology (KIT). In this regard, I would like to express my sincere gratitude to Prof. Dr. Anke-Susanne Müller for accepting and supervising me as a doctoral student at KIT and to enable this collaboration of KIT and CERN.
On the CERN side I would like to express special gratitude to Dr. Daniel Wollmann for providing the possibility to conduct my research at CERN by opening and supervising my doctoral student position and the collaboration with KIT, within the context of the HL-LHC project. During the three years at CERN I have experienced strong support and scientific input from him as my direct supervisor at CERN for which I am especially grateful.
I would like to thank Dr. Axel Bernhard as my supervisor at KIT for regular fruitful discussions, helpful input and knowledge exchange. The contact to the LAS working group was an important factor for me to keep a constant link to my home-university.
I would like to thank Prof. Dr. Rüdiger Schmidt for valuable input during the regular section meetings, especially in the design phase of the experiments where this work could benefit from his experience of previous beam impact experiments. Furthermore, special thanks for kindly accepting to co-review this thesis.

The experiments were performed under the direction of the HL-LHC project, work package WP7 (machine protection) at CERN. For their contributions to the successful completion of the experiments covered in this thesis I would like to express my deepest gratitude to (in no specific order):

- The TE-MPE-PE section at CERN, where my position was integrated. Due to the variety of topics studied in this section, many experts on different branches of accelerator physics could be easily reached out to. The experiment, covering several domains could benefit a lot from it. Special thanks to Dr. Vivien Raginel for introducing me to the topic of damage mechanisms in superconducting accelerator magnets, Dr. Matthias Mentink for helpful input concerning Nb_3Sn, and the simulation experts, Lorenzo Bortot *et al.* for valuable input on COMSOL and other simulation tools.
- The TE-MPE-EE section supervised by Dr. Felix Rodriguez Mateos, from which constant support both in the design, set-up and execution of the experiments was provided. I would like to thank him and his team, especially Mathieu Favre, Krzysztof Stachon, Giorgio D'Angelo, Arnaud Monteuuis, Mateusz Bednarek, who were all heavily involved in the experiments and led them to success. Furthermore Dr. Dietrich Hagedorn for the valuable input and experience of diode irradiation studies.

- Sylvain Kaufmann for providing laboratory space and equipment in the radiation soldering workshop and valuable input on soldering techniques.
- The HiRadMat team, Dr. Fiona Harden, Dr. Yacine Kadi, Aymeric Bouvard and Vincent Clerc, for supporting the experiment and guiding it to a successful outcome, both with technical integration in the facility and the agile time management.
- The magnet group at CERN, TE-MSC, especially Dr. Amalia Bellarino and Dr. Bernardo Bordini for providing the Nb_3Sn samples, Dr. Glyn Kirby for valuable input during the cryostat design phase and on discussions about measurement techniques, Christian Scheuerlein and Dr. Felix Wolf for valuable discussions on Nb_3Sn.
- The R2E and CHARM team at CERN, Dr. Ruben Garcia Alia, Dr. Salvatore Danzeca, Jerome Lendaro for flawless support during the planning and integration phase of the experiment in CHARM and the the successful dismantling afterwards.
- Dr. Angelo Infantino, Melanie Krawina, Anton Lechner, Dr. Robert Froeschl and Dr. Helmut Vincke and Dr. Chiara Cangialosi for the input concerning FLUKA and for performing certain FLUKA simulations.
- Prof. Dr. Carmine Senatore at the University of Geneva (UniGe), Department of Quantum matter Physics (DQMP), Group of applied Superconductivity, with his team Dr. Marco Bonura, Damien Zurmuehle, Dr. Christian Barth, for performing the critical transport current measurements and the very valuable discussions on the damage mechanisms of superconductors.
- The EN-STI team and workshop for the last-minute fabrication of parts for the experimental setup and for providing the laboratory space in the radioactive workshop for dismantling works.

Within the context of this thesis two technical students were supervised and their scientific work was documented in an internal report [OWW18] and a Bachelor thesis [Sch20]. I would like to thank Andreas Oslandsbotn for his support and work during the late design phase of the HiRadMat experiment, the sometimes hectic and stressful implementation phase before and in the HiRadMat facility, as well as during the dismantling and sample extraction. Likewise, I would like to thank deeply Jonathan Schubert for his contribution to the project, both in his theoretical works in form of detailed multi-physics simulations and the help in sample preparation and the microscopical analysis. Their work done was extremely valuable and the clear and detailed documentation of it helped and will help to introduce the following peers to quickly dive into the study details.

Publications and conference contributions

Articles

- “**Characterization of the radiation tolerance of cryogenic diodes for the High Luminosity LHC inner triplet circuit**”, A. Will *et al.*
  In *Phys. Rev. Accel. Beams* **23** (5), Paper 053502, May 2020.
- “**Impact of 440 GeV Protons on Superconductors in a Cryogenic Environment**”, A. Will *et al.* In *Journal of Physics: Conference Series* **1559**, Paper 012060. Proc. of the EUCAS 2019.

Conference proceedings

- “**Characterisation of the radiation hardness of cryogenic bypass diodes for the HL-LHC inner triplet circuit**”, D. Wollmann, A. Will *et al.* Presented at the *IPAC19*, Melbourne, Australia. Paper THPTS067.
- “**Beam Impact Experiment of 440GeV/p Protons on Superconducting Wires and Tapes in a Cryogenic Environment**”, A. Will *et al.* Presented at the *IPAC19*, Melbourne, Australia. Paper THPTS066
- “**Experimental Setup to Characterize the Radiation Hardness of Cryogenic Bypass Diodes for the HL-LHC Inner Triplet Circuits**”, A. Will *et al.* Presented at *IPAC18*, Vancouver, Canada. Paper WEPMG006

Co-authored papers

- “**Performance of the Large Hadron Collider’s Cryogenic Bypass Diodes Over the First Two Physics Runs, Future Projects, and Perspectives**”, G. D’Angelo *et al.* In *IEEE Transactions on Applied Superconductivity* **30** (4), June 2020. Paper
- “**First Experimental Results on Damage Limits of Superconducting Accelerator Magnet Components Due to Instantaneous Beam Impact.**”, V. Raginel *et al.* In *IEEE Transactions on Applied Superconductivity* **28** (4), June 2018. Paper

Bibliography

[Abr+15] D. Abraimov, A. Ballarino, C. Barth, L. Bottura, R. Dietrich, et al.: *"Double disordered YBCO coated conductors of industrial scale: high currents in high magnetic field"*. Superconductor Science and Technology **28**.11 (2015), p. 114007. doi: `10.1088/0953-2048/28/11/114007` (cit. on p. 41).

[Abr57] A. A. Abrikosov: *"On the Magnetic Properties of Superconductors of the Second Group"*. Journal of Experimental and Theoretical Physics **32**.6 (1957) (cit. on p. 25).

[Ada+99] J. D. Adam, D. Leroy, L. R. Oberli, and D. Richter: *"Strand Coating for the Superconducting Cables of the LHC Main Magnets"*. IEEE Trans. Appl. Supercond. **9**.2 (1999). doi: `10.1109/77.783400` (cit. on p. 35).

[Amb15] G. Ambrosio: *"Nb_3Sn High Field Magnets for the High Luminosity LHC Upgrade Project"*. IEEE Transactions on Applied Superconductivity **25**.3 (2015), pp. 1–7. doi: `10.1109/TASC.2014.2367024` (cit. on p. 13).

[ANS] ANSYS: *Mechanical and Multiphysics simulation software by ANSYS Inc., Program Version 2029-R1*. url: `https://www.ansys.com` (cit. on p. 58).

[Apo+17] G. Apollinari, I. Bejar Alonso, O. Bruning, P. Fessia, M. Lamont, et al.: *"High-Luminosity Large Hadron Collider (HL-LHC): Technical Design Report V. 0.1"*. CERN Yellow Reports: Monographs. Geneva: CERN, 2017. doi: `10.23731/CYRM-2017-004` (cit. on pp. 5, 10, 12, 13).

[AGP08] D. Arbelaez, A. Godeke, and S. Prestemon: *"An improved model for the strain dependence of the superconducting properties of Nb3Sn"*. Superconductor Science and Technology **22** (2008), p. 025005. doi: `10.1088/0953-2048/22/2/025005` (cit. on p. 38).

[Bal19] B. J. Baliga: *"Fundamentals of Power Semiconductor Devices"*. Cham: Springer International Publishing, 2019. doi: `10.1007/978-3-319-93988-9` (cit. on pp. 83, 87, 88).

[BCS57] J. Bardeen, L. N. Cooper, and J. R. Schrieffer: *"Theory of Superconductivity"*. Physical Review **108**.5 (1957), pp. 1175–1204. doi: `10.1103/PhysRev.108.1175` (cit. on p. 25).

[BMS15] C. Barth, G. Mondonico, and C. Senatore: *"Electro-mechanical properties of REBCO coated conductors from various industrial manufacturers at 77 K, self-field and 4.2 K, 19 T"*. Superconductor Science and Technology **28**.4 (2015), p. 045011. doi: `10.1088/0953-2048/28/4/045011` (cit. on p. 41).

[Bar+18] C. Barth, B. Seeber, A. Rack, C. Calzolaio, Y. Zhai, et al.: *"Quantitative correlation between the void morphology of niobium-tin wires and their irreversible critical current degradation upon mechanical loading"*. Scientific Reports **8** (2018). doi: `10.1038/s41598-018-24966-z` (cit. on p. 40).

[Bau13] T. Baumgartner: *"Effects of fast neutron irradiation on critical currents and intrinsic properties of state-of-the-art Nb3Sn wires"*. PhD thesis. Technische Univeristaet (TU) Wien, Atominstitut, 2013. url: `https://repositum.tuwien.at/handle/20.500.12708/13224` (cit. on p. 37).

[Bea62] C. P. Bean: *"Magnetization of Hard Superconductors"*. Phys. Rev. Lett. **8** (6 1962), pp. 250–253. doi: `10.1103/PhysRevLett.8.250` (cit. on p. 28).

[Bea64] C. P. Bean: *"Magnetization of High-Field Superconductors"*. Rev. Mod. Phys. **36** (1 1964), pp. 31–39. doi: `10.1103/RevModPhys.36.31` (cit. on p. 28).

[Bej15] I. Bejar Alonso: "WP11 in a nutshell – 11T Dipoles". Overview report on HL-LHC WP11 activities. 2015. url: `https://edms.cern.ch/document/1559231/1.0` (cit. on p. 12).

[BP18] K. W. Boer and U. Pohl: *"Semiconductor physics"*. New York, NY: Springer Berlin Heidelberg, 2018 (cit. on pp. 83, 84).

[Böh+14] T. Böhlen, F. Cerutti, M. Chin, A. Fasso, A. Ferrari, et al.: *"The FLUKA Code: Developments and Challenges for High Energy and Medical Applications"*. Nuclear Data Sheets **120** (2014), pp. 211–214. doi: `10.1016/j.nds.2014.07.049` (cit. on pp. 16, 46, 48, 89).

[Bor+13] B. Bordini, P. Alknes, L. Bottura, L. Rossi, and D. Valentinis: *"An exponential scaling law for the strain dependence of the Nb $_3$ Sn critical current density"*. Superconductor Science and Technology **26**.7 (2013), p. 075014. doi: `10.1088/0953-2048/26/7/075014` (cit. on p. 39).

[Bor] B. Bordini: *Private communication with Dr. B. Bordini, CERN (TE-MSC-SCD), June 2018* (cit. on p. 46).

[Bot00] L. Bottura: *"A practical fit for the critical surface of NbTi"*. IEEE Transactions on Appiled Superconductivity **10**.1 (2000), pp. 1054–1057. doi: `10.1109/77.828413` (cit. on p. 31).

[BB09] L. Bottura and B. Bordini: *"$J_c(B,T,\varepsilon)$ Parameterization for the ITER Nb$_3$Sn Production"*. IEEE Transactions on Applied Superconductivity **19**.3 (2009), pp. 1521–1524. doi: `10.1109/TASC.2009.2018278` (cit. on p. 31).

[Bou+06] T. Boutboul, S. Le Naour, D. Leroy, L. Oberli, and V. Previtali: *"Critical Current Density in Superconducting Nb-Ti Strands in the 100 mT to 11 T Applied Field Range"*. IEEE Transactions on Applied Superconductivity **16**.2 (2006), pp. 1184–1187. doi: `10.1109/TASC.2006.870777` (cit. on p. 35).

[Bri11] M. Brice: *Pictures and panorama of the Tunnel HiRadMat*. 2011. url: `https://cds.cern.ch/record/1383880` (cit. on p. 8).

[Bru+04] O. Bruning, P. Collier, S. Lebrun P. and Myers, R. Ostojic, and P. Poole J. and Proudlock: *"LHC Design Report"*. CERN Yellow Reports: Monographs. Geneva: CERN, 2004. doi: `10.5170/CERN-2004-003-V-1` (cit. on pp. 6, 10, 34, 35, 91).

[Car98] J.-L. Caron: "LHC quadrupole cross section". AC Collection. Legacy of AC. Pictures from 1992 to 2002. 1998. url: `http://cds.cern.ch/record/841485` (cit. on p. 11).

[CER] CERN: *News website, news from 10th April 2017 by Harriet Jarlett, " What happened while the LHC slept over winter? A round up of the upgrades and maintenance during the 2016/2017 extended year-end technical stop"*. url: `https://home.cern/news/news/cern/what-happened-while-lhc-slept-over-winter` (cit. on p. 96).

[CHA] CHARM: *Facility website*. url: `http://charm.web.cern.ch/` (visited on 11/2019) (cit. on pp. 1, 8).

[CM09] L. Charnay and V. Montabonnet: *LHC13kA-18V Main Quadrupole Circuit Power Converter*. 2009. url: `https://edms.cern.ch/document/973221/2` (cit. on p. 18).

[Che+10] N. Cheggour, L. F. Goodrich, T. C. Stauffer, J. D. Splett, X. F. Lu, et al.: *"Influence of Ti and Ta doping on the irreversible strain limit of ternary Nb3Sn superconducting wires made by the restacked-rod process"*. Superconductor Science and Technology **23**.5 (2010), p. 052002. doi: `10.1088/0953-2048/23/5/052002` (cit. on p. 40).

[Che+19] N. Cheggour, T. C. Stauffer, W. Starch, L. F. Goodrich, and J. D. Splett: *"Implications of the strain irreversibility cliff on the fabrication of particle-accelerator magnets made of restacked-rod-process* Nb_3Sn *wires"*. Scientific Reports **9**.1 (2019), p. 5466. doi: `10.1038/s41598-019-41817-7` (cit. on p. 40).

[Col08a] T. A. Collaboration: *"The ATLAS Experiment at the CERN Large Hadron Collider"*. Journal of Instrumentation **3**.08 (2008), S08003–S08003. doi: `10.1088/1748-0221/3/08/s08003` (cit. on p. 12).

[Col08b] T. C. Collaboration: *"The CMS experiment at the CERN LHC"*. Journal of Instrumentation **3**.08 (2008), S08004–S08004. doi: `10.1088/1748-0221/3/08/s08004` (cit. on p. 12).

[COM] COMSOL: *Multiphysics v. 5.4. COMSOL AB,* Stockholm, Sweden. url: `www.comsol.com` (cit. on pp. 104–106).

[Dai99] S. Dailler: "Cross section of LHC dipole / Dipole LHC: coupe transversale." AC Collection. Legacy of AC. Pictures from 1992 to 2002. 1999. url: `https://cds.cern.ch/record/842530` (cit. on p. 11).

[Dav11] A. Davies: *Material properties data for heat transfer modeling in* Nb_3Sn *magnets*. Internship Report Ilinois Acceleration Institute. 2011. url: `https://eddata.fnal.gov/lasso/summerstudents/papers/2011/Davies.pdf` (visited on 11/04/2020) (cit. on pp. 48, 61).

[Den04a] W. Denis Markiewicz: *"Invariant formulation of the strain dependence of the critical temperature Tc of Nb3Sn in a three term approximation"*. Cryogenics **44**.12 (2004), pp. 895–908. doi: `10.1016/j.cryogenics.2004.06.004` (cit. on p. 39).

[Den04b] R. Denz: *"Radiation Resistance and Life Time Estimates at Cryogenic Temperatures of Series Produced By-Pass Diodes for the LHC Magnet Protection"*. *AIP Conference Proceedings*. Vol. 711. Anchorage, Alaska (USA): AIP, 2004, pp. 763–772. doi: `10.1063/1.1774640` (cit. on pp. 95, 108, 111).

[DH00] R. Denz and D. Hagedorn: "Expected Lifetime of By-Pass Diodes for the LHC Magnet Protection Subjected to Liquid Helium Temperatures and Irradiation". *Advances in Cryogenic Engineering Materials*. Ed. by U. B. Balachandran, K. T. Hartwig, D. U. Gubser, and V. A. Bardos. Boston, MA: Springer US, 2000, pp. 375–382. doi: `10.1007/978-1-4615-4293-3_48` (cit. on p. 95).

[Dre19] A. Drees: *RHIC quench diode radiation damage*. Tech. rep. BNL-211674-2019-COPA. Brookhaven National Lab. (BNL), Upton, NY (United States), 2019. url: `https://www.osti.gov/biblio/1561260` (visited on 10/07/2020) (cit. on p. 91).

[Dyn] Dynex: *Dynex Semiconductor Ltd. (Lincoln, GB)*. url: `https://dynexsemi.com/` (cit. on p. 100).

[Ebe+18] P. Ebermann, J. Bernardi, J. Fleiter, F. Lackner, F. Meuter, et al.: *"Irreversible degradation of Nb3Sn Rutherford cables due to transverse compressive stress at room temperature"*. Superconductor Science and Technology **31**.6 (2018), p. 065009. doi: `10.1088/1361-6668/aab5fa` (cit. on pp. 40, 41).

[Eft+11] I. Efthymiopoulos, C. Hessler, H. Gaillard, D. Grenier, M. Meddahi, et al.: *"HiRadMat: A New Irradiation Facility for Material Testing at CERN"*. *Proceedings of the 2nd International Particle Accelerator Conference*. IPAC 2011 (San Sebastian, Spain). 2011. url: `https://accelconf.web.cern.ch/IPAC2011/papers/tups058.pdf` (cit. on pp. 1, 7, 8).

[Eki87] J. Ekin: *"Relationships between critical current and stress in NbTi"*. IEEE Transactions on Magnetics **23**.2 (1987), pp. 1634–1637. doi: `10.1109/TMAG.1987.1064844` (cit. on p. 34).

[Eki78] J. W. Ekin: *"Current transfer in multifilamentary superconductors. I. Theory"*. Journal of Applied Physics **49**.6 (1978), pp. 3406–3409. doi: `10.1063/1.325245` (cit. on p. 27).

[Eki80] J. W. Ekin: *"Strain scaling law for flux pinning in practical superconductors. Part 1: Basic relationship and application to Nb3Sn conductors"*. Cryogenics **20**.11 (1980), pp. 611–624. doi: `https://doi.org/10.1016/0011-2275(80)90191-5` (cit. on pp. 31, 38).

[Eki06] J. Ekin: *"Experimental Techniques for Low-Temperature Measurements"*. Oxford University Press, 2006. doi: `10.1093/acprof:oso/9780198570547.001.0001` (cit. on pp. 28, 38).

[Evr+11] S. Evrard et al.: *HiRadMat safety file - Descriptive part*. 2011. url: `https://edms.cern.ch/document/1145711/3` (cit. on pp. 1, 7, 8).

[FA+] P. Ferracin, G. Ambrosio, et al.: *Cross section of the inner quadrupole triplet magnets (MQXF)*. url: `https://edms.cern.ch/document/1865374/5` (cit. on p. 13).

[Fer+14] P. Ferracin, G. Ambrosio, M. Anerella, F. Borgnolutti, R. Bossert, et al.: *"Magnet Design of the 150 mm Aperture Low-β Quadrupoles for the High Luminosity LHC"*. IEEE Transactions on Applied Superconductivity **24**.3 (2014), pp. 1–6. doi: `10.1109/TASC.2013.2284970` (cit. on p. 5).

[FA18] P. Ferracin and M. Anerella: *"The HL-LHC Low-beta Quadrupole Magnet MQXF: From Short Models to Long Prototypes"*. Brookhaven National Lab. (BNL), Report number BNL-211583-2019-CPPJ (2018). url: `https://www.osti.gov/biblio/1524523` (cit. on p. 38).

[Fer18] J. Ferradas: *Electromechanical characterization of Nb3Sn conductors at University of Geneva*. Workshop on Nb3Sn technology for accelereator magnets, Paris, contribution 3154561. 2018. url: `https://indico.cern.ch/event/743626/contributions/3154561/` (cit. on pp. 40, 61).

[Fer+05] A. Ferrari, P. R. Sala, A. Fassò, and J. Ranft: *"FLUKA: A multi-particle transport code"*. CERN Yellow Reports: Monographs. Geneva: CERN, 2005. doi: `10.5170/CERN-2005-010` (cit. on pp. 16, 46, 48, 89).

[FC17] S. Fields and L. Carver: *"Analyzing the LHC Magnet Quenches"*. IEEE Spectrum (2017). url: `https://spectrum.ieee.org/computing/software/analyzing-the-lhc-magnet-quenches` (cit. on p. 5).

[Flo+07] E. Floch, E. Mustafin, G. Moritz, H. Ramakers, A. Golubev, et al.: *"Irradiation of Bypass Diodes up to 2.2E14 Neutron cm^2 and 1.3 kGy for the FAIR Project"*. IEEE Transactions on Applied Superconductivity **17**.2 (2007), pp. 2462–2465. doi: `10.1109/TASC.2007.897854` (cit. on pp. 95, 108, 111).

[Gar+18] R. Garcia Alia, M. Brugger, F. Cerutti, S. Danzeca, A. Ferrari, et al.: *"LHC and HL-LHC: Present and Future Radiation Environment in the High-Luminosity Collision Points and RHA Implications"*. IEEE Transactions on Nuclear Science **65**.1 (2018), pp. 448–456. doi: `10.1109/TNS.2017.2776107` (cit. on pp. 6, 96).

[Gha+04] A. Gharib, D. Hagedorn, A. Della Corte, C. Fiamozzi Zignani, S. Turtu, et al.: *"Cryogenic Testing of High Current By-Pass Diode Stacks for the Protection of the Superconducting Magnets in the LHC"*. *AIP Conference Proceedings*. Vol. 711. Anchorage, Alaska (USA): AIP, 2004, pp. 755–762. doi: `10.1063/1.1774639` (cit. on p. 95).

[God06] A. Godeke: *"Performance boundaries in Nb3Sn superconductors"*. PhD thesis. University of Twente, Enschede, The Netherlands, 2006 (cit. on pp. 31, 35, 37).

[God+13] A. Godeke, G. Chlachidze, D. Dietderich, A. Ghosh, M. Marchevsky, et al.: *"A review of conductor performance for the LARP high-gradient quadrupole magnets"*. Superconductor Science and Technology **26** (2013), p. 095015. doi: `10.1088/0953-2048/26/9/095015` (cit. on p. 28).

[God+06] A. Godeke, B. ten Haken, H. ten Kate, and D. C. Larbalestier: *"A general scaling relation for the critical current density in Nb3Sn"*. Superconductor science and technology **19**.10 (2006). A review article, pp. 100–116. doi: `10.1088/0953-2048/19/10/R02` (cit. on pp. 32, 38).

[God+09] A. Godeke, D. Turrioni, T. Boutboul, N. Cheggour, L. F. Goodrich, et al.: *"Interlaboratory Comparisons of NbTi Critical Current Measurements"*. IEEE Transaction on Applied Superconductivity **19**.3 (2009). doi: `10.1109/TASC.2009.2019096` (cit. on p. 35).

[Goo+11] L. Goodrich, N. Cheggour, X. Lu, J. Splett, T. Stauffer, et al.: *"Method for determining the irreversible strain limit of Nb3Sn wires"*. Superconductor Science and Technology **24** (2011), p. 075022. doi: `10.1088/0953-2048/24/7/075022` (cit. on p. 40).

[GF82] L. F. Goodrich and F. R. Fickett: *"Critical current measurements: a compendium of experimental results"*. Cryogenics; (United Kingdom) **22:5** (1982). doi: `10.1016/0011-2275(82)90120-5` (cit. on p. 28).

[GHT01] F. Guarino, C. Hauviller, and M. Tavlet: *"Compilation of radiation damage test data"*. CERN Yellow Reports: Monographs. Geneva: CERN, 2001. doi: `10.5170/CERN-2001-006` (cit. on p. 17).

[Har17] F. Hartmann: *"Evolution of Silicon Sensor Technology in Particle Physics"*. 2nd ed. 2017. Springer Tracts in Modern Physics vol. 275; Springer eBook Collection. Cham: Springer, 2017. url: `https://doi.org/10.1007/978-3-319-64436-3` (cit. on pp. 83, 85, 89).

[Has] Hastelloy: *Hastelloy® mechanical properties, Haynes International Website.* url: `http://www.haynesintl.com/alloys/alloy-portfolio_/High-temperature-Alloys/haynes-r-41-alloy/elastic-modulus` (cit. on p. 41).

[HiR] HiRadMat: *Irradiation facility website.* url: `https://espace.cern.ch/hiradmat-sps/Wiki%20Pages/Home.aspx` (visited on 11/2020) (cit. on pp. 1, 7, 8).

[HA01] A. G. Holmes-Siedle and L. Adams: *"Handbook of radiation effects"*. 2nd ed. Oxford ; New York: Oxford University Press, 2001 (cit. on pp. 83, 90).

[Hol+12] E. B. Holzer, B. Dehning, E. Effnger, J. Emery, V. Grishin, et al.: *"Beam Loss Monitoring for LHC Machine Protection"*. Physics Procedia **37** (2012). Proceedings of the 2nd International Conference on Technology and Instrumentation in Particle Physics (TIPP 2011), pp. 2055–2062. doi: `https://doi.org/10.1016/j.phpro.2012.04.110` (cit. on p. 17).

[IEC] IEC 61788. Norms and standards on various procedures for e.g. critical current measurements of Nb-Ti, Nb_3Sn and critical temperature and RRR measurements. (cit. on p. 28).

[Inf17] A. Infantino: *"FLUKA Monte Carlo Modelling of the CHARM Facility's Test Area: Update of the Radiation Field Assessment"*. CERN-ACC-NOTE-2017-0059 (2017). url: `https://cds.cern.ch/record/2291683/files/ATS_Note_Infantino_v1.0.pdf` (cit. on pp. 1, 8, 9).

[IFK18] A. Infantino, R. Froeschl, and M. Krawina: *"R2E and RP FLUKA simulations for the CHARM cryo-cooler test"*. CERN-EDMS-1907770 internal report (2018) (cit. on pp. 103, 107).

[Jew08] M. Jewell: *"The effect of strand architecture on the fracture propensity on niobium-tin composite wires"*. PhD thesis. University of Wisconsin - Madison, 2008. url: `https://fs.magnet.fsu.edu/~lee/asc/pdf_papers/theses/mcj08phd.pdf` (cit. on pp. 40, 66).

[KHS63] Y. B. Kim, C. F. Hempstead, and A. R. Strnad: *"Magnetization and Critical Supercurrents"*. Phys. Rev. **129** (2 1963), pp. 528–535. doi: `10.1103/PhysRev.129.528` (cit. on p. 28).

[Kul18] K. Kulesz: *"Damage limits of superconducting magnet components due to beam impact and exposition to high temperature"*. Master Thesis. Warsaw University of Technology, Poland, 2018. url: `https://cds.cern.ch/record/2637241` (cit. on pp. 58, 76).

[Lec18] A. Lechner: *"Particle interactions with matter"*. CERN Yellow Reports: School Proceedings **Vol 5** (2018), 47 Pages. doi: `10.23730/CYRSP-2018-005.47` (cit. on pp. 15–17).

[LL03] P. Lee and D. Larbalestier: *"Niobium-Titanium Superconducting Wires: Nanostructures by Extrusion and Wire Drawing"*. Wire Journal International **36** (2003), pp. 61–66 (cit. on p. 34).

[LML88] P. Lee, J. Mckinnell, and D. Larbalestier: *"Progress in the Understanding and Manipulation of Microstructure in High Jc Nb-Ti Alloy Composites". Proceedings of the International Symposium on new Developments in Applied Superconductivity* (Osaka, Japan). Vol. 15. 1988 (cit. on p. 34).

[Ler+19] G. Lerner, R. Garcia Alia, M. Sabate Gilarte, A. Tsinganis, and F. Cerutti: *Update on HL-LHC radiation levels on equipment in the IP1-IP5 LSS*. Presentation at the 9th HL-LHC Collaboration Meeting, Fermilab, USA. 15. October 2019. url: `https://indico.cern.ch/event/806637/contributions/3574371/` (cit. on pp. 6, 96).

[LR16] C. Leroy and P.-G. Rancoita: *"Principles of radiation interaction in matter and detection"*. 4th edition. New Jersey: World Scientific, 2016 (cit. on pp. 15, 83, 85, 87, 89, 92, 93).

[LR12] C. Leroy and P.-G. Rancoita: *"Silicon solid state devices and radiation detection"*. New Jersey [u.a.]: World Scientific, 2012. doi: `10.1142/8383` (cit. on pp. 16, 83, 87, 93).

[LG17] Y. Li and Y. Gao: *"GLAG theory for superconducting property variations with A15 composition in Nb3Sn wires"*. Scientific Reports **7** (2017), p. 1133. doi: `10.1038/s41598-017-01292-4` (cit. on p. 61).

[LL35] F. London and H. London: *"The electromagnetic equations of the supraconductor"*. Proceedings of the Royal Society of London. Series A - Mathematical and Physical Sciences **149**.866 (1935), pp. 71–88. doi: `10.1098/rspa.1935.0048` (cit. on p. 23).

[Lub82] M. S. Lubell: *Empirical scaling formulas for critical current and critical field for commercial NbTi*. 1982. url: `https://digital.library.unt.edu/ark:/67531/metadc1071027/` (visited on 10/28/2020) (cit. on p. 31).

[Mar08] D. Markiewicz: *"Comparison of strain scaling functions for the strain dependence of composite Nb3Sn superconductors"*. Superconductor Science and Technology **21**.5 (2008), p. 054004. doi: `10.1088/0953-2048/21/5/054004` (cit. on p. 39).

[Mar04] W. Markiewicz: *"Elastic stiffness model for the critical temperature Tc of Nb3Sn including strain dependence"*. Cryogenics **44**.11 (2004), pp. 767–782. doi: `10.1016/j.cryogenics.2004.03.019` (cit. on p. 39).

[MLL89] C. Meingast, P. J. Lee, and D. C. Larbalestier: *"Quantitative description of a high J_c Nb-Ti superconductor during its final optimization strain. I. Microstructure, T_c , H_{c2} , and resistivity"*. Journal of Applied Physics **66**.12 (1989), pp. 5962–5970. doi: `10.1063/1.343624` (cit. on p. 34).

[Men08] M. G. T. Mentink: *"Critical surface parameterization of high J_c RRP Nb_3Sn strand"*. Internship report. University of Twente / Lawrence Berkeley National Laboratory, 2008 (cit. on p. 31).

[Men14] M. G. T. Mentink: *"An experimental and computational study of strain sensitivity in superconducting Nb3Sn"*. PhD thesis. Netherlands: University of Twente, 2014. doi: `10.3990/1.9789036536356` (cit. on pp. 31, 35, 39).

[Meya] M. Meyer: *CERN, Electron- and optical microscopy analysis at the EN-MME-MM microscopy Laboratory.* (Cit. on pp. 36, 38, 72).

[Meyb] M. Meyer: *Technical report on the microscopical "characterization of Nb3Sn strands impacted at 4K by proton beam [of] 440GeV"*. CERN - EN-MME-MM microscopy Laboratory. url: `https://edms.cern.ch/document/2363700/1` (cit. on pp. 73–75, 77).

[Mit05] N. Mitchell: *"Finite element simulations of elasto-plastic processes in Nb3Sn strands"*. Cryogenics **45**.7 (2005), pp. 501–515. doi: `https://doi.org/10.1016/j.cryogenics.2005.06.003` (cit. on p. 61).

[Mob19] E. Mobs: *"The CERN accelerator complex - 2019. Complexe des accélérateurs du CERN - 2019"* (2019). General Photo. url: `https://cds.cern.ch/record/2684277` (cit. on p. 7).

[NIA08] A. Nijhuis, Y. Ilyin, and W. Abbas: *"Axial and transverse stress-strain characterization of the EU dipole high current density Nb3Sn strand"*. Superconductor Science and Technology **21**.6 (2008), p. 065001. doi: `10.1088/0953-2048/21/6/065001` (cit. on p. 64).

[Oom00] M. Oomen: *"AC loss in superconducting tapes and cables"*. PhD thesis. Netherlands, 2000. url: `https://research.utwente.nl/en/publications/ac-loss-in-superconducting-tapes-and-cables` (cit. on p. 29).

[Osa93] K. Osamura, ed.: *"Composite superconductors"*. Applied physics 3. New York: CRC press, 1993 (cit. on p. 34).

[OWW18] A. Oslandsbotn, A. Will, and D. Wollmann: *Beam Impact on Superconductor short samples of Nb3Sn, Nb-Ti and YBCO*. CERN internal report, TE-MPE-PE. 2018. url: `https://edms.cern.ch/document/2068064/1` (cit. on pp. 45, 47–50, 78, 126).

[Ott+15] S. Otten, M. Dhalle, P. Gao, W. Wessel, A. Kario, et al.: *"Enhancement of the transverse stress tolerance of REBCO Roebel cables by epoxy impregnation"*. Superconductor Science and Technology **28**.6 (2015), p. 065014. doi: `10.1088/0953-2048/28/6/065014` (cit. on p. 41).

[PI13] E. Pavarini and Institute for Advanced Simulation, eds.: *"Emergent phenomena in correlated matter: lecture notes of the Autumn School Correlated Electrons 2013 at Forschungszentrum Jülich, 23 – 27 September 2013"*. Schriften des Forschungszentrums Jülich Reihe Modeling and Simulation 3. OCLC: 862816584. Jülich: Forschungszentrum Jülich, 2013. url: `https://www.cond-mat.de/events/correl13/` (cit. on p. 26).

[Pfe20] S. Pfeiffer: *"The Microstructure of Nb_3Sn Superconductors for the Future Circular Collider Project and its Impact on the Performance"*. PhD thesis. Technical University (TU) of Vienna, 2020. url: `https://repositum.tuwien.at/handle/20.500.12708/15545` (cit. on p. 72).

[Prz68] J. S. Przybyszewski: *"Stress-Strain Behavior of Cold-Welded Copper-Copper Microjunctions in Vacuum as determined from electrical Resistance Measurements"*. NASA Technical Note D-4743 (1968). url: `https://ntrs.nasa.gov/citations/19680022045` (cit. on p. 61).

[Rag+17] V. Raginel et al.: *"Change of Critical Current Density in Nb-Ti and Nb3Sn Strands After Millisecond Heating"*. *Proc. of International Particle Accelerator Conference (IPAC'17), Copenhagen, Denmark, 14-19 May, 2017* (Copenhagen, Denmark). International Particle Accelerator Conference 8. Geneva, Switzerland: JACoW, 2017, pp. 3528–3531. doi: `https://doi.org/10.18429/JACoW-IPAC2017-WEPVA111` (cit. on p. 43).

[Rag+18] V. Raginel, M. Bonura, D. Kleiven, K. Kulesz, M. Mentink, et al.: *"First Experimental Results on Damage Limits of Superconducting Accelerator Magnet Components Due to Instantaneous Beam Impact"*. IEEE Trans. Appl. Supercond. **28**.4 (2018), p. 8800310. doi: `10.1109/TASC.2018.2817346` (cit. on pp. 43, 52).

[Rag18] V. Raginel: *"Study of the Damage Mechanisms and Limits of Superconducting Magnet Components due to Beam Impact"*. Presented 04 Jul 2018. PhD thesis. 2018. url: `https://cds.cern.ch/record/2628622` (cit. on pp. 43–45, 58, 76).

[Rav15] E. Ravaioli: *"CLIQ: a new quench protection technology for superconducting magnets"*. OCLC: 911393946. PhD thesis. Enschede: University of Twente, 2015 (cit. on pp. 19, 98).

[RGM05] F. Ravotti, M. Glaser, and M. Moll. CERN Report TS-Note-2005-002 (2005). url: `https://edms.cern.ch/document/590497/1` (visited on 04/17/2020) (cit. on p. 107).

[Ros03] L. Rossi: *"Proceedings of the 2003 Particle Accelerator Conference, Postland, Oregon U.S.A., May 12-16, 2003"*. Portland, OR, USA: IEEE, 2003. url: `https://accelconf.web.cern.ch/p03/papers/toab001.pdf` (cit. on p. 10).

[Rou18] C. Rout: *Data extracted from an internal report of Dynex Semiconductor Ltd. (Lincoln, GB).* 2018 (cit. on p. 100).

[Rus10] S. Russenschuck: *"Field computation for accelerator magnets : analytical and numerical methods for electromagnetic design and optimization"*. Weinheim: Wiley-VCH, 2010 (cit. on p. 10).

[San17] C. Sanabria: *"A new understanding of the heat treatment of Nb3Sn superconducting wires"*. PhD thesis. Florida State University, Tallahassee, USA, 2017 (cit. on pp. 35, 37).

[Sch+15] C. Scheuerlein, B. Fedelich, P. Alknes, G. Arnau, R. Bjoerstad, et al.: *"Elastic Anisotropy in Multifilament Nb3Sn Superconducting Wires"*. IEEE Transactions on Applied Superconductivity **25**.3 (2015), pp. 1–5. doi: `10.1109/TASC.2014.2371693` (cit. on pp. 39, 40, 61).

[Sch+10] C. Scheuerlein, I. Pong, C. Senatore, M. Di Michiel, L. Thilly, et al.: *"Temperature Induced Degradation of Nb Ti/Cu Composite Superconductors"*. Journal of Physics Conference Series **234** (2010). doi: `10.1088/1742-6596/234/2/022031` (cit. on p. 43).

[SW04] R. Schmidt and J. Wenninger: *"Machine Protection Issues and Strategies for the LHC"*. LHC-Project-Report-784. CERN-LHC-Project-Report-784 (2004). url: `https://cds.cern.ch/record/794624` (cit. on pp. 16, 17).

[SZ19] D. Schoerling and A. V. Zlobin, eds.: *"Nb3Sn Accelerator Magnets: Designs, Technologies and Performance"*. Particle Acceleration and Detection. Cham: Springer International Publishing, 2019. doi: `10.1007/978-3-030-16118-7` (cit. on pp. 9, 10, 12, 29, 30, 35, 37, 38).

[Sch06] D. K. Schroder: *"Semiconductor material and device characterization"*. 3rd ed. OCLC: ocm59360243. [Piscataway, NJ] : Hoboken, N.J: IEEE Press ; Wiley, 2006 (cit. on p. 83).

[Sch20] J. Schubert: *"Damage Study on Single Strand Nb3Sn - Ultra-Fast Beam Impact in Cryogenic Environment, Simulation with Finite Element Method"*. Bachelor Thesis. University of Jena, Germany, 2020 (cit. on pp. 61, 62, 67, 126).

[Sek+04] T. Sekitani, N. Miura, S. Ikeda, Y. Matsuda, and Y. Shiohara: *"Upper critical field for optimally-doped $YBa_2Cu_3O_{7-\delta}$"*. Physica B: Condensed Matter **346-347** (2004). Proceedings of the 7th International Symposium on Research in High Magnetic Fields, pp. 319–324. doi: `https://doi.org/10.1016/j.physb.2004.01.098` (cit. on p. 41).

[Sen+15] C. Senatore, C. Barth, M. Bonura, M. Kulich, and G. Mondonico: *"Field and temperature scaling of the critical current density in commercial REBCO coated conductors"*. Superconductor Science and Technology **29**.1 (2015). doi: `10.1088/0953-2048/29/1/014002` (cit. on p. 41).

[Sho49] W. Shockley: *"The Theory of p-n Junctions in Semiconductors and p-n Junction Transistors"*. Bell System Technical Journal **28**.3 (1949), pp. 435–489. doi: `10.1002/j.1538-7305.1949.tb03645.x` (cit. on p. 86).

[SDR92] N. J. Simon, E. S. Drexler, and R. P. Reed: *"Properties of copper and copper alloys at cryogenic temperatures. Final report"* (1992). NIST monograph 177 (cit. on p. 61).

[Sum] Sumitomo: *SHI Cryogenics Group, Website*. url: `http://www.shicryogenics.com/products/pulse-tube-cryocoolers/rp-082b2-4k-pulse-tube-cryocooler-series/` (visited on 04/17/2020) (cit. on p. 105).

[Sum+91] L. Summers, M. Guinan, J. Miller, and P. Hahn: *"A model for the prediction of Nb3Sn critical current as a function of field, temperature, strain, and radiation damage"*. IEEE Transactions on Magnetics **27**.2 (1991), pp. 2041–2044. doi: `10.1109/20.133608` (cit. on p. 31).

[TH05] D. M. J. Taylor and D. P. Hampshire: *"The scaling law for the strain dependence of the critical current density in Nb3Sn superconducting wires"*. Superconductor Science and Technology **18**.12 (2005), S241–S252. doi: `10.1088/0953-2048/18/12/005` (cit. on p. 39).

[tGt95] B. ten Haken, A. Godeke, and H. ten Kate: *"The Influence of Compressive and Tensile Axial Strain on the Critical Properties of Nb3Sn Conductors"*. IEEE transactions on applied superconductivity **5**.5 (1995), pp. 1909–1912. doi: `10.1109/77.402955` (cit. on p. 38).

[Tho+16] A. Thornton, J. Mekki, M. Brugger, R. G. Alia, N. C. D. S. Mota, et al.: *"CHARM: A Mixed Field Facility at CERN for Radiation Tests in Ground, Atmospheric, Space and Accelerator Representative Environments"*. IEEE Transactions on Nuclear Science **63**.4 (2016), pp. 2106–2114. doi: `10.1109/TNS.2016.2528289` (cit. on pp. 1, 8).

[Tho16] A. Thornton: *"CHARM Facility Test Area Radiation Field Description"* (2016). url: `https://cds.cern.ch/record/2149417` (cit. on pp. 1, 8, 9, 104).

[Tin04] M. Tinkham: *"Introduction to superconductivity"*. 2. ed. Dover books on physics. OCLC: 728146785. Mineola, NY: Dover Publ, 2004 (cit. on pp. 23–25).

[Tod] E. Todesco: *Layout of the inner triplet strings*. Image from "HiLumi LHC Work Package 3 - Magnets for Insertion Regions" HiLumi Intranet Website. url: `https://espace.cern.ch/HiLumi/WP3/SitePages/Home.aspx` (cit. on p. 13).

[Uni] University of Geneva (UniGe): *Department of Quantum matter Physics (DQMP), Group of applied Superconductivity, Prof. C. Senatore, M. Bonura, D. Zurmuehle, C. Barth, et al.* (Cit. on pp. 51, 54).

[Uso+19] A. Usoskin, U. Betz, J. Gnilsen, S. Noll-Baumann, and K. Schlenga: *"Long-length YBCO coated conductors for ultra-high field applications: gaining engineering current density via pulsed laser deposition/alternating beam-assisted deposition route"*. Superconductor Science and Technology **32**.9 (2019). doi: `10.1088/1361-6668/ab2cba` (cit. on pp. 41, 42).

[Uso+18] A. Usoskin, C. Senatore, A. Kario, W. Goldacker, A. Meledin, et al.: *"Double-Disordered HTS-Coated Conductors and Their Assemblies Aimed for Ultra-High Fields: Large Area Tapes"*. IEEE Transactions on Applied Superconductivity **28**.4 (2018), pp. 1–6. doi: `10.1109/TASC.2018.2801348` (cit. on p. 41).

[Van11] B. Van Zeghbroeck: *"Principles of Semiconductor Devices. Chapter 2.7.2.2, Fig. 2.7.4, Resistivity of n-type and p-type silicon versus doping density."* University of Colorado - online resource, 2011. url: `https://ecee.colorado.edu/~bart/book/contents.htm` (visited on 04/07/2021) (cit. on pp. 99, 100).

[VU77] V. S. Vavilov and N. A. Ukhin: *"Radiation Effects in Semiconductors and Semiconductor Devices"*. Boston, MA: Springer US, 1977. doi: `10.1007/978-1-4684-9069-5` (cit. on pp. 83, 88).

[WR96] K. Wang and R. Reeber: *"Thermal Expansion of Copper"*. High Temperature and Materials Science **35** (1996), pp. 181–186 (cit. on p. 61).

[Wil+18] A. Will, D. Wollmann, A. Bernhard, G. D'Angelo, R. Denz, et al.: *"Experimental Setup to Characterize the Radiation Hardness of Cryogenic Bypass Diodes for the HL-LHC Inner Triplet Circuits"*. *Proceedings of the 9th International Particle Accelerator Conference*. IPAC 2018 (Vancouver, Kanada). JACoW Publishing, Geneva, 2018. doi: `10.18429/JACoW-IPAC2018-WEPMG006` (cit. on pp. 96, 99).

[Wil+20a] A. Will, D. Wollmann, G. D'Angelo, R. Denz, D. Hagedorn, et al.: *"Characterization of the radiation tolerance of cryogenic diodes for the High Luminosity LHC inner triplet circuit"*. Phys. Rev. Accel. Beams **23** (5 2020), p. 053502. doi: `10.1103/PhysRevAccelBeams.23.053502` (cit. on pp. 95, 97–99, 102, 110–112, 114–121).

[Wil+19] A. Will, D. Wollmann, A. Oslandsbotn, Y. Bastian, A. Bernhard, et al.: *"Beam Impact Experiment of 440GeV/p Protons on Superconducting Wires and Tapes in a Cryogenic Environment". Proceedings of the 10th International Particle Accelerator Conference*. IPAC 2019 (Melbourne, Australien). JACoW Publishing, Geneve, 2019. doi: `10.18429/JACoW-IPAC2019-THPTS066` (cit. on pp. 45, 47, 49).

[Wil+20b] A. Will, D. Wollmann, J. Schubert, A. Bernhard, M. Bonura, et al.: *"Impact of 440 GeV Proton beams on Superconductors in a Cryogenic Environment"*. Journal of Physics: Conference Series **1559** (2020), p. 012060. doi: `10.1088/1742-6596/1559/1/012060` (cit. on pp. 45, 52, 53, 55, 59, 60).

[Wil+15] G. Willering, C. Giloux, M. Bajko, M. Bednarek, L. Bottura, et al.: *"Performance of the cold powered diodes and diode leads in the main magnets of the LHC"*. IOP Conference Series: Materials Science and Engineering **101** (2015), p. 012076. doi: `10.1088/1757-899X/101/1/012076` (cit. on pp. 95, 96).

[Wil96] M. N. Wilson: *"Superconducting materials for magnets"* (1996). doi: `10.5170/CERN-1996-003.47` (cit. on p. 29).

[WW97] M. Wilson and R. Wolf: *"Calculation of minimum quench energies in Rutherford cables"*. IEEE Transactions on Appiled Superconductivity **7**.2 (1997), pp. 950–953. doi: `10.1109/77.614662` (cit. on p. 27).

[Wol+19] D. Wollmann, A. Will, A. Bernhard, C. Cangialosi, F. Cerutti, et al.: *"Characterisation of the radiation hardness of cryogenic bypass diodes for the HL-LHC inner triplet circuit". Proceedings of the 10th International Particle Accelerator Conference*. IPAC 2019 (Melbourne, Australien). JACoW Publishing, Geneva, 2019. doi: `10.18429/JACoW-IPAC2019-THPTS067` (cit. on p. 99).

[XTG95] Y. Xu, M. Tu, and P. J. Gielisse: *"Determination of the thermal expansion of Nb3Sn superconducting composites by digital microimage processing"*. Ed. by J. D. Hodge. San Diego, CA, United States, 1995, p. 69. doi: `10.1117/12.218166` (cit. on p. 40).

[Zho+14] C. Zhou, M. Dhalle, H. H. J. ten Kate, and A. Nijhuis: *"Current transfer length in multi-filamentary superconducting NbTi and Nb $_3$ Sn strands; experiments and models"*. Superconductor Science and Technology **27**.9 (2014), p. 095014. doi: `10.1088/0953-2048/27/9/095014` (cit. on p. 27).

A Appendices

A.1 Cryogenic diode scaling parameters

Source code A.1 – The fit-parameters obtained for diodes D1, D2, D3 and D4 are shown in a Python list syntax. Fit-results for both linear and exponential saturation current model are listed.

```
# Parameters read as:
# [ KIl, Is0, Vt0, KRse, Rs0e, KRsh, Rs0h ]

# Exp-model
FitCoeffsExp = [
[-9.68e-15,1.04e-01,1.85e+01,3.15e-18,3.97e-06,1.52e-19,5.73e-05],#D1
[-3.55e-15,3.35e-01,2.16e+01,2.61e-18,-7.01e-07,6.81e-20,5.06e-05],#D2
[-1.3e-15,3.15e-01,2.16e+01,2.66e-18,-2.10e-06,3.7e-20,4.42e-05],#D3
[-1.49e-15,3.43e-01,2.18e+01,2.63e-18,-1.98e-06,4.21e-20,4.53e-05],#D4
]

# Lin-model
FitCoeffsLin = [
[-3.67e-16,8.66e-02,1.87e+01,2.e-18,5.94e-06,6.50e-20,7.96e-05],#D1
[-8.09e-16,3.20e-01,2.15e+01,2.42e-18,-1.69e-07,5.55e-20,5.34e-05],#D2
[-3.49e-16,3.12e-01,2.16e+01,2.63e-18,-2.03e-06,3.58e-20,4.45e-05],#D3
[-4.27e-16,3.39e-01,2.18e+01,2.58e-18,-1.87e-06,4.03e-20,4.57e-05],#D4
]
```

Source code A.2 – Numerical implementation in Python of the components of the Shockley Equation as in Eqs. (6.12,6.23,6.31,8.4). The functions were used both to fit the measured data and to interpolate or calculate the diode forward characteristics at 77 K as a function of current and 1 MeV neq. fluence.

```
import numpy as np

# ======= Functions and constants ======= #

kB = 1.38064852e-23
e = 1.602e-19


# == Series Resistance
def Rsf(params, phi):
    KRse, Rs0e, KRsh, Rs0h = params
    Rs = 1/( np.power(Rs0e + KRse*phi,-1) + np.power(Rs0h + KRsh*phi,-1) )
    return Rs


# == Saturation Current lin.
def Is_lin(params, phi):
    KIl, Is0 = params
    Is = Is0 + KIl*phi
    return Is


# == Saturation Current exp.
def Is_exp(params, phi):
    KIl, Is0 = params
    Is = Is0*np.exp(KIl*phi)
    return Is


# == Shockley forward voltage
def Uff(params, phi, I):
    KIl, Is0, Vt0, KRse, Rs0e, KRsh, Rs0h = params

    Rs = Rsf([KRse, Rs0e, KRsh, Rs0h],phi)

    ## choose on of the two by commenting out
    Is = Is_exp([KIl, Is0], phi)
```

```
    #Is = Is_lin([KI1, Is0], phi)

    return I*Rs + Vt0*kB*77./e * np.log(I/Is+1)
```

Source code A.3 – Minmal example to calculate the forward voltage of diode D1 at a constant current current of 18 kA and a 1 MeV neq. fluence of $\Phi_{\mathrm{neq}} = 10^{14}\,\mathrm{cm}^{-2}$.

```
# == Calculate Uf == #
ForwardVoltage = Uff(FitCoeffsExp[0], 1e14, 18e3)
print(ForwardVoltage)
```

Source code A.4 – Example for a plot of the calculated values. The example plots the forward voltages of diodes D1, D2 and D4 as a function of the 1 MeV neq. fluence at a current of 18 kA for and a 1 MeV neq. fluence levels of $\Phi_{\mathrm{neq}} = 10^{13}\,\mathrm{cm}^{-2}$ to $\Phi_{\mathrm{neq}} = 10^{15}\,\mathrm{cm}^{-2}$.

```
# === plot example === #
import matplotlib.pyplot as plt

fig1 = plt.figure()
ax = fig1.add_subplot(111)
ax.set_ylabel("$U_f$ (V)")
ax.set_xlabel("$\Phi_{neq}$ (cm$^{-2}$)")

phi = np.linspace(1e13,1e15,100)
If = 18e3

# Diode D1
ax.plot(phi, Uff(FitCoeffsExp[0], phi, If), label="Diode D1")
# Diode D2
ax.plot(phi, Uff(FitCoeffsExp[1], phi, If), label="Diode D2")
# Diode D4
ax.plot(phi, Uff(FitCoeffsExp[3], phi, If), label="Diode D4")

ax.legend()
plt.show()
```

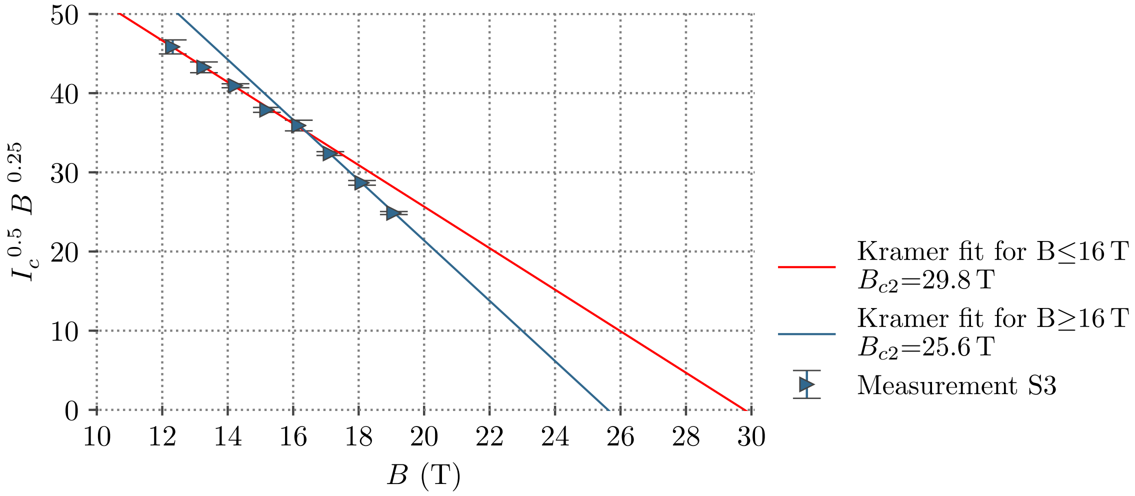

Figure A.1 – Critical current measurement results of sample S3 from batc B1 in Kramer representation as in Eq. 4.15 with two linear fits. The linear fit in red represents a fit to data where $B \leq 16$ T, the blue line represents a fit to data where $B \geq 16$ T.

A.2 Kramer fit analysis for sample B1-S3

Sample S3 from the Nb_3Sn batch B1 showed an unusual behaviour in the critical current measurements. A kink in the measured curve was visible around 16 T as shown in Fig. A.1. The Kramer fit analysis on both the lower field region $B \leq 16$ T and the upper field region $B \geq 16$ T was performed and the results for the upper critical field B_{c2} are shown in the figure legend. A non physical value larger than the theoretical upper critical field at zero temperature (≈29.5 T) is observed from the fits on the lower field region. The result of the upper field region is very close to the theoretical value at 4.2 K of 25.9 T and seems more plausible.